Effect of aeroelasticity on the acoustic signature of TOP contoured rocket nozzles in overexpanded conditions

M. Formidabile

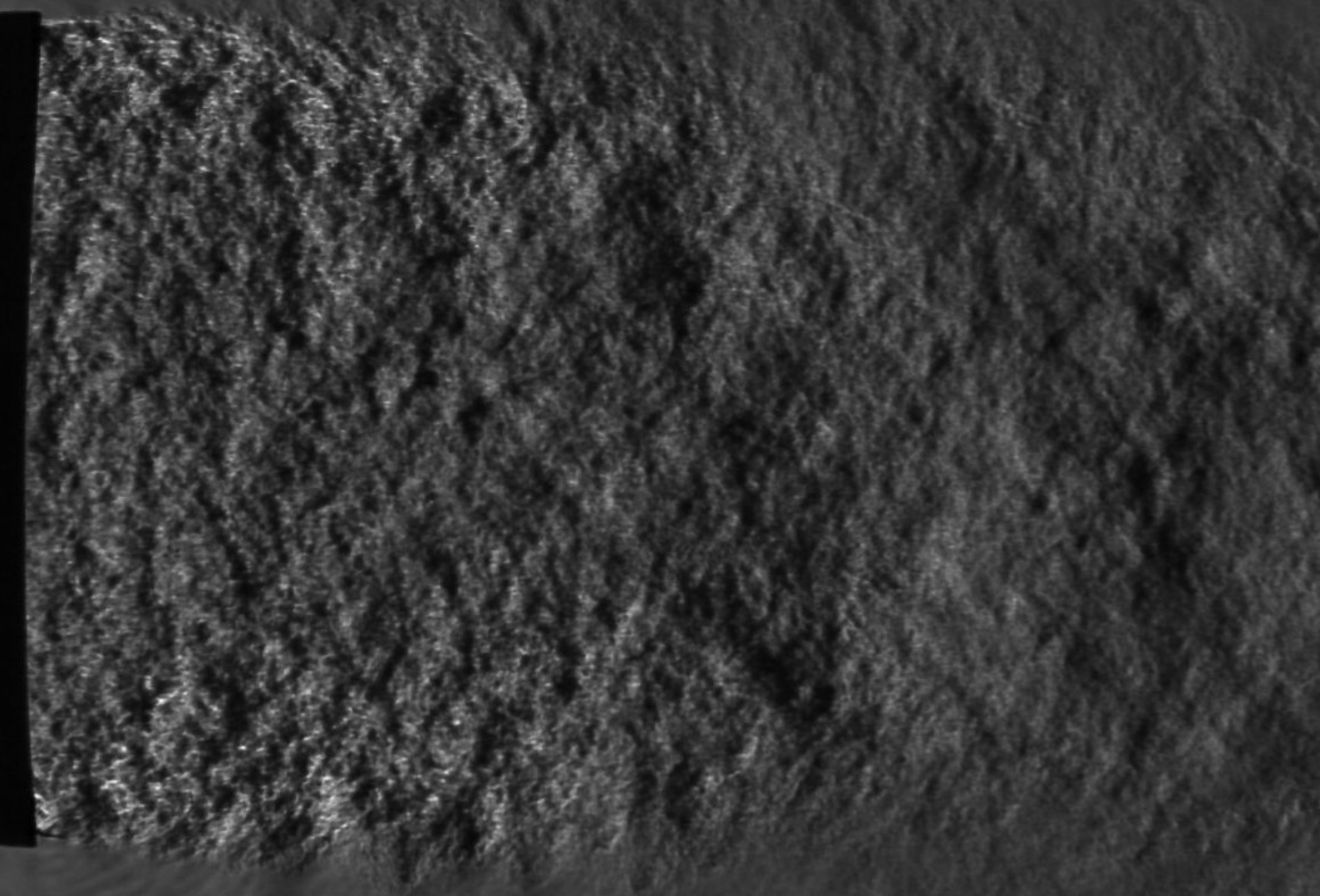

TU Delft

Effect of aeroelasticity on the acoustic signature of TOP contoured rocket nozzles in overexpanded conditions

by

M. Formidabile

in partial fulfillment of the requirements for the degree of

Master of Science
in Aerospace Engineering

at the Delft University of Technology
to be defended publicly on May 22, 2023 at 14:30

THESIS COMMITTEE:

Chair:	Dr. Ir. B. W. Van Oudheusden
Supervisors:	Dr. Ir. F. F. J. Schrijer
	Dr. Ir. W. J. Baars
Examiner:	Dr. I. Langella

Cover: Acoustic waves seen from a Schlieren frame (Personal image)

An electronic version of this thesis is available at `http://repository.tudelft.nl/`.

TU Delft

Acknowledgements

This project marks the culmination of my aerospace studies and my time in Delft. Although this was a one year long effort, many more years and encounters were needed before I could cross path with this fascinating topic. It all started on a summer day when I was reading about combustion instabilities in rocket engines. I recall not understanding a single word, but, as I kept on thinking back to it, I decided I would have made everything I could to work on a project that would bring me as close as possible to figuring it out.

And I would not be here today recounting this achievement if it wasn't for the immense trust that Prof. W. Baars and Prof. F. Schrijer have had in me. Thank you for giving me this opportunity: your experience and encouragements have been essential in pushing me explore and understand research areas that were previously hidden to me. I really hope I did this project justice. On a similar note, I would like to extend my thanks to the other committee members, Prof. B. Van Oudheusden and Prof. I. Langella, for taking the time to read this thesis.

This was an experimental project, and the biggest lesson I have learnt is that it really takes a *village*. That is why I would like to express my gratitude for the technical support staff of the HSL for the invaluable help that they were generous enough to offer me while I was setting up my experiments: thank you Dennis Bruikman, Peter Duyndam, Frits Donker Duyvis and Henk-Jan Siemer. On a similar note, I would like to also thank Ed Rossen, Peter den Dulk and Rob van der List from the DEMO lab, who manufactured some of the components I designed, and Victor Horbowiec for his support in the Composites Lab.

Next, I would like to thank Jurij Sodja for his enthusiasm and availability in letting me arrange the ground vibration test campaign and for entrusting me to Stefan de Boer, who saved me countless times during the setup phase.
In the same vein, I also have my fellow colleague Oliver Pearse to thank, for introducing me to the ASCENT test rig and for sharing numerous suggestions on running the facility and on manufacturing nozzles.
Furthermore, having spent almost 2 months in the ST-15 wind tunnel to set up and run my experiments, I definitely owe a great debt of gratitude to all the people who have passed by my desk and shared invaluable advice. Among the many, special thanks go to Prof. Andrea Schiacchitano, Gabriel Gonzalez and Edoardo Saredi for their help with using DaVis and to Alessandro D'Aguanno and Giulio Dacome for assisting me with the setup and for their troubleshooting skills. I am also grateful for those times Joachim Bron, and many others, were there with me to *make some noise*.
Finally, I cannot thank Luis Laguarda enough for his invaluable input in the last stretch of this work, which has greatly benefited from our intense technical discussions of the past weeks.

On a personal note, I would like extend my gratitude to all the professors and PhD students I have met in the HSL and that have made me understand what dedication and real passion for research truly mean. Thanks especially to Ata Başkaya, Giulio Dacome and Jane Bulut for their friendship and for our lunch and coffee breaks together.

For someone who likes hiking, I really thrive from stimulating challenges and steep paths. Yet, this was by far the highest mountain I ever climbed, and so I feel even more privileged to stand here and experience such a feeling of accomplishment. From up here the sky is clear, and looking down I am happy to see all the people who have helped me reach this goal: *dank jullie wel!*

M. Formidabile
Delft, 12th May 2023

Abstract

Thrust Optimised Parabolic (TOP) contoured nozzles, with large area-ratios, are commonly employed in rocket propulsion systems as they feature an excellent thrust-to-weight ratio, making their design versatile enough to be operated under a broad range of altitudes. A significant shortcoming to this design, however, is that, during the startup and shutdown transients of a Liquid Rocket Engine (LRE), and to a lesser extent also of a Solid Rocket Motor (SRM), the internal nozzle flow progresses through a series of overexpanded flow states - commonly referred to as Free Shock Separation (FSS) and Restricted Shock Separation (RSS). These have been documented to produce critical loads associated with asymmetric flow separation and Shock Wave - Boundary Layer Interaction (SWBLI). Nozzle wall deformations, and their aeroelastic coupling to the flow, have also been found to greatly contribute to exacerbate the vibroacoustic loading at which payload and vehicle structures are subjected to when the engine is operated at off-design conditions. Ignition and lift-off phases, in fact, produce the highest amounts of acoustic energy. Yet, historically, the intricate nature of the different flow states that characterise ignition, combined with a limited understanding of supersonic jet noise phenomena, has made empirical noise prediction approaches difficult to be compiled in reliable and versatile methodologies. Advancements in the understanding of the phenomenology of jet noise and in computer technologies has led to promising results in recent numerical studies aimed at characterising the acoustic environment around launch pads. However, these, together with a number of improved empirical models, still assume full-flowing conditions, thereby placing little emphasis in accounting for the increased noise levels occurring during startup. In this context, experimental investigations in a laboratory environment still represent an important tool for rocket noise studies. Nevertheless, the few that have been conducted in the past have all employed thick-walled metal nozzles in which structural vibrations are absent and fluid-structure interactions suppressed.

Given the importance of understanding how the interaction between the developing flow and the vibrating nozzle walls has an effect on supersonic noise generation and propagation, this thesis work aims at proving that the acoustic loading of TOP contoured nozzles during startup and shutdown operations is greatly dependent on nozzle compliancy. This is demonstrated by means of cold flow tests on a stiff-walled aluminium nozzle, which serves as a baseline test case, and on a urethane-based compliant walled nozzle, both featuring the same TOP contour and having equal gasdynamic properties. Test are conducted under comparable flow conditions and test parameters are measured by means of acoustic and optical techniques. Simultaneous recordings are performed and include the nozzle-wall deformation, by means of stereoscopic tracking of tracers on the nozzle lip, the imprint of the near-field acoustic signature, by means of arrays of pressure-microphones, and Schlieren imaging of the jet plume. Measurement data allows for a Fourier decomposition of the nozzle lip displacement and of the acoustic pressure field in azimuth. Reconstruction of the instantaneous plume development enables the identification of the main flow structures responsible for noise generation.

Comparison of results between the two test articles highlights a different spectral content and directivity pattern. Correlation between the structural displacements and the acoustic signal, together with the use of Dynamic Mode Decomposition (DMD), quantitatively aids the investigation of how Fluid Structure Interactions (FSI) have an impact on the generation of an aeroelastic tone at 180 Hz. Findings suggest that its production is the result of the periodic thickening and thinning of the shear layer owing to the heightened flapping motion of the nozzle lip preceding RSS transition, driven by an intensified shock foot instability. The outcome of this work offers a clearer understanding on the noise generation mechanisms in rocket engines during transient operations, while providing crucial validation data for Computational Aero Acoustics (CAA) and FSI simulations on similar nozzles.

Contents

List of Figures

List of Tables

Acronyms

BBSN	Broadband Shock Noise	3, 24–27, 29, 30, 34, 64, 65, 67, 68, 80, 81
CAA	Computational Aero Acoustics	v
CFD	Computational Fluid Dynamics	20
CSD	Computational Structural Dynamics	20
DMD	Dynamic Mode Decomposition	v, 76–78, 80
EER	End Effect Regime	2, 3, 14, 16, 36, 42
FFT	Fast Fourier Transform	57, 58
FRF	Frequency Response Function	40, 41, 51, 52
FSI	Fluid Structure Interactions	v, 4, 77, 79
FSS	Free Shock Separation	v, 2, 3, 7, 9, 11, 14, 16–18, 22, 25, 34, 35, 46, 67, 69, 80
GVT	Ground Vibration Testing	5, 40, 51, 60, 61, 72, 79, 80
IPR	Iterative Particle Reconstruction	6, 54–56, 80, 81
LRE	Liquid Rocket Engine	v, 7
MAC	Modal Assurance Criterion	61
MIF	Mode Indicator Function	51
MLMM	Maximum Likelihood estimation of a Modal Model	52
MOC	Method Of Characteristics	8
NPR	Nozzle Pressure Ratio	1, 5–7, 11–13, 16, 18, 25–27, 30, 36, 37, 42, 49, 51, 57, 62–67, 70, 80
OASPL	Overall Sound Pressure Level	3, 30–32, 34, 44, 62, 66, 67, 80
OASWL	Overall Sound Power Level	32
OTF	Optical Transfer Function	54, 55
PIV	Particle Image Velocimetry	55, 81
PSD	Power Spectral Density	57, 58
PTU-X	Programmable Timing Unit	47
PTV	Particle Tracking Velocimetry	46, 55
RAM	Random Access Memory	47
RSS	Restricted Shock Separation	v, 2, 3, 7, 9, 11, 13, 16–18, 28, 34, 35, 46, 66–69, 72, 73, 81
SLS	Space Launch System	3
SPSL	Sound Pressure Spectrum Level	58, 65
SRM	Solid Rocket Motor	v, 7
SRS	Shock Response Spectrum	17
SSME	Space Shuttle Main Engine	2, 3, 8, 20, 31
SWBLI	Shock Wave - Boundary Layer Interaction	v, 3, 7, 9–11, 17

TIC	Truncated Ideal Contour	8, 9, 11, 25, 27, 29
TOC	Thrust Optimised Contour	8, 9
TOP	Thrust Optimised Parabolic	v, 2, 3, 5, 8–14, 25, 27–29, 35, 44, 68, 79, 81
TR	Transonic Resonance	29, 66, 80, 81
VAL	Vibroacoustic Loading	2, 3
VSC	Volume Self-Calibration	54
WPS	Wavelet Power Spectrum	64, 68, 69, 71

List of symbols

Roman symbols

A	Area	m^2
a	Speed of Sound	m/s
D or d	Diameter	m
$D.I.$	Directivity Index	dB
f	Frequency	Hz
F	Thrust	N
J	Inertia	kgm^2
j	Complex unit	–
k	Spring constant	N/m
k	Wavenumber	$1/m$
l	Length	m
L_C	Potential core length	m
L_P	Sound peak location	m
L_S	Supersonic core length	m
L_w	Overall sound power level	m
M	Mach Number	-
M_c	Convective Mach Number	-
M_m/M_a	Mechanical / Aerodynamic torque	kgm^2/s^2
m	Mass	kg
$\dot{m}$	Mass Flow Rate	kg/s
p	Pressure	Pa
p'	Pressure fluctuation	Pa
q	Dynamic pressure	Pa
r	Radius	m
R	Specific Gas Constant	$J/kg/K$
R_d	Dynamic Response Factor	–
s	Shock spacing	m
SPL	Sound Pressure Level	dB
St	Strouhal number	–
Sr^*	Modified Strouhal number	–
t	Time	s
T	Temperature	K
u	Streamwise velocity component	m/s
v	Velocity	m/s
w	Vorticity	$1/s$
W_{OA}	Acoustic power	W
x	Streamwise coordinate	m
y	Transverse coordinate	m

Greek symbols

α	Time fraction of high-frequency unsteadiness	-
β	Shock parameter	–
∂	Partial derivative	–
Δ	Change in variable	-
ϵ	Nozzle geometric expansion	-
η	Efficiency	-
$\sum$	Sum	-

γ	Specific Heat Ratio	-
γ_{xy}	Linear coherence	-
Γ	Locus of shock points on a shock polar	-
Λ	Gol'dberg number	–
μ	Mach angle	deg
∇	Gradient	–
ν	Kinematic viscosity	m^2/s
ρ	Density	kg/m^3
τ	Shear stress	Pa
τ_n	Natural oscillation period	s
ϕ	Polar angle between nozzle exit plane and microphone	deg
ω_n	Natural angular frequency of an uncoupled system	Hz
ω_n/Ω_n	Natural angular frequency of a coupled aeroelastic system	Hz

Subscripts & Superscripts

0	(Superscript) Total quantity
0	(Subscript) Interaction origin
1	Pre-shock condition
2	Post-shock condition
$*$	Referring to throat
a	Referring to ambient conditions
c	Referring to settling chamber
e	Referring to the nozzle exit
f	Final quantity
i	Initial quantity
in	Referring to the interaction region
p	At constant pressure
pl	Referring to the plateau region
s	Referring to separation
v	At constant volume
w	Referring to the wall
∞	Referring to the free stream

1

Introduction

Launch vehicles, commonly referred to as *rockets*, are one of the most complex systems that humans have been able to envision and create. In order to escape Earth's gravity, they all rely on a propulsion system to produce momentum. Chemical propulsion systems typically consist of a propellant feed system, a combustion chamber and an exhaust nozzle. The purpose of this latter component is that of converting the propellants' internal energy into kinetic energy, accelerating the gases as much as possible before reaching the nozzle's exit plane, thereby producing thrust. These principles are neatly expressed in two equations that form the foundation of rocket theory:

$$\Delta V = v_e \ln \frac{m_i}{m_f} \tag{1.1}$$

$$F = \dot{m} v_e + \left(p_e - p_a\right) A_e \tag{1.2}$$

With the objective of maximizing the rocket's ascent velocity ΔV, and neglecting aerodynamic drag, two main design principles can be deduced from Equation 1.1, commonly referred to as the *Tsiolkovsky equation*: first, the exhaust velocity v_e of the combustion gases ought to be maximized - this is also advantageous to produce high thrust, as seen in the momentum term of Equation 1.2. Second, as the ΔV is proportional to the ratio of initial and final mass, it can be inferred that a launch system should, therefore, lose as much mass as possible through propellants expulsion and, most importantly, should be left with as little mass as possible. This is why, when designing a rocket, one of the main requirements concerns the minimization of structural mass.
A few final considerations on thrust refer to the second term of the thrust equation (Equation 1.2): first, assuming nominal operations, p_e remains constant and is a parameter given by the thrust chamber design; on the other hand, as rockets move through the atmosphere, the ambient pressure p_a decreases, and therefore the pressure term is not constant: it can be positive during underexpanded operations, null during optimum expansion, and negative during overexpanded operations. It can be shown that maximum thrust is achieved during optimal expansion, that is, when $p_e = p_a$. Furthermore, according to the Ideal Rocket Theory, in the context of momentum flux from the nozzle exit, it is desirable to expand the gases to the lowest possible p_e in order to achieve the highest possible v_e:

$$v_e = \sqrt{\frac{2\gamma}{\gamma - 1} \cdot R \cdot \mathrm{T_c} \cdot \left[1 - \left(\frac{\mathrm{p_e}}{\mathrm{p_c}}\right)^{(\gamma - 1/\gamma)}\right]} \tag{1.3}$$

A direct consequence of designing thrust chambers for low exit pressures is that engines operating at sea level experience overexpanded flow states, which lead to the formation of shock and expansion waves. What is even more relevant in the context of this research effort is that, during the startup phase of liquid propellant engines, the pressure in the combustion chamber, due to the turbopump system still accelerating to achieve the required pressure head, is ramping from ambient to the nominal operating pressure defined by the design Nozzle Pressure Ratio (NPR). Albeit for just a few seconds, this causes the exhaust gases to expand to pressures which are lower than the design p_e, which might result in flow separation given by the extreme adverse pressure gradients experienced by the flow at the shock front (Frey and Hagemann, 1999). Asymmetric flow separation is, in fact, at the basis of violent vibroacoustic loads generation. In some occasions off-axis forces generated as a result of unsteady flow separation have caused catastrophic consequences: some notable examples are, for instance, that of the J-2S engine which was torn from its gimbal structure (Nave and Coffey,

1973), or that of the Space Shuttle Main Engine (SSME) for which fatigue cracks and rupturing of the nozzle's coolant feed lines were identified; similar issues have also been reported on the Japanese LE-7A (Watanabe et al., 2002) or the European Vulcain engines (Hagemann et al., 2003).

These engines have one relevant thing in common: they all utilize high area ratio nozzles with TOP contours; these nozzles are commonly employed in many modern day launch vehicles owing to, not only their high reliability, but mainly their performance: they feature an excellent thrust-to-weight ratio, making this design versatile enough to be operated under a broad range of altitudes (Rao, 1958). A significant shortcoming to this design, however, is that during startup and shutdown operations, the internal nozzle flow progresses through a series of flow states (FSS, RSS and End Effect Regime (EER)) that are known to produce critical loads both structurally and acoustically, on the vehicle itself, as well as on the surrounding environment.

Figure 1.1: TOP contoured nozzles of the Space Shuttle Columbia's three RS-25s engines, following the landing of STS-93 (*Courtesy*: NASA)

As a matter of fact, another direct consequence of the intricate nature of the different flow states that characterise ignition concerns the high intensity acoustic loading that the rocket experiences while still on the launch pad. Rocket launches, in fact, generate huge amounts of acoustic energy during all phases of sub-orbital flight. However, ignition and liftoff phases have been documented to be those inducing the highest amounts of Vibroacoustic Loading (VAL) due to main engines startup, even more than during transonic and Max-Q phases.

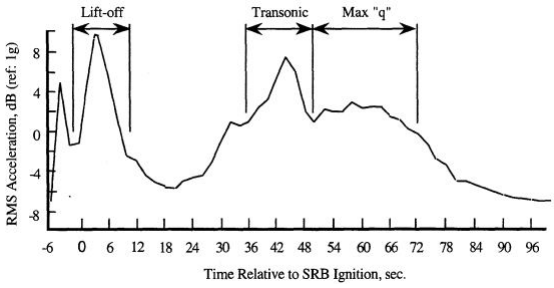

Figure 1.2: Space Shuttle vibroacoustic loading data compiled by Himelblau et al. (2001)

These elevated acoustic levels do not just represent a threat for the surrounding environment, but are especially critical for the payload that the launcher carries. As documented by Onoda and Minesugi (1997), in fact, Overall Sound Pressure Level (OASPL) measured inside the payload bay of the Japanese MV solid launcher can reach up to 144 dB. Similarly, during static fires of the Saturn V first-stage engines, an approximate OASPL of 204 dB was recorded, making it one of the loudest sounds ever generated (Lubert et al., 2022). Even though satellite components are designed to withstand highly energetic broadband waves, acoustic levels of this kind are still responsible for 60% of first day failures (Griffin et al., 2000), and it is estimated that a 40% satellite mass increase is typically required just to survive the launch environment (Henderson et al., 2003).

The most straightforward solution to avoid catastrophic structural failures or environmental sound pollution would be to design a rocket nozzle that can withstand vibroacoustic loads. This, however, is not a simple task, as there are a number of different parameters that have an effect on VAL, including jet parameters, noise mitigation practices, launch pad and vehicle geometry, and so forth. During overexpanded operations, then, geometric and plume physics parameters are even harder to gauge. In fact, the intricate nature of SWBLI makes it very difficult to predict said loads for a specific nozzle design, and not always sub-scale tests can give an accurate representation of the vibroacoustic characteristics observed in full scale engines. Furthermore, considering the financial burden of performing field testing, only a few are typically carried out, at the later stages of the design process, when not many changes are still possible. Therefore, given the large VAL uncertainty on both vehicle and payload, design optimization is extremely challenging, and, historically, all of these difficulties have often practically translated into the choice of adopting high safety margins, which, however, result in an increased overall launch vehicle mass (Lubert et al., 2022).

Great uncertainly also arises from the difficulty of characterising jet noise. As far as acoustic prediction is concerned, in fact, the recent pioneering work of Seiner and Yu (1981), Zaman et al. (2002), Raman (1999) and many more, has shown how supersonic jets behave rather differently compared to their subsonic counterpart. Together with turbulence mixing noise, additional noise generation mechanisms can be identified in supersonic jets operating at off-design conditions, that include shock-associated noise and resonance. Overall, rocket plumes and supersonic jets share many similarities. Nevertheless, the acoustic radiation phenomena of rocket plumes are substantially different from those of other supersonic jets, such as afterburning turbojets, due to the extreme conditions at which rockets typically operate, thus often making prediction approaches difficult to be compiled in reliable methodologies.
For over 50 years, the work of Eldred (1971), published in the NASA SP-8072 report, has represented the foundation for the prediction of launch vehicles acoustics, and it is still being used today in noise preliminary analyses. It was compiled as a mean to gather existing data from the Apollo programs, but a few major shortcomings that arose from wrong assumptions and a limited understanding of jet noise during those years, were revealed early on when gross disagreements where found between the predictions and the measured data of the SSME (Lubert et al., 2022).

The recent development of the next generation of launch vehicles, such as the European Ariane VI and VEGA or NASA Space Launch System (SLS) has revived interest in the topic. This time, given the performance improvements of supercomputers, the design of launch pads based on the prediction of the acoustic environments surrounding it, was possible through numerical studies (Casalino et al., 2012). Nevertheless, regardless of the current limitations of this type of analyses, these studies have mostly focused on predicting noise propagation and interaction with launch pad structures and, together with a number of improved empirical models (Plotkin et al., 2009, McInerny and Ölçmen, 2005), they all assume full-flowing or adapted flow conditions, placing little emphasis in predicting transient ignition noise.

Some recent efforts, both numerically and experimentally, have recognised the need for a comprehensive characterisation of the ignition transient; yet they have primarily focused on assessing the nature and magnitude of the side loads that develop during the different overexpanded nozzle flow states (Baars et al., 2012, Baars and Tinney, 2013, Wang et al., 2014, Östlund et al., 2004, Zhao et al., 2013). On the other hand, only slim efforts have been made to study the acoustic signature emitted during the ignition transient of TOP contoured nozzles, as listed in Table 1.1. From these studies, it has emerged that various noise sources are present in the noise spectra of overexpanded rocket nozzles undergoing FSS and RSS states, as well as the EER. These can be traced back to supersonic jet noise sources, with a predominance of Broadband Shock Noise (BBSN)

at steeper angles and turbulent mixing noise at shallower angles to the jet axis. Nevertheless, regardless of their specific research objectives, all these studies share some commonalities, that bring about a number of limitations in the results that they provide. Apart from the study of Tinney et al. (2017), they all employ thick walled metal nozzles in which structural vibrations are suppressed, and, as such fluid-structure interactions are absent.

Table 1.1: Summary of previous cold flow acoustics studies on sub-scale TIC/TOP contoured nozzles during overexpanded operations

Study	Contour	Material	r^* [mm]	ϵ	NPR @ FSS –>RSS	Unsteadiness frequency [kHz]	Source
1	TIC/TOP	Aluminum	19.04	38	30	0.1 - 30	Donald et al. (2014)
2	TOP	AL-6061-T6	6.35	30.29	24	0.1 - 20	Canchero et al. (2016a)
3	TOP	AL-6061-T6	6.35	30.29	24	-	Canchero et al. (2016b)
4	TOP	AL-6061-T6	6.35	30.29	24	0.1 - 20	Rojo et al. (2016)
5	TOP	Polyurethane	6.35	30.29	24	0.1 - 20	Tinney et al. (2017)
6	TIC/TOP	Acrylic glass	10	20.48	24	0.1 - 3	Stark et al. (2019)

In this sense, Rojo et al. (2016) have given a preliminary demonstration that to be able to fully characterise the acoustic loads in a laboratory environment, such that consistent parallels can be drawn with full scale studies, compliant walled nozzles ought to be used, in place of the more traditional thick-walled ones, in order to account for aeroelastic effects. Yet, the only existing experimental study that was performed using a compliant walled nozzle consisted in taking single-point measurements from a condenser-type microphone placed at the nozzle base (Tinney et al., 2017). These measurements, however, cannot detect the direction of the approaching sound waves and, if not coupled with synchronised recordings of the unsteady structural dynamics and of the developing flow, they cannot provide detailed information on what are the sources of a possibly different acoustic signature.

(a) Nozzle test stand

(b) Fully instrumented TOP contoured stiff nozzle

Figure 1.3: Fully anechoic chamber and high-speed jet lab at The University of Texas at Austin used for TOP contoured nozzles environmental testing by Donald et al. (2012)

To the best of the author's knowledge, research on the combined effect of FSI on the acoustic imprint of rocket nozzles during transient operations has not been performed. Therefore, aiming to fill this research gap, full advantage of the ASCENT nozzle test rig, situated in the High Speed Laboratory of the Delft University of Technology is taken to further investigate the acoustic signature of lab-scale overexpanded compliant walled rocket nozzles during cold flow operations. This research represents a valuable asset to further understand what impact structural vibrations have in sound production, and which are the effects on jet noise given by a deforming nozzle structure, thereby offering valuable information to be used in noise prediction models, as well as numerical studies, which traditionally only account for jet noise sources in full-flowing conditions, and employ stiff structures.

1.1. Problem statement

Having defined the necessary background, the research objective of the current work is summarised as follows:

Identify the dominant vibroacoustic features of stiff and compliant walled sub-scale TOP contoured rocket nozzles during transient startup and shutdown operations, to assess which role different flow regimes play in sound production and radiation and what impact fluid-structure interactions have on the noise generated by a supersonic overexpanded jet.

Based on the overall objective, the thesis work aims at answering the following research question:

Which effects does aeroelasticity have on the vibroacoustic loads generated during the transient startup and shutdown of TOP contoured rocket nozzles?

This question can be further broken down into multiple detailed sub-questions:

- **What does the acoustic signature of compliant and stiff walled nozzles look like during overexpanded flow operations?**
  - What is the evolution with NPR of the acoustic pressure field radiated by the two nozzles during transient startup and shutdown operations? How do their acoustic power spectra differ in terms of emitted energy?
  - Which noise components (turbulent mixing noise, BBSN, resonance) can be recognised in their spectra and how is the flow responsible for their generation?
  - At which NPRs are the highest acoustic levels reported during transient tests and for which of the two nozzles?
- **How do the vibrations of a compliant nozzle affect its acoustic radiation compared to a stiff nozzle during overexpanded flow operations?**
  - Which are the natural frequencies at which the employed test articles naturally resonate?
  - What is the azimuthal mode composition of the structural vibrations for the compliant walled nozzle during transient and steady test runs? How does the activity of the structural azimuth modes vary with NPR and which modes are dominant in the considered range? At which frequencies are structural oscillations the highest?
  - What is the azimuthal mode composition of the radiated acoustic field for the two nozzles? At which frequencies is an increased acoustic activity revealed?
  - What effects do flow asymmetries have on noise propagation?
  - How and at which frequencies do flow-structure interactions affect the acoustic field? How is the flow responsible for a different acoustic pressure field?
  - In the presence of aeroelastic tones, what is their noise producing mechanism?

1.2. Research methodology

In relation to the objective presented, the experimental work will practically comprise a series of different types of investigations which, in turn, combine a number of measurement techniques, each of which will serve as a tool to understand selected aspects of the acoustic-fluid-structure problem.

Table 1.2: Direct outputs per measurement system

Measurement system	Variables measured
Accelerometers + hammer	Frequency response function
Total pressure sensor	Total pressure in settling chamber (NPR)
Microphone array	Acoustic pressure
Lip tracking	Compliant nozzle lip displacement
Schlieren	Density gradients (shock locations, shear layer development)

The test articles that are going to be subject of the investigation comprise a stiff walled aluminium nozzle, which serves as a baseline test case, and a urethane-based compliant walled nozzle. They both feature the same TOP contour and have equal gasdynamics properties. First, using accelerometers and a hammer tip, which provide a measure of the structure's frequency response function, Ground Vibration Testing (GVT) is performed on both articles in order to characterise their modal behaviour and infer on their natural frequencies and resonant properties. Next, at the core of the research, two distinct cold flow test campaigns are

conducted using the ASCENT nozzle test rig situated in the High Speed Laboratory of the Delft University of Technology. The rig allows to perform steady and transient startup and shutdown ramps by taking advantage of compressed air stored in a pressure vessel outside of the facility. In both occasions, a setup that allows for the simultaneous recording of data from a number of systems is put in place. First, as a preliminary quantification of the acoustic field and nozzle deformation, a line array of microphones located at the side of the jet, and a stereoscopic lip tracking system are employed, respectively. The former detects acoustic pressure fluctuations and allows for the determination of the main noise mechanisms and acoustic waves directivity; the latter, only used when testing the compliant walled nozzle, allows for the measurement of the instantaneous displacement of its lip, by means of a non-intrusive full field optical technique, which uses the Iterative Particle Reconstruction (IPR) algorithm (Wieneke, 2012) for the reconstruction of the unsteady nozzle dynamics. By performing transient ramps, it is possible to obtain a full overview of the acoustic signals in relation to the instantaneous NPR, by means of a joint time-frequency analysis (Torrence and Compo, 1998), that allows for extraction of the spectral energy content from the acoustic pressure fluctuations. At the same time, given the azimuthal spatial configuration of the nozzle lip tracers, decomposition of the wall vibration in terms of time-dependent Fourier-azimuthal mode coefficients is achieved by spatially Fourier transforming the markers fluctuation in azimuth. In this way, specific fluid-structural phenomena and NPRs of interest are identified. Finally, the last campaign consists in employing, again, a similar configuration for the lip tracking system. However, this time, the microphones are placed azimuthally around the jet plume, to allow for an analogous spatial reconstruction of the acoustic signal in azimuth. Additionally, images of the flow are acquired using Schlieren photography (Settles, 2001), such as to qualitatively observe the development of the plume during both fixed and transient test runs, and to quantitatively infer on flow discontinuities. Finally, based on the results obtained from this configuration, correlations of the structural and acoustic modes, together with a comparison between the stiff and compliant nozzle cases, will quantitatively highlight the impact that aeroelasticity has on noise directivity and spectral signature.

1.3. Report outline

An overview of the contents of the present report is hereby presented. First, from literature findings, chapter 2 and chapter 3 give an overview of the main theoretical principles upon which the current thesis work is based. Specifically, the former illustrates the foremost flow phenomena that are responsible for the heightened dynamic loads on the nozzle structure during the ignition transient. The latter provides a timely review of the current state-of-the-art in supersonic jet noise and launch vehicle acoustics while also offering insights into the inherent difficulties of jet noise prediction. This is followed, in chapter 4, by a thorough description of the experimental methodology that has been employed to achieve the outlined objective. In particular, test articles, facilities, setup of the measurement systems and their working principles are detailed. Given the large amount of data gathered during testing, chapter 5 summarises the main processing strategies that have been implemented to obtain usable information from the measured variables and outlines the theoretical frameworks employed to extract meaningful results from each typology of data. Next, chapter 6 presents the results of the experimental investigation: the discussion consists in comparing the findings with the existing literature and in critically assessing the observations made, while highlighting the main advances on the topic. Finally, in chapter 7, conclusions are summarised, research questions answered and indications for future research investigations given.

2

Flow separation in rocket nozzles

It has been vastly demonstrated that for NPR values lower than nominal, different flow and shock patterns can develop inside nozzles. These flow states can occur in both SRMs and LREs, but are more prolonged in the latter due to the longer time needed for the turbine to produce the required pressure head in order for the nozzle to flow full (Donald et al., 2012). Full flowing conditions correspond to the situation when the internal flow structure is no longer changing with increasing back pressure as the incipient separation point has reached the nozzle lip. Broadly, two categories of flows can be identified: flows featuring FSS and flows featuring RSS, whose occurrence largely depends on the nozzle contour that is being used (Frey and Hagemann, 1999, Nave and Coffey, 1973).

In light of this, a preliminary overview of commonly employed nozzle contours is given in section 2.1. Next, FSS and RSS flows are introduced and discussed in section 2.3 and 2.4, respectively. To better complement this subject, a review of SWBLI is also given. Finally, an overview of the dynamic loads that such regimes cause on the engine's structure is given in section 2.5. This summary will aid the interpretation of the results obtained in the current work that are going to be further discussed in subsection 6.2.1.

2.1. Nozzle contours

In practical applications, the need for highly performing rocket engines has spurred interest to design various nozzle shapes, to obtain the best compromise between thrust production and weight.

Even if, in a design optimization, many constraints shall be considered - manufacturing techniques, overall dimensions, cooling requirements, and many more - nozzle weight reduction remains, in fact, one of the primary objectives: heavy nozzles are hard to fabricate and handle and cause significant loads and power requirements on the TVC system. For these reasons, a reduction in length is typically deemed appropriate. The issue with this, however, is given by the difficulty to minimize efficiency losses, which, in a rocket engine are, broadly, of three kinds: viscous drag losses are due to viscous forces at the nozzle wall which act against the main flow direction. Kinetic losses are due to the difficulty to reach chemical equilibrium given the high velocity of the combustion gases that are readily accelerated out of the combustion chamber.

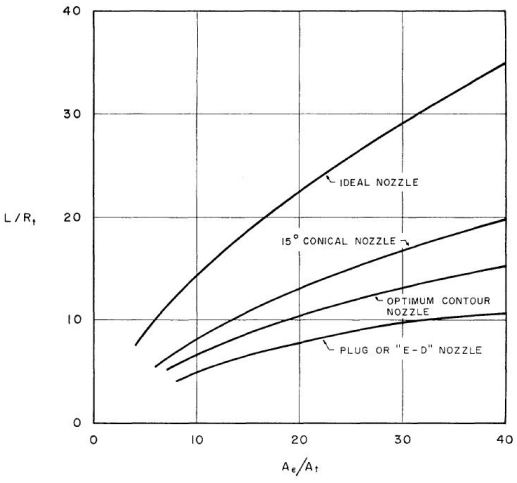

Figure 2.1: Length comparison for various types of nozzles (Rao, 1961)

Divergence losses, finally, are due to the incorrect alignment that the exhaust flow has with respect to the nozzle axis. The flow, instead of travelling *straight* as a 1-D flow, has a radial component, not involved in

thrust production. Overall, the efficiency is a combination of the three:

$$\eta_{nozzle} = \eta_{div} \cdot \eta_{kin} - (1 - \eta_{visc})$$

Length reduction mainly conflicts with minimising the divergence losses, while drag and viscous losses greatly benefit from a shortening of the nozzle. In conclusion, great part of the past 50 years of research has focused its efforts on finding optimal contours that, even with constrained lengths, are able to deliver high thrust: practically, lengths can be reduced if a suitable way to expand the flow immediately downstream of the throat, while using the remaining contour to only turn the flow to achieve uniform axial flow, is found (Rao, 1961).

Given the subsonic velocities in the convergent part of rocket nozzles, their design is relatively simple and mainly determined by the combustion chamber requirements. The main precaution is taken to minimize pressure losses and that is generally obtained through a rounded and smooth curvature, which is able to keep the flow attached. Greater complexity and accuracy, on the other hand, are required for the design of the divergent part of the nozzle. Many different contours have been designed, including plug and annular nozzles; however, given their relevance in this research effort, only Truncated Ideal Contour (TIC) and TOP nozzles are going to be treated here. TIC nozzles, in fact, were employed, for instance, in the Viking and RD-0120 engines, but they have also been extensively used during experimental campaigns (Frey and Hagemann, 1999, Donald et al., 2012, Martelli et al., 2010); the TOP contour, on the other hand, is the one typically used in large area-ratio nozzles, such as the Vulcain and the SSME.
In the following sections an overview of the most commonly employed nozzle contours is given, together with their associated design techniques. Finally, details on the type of flow they are able to generate given their internal characteristics are discussed.

2.1.1. Truncated Ideal Contour Nozzles

Contrary to conical nozzles, which tend to register high thrust losses given the large flow divergence at the exit plane, ideal contour nozzles are designed in such a way to turn the flow closer to the axial direction, thereby reducing thrust losses.

Their profile is obtained by using the Method Of Characteristics (MOC); as shown in Figure 2.2, the initial expansion in the divergent section occurs along the circular arc TN, which also represents a solid boundary onto which the non-slip condition is applied. The line TO, instead, defines a constant Mach number line. In this way, the kernel TNKO is entirely defined by the throat conditions. Finally, the last characteristics NK, together with the Mach number at K, are determined by the specific design criteria for the exit flow. In order to *complete* the contour, that is, line NE, a series of control surfaces P^iE^i are defined such that the mass flow across N^iP^i equals that across P^iE^i, until an axial flow is obtained.

In order to obtain an axial flow, considerable lengths are necessary, which makes these ideal contour nozzles heavy. Furthermore, the thrust contribution of the last portion of the nozzle is negligible, or worse, it might even give a negative contribution when the friction forces outweigh the pressure forces. For this reason, the nozzle is effectively *truncated* and, typically, in the industry, the method proposed by Ahlberg et al. (1961) is employed: it allows to graphically select the optimum contour for a given number of design parameters (C_f, ϵ...).

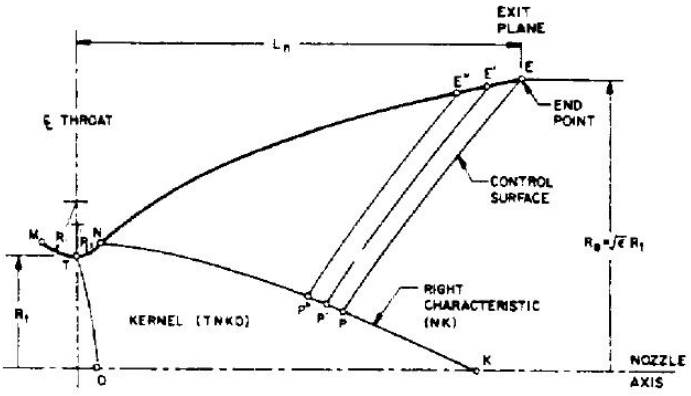

Figure 2.2: Ideal contour nozzle (Huzel and Huang, 1967)

2.1.2. Thrust Optimized Parabolic Contour Nozzles

Rao (1958) proposed a skewed-parabola approximation of the Thrust Optimised Contour (TOC) nozzles; this was done not only to further simplify the approach to design nozzles, but also to optimise the contour for greater thrust generation. Given a certain nozzle efficiency and length fraction it is possible to select the

optimum expansion ratio. Then, given ϵ, the initial circular arc angle θ_N and the final parabolic contour angle θ_E follow accordingly. The contour NE is finally obtained from the parabola equation:

$$\left(\frac{y}{r^*} + b\frac{x}{r^*}\right)^2 + c\frac{x}{r^*} + d\frac{y}{r^*} + e = 0$$

What makes TOC and TOP contours drastically different is the presence, in the latter, of an internal shock upstream of the last left running characteristic line. It forms due to a geometrical discontinuity between the throat circular arc and the divergent parabolic contour: because the compression waves form and coalesce before the last characteristic line, they have an impact on the nozzle wall properties, yielding a higher wall pressure at the exit, and proving as an effective solution for flow separation in sea-level operated engines.

2.2. Shock wave - Boundary layer interactions

Before detailing the mechanisms that characterise FSS and RSS flows, an overview of SWBLIs is warranted. As pointed by Baars et al. (2012), in fact, nozzles with wall-separated flows feature an internal shock system that can be associated with SWBLIs. Also Martelli et al. (2020) argue that the wall pressure spectra obtained in their computational efforts on an overexpanded TIC nozzle are qualitatively similar to canonical SWBLI measurements obtained for different geometries and shock topologies.

Babinsky and Harvey (2011) list 5 different types of basic interactions that can occur between a shock wave and a boundary layer, that can lead to flow separation. It should be, however, remarked that SWBLIs do not necessarily lead to flow separation - in that case only a *weak* interaction is occurring. SWBLIs, in fact, should be regarded as a *competition* between the viscous forces in the flow, the velocity distribution in the boundary layer and the pressure gradient: if shocks are weakly interacting, the shear stress is able to counteract their action by transferring enough momentum from the outer-velocity regions of the flow, thereby keeping the boundary layer attached.

In the context of flow separation in rocket nozzles due to SWBLIs, the type of interaction worth examining more in depth is the one involving an incident shock impinging on a wall. Although this mechanism differs from the one implicated in FSS, it introduces some features and phenomena that will ease the understanding of the workings of a nozzle separated flow.

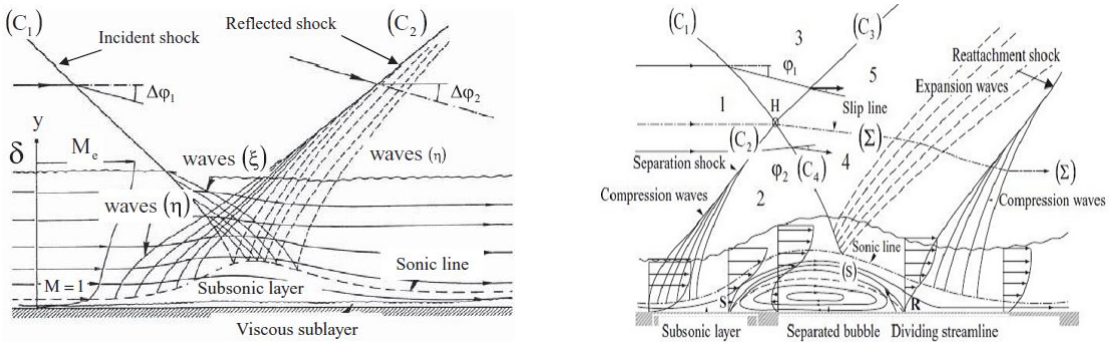

(a) Detail of the incident shock penetrating the boundary layer

(b) Flow separation induced by an incident shock

Figure 2.3: 2D SWBLI schematics (Babinsky and Harvey, 2011)

An incident shock wave (defined as C_1 in Figure 2.3) can, in fact, induce separation. Due to the presence of a velocity gradient within the boundary layer, warranted by the no-slip condition at the wall, as the shock enters this region, it bends due to the progressively lower Mach numbers of the flow, and based on the $\theta - \beta - M$ expression, it increases its angle while decreasing its intensity, until it vanishes as it approaches the sonic line, where it takes the name of *shock foot*. The pressure rise through the shock, which steadily declines towards the wall, is experienced upstream and is transmitted all the way to the subsonic layer, which dilatates. This configuration acts as a ramp, thereby inducing compression waves to form in the outer supersonic region of the flow, which eventually coalesce to form a reflected shock C_2. if C_2 is strong enough, it can cause the incoming flow to stagnate or even reverse, leading to separation. At the same time, accordingly with Edney's

classification (Edney, 1968), C_1 and C_2 interact at point H, producing the reflected shocks C_3 and C_4, as depicted in Figure 2.3b. This latter shock penetrates the separated region. However, the discontinuity between the near-constant pressure registered in the separated region and the pressure rise across the shock, leads to the formation of an expansion fan, which, in turn, pushes the shear layer towards the wall, and, if strong enough, reattaches the flow in R.

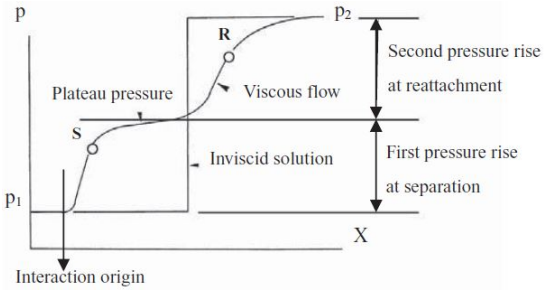

Figure 2.4: Wall pressure distribution in a shock separated flow (Babinsky and Harvey, 2011)

Low frequency unsteadiness of shock wave - boundary layer separated flows

Until now, the discourse around SWBLIs and flow separation has been treated without considering how these phenomena are inherently unsteady. The descriptions given in section 2.2, in fact, only offer a somewhat *idealized* picture, that is, the interactions between shocks and boundary layer, together with the characteristic lengths of the observations, have been treated as if they are *frozen* in space and time.
These kind of interactions, however, have been shown to cause an exacerbation of thermal, acoustic and structural loads on a wide number of different flow configurations (Babinsky and Harvey, 2011), including overexpanded rocket nozzles (Baars et al., 2012, 2015), and, to a great extent, the cause is attributable to their underlying unsteadiness. Verma et al. (2006) found that origin of side loads in overexpanded TOP nozzles can be directly attributed to the unsteady characteristics of both the separation and the reattachment shock, which cause an unsteady pulsation of the separation point, thereby resulting in azimuthally varying wall pressure distributions.

Models proposed by Schmucker (1984a) and Dumnov (1996) for the assessment of side loads are indeed mostly based on the consideration of said local unsteadiness, while Zaman et al. (2002) and Raman (1999) argue that shock-flow unsteadiness is accompanied by the emission of acoustic tones, giving rise to acoustic phenomena like *transonic resonance* and *screech*. Similarly, Martelli et al. (2020), Olson and Lele (2013) and Bakulu et al. (2021) argue that the unsteadiness is rooted in an aeroacoustic feedback loop between the internal separation shock and the external shear layer; these views will be later touched upon in chapter 3.

Figure 2.5: Azimuthally dependent incipient separation lines (*Courtesy*: NASA)

In broad terms, SWBLI unsteadiness is understood to be associated with the low-frequency oscillations of the shock foot of the separation shock within the interaction region, and study on the topic has involved both practical designers (Olson and Lele, 2013, Eitner et al., 2021, Du et al., 2021) - low frequency pressure peaks can become undesirable if a coupling with aerostructures' eigenfrequencies occurs - and fundamental researches, as well (Dolling, 2001, Clemens and Narayanaswamy, 2014): today, in fact, there is still no general agreement as to which are the sources of unsteadiness (Clemens and Narayanaswamy, 2014). Two opposite currents prevail in the recent literature: one associating low pressure unsteadiness to an upstream mechanism related to the large scale coherent turbulent structures in the upstream boundary layer (Erengil and Dolling, 1994, Ganapathisubramani et al., 2007), the other attributing the unsteadiness to a downstream mechanism, namely the breathing motion of the separation bubble (Piponniau et al., 2009). As pointed by Clemens and Narayanaswamy (2014), however, since both mechanisms have been observed, a model accounting for both upstream and downstream mechanisms is more plausible, with the upstream influences

being reduced with increasing separation lengths, while the downstream ones being exacerbated for strongly separated flows.

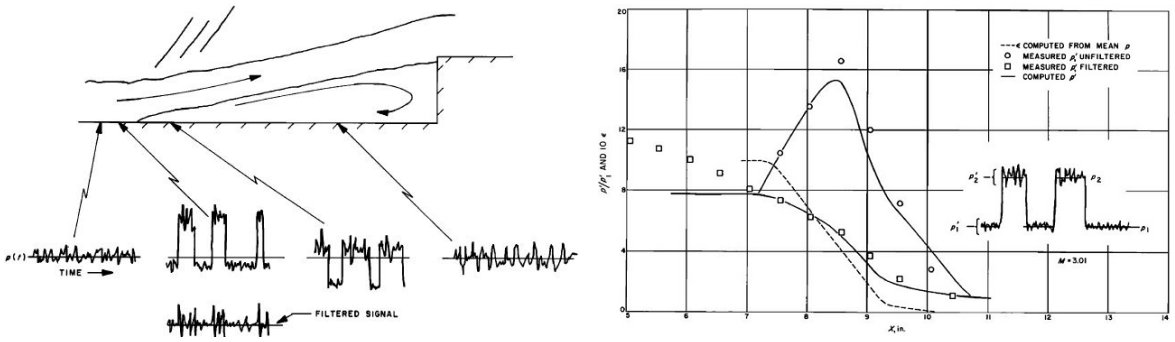

(a) Pressure time series in the separated region

(b) Pressure distribution in the interaction region

Figure 2.6: Low frequency unsteadiness (Kistler, 1964)

2.3. Free shock separation

As opposed to RSS, free shock separation can occur in every type of nozzle contour because it does not require the presence of an internal shock, and is mainly governed by SWBLIs. This flow state, in fact, was first documented by Arens and Spiegler (1963) on a conical nozzle. After that, copious literature has followed to investigate the phenomenon both experimentally (Nave and Coffey, 1973, Hagemann et al., 2003, Baars et al., 2012) and numerically (Martelli et al., 2020, Aghababaie and Theunissen, 2015), primarily on TIC and TOP nozzles, whereas an extensive historical survey on flow separation in rocket nozzle research has been carried out by Stark (2013). Even though a FSS state does not require an internal shock to be induced, in TOP nozzles, compared to other contours, it might result in a different shock configuration given the interactions that the internal and the separation shock might have.

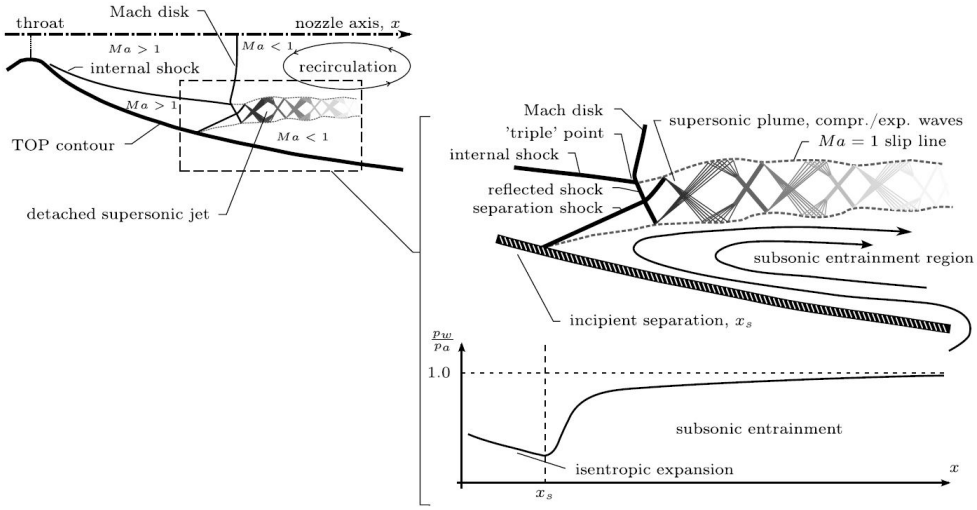

Figure 2.7: Internal shock structure during FSS in a TOP nozzle (Baars et al., 2012)

FSS typically occurs at low NPRs; Tinney et al. (2017) determined that in a lab-scale TOP nozzle with $r^* = 6.35$ mm and design Mach number of 5.24, separation occurs at NPR values as low as 6. When the pressure in the settling chamber is still not nominal, the flow in the divergent section is isentropically expanded to lower pressure values than expected from the on-design conditions; operations at sea-level readily induce the flow to separate at x_s given the strong adverse pressure gradient between the expansion region and the subsonic entrainment region. The interactions that unfold from this point on are closely related to the physics of SWBLIs: the separated region, in fact, can be thought of as a ramp which induces the formation of compression waves in the incoming supersonic flow that coalesce to form an oblique separation shock. In a 3-D geometry such that of a nozzle, oblique shocks have a conical shape (Martelli et al., 2020) and the direct reflection of said

shock leads to the formation of a Mach reflection towards the nozzle's centerline, across which the flow slows to subsonic velocities.

Nasuti and Onofri (2009) point that this always occurs in axysymmetric geometries, even for weaker waves, since a shock, propagating towards the axis, increases its strength, so much so that the only possible reflection is a Mach reflection. Furthermore, as depicted in Figure 2.7, the Mach disk is *curved*. This is a direct consequence of flow non-uniformities upstream of the shock, which occur when the Mach disk lies in the kernel region, characterised by a slightly negative radial gradient: to satisfy the Rankine-Hugoniot jump equations, if a negative pressure gradient in the radial direction exists upstream, also the downstream flow will show a pressure gradient in the same direction and, to smooth said gradients, the shock moves as indicated in Figure 2.8, showing a curved profile (Nasuti and Onofri, 2009).

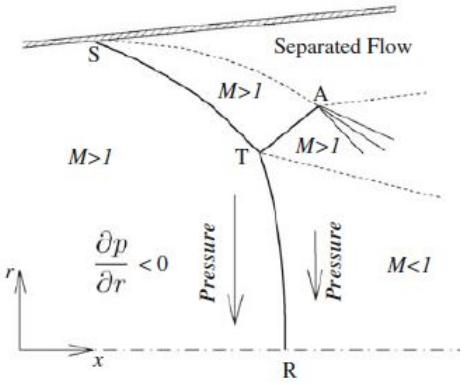

Figure 2.8: Non-uniform flow direct Mach reflection (Nasuti and Onofri, 2009)

In TOP nozzles, a further interaction ensues from the presence of the internal shock. As seen from Figure 2.7, internal shock and Mach disk interact to form a reflected shock at a "*triple-point*" and this latter shock, in turn, interacts with the separation shock. Finally, a series of compression and expansion waves develops hereon in the separated region between the recirculation zone and the entrainment region. If the NPR remains low, the flow does not reattach and the FSS behaviour is clearly visible from the exhaust plume in which the flow is not attached to the nozzle lip. As far as the static wall pressure is concerned, various measurements (Tinney et al., 2017, Donald et al., 2012, Baars et al., 2011) have shown that the flow expands isentropically until the incipient separation, upon which it starts rising again to near ambient pressure, given the influence of the entrainment flow.

2.3.1. Separation criteria

For the specific case of free shock separation, a number of empirical or semi-empirical models have been developed from experimental data to predict the occurrence of separation, a collection of which has been gathered by Stark (2013), as shown in Figure 2.9.

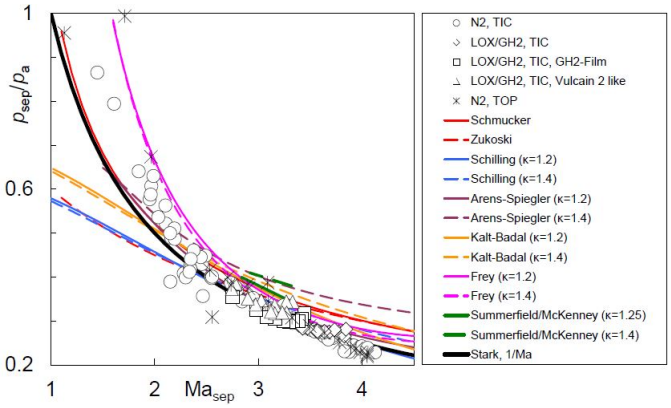

Figure 2.9: Summary of separation criteria available from literature (Stark, 2013)

Such a criterion, in fact, is necessary to determine at which wall pressure separation occurs; in this way, also information on the separation location and duration can be gathered and, possibly, associated with increased loading periods. An early criterion was first proposed by Summerfield et al. (1954) who suggested that separation occurs when the wall pressure is in the range of 40% of the ambient pressure. Among the many criteria that have followed, the ones that have been more vastly employed are the ones of Schmucker (1984b), described in Equation 2.1 and Stark and Wagner (2009), seen in Equation 2.2.

$$\frac{p_s}{p_a} = (1.88M_s - 1)^{-0.64} \tag{2.1}$$

$$\frac{p_s}{p_a} = \frac{1}{M_s} \tag{2.2}$$

In particular, Stark and Wagner (2009) carried out cold flow studies and later demonstrated the fitness of their criterion for both cold and hot turbulent flows and showed improved prediction, compared to the Schmucker criterion, as shown in Figure 2.10. Furthermore, an effort was taken to compare the applicability of the criterion for film cooled nozzles and a longer separation zone was recognized.

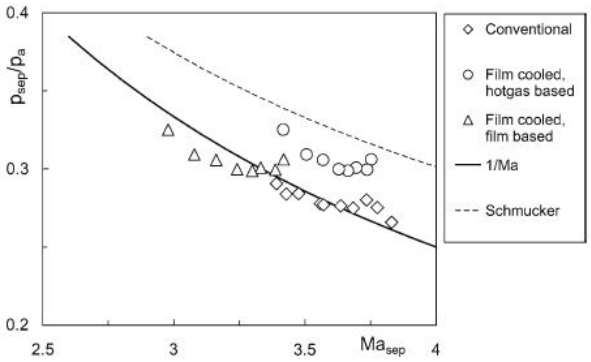

Figure 2.10: Hot flow separation pressure versus wall Mach number with and without film cooling (Stark and Wagner, 2009)

Nevertheless, as pointed by Östlund (2002), in spite of the enormous progress of the last 50 years, significant scatter of the data is still noticeable. He attributes this issue to the fact that all the proposed criteria tend to use a single expression to describe *two* separate mechanisms that are responsible for the pressure rise. The pressure recovery, in fact, should be divided into two contributions, one for the pressure rise p_{in}/p_{pl} over the interaction length, and one for the pressure rise p_{pl}/p_a in the recirculation zone, which is affected by the downstream conditions and the nozzle geometry. Although some authors (Östlund, 2002, Zukoski, 1967) have addressed this matter by proposing improved variants, these still represent *empirical* criteria, which lack a *physical* model that accounts for other influencing parameters. This is why, for phenomena of this kind, the *generalised free interaction theory* by Carriere et al. (1968) offers a promising model to build upon. Said theory, in fact, cannot be used *alone* as it predicts the length of the separated region, rather than that of the interaction zone - dependent on downstream conditions - which, more fittingly, is needed for correlation with p_{in}/p_{pl}. Since a similar model is not available for contoured nozzles, empirical formulas have been proposed by Vasilev et al. (1969). More recently, Reijasse and Birkemeyer (2001) instead, have developed a correlation between the height of the mixing layer at the nozzle exit and the interaction length; this result can be used together with Carriere et al. (1968) law to predict the pressure distribution in the interaction zone.

2.4. Restricted shock separation

TOP nozzles can feature an additional flow state when the NPR is increased. Transition to RSS, for a long time, was believed to only occur on sub-scale models during cold flow testing (Frey and Hagemann, 1999); the conclusion that such flow state is independent on working gas or nozzle size was only drawn when RSS transition was first documented on the full scale J-2S engine in 1973 (Nave and Coffey, 1973).

In broad terms, transition to the RSS state can occur when the incipient separation point is located further downstream due to the higher pressure in the settling chamber. Given these conditions, the reflected shock - originated at the intersection between Mach disk and internal shock - has gained more strength before interacting with the separation shock. In this way, a radial outward momentum is transmitted to the fluid, which, if greater than the momentum induced by the separation shock - that drives the flow away from the wall - can reattach the flow (Frey and Hagemann, 2000). A supersonic plume, within which a succession of

expansion and compression waves develops, now travels along the wall, bounding, underneath it, an annular separation bubble. Depending on the pressure, the flow might separate and reattach again, thus creating a second separation bubble.

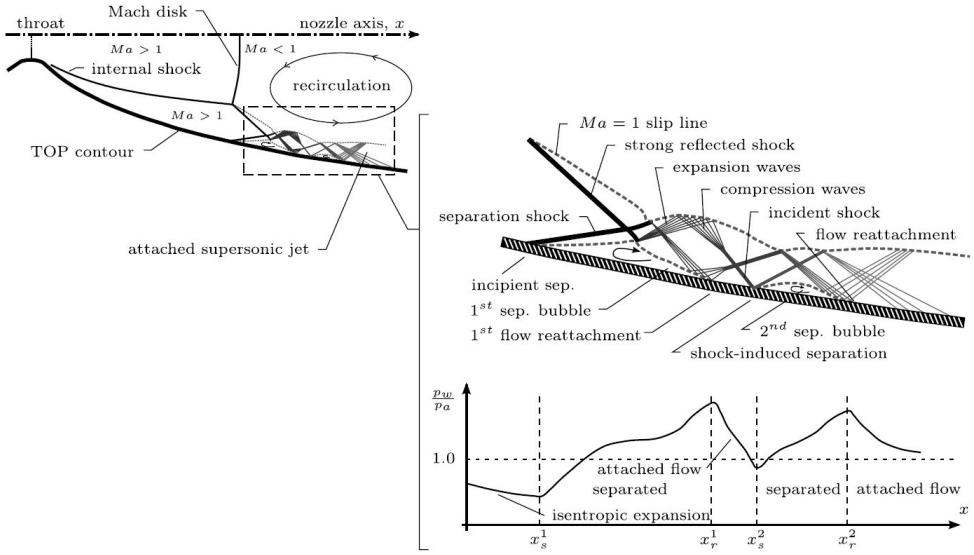

Figure 2.11: Internal shock structure during RSS in a TOP nozzle (Baars et al., 2012)

As seen from Figure 2.11, the static wall pressure shows a more complex pattern and it can be seen rising above ambient conditions due to shock waves impinging on the wall. The plateau pressure, on the other hand, is significantly below ambient pressure due to the recirculation bubble being bounded by the supersonic jet above it, and this is also what causes the separation point to be located further downstream as opposed to the FSS case. Upon further increasing the pressure ratio, the separation point and, consequently, the recirculation bubble, move further downstream, up until the reattachment point is at the nozzle exit. When said condition occurs, the bubble opens up again to the ambient flow, bringing the pressure in the recirculation zone to a higher value. This readily moves the separation point further upstream, thereby bringing again the flow to a FSS state. Such re-transition from RSS to FSS is often referred to as EER. If the flow pulsates between FSS and RSS, a *partial* RSS or pRSS is established.

Nasuti and Onofri (2009) and Frey and Hagemann (1999) have attributed the transition to the curved profile of the central Mach disk. The two groups, however, address the flow behaviour differently.

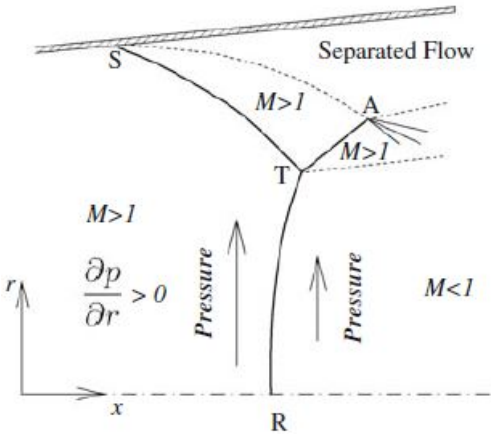

Figure 2.12: Non-uniform flow inverse Mach reflection (Nasuti and Onofri, 2009)

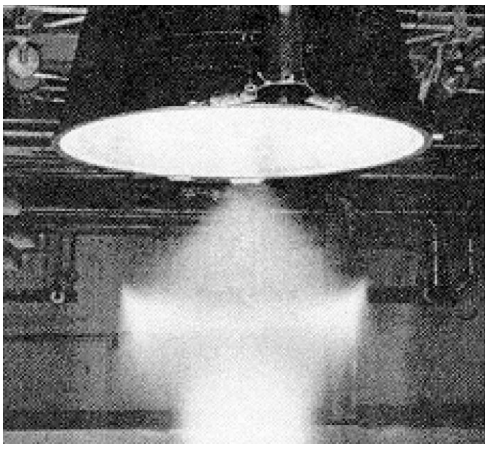

Figure 2.13: Cap-shock pattern observed during testing of the Vulcain engine at DLR Lampoldshausen (Frey and Hagemann, 1999)

Nasuti and Onofri (2009) explain that, for TOP contours, the presence of an internal shock induces a positive

radial pressure gradient downstream of the kernel region, as seen in Figure 2.12. Due to said upstream flow non-uniformity, the Mach disk experiences an inverse reflection in order to smoothen the gradients across it. Behind the shock, the pressure on the axis is lower than anywhere else in the subsonic bubble, and therefore, the flow experiences an adverse pressure gradient along the axis. A major consequence to said velocity and entropy gradients is the formation, according to Crocco's theorem ($u \times w = v\nabla p_0$), of a *rotational* flow downstream of the inverse reflection, whose vorticity increases as the non-uniformities upstream become larger. The occurrence of said trapped vortex in the nozzle core, as a result of an upstream mechanism, is often referred to as *inviscid separation* - as opposed to viscous separation occurring in the boundary layer - and is what causes the flow to deviate from the centerline, thereby reattaching the flow. The appearance of the trapped vortex pattern has been confirmed by the numerical simulation of Chen et al. (1994).
Frey and Hagemann (1999), on the other hand, find a different explanation for the transition, through the observation of the exhaust plume. In particular, they attribute the transition to the so-called *cap-shock* pattern, only observed in the plume of TOP nozzles with a strongly 2-D flowfield, during overexpanded operations, and interpreted as an inverse Mach reflection of the internal shock.

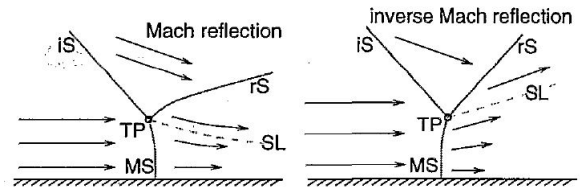

Figure 2.14: Direct Mach reflection and inverse Mach reflection (Frey and Hagemann, 1999)

Frey and Hagemann (1999) have pointed that the cap shock pattern, at the origin of flow transition between FSS and RSS states in overexpanded rocket engines, can be interpreted as an *inverse* Mach reflection. This latter shock pattern differs from a direct Mach reflection in that the slip line that originates at the triple point between the incident shock, the reflected shock and the Mach stem is towards away from the wall, as shown in Figure 2.14.

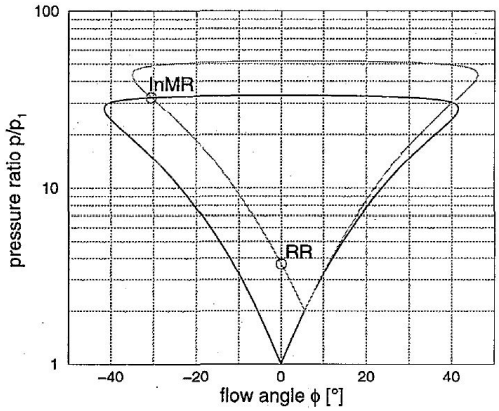

Figure 2.15: Shock polar of an inverse Mach reflection (Frey and Hagemann, 1999)

Furthermore, as opposed to a direct reflection, the Mach stem for an inverse reflection is slightly canted downstream, with a convex upstream curvature. This allows the flow downstream of the triple point to be naturally curved downward; in this way, the reflected shock does not need to turn the flow and is strong enough to produce a subsonic flow, as also seen from the polar in Figure 2.15.
For low pressure ratios, in fact, the internal shock interacts with the strong normal shock at the nozzle centerline, thereby producing a reflected conical shock, that is, the cap-shock. Multiple evidences suggest that said reflected shock should be interpreted as an inverse reflection, rather than a regular one. First, by comparing the numerical simulation in Figure 2.16 and the shock polar in Figure 2.15, the hypothesis of a regular reflection (RR) is discarded given the existence of a triple point. Furthermore, the flow upstream of the Mach stem is non-uniform, while the stem is straight: this means that the shock is straight at the centerline but, from the point of view of the flow, which is divergent towards the triple point, it is convex, as opposed to regular reflec-

tions which are concave. Finally, similarly to what Nasuti and Onofri (2009) had suggested , the decreasing strength of the Mach stem from the centerline to the triple point, coupled with the adverse pressure gradient on the nozzle axis behind the strong shock, induce a vorticity behind the inverse Mach reflection, which reattaches the flow to the wall.

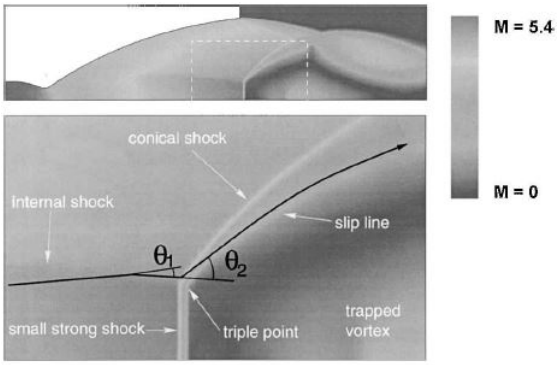

Figure 2.16: Numerical simulation of the Vulcain nozzle flow (Hagemann et al., 2002)

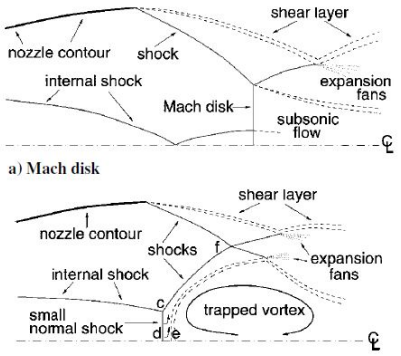

Figure 2.17: Shock patterns in the exhaust plume of TOP nozzles (Frey and Hagemann, 2000)

2.4.1. Hysteresis effect

Numerous experimental campaigns on the J-2S subscale model (Frey and Hagemann, 1999, Hagemann et al., 2003, Frey and Hagemann, 2000, Hagemann et al., 2002) have attested that an *hysteresis* behaviour exists at start-up and shut-down, that is, transition between FSS and RSS occurs at different pressure ratios, depending whether the pressure is increasing or decreasing. More specifically, from the wall pressure distributions, Hagemann et al. (2002) observed that, during start-up, the transition from FSS to RSS occurs at a higher pressure ratio, compared to the backward retransition from RSS to FSS during shut-down, which, on the contrary, occurs at a lower NPR. EER, on the other hand, does not seem to be affected by hysteresis. A similar trend can be observed from the numerical simulations of Martelli et al. (2010): comparing the two images in Figure 2.18 it can be seen that during the up-ramping operations, the flow transition from FSS to RSS - the transition being represented by the intersection of the internal shock with separation shock at the triple point - at a higher NPR compared to the retransition from RSS to FSS during the down-ramping operations.

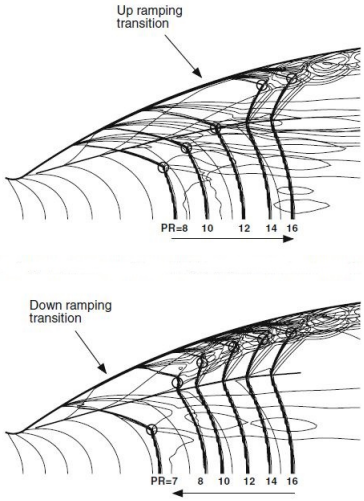

Figure 2.18: Hysteresis explained through Mach contour lines (Martelli et al., 2010)

One possible explanation for said phenomenon is to consider the plateau pressure p_{pl}, which, as detailed in section 2.3 and 2.4, has a lower value during the RSS state compared to the FSS state. In the framework of up-ramping and down-ramping operations, this translates to the possibility of having two different p_{pl} values for the same p_c/p_a, and, correspondingly, two different separation locations. Frey and Hagemann (2000) suppose that during down ramping operations, being the separation point moved downstream when the flow is in RSS, the separation shock is *shorter*; in this way, the conical shock, being *longer*, can impart more momentum towards the wall, thereby keeping the flow attached for longer.

2.5. Dynamic loads and aeroelastic effects

A peculiar behaviour that has been consistently observed in both sub-scale and full-scale rocket nozzles during transient operations involving a separated flow concerns the occurrence of increased side loads, which,

in some occasions, have caused severe damage to the engine (Nave and Coffey, 1973, Watanabe et al., 2002, Hagemann et al., 2003), and have often resulted in overconservative designs. Within the frame of the J-2S testing, Nave and Coffey (1973) were the first to make hypotheses as to which could be potential sources of increased loading. Their list, among others, included:

- Flow transition from FSS to RSS and back
- Asymmetric separation line
- Aeroelastic coupling
- Pressure fluctuations in the separated regions due to SWBLI

2.5.1. Loads due to flow transition from FSS to RSS

Only in 1999 Mattsson et al. (1999) were able to experimentally demonstrate that the distinct side-loads peaks in the response spectra are caused by flow transition. Assuming that flow transition from one state to the other requires a finite time, a phase difference, during which one side of the nozzle is still experiencing separation, whereas on the other side the flow has already reattached, might exist. As touched upon in section 2.4, when the flow is in RSS state, the separation point is located further downstream; in this context, it is, therefore, straightforward to infer that, at the beginning of the transition, the wall pressures on the opposite sides of the nozzle are different, with one side experiencing larger pressure loads. Nguyen et al. (2003) found that for both transition and re-transition, the duration of the event is of the order of a few milliseconds ($\approx$ 50 ms), indicating that it is possible to approximate the pressure loads to an instantaneous pulse. More specifically, using the *pulse excitation theory*, and based on the Shock Response Spectrum (SRS) of a nozzle experiencing flow transition, the dynamic response factor $R_d = x_{max}/x_0$, that is, the amplification of the applied load due to the dynamic system, can be approximated by a half-sine pulse (Östlund et al., 2004).

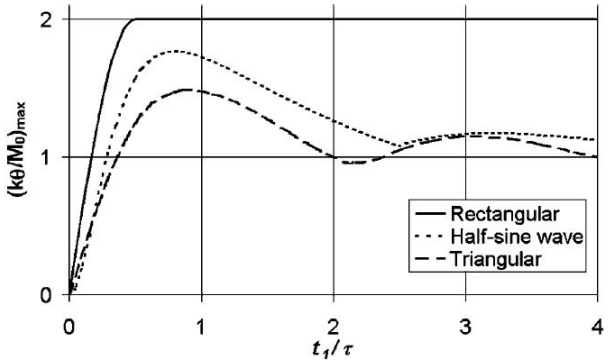

Figure 2.19: Response factor for different pulse shapes (Östlund et al., 2004)

Assuming a pulse duration t_p, a peak load F_0 and that the system can be modelled as a single degree of freedom mass-spring system, of mass m and spring constant k, it can be described via the following equation:

$$m\ddot{x} + kx = \begin{cases} F_o \sin(\pi t/t_p) & t \le t_p \\ 0 & t \ge t_p \end{cases} \tag{2.3}$$

With $\omega_n = \sqrt{k/m}$ being the natural frequency and $\tau_n = 2\pi/\omega_n$ being the natural oscillation period - very small for stiff systems - the solution of the above system can be split into a solution for the forced vibration, when the load is applied, and a solution for the free vibration; from these it becomes clear that the response of the structure is mainly dependent on the pulse duration and the resonant frequency of the structure:

$$\frac{x(t)}{x_{st,0}} = \frac{1}{1-(\tau_n/2t_p)^2}\left[\sin\left(\pi\frac{t}{t_p}\right) - \frac{\tau_n}{2t_p}\sin\left(2\pi\frac{t}{\tau_n}\right)\right] \quad t \le t_p \quad \text{forced vibration} \tag{2.4}$$

$$\frac{x(t)}{x_{st,0}} = \frac{(\tau_n/t_p)\cos(\pi t_p/\tau_n)}{(\tau_n/2t_p)^2 - 1}\sin\left[2\pi\left(\frac{t}{\tau_n} - \frac{1}{2}\frac{t_p}{\tau_n}\right)\right] \quad t \ge t_p \quad \text{free vibration} \tag{2.5}$$

From the above equations and from Figure 2.19 it is evident that when the natural period of the system is close to the pulse duration, significant amplification occurs.

2.5.2. Asymmetric separation line

As previously hinted, when part of the nozzle's internal flow is in RSS state, whereas the rest is still in FSS state, the structure is subjected to an imbalanced load. This physically translates to having a tilted separation line, which in 3D is configured as a zig-zag pattern in azimuth, as seen in Figure 2.5. Based on this observation, Schmucker (1984a) developed a model to quantify the side loads due to asymmetric separation; the formula that he obtained is as follows (full derivation can be found in (Schmucker, 1984a) or (Östlund, 2002)):

$$F_{sl} = 2K_g K_i \frac{r_{sep}}{r^*} r^{*2} \frac{p_{sep}}{p_a} \frac{p_a}{p_c} p_a \left(1 - \frac{p_{sep}}{p_a}\right) \frac{1}{\frac{d(p_w/p_c)}{d(x/r^*)}} \frac{1}{1 - \frac{1+\frac{\gamma-1}{2}M_{sep}^2}{(1.88M_{sep}-1)M_{sep}} \frac{1.2032}{\gamma}} \tag{2.6}$$

K_i is a fluctuation coefficient that needs to be determined experimentally; Schmucker (1984a) found that for the J2-D engine $K_i \approx 0.05$. K_g, instead, describes the shape of the asymmetrical separation line, with:

$$K_g = \begin{cases} 1 & \text{unisymmetry at } 180° \text{ of nozzle circumference} \\ \pi/4 & \text{inclined separation line} \\ 0.3 \div 0.4 & \text{effective value, used by Schmucker in the model} \\ 0 & \text{symmetrical separation line} \end{cases}$$

Aside geometric parameters, such as r^*, one of the principal contributing factors to side loads is the wall pressure gradient $d(p_w/p_c)$: as the NPR is increased and the separation location is moved towards the nozzle exit, the wall pressure gradient is decreased, resulting in increased side loads. The limit case occurs when the forward separation boundary has reached the nozzle exit: in this occasion F_{sl} has its maximum value. Schmucker, in fact, experimentally found that maximum side loads are obtained for chamber pressures 10% ÷ 20% below full flowing pressure.

2.5.3. Effects of aeroelasticity

Up to now, the underlying assumption made in the discourse around increased pressure loads is that of the nozzle having a stiff structure. In reality, however, during actual hot firing of a rocket engine, rather than undergoing only static deformations, nozzles often flex or deform in response to the lateral aerodynamic forces and it is, therefore, important to account for the aeroleastic contribution during analysis efforts. Nozzle's elasticity is one of the contributing factors to the increased loading: a *closed loop* between the mechanical structure of the nozzle and the internal flow might be established when slight variations in wall pressure induce a distortion of the contour, which, in turn, further modifies the wall pressure, thereby resulting in a significant amplification of the initial load.

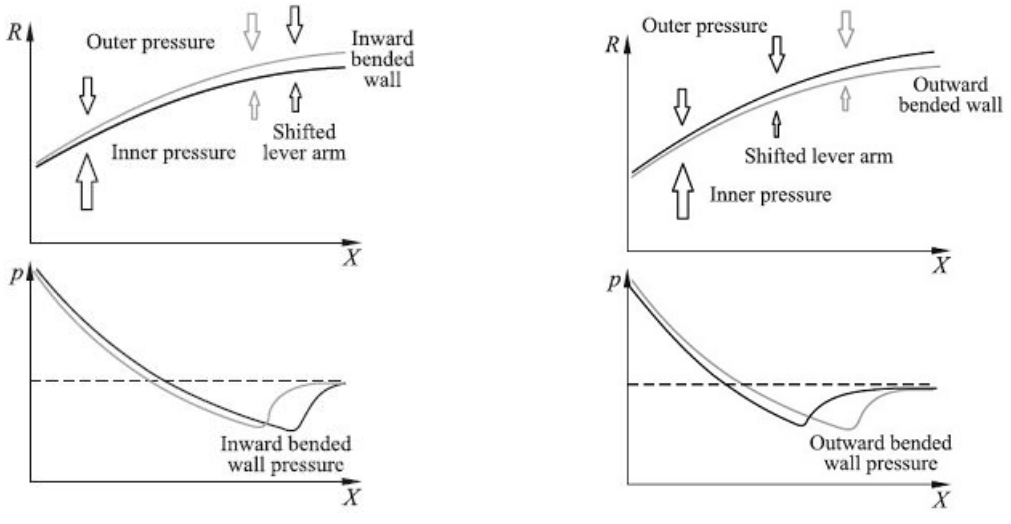

(a) Inward wall deflection

(b) Outward wall deflection

Figure 2.20: Effect of wall deflection in a nozzle separated flow (Génin et al., 2015)

Génin et al. (2015) explain this behaviour by comparing the different scenarios that could be established based on whether the nozzle is full flowing or separated, and aids the understanding of said mechanisms

with a simple visual representation shown in Figure 2.20. If the nozzle is full flowing and presents an inward bent wall, recompression will increase, thereby reducing the pressure difference which is causing the bending; similarly, if it presents an outward bent wall, recompression will be reduced, thereby increasing the pressure difference between the inner and outer wall, such that to induce an inward momentum that decreases the bending. When dealing with nozzle separated flows, however, the disturbances get amplified. For the case of an inward bent wall, the recompression would shift the separation downstream and, assuming that side loads act at the separation point, this would increase the lever arm and consequently, increase the bending force, which would cause further inner deflection. Similarly, for the case of an outward bent nozzle wall, the separation point would shift upstream, decreasing the lever arm, and, therefore, in absence of a restoring force, further increasing the outward deflection. This mechanism was indeed observed during the testing phases of the current research of the current research and a detailed analysis of these findings is going to be discussed in subsection 6.2.1.

The binary behaviour of inward and outward deflections, however, is a simplifying approach: nozzles, in fact, vibrate depending on their natural frequencies, which result in different types of deformations: bending, torsional, axial. Each deformation *mode* have a *fundamental* and several *harmonics*, which, in turn, result in different deformation patterns, as shown in Figure 2.21 specifically for the bending mode, which is the only addressed in this thesis.

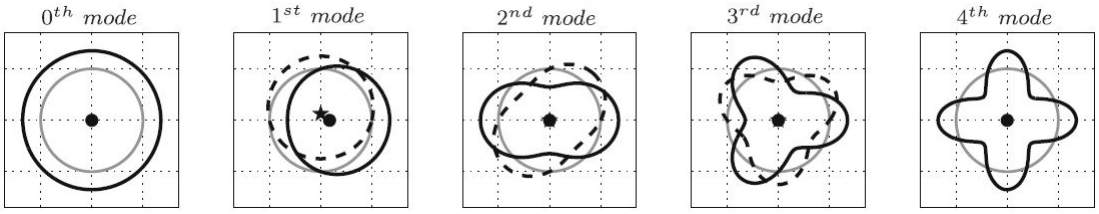

Figure 2.21: Fundamental and higher harmonics of the bending mode: 0^{th} = breathing mode, 1^{th} = pure bending, 2^{th} = ovalization, 3^{th} = triangular mode, 4^{th} = square mode. Dashed lines correspond to the imaginary Fourier coefficients (Baars and Tinney, 2013)

What is even more relevant in this context is that the introduction of a flow in a nozzle makes it a combined system, with resonant properties, that is, eigenfrequencies, different from those of the isolated nozzle system. In the early 1990s, Pekkari (1993) first introduced a model that could predict the stability of the first bending mode of the Vulcain engine and predict the shift in eigenfrequency for the combined system. The model consists of two parts: the first deals with the equations of motion of the thrust chamber when it is subjected to aerodynamic loads, whereas the second accounts for the variation in aerodynamic loads as a result of the elastic deformation of the nozzle contour. Before separation, Pekkari's model computes the pressure shift due to nozzle deformation based on the linearised supersonic flow theory, whereas assumes constant ambient pressure after separation; experimental evidence, however, has shown that this approach tends to overpredict the shift. In this regard, Östlund et al. (2004) have proposed an improvement to the model such that the pressure shift before separation is extracted from 3D Euler simulations, and the separation is assessed simply using the empirical criterion by Summerfield et al. (1954).

Considering that the bending mode is the one most affecting nozzle stability, and assuming that the characteristic timescales of the flow are one order of magnitude larger than the timescales of the system deformations, the coupled system can be assumed to be quasi-static and the equation of motion for the bending of the nozzle is as follows:

$$J_y\ddot{\theta} = M_m(\theta) + M_a(\theta) \tag{2.7}$$

With M_a and M_m being the aerodynamic and mechanical torque respectively. The mechanical torque is nothing but the restoring torque of the spring in the nozzle suspension: $M_m(\theta) = -k\theta$, with k being the spring stiffness.
With $\omega^2 = k/J_y$ being the natural frequency of the isolated nozzle system, and Ω being the eigenfrequency of the coupled system, Equation 2.7 can be rewritten as:

$$-J_y\Omega^2\theta = -k\theta + M_a(\theta) \quad \longrightarrow \quad \left(\frac{\Omega}{\omega}\right)^2 = 1 - \frac{M_a(\theta)}{k\theta} \tag{2.8}$$

The expression for $M_a(\theta)$ is at the core of the model from Pekkari (1993) and Östlund et al. (2004); its lengthy derivation and can, therefore, be found in their referenced work. What is more relevant in the current analysis is that low stiffness favours instability; Equation 2.8, in fact, shows that:

- If $M_a(\theta)/k\theta < 0$, it means that the aerodynamic torque is acting in the opposite direction of the nozzle wall deformation, thereby restoring the system to its initial position. As a result, the coupled system is stiffer and its eigenmode is shifted to a higher frequency $\Omega > \omega$
- If $M_a(\theta)/k\theta \in [0;1]$ it means that the aerodynamic torque is acting in the same direction of the nozzle wall deformation. As a result, the system is weaker and its eigenmode is shifted to a lower frequency $\Omega < \omega$
- If $M_a(\theta)/k\theta > 1$ it means that $(\Omega/\omega)^2 \in \mathbb{C}$, that is, the coupled system becomes aeroelastically unstable and the deformations grow exponentially, until failure occurs

This simple expression can be easily employed to investigate whether a structure has undergone a stiffening or a weakening process. An example of its application is, in fact, provided in subsection 6.2.2 when comparing the coupled system vibration frequency against the one measured during static testing.

Östlund et al. (2004) further observed that aeroelastic effects become significant and cannot be ignored in weak nozzle structures: as observed in Figure 2.22 a nozzle with a low spring constant, designated as *super weak*, becomes unstable when the separation is close to the nozzle exit. Moreover, tests showed that the breathing and the pure bending mode are the one giving the greatest contribution, whereas the square mode has almost a negligible contribution. Even though models have been able to accurately predict the stability of the fundamental bending mode, they are not able to do the same for the higher order modes, which require more complex methods to be evaluated.

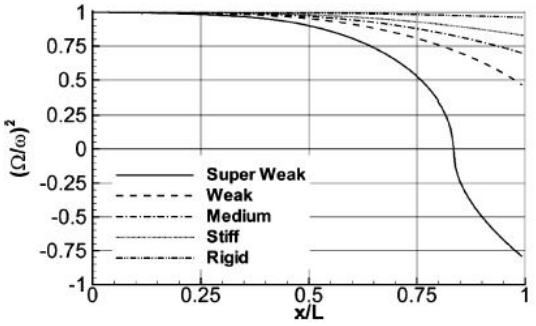

Figure 2.22: Aeroelastic stability of the S1 nozzle for different spring setups (Östlund et al., 2004)

Only in 2008, Zhang and Fuchiwaki (2008) were able to propose a coupled Computational Structural Dynamics (CSD)/Computational Fluid Dynamics (CFD) methodology that could cover the behaviour of higher-order bending modes. Blades et al. (2012) developed a similar methodology to demonstrate the aeroelastic deformation of a SSME nozzle during transient start-up. However, it was later pointed that the transient time in Blades et al. (2012) analysis ranged from 0.78 to 0.811 s, which does not match with the time at which a major side load event occurs, that is, FSS to RSS transition. Zhang et al. (2017) approach was also further demonstrated by Zhao et al. (2013) for the analysis of the J-2S nozzle.
Nevertheless, a shortcoming to all these studies is that they only offer *loosely coupled* aeroelastic solution, due to the fact that the CFD and CSD codes where only connected through an interface code. Wang et al. (2014) were the first to implement CSD formuations into the CFD code, so as to obtain a fully coupled solution, and, based on their approach, Zhang et al. (2017) studied the behaviour of the J-2S nozzle by varying either the material properties (Young's modulus) or the wall thickness: it was observed that by decreasing the Young's modulus, maximum displacement increases until the nozzle, with a mass density of 2700 kg/m^3 and wall thickness of 0.05 m, becomes aeroelastically unstable for $E \approx 7 \times 10^9$ N/m^2.

Apart from numerical studies, also a number of experimental investigations have been carried out with the intent of assessing the stability of higher order modes. Early experiments by Tuovila and Land (1968) compared the behaviour of various nozzles, fabricated with either aluminum or with glass-fiber laminates, and having different wall thicknesses. Brown et al. (2002) observed that ovalization was the predominant mode during transient operation and that separation was the main driver of the instability. Yet, no such study has shown the effect of nozzle aeroelasticity on vibroacoustic loads. A recent effort in this direction was taken by Tinney et al. (2017): by comparing the vibroacoustic signature of stiff and compliant poliurethane-based lab-scale nozzles to that of full scale launch data, it was observed that statistical metrics (skewness and kurtosis) require some level of aeroelasticity for the lab-scale and full-scale data to coincide. Overall, experiments on nozzles featuring different degrees of compliancy have shown that vibrations become undamped for soft compliant nozzles (hardness = 90A), whereas medium (hardness = 95A) and hard (hardness = 70D) compliant nozzles only present negligible displacements. Even though this study represents a first effort into a better

understanding of vibroacoustic loading, no investigation on the stability behaviour of the bending modes was performed.

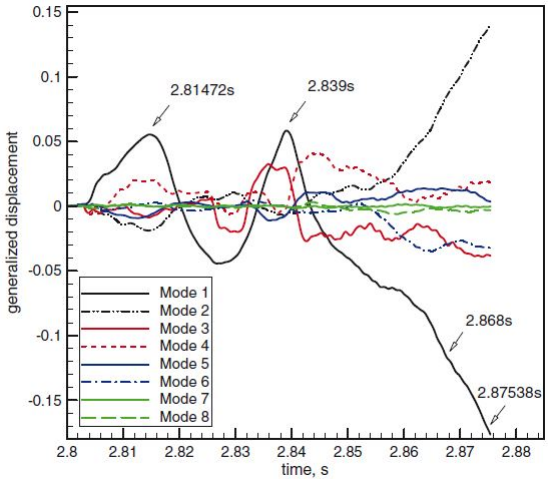

Figure 2.23: Generalised displacement histories for different modes, on a transient analysis of a SSME nozzle (Wang et al., 2014)

3

Supersonic jet noise

In the last century, the discourse around jet noise has been mainly dominated by the work of Lighthill and Newman (1952), whom were able to characterise, through their *acoustic analogy*, the mechanisms of subsonic jets and quantify their noise footprint as a function of the jet velocity. Nevertheless, the more recent pioneering work of Seiner and Yu (1981), Zaman et al. (2002) and Raman (1999), and many more, showed that supersonic jets behave rather differently compared to their subsonic counterpart and comprise different generation mechanisms. Together with turbulence mixing noise, an additional noise component, that is, shock-associated noise, can be found in supersonic jets operating at off-design conditions. In turn, some require full-flowing conditions to be initiated, while others also occur during FSS state, and are more relevant to the current research. A detailed breakdown of supersonic jet noise production mechanisms is found Figure 3.1, while a physical description of each is found in the following sections, together with an overview of the most eminent models that have been developed to characterise them. It should be, however, noted that most of these refer to full-flowing nozzles and are unsuitable when dealing with non-full-flowing cases, as the results presented in chapter 6 will later highlight.

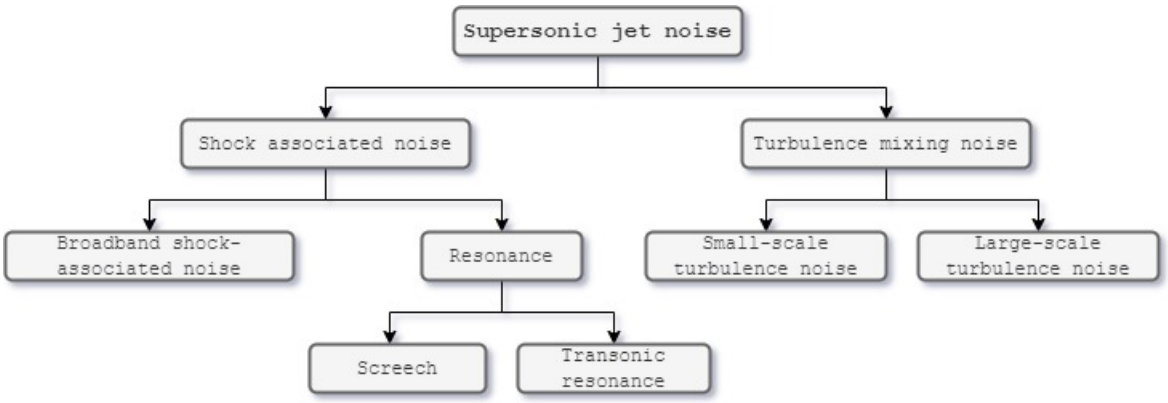

Figure 3.1: Overview of different supersonic jet noise sources

3.1. Turbulence mixing noise

Turbulent mixing noise, as the name suggests, is the result of acoustic radiation from the turbulent structures forming in the jet plume, when turbulent pressure fluctuations arise in the flow due to the fluctuation in turbulent kinetic energy. Broadly speaking, radiation occurs in the form of Mach waves when the convective speed of the turbulent eddies is greater than the ambient speed of sound. However, as simple as it may *sound*, due to the chaotic nature of turbulence and the broad number of time and length scales it involves, it represents one of the most complex noise mechanisms of supersonic jets. As of today, in fact, there is still controversy as to which are the sources of turbulent noise, and the research community has been historically divided into two main currents: on the one side, in the framework of acoustic analogy of Lighthill (1954), the

approach consists in rearranging the wave equations in such a way to have a *wave propagator* on the left-hand-side and the remaining terms acting as an equivalent source on the right-hand-side; in this context, turbulent noise sources have been modelled as *quadrupoles*. These predictions, however, fail to be accurate in the peak noise directions, at shallower angles to the jet axis. On the other hand, the second approach, based on experimental observations (Tam et al., 2008), postulates that turbulent mixing noise is produced by two distinct noise sources, which can be grossly categorized into small and large turbulent structures (Tam et al., 2008), that can be modelled as linear instability waves. Before delving into the details of turbulent mixing noise, a brief review of turbulence in free shear jets is deemed appropriate.

The overall anatomy of a supersonic full-flowing jet is presented in Figure 3.2 and features three main components: a potential core, a supersonic mixing region bounded by the sonic line and a subsonic mixing region between the sonic line and the outer turbulent shear layer. The potential core is that region characterised by a uniform mean velocity, which initially runs parallel to the nozzle exit; however, due to continuous air entrainment from the quiescent ambient fluid, a turbulent annular shear layer starts forming, thereby leading to an increase in shear layer thickness and consequent narrowing of the potential core diameter. Within the mixing layer, the dominant entities are the large turbulent eddies which convect downstream and gradually cascade, both energy-content wise and scale wise, into smaller eddies (Pope, 2000).

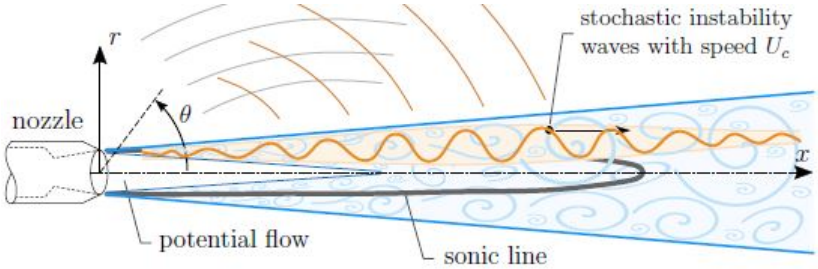

Figure 3.2: Main features of a supersonic jet plume - Courtesy of Baars and Tinney

As hinted earlier, these eddies can be regarded as the source of turbulent mixing noise, both in subsonic and supersonic jets. The smaller eddies are typically associated with background noise and propagate beyond the Mach angle (upstream and sideline directions), formed by the radiation of the large scale structures, due to the fact that they are not only convected downstream but also refracted owing to the density and velocity gradients in the mixing layer (Tam et al., 2008). It's the larger eddies, however, that make up the greater portion of supersonic jet noise - mainly in the downstream direction, at the Mach cone half-angle $\phi = \arccos(a_\infty/U_c)$, with U_c being the convective speed of the turbulent eddies. Yet, only a small portion of turbulent kinetic energy is converted into noise. Pressure fluctuations travelling with subsonic phase velocities rapidly decay and do not propagate to the far field. For this reason, the flow field outside of the jet is commonly divided into a *hydrodynamic* non radiating region and an *acoustic* radiating region. For a subsonic jet, the former, is further divided into a non-linear hydrodynamic region, with pressure intensity decaying at a rate $\propto kr^{-7/3}$, and a linear hydrodynamic region, in which pressure intensity decays at a rate $\propto kr^{-6.67}$; in the latter, that is, the acoustic region, pressure intensity was found to be decaying with an approximate rate of kr^{-2} (Arndt et al., 1997). In this context, r defines the distance from the jet centerline, whereas k, being the frequency-wavenumber, clearly indicates that these decaying trends, as well as the boundaries of each region, are frequency-dependent. In other words, the dividing line between near field and far field is frequency dependent, rather than a rigidly fixed location in space (Arndt et al., 1997). In the context of the current research, a few short considerations on this matter are given in subsection 4.3.2.

Large scale turbulent eddies have been the subject of plenty theoretical investigations (Oertel Sen, 1980, Tam and Burton, 1984a,b, Tam and Hu, 1989, Tam and Chen, 1994) to identify their link to acoustic radiation. From the observations of Oertel Sen (1980), it became apparent that high speed jets feature three families of *instability waves* - or, equivalently, *Mach waves* - each moving at a different convection velocity w, w', w'', only depending on two parameters: the jet Mach number M_j and the ratio of sound speeds inside and outside of the jet:

$$\frac{w}{a_a} = \frac{M_j}{1 + a_a/a_i} \qquad \frac{w'}{a_a} = \frac{M_j + w/a_a}{1 + a_a/a_i} \qquad \frac{w''}{a_a} = \frac{M_j - w/a_a}{1 + a_a/a_i}$$

Early interpretations from Tam and Hu (1989), theoretically proved the existence of three wave solutions, the first two both exhibiting an acoustic near field in the form of Mach wave radiation, while the latter, confined within the jet, presenting no acoustic radiation at all. This and other studies, however, did not provide evidences as to which are the mechanisms initiating Mach waves. Some more recent studies from Ortel Sen et al. (2010, 2012), Oertel Sen et al. (2013) have attempted to provide such an answer, by proposing a *vortex-train* model: as the shear layer of a jet develops into coherent turbulent structures, a sheet of vortex pairs forms, each travelling behind the other, as illustrated in Figure 3.3. The vortices adjacent to the quiescent outside fluid travel at a speed w'', whereas those that share a boundary with the inner jet travel at a speed w'; finally, the center of the vortex pairs moves at w. A central point to the theory is the concept of *gas dredging* (Ortel Sen et al., 2010), wherein rear vortices entrain gas into the shear layer from outside, while the inner fortices entrain gas into the shear layer from inside the jet. Because the convection speeds w', w'' are greater than the speed of sound, Mach waves are formed.

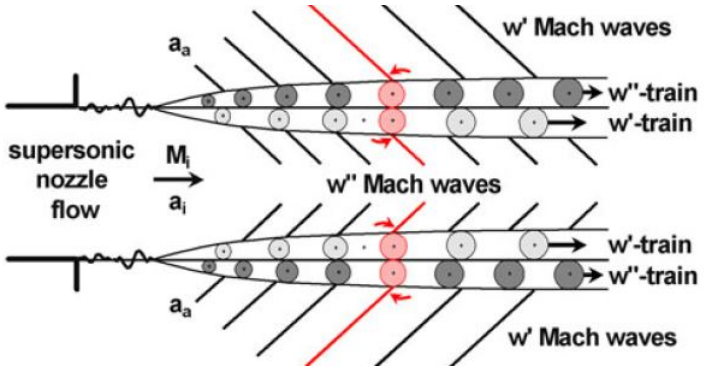

Figure 3.3: Hypotetical vortex-train model of Oertel Sen et al. (2013)

In this context, instability waves and coherent large scale turbulent structures are *synonymous*, with the former representing the mathematical description of the latter. Tam and Chen (1979), in fact, proposed a stochastic instability model based on the observation that turbulence statistics in high speed flows features a self-similar behaviour in the downstream direction, due to the slow spreading rate of the jet. When this is the case, and a state of quasi-equilibrium is established, the large scale fluctuations can be represented by the superposition of their main normal modes, that is, instability waves. Nevertheless, Tam and Burton (1984a,b) pointed that the classical hydrodynamic stability theory could not be employed to predict acoustic radiation by instability waves as its solutions are based on the assumption that wave disturbances decay to zero far from the mixing layer. Consequently, they developed a *global* solution based on the method of matching asymptotic expansions, which features two solutions, an inner one, valid within the jet, which parameterises the instability wave itself, and an outer one, constructed by the method of Fourier transform, which describes the acoustic field outside of the jet. To reflect the broadband nature of turbulent mixing noise, this model was later extended by Tam and Chen (1994), who constructed a broadband solution based on the modulation of the waves' amplitude and on the superposition of instability waves of all frequencies and azimuthal mode numbers. Amplitude modulation, in fact, is fundamental to noise generation: instability waves, generated at the nozzle exit, grow rapidly as they propagate downstream, until they reach their maximum amplitude, after which they become damped. This growth/decay behaviour mathematically translates into having a disturbance with a broadband of wavenumbers, such that its spectrum can feature both subsonic and supersonic phase velocities ω/k; while the former cannot propagate sound, the latter are the ones responsible for acoustic radiation to the far field, even in subsonic jets. These organised structures are coherent over several jet diameters, and can be, therefore, regarded as non-compact sources with a distinct directivity pattern.

3.2. Broadband Shock Noise

BBSN was first observed by Harper-Bourne and Fisher (1973). Their primary interest, however, was in relation to jets ejected from converging nozzles, and it was later shown that, in some aspects, their model failed to predict jet noise for C-D nozzles. Much of today's understanding of BBSN is owed to the experimental ob-

servation of Pao and Seiner (1983) and Norum and Seiner (1982) and to the development of analytical models by Tam (1995) and Tam and Tanna (1982).

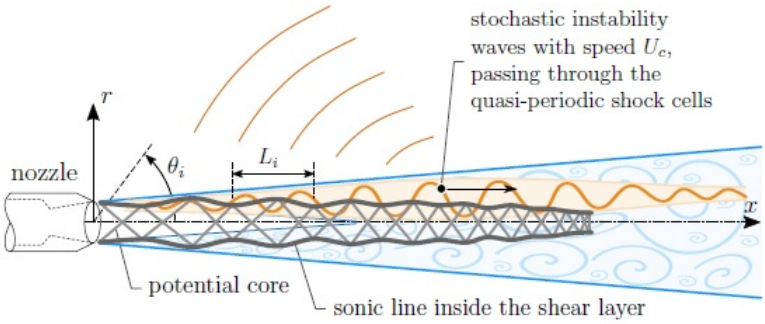

Figure 3.4: BBSN generation mechanism - Courtesy picture of Baars and Tinney

BBSN occurs when non-ideally expanded jets present shock cell structures within their plume. A shock cell can be broadly defined as a succession of shock and expansion waves which develop into said cell-like structure due to the reflection into the jet that they undergo from the turbulent shear layer. Outside of the jet, in fact, the flow is subsonic and cannot accommodate a supersonic flow, which, consequently, is reflected at the sonic line. The first shock cell forms at the nozzle lip, in an effort to adapt the jet pressure to that of the ambient; where the shear layer is the thinnest and the turbulent eddies are small. The shock-expansion reflection process continues downstream and multiple shock-cells are formed, in a quasi-periodic pattern, each with progressively weaker strength due to turbulence dissipation and a thickening of the shear layer. BBSN is the result of the weak interaction between these shock-cells and the large turbulent structures propagating downstream and passing though the cells. The convection of the turbulent eddies through the shock-cell is able to distort the turbulent eddies and viceversa. This interaction gives rise to upstream travelling disturbances, some being hydrodynamic and having subsonic phase velocities, and others having supersonic phase velocities. The former decay rapidly, while the latter are the ones typically associated with noise generation, in the form of Mach waves, which propagate to the far-field.

Being a phenomenon occurring in non-ideally expanded jets, it also concerns overexpanded rocket nozzles. Donald et al. (2014), in fact, have reported a noise spectra during FSS featuring a signature typical of BBSN. Similarly, Tinney et al. (2017) noticed that BBSN are less pronounced in compliant nozzles, as opposed to the case of a stiff aluminum nozzle, operating at similar conditions. Furthermore, Donald et al. (2012) have interestingly observed a glaring difference in the noise spectra between TIC and TOP nozzles at various pressure ratios ($25 < NPR < 50$): while for a TIC nozzle both turbulent mixing noise at downstream angles and BBSN at upstream angles are present, for a TOP nozzles, BBSN seems to be the dominant noise mechanism, with a very slim trace of turbulent mixing noise at shallower angles. In this regard, Zaman et al. (2002) has pointed that the excess broadband noise seems to occur in nozzles having a larger half-angle in the divergent section.

A deterministic linear model that explains sound generation from shock - turbulence interaction was first proposed by Ribner (1985) based on the observation of Hollingsworth and Richards (1955): a shock-vortex interaction can produce a cylindrical acoustic wave partly cut off by the shock. Based on the division proposed by Ellzey et al. (1995), the family of shock-vortex interactions can be broadly divided into four different kinds, based on the strength of both the shock and the vortex. For the case of BBSN, the interaction ought to involve a strong vortex and a strong shock, with matching vortex and downstream flow field velocities.
During the early stages of the interaction (Figure 3.5a), the shock undergoes a distortion when a vortex passes through it, which results in the formation of an upper and a lower diffracted branch, the former propagating downstream faster than the latter, whose motion is opposed to that of the shock. A reflected shock, which connects the lower and upper branches of the diffracted shocks, passes though the core of the vortex. Once the shock structure is convected further downstream, it develops into a complex pattern: the Mach stem, together with both incident shocks forms the *transmitted* shock, which slowly becomes planar again, whereas the reflected shocks travel at different velocities: the upper shock, still diffracting around the vortex is slower compared to the lower one. As far as the pressure field is concerned, behind the shock front, a region of weak expansion exists where the the upper diffracted shock meets the reflected shock, while a region of weak

compression exists where the vortex velocity opposes the shock propagation. This pressure field, commonly referred to as *precursor* (Ribner, 1985), propagates radially outward from the vortex and it is typically idealised as a quadrupolar pressure variation with a source strength proportional to r^{-2} (Pao and Seiner, 1983). When the precursor wave front interacts with the lower reflected shock (MR2 in Figure 3.5b), an acoustic wave develops and travels to the far-field.

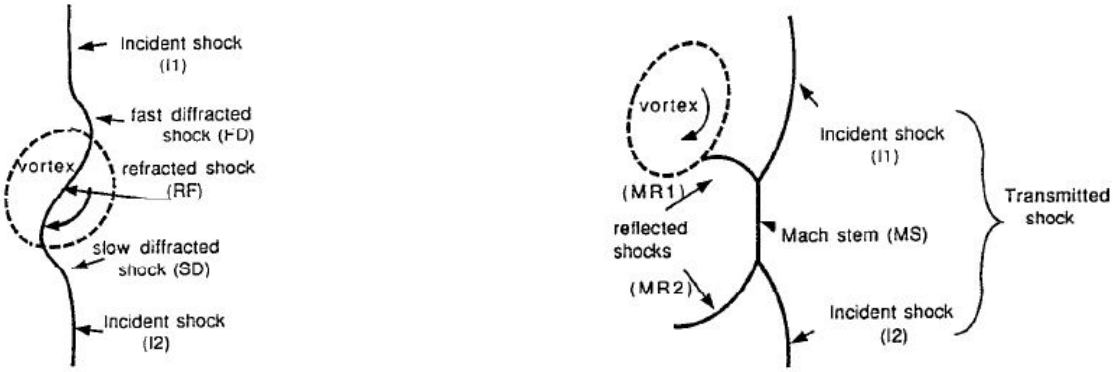

(a) *Early* stages of strong shock - strong vortex interaction

(b) *Late* stages of strong shock - strong vortex interaction

Figure 3.5: Strong shock - Strong vortex interaction (Ellzey et al., 1995)

Harper-Bourne and Fisher (1973) modelled BBSN as being generated where the shock tips intersect with the shear layer. The succession of shock cells and turbulence causes the sound waves to interfere constructively and destructively, thereby forming a distinguishable hump in the acoustic spectra. The point sources are correlated and the phase difference between adjacent sources is a function of the time needed for the turbulent eddies to traverse the cell. The acoustic frequency spectrum is broadband in nature and presents an amplitude rise with frequency up to a peak frequency, with a slope proportional to ω^4 - ω being the angular frequency; it, then, decreases at higher frequencies, with a decay rate of ω^2. Pao and Seiner (1983) argue that the ω dependency in the frequency spectrum can be traced back to physical characteristics of the the shock-vortex interaction: the high frequency behaviour, for instance, implies that the noise is highly impulsive and the high-pressure spot formed in the interaction might be responsible for it. Norum and Seiner (1982) also point that the peak frequency is noticeably higher for the case of hot jets compared to cold jets.
Furthermore, as opposed to turbulent mixing noise, BBSN exhibits a frequency shift with measurement angle, indicative of an apparent Doppler effect, with the peak frequency decreasing for steeper angles with respect to the jet axis (Donald et al., 2012). The peak frequency is also affected by shock-cells spacing and eddies convection velocities, with the peak Strouhal number decreasing with increasing NPR (Norum and Seiner, 1982). As also noted experimentally by Donald et al. (2012), the peak wavelength of BBSN is equivalent to the length of the shock cell, which braodens as the NPR is increased. The expression that Harper-Bourne and Fisher (1973) obtained for the peak frequency is as follows:

$$f_p = \frac{u_c}{s}(1 - M_c cos\theta) \tag{3.1}$$

With θ being the observation angle, $u_c = 0.7U_j$ the eddies convection velocity and $s = 1.1 \times D\beta$ the average shock cell spacing, proportional to the shock parameter $\beta = \sqrt{M_j^2 - 1}$. Nevertheless, for this model a good correlation with experimental data was only found for converging nozzles. Norum and Seiner (1982) consequently found a better correlation for the average shock cell spacing, obtained in the form $s/D = a\beta^b$, with [a;b] = [1.1;1.17] for a M = 1.5 nozzle flow. To account for the Doppler effect, the variation in peak frequency is computed as $f_p = f_\psi(1 - M_c cos\psi)$, with f_ψ being the peak frequency measured at the far-field angle ψ (Pao and Seiner, 1983, Norum and Seiner, 1982).

Tam and Tanna (1982), instead, developed an analytical model on the basis of instability theory. The velocity fluctuations associated with the large scale turbulent structures can be represented as a superposition of the hydrodynamic instability wave modes of the flow:

$$u_t = Re\left[A(x)\Psi(r)e^{(kx-\omega t)}\right] \tag{3.2}$$

where $A(x)$ represents the dimensionless spatial amplitude, which describes the growth and decay of the instability waves in the flow direction: after an initial increase close to the nozzle exit, it reaches a peak which depends on the wave frequency, to, then, decrease again further downstream.
Based on their model, a similar peak frequency expression was developed in terms of the shock cell spacing ($L_s = 2\pi/\kappa_1$):

$$f = \frac{u_c}{s(1 + u_c cos\theta / a_\infty)} \tag{3.3}$$

The spectrum, overall, peaks at a frequency close to that defined in Equation 3.3; the reason it does not peak at that exact frequency is due to the dependence on $A(x)$, which broadens the wavenumber spectrum, thereby producing wave components radiating at different phase velocities and angular directions, resulting in the observed Doppler effect.

Finally, scaling laws for the prediction of noise intensity have typically linked noise intensity to the shock parameter β: Harper-Bourne and Fisher (1973) have suggested that $I_{BBSN} \propto \beta^4$ for $0.5 < \beta < 1.2$, whereas Kandula (2011) has found that $I_{BBSN} \propto \beta^{4.2}$ for $0.2 < \beta < 2$. A similar relationship was proposed by Tam and Tanna (1982): $I_{BBSN} \propto \left(M_j^2 - M_d^2\right)$, with M_d, the design Mach number. These expressions, however, typically fail for higher β due to the large portion of subsonic flow that forms downstream of the Mach disk.

3.3. Screech

Even though screech is still the least understood and predictable component of jet noise, it was first reported by Powell (1953) in the 1950's and plenty contributions to the topic have followed with the work of Tam (1995), Raman (1999, 1998) and many others. Broadly it consists in tonal emission at medium frequencies and, even though it is typical of the acoustic signature of military jets, screech tones were recently observed in multiple studies involving overexpanded lab-scale TOP and TIC nozzles, at relatively high NPRs (Donald et al., 2014, Canchero et al., 2016a, Rojo et al., 2016), when the nozzle is in full-flowing conditions. From early schlieren observations of both circular and rectangular nozzle flows, Powell (1953) was readily able to define the main features of the phenomenon and suggest that the tonal emission was due to a self-sustaining aeroacoustic feedback loop, comprised of four main processes:

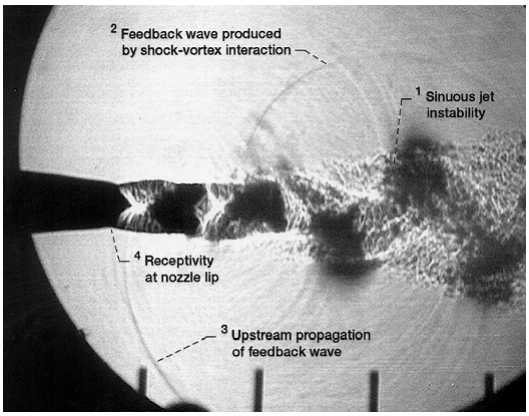

(a) Schlieren visualization of the main components of the screech feedback loop

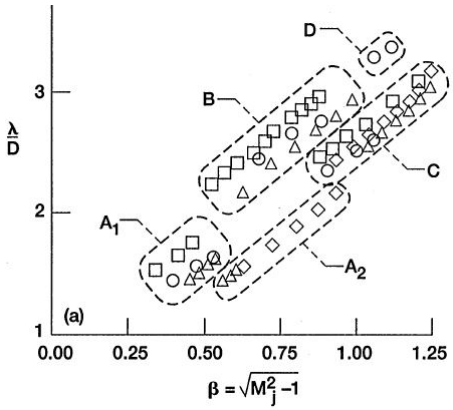

(b) Staging of screech in circular jets

Figure 3.6: Screech (Raman, 1998)

1. Downstream propagation of energy via hydrodynamic instabilities up to the point where a disturbance in the flow - namely, the shock cell - is present
2. Conversion of the energy associated with the downstream-propagating instabilities into an upstream-propagating disturbance due to the interaction between the travelling instabilities and the flow disturbance
3. Upstream propagation of the disturbance up to the near-nozzle shear layer in the form of acoustic reflections
4. Excitement of the near-nozzle lip shear flow by the upstream propagating acoustic disturbance, thereby triggering newer instabilities

The cycle repeats itself and the feedback loop is complete, as seen in Figure 3.6a. Therefore, it can be deduced that the essential elements that warrant the production of screech tones are two: a full-flowing flow, such that the shear layer, being at the nozzle lip, can trigger newer instabilities, and shocks. The former requirement clarifies why screech tones in TOP nozzles are typically recorded after transition to a RSS flow has occurred. As for the latter, shocks need to be strong enough in order for the loop to be initiated. Nevertheless, the relationship between shock strength and screech amplitude is rather weak (Raman, 1998): once screech is produced, a further increase in shock strength does result in louder tones. Analytical models that can formally predict screech amplitude, however, are lacking, due to the difficulty to characterise the influence that the near-field has on the feedback loop.

Powell (1953) also indicated that, in order for the feedback loop to be self-sustaining, two criteria have to be met:

$$\frac{N}{f_s} = \frac{h}{u_1} + \frac{h}{u_2} + \varphi \tag{3.4}$$

$$q_d \eta_g \eta_u \eta_r \geq 1 \tag{3.5}$$

Equation 3.4, the *phase criterion*, defines the frequency f at which the shear layer becomes naturally unstable: f is seen to depend on the distance h being a multiple of the shock cell spacing, the velocities u_1 and u_2, being the downstream and upstream perturbation speeds respectively, and N, that is, an integer value which defines the number of new disturbances that are generated in the time it takes for the loop to close.
Equation 3.5, the *amplitude criterion*, on the other hand, defines the gain that is associated with each of the four stages of the loop, which is essentially linked to the growth rate q_d of the instabilities - the only term in the expression greater than one - as they extract energy from the mean flow. Finally, even though instability wavepackets show a gain, they do not grow exponentially, as opposed to non-shock containing jets, but rather a fluctuating amplitude behaviour given by shock modulation is observed (Raman, 1999, Edgington-Mitchell, 2019). Nevertheless, models for a correct prediction of instability modulation by shocks are still not available.

As far as tonal emission is concerned, it is the consequence of the energy transformation mechanisms that convert the downstream-propagating energy into an energy form that can travel upstream; for the case of screech, it appears to be the result of a *vortex/shock reflection interaction*, in a process commonly referred to as *shock leakage*, a model by Manning and Lele (2000), with experimental evidences arising from the work of Edgington-Mitchell et al. (2014). Said model describes the generation of an upstream travelling acoustic wave as a result of the reflected shock in the shock cell leaking past the sonic line due to the interaction with the shear layer vorticity.
Once acoustic disturbances have travelled upstream, they are able to excite the shear layer. This process is usually termed *receptivity*, and it has been shown to accommodate acoustic forcing when the shear layer is the thinnest. Tam (1986) was able to provide a qualitative criteria to describe the occurrence of excitation, that is, the incident sound wave and the instability wavepacket need to have the same frequency and phase velocity. This has been shown to occur near the nozzle lip.

As far as the screech frequency is concerned, from Equation 3.4, Powell was able to derive a simpler relation that could directly link the fundamental screech frequency to the shock cell spacing s:

$$f_s = \frac{u_c}{s(1+M_j)} \tag{3.6}$$

Equation 3.6 is based on the premise that the fundamental tone and the first harmonics radiate most strongly upstream and to the side-line, respectively. Norum (1983), however, later pointed that, even though screech mostly radiates upstream, it is not necessarily true that the emission with maximum amplitude is exactly upstream. This finding came about with the discovery of mode staging. Screech, in fact, exhibits a staging behaviour, with complex directivity patterns. As shown in Figure 3.6b, mode shifting is characterised by discontinuous changes in frequency, with the dominant screech mode jumping to lower frequencies as the jet Mach number is increased. Lip geometry and thickness, as well as temperature have also been shown to affect staging (Norum, 1983). Despite the mechanisms behind mode staging being still unresolved (Edgington-Mitchell, 2019), four modes have been identified, each with a different azimuthal structure of both the sound field and of the downstream propagating instability; A is the *axysimmetrical* mode, B and D are the *flapping* modes and C is the *helical* mode. Together with screech frequency, also screech amplitude is mode dependent, with the loudest tones observed for the B and C modes (Raman, 1998).

Even though Powell's feedback loop model is the most widely accepted, Tam et al. (1986) proposed the "*weakest link*" feedback model and suggested that screech could be a special case of BBSN, with the screech frequency being the lower bound of the BBSN spectra, and the tonal emission in the form of Mach wave radiation being the result of the weak interaction between the large scale turbulent structures and the nearly periodic shock cell. The authors suggested a semi-empirical screech frequency based on the assumption that the jet mixing layer bounds the shock-cell system; assuming $u_c \approx 0.7U_j$, they found that the finite thickness of the mixing layer could decrease the shock cell spacing by 20% compared to the vortex sheet shock cell model of Prandtl (1904) prediction; the following expression for the fundamental tone was obtained:

$$\frac{f_s D_j}{U_j} = \frac{0.67}{\sqrt{\left(M_j^2 - 1\right)}} \left[1 + 0.7 M_j \left(1 + \frac{\gamma - 1}{2} M_j^2 \right)^{-1/2} \left(\frac{T_\infty}{T^0} \right)^{-1/2} \right]^{-1} \tag{3.7}$$

3.4. Transonic resonance

Transonic Resonance (TR) is characterised by the emission of acoustic tones, whose features are different from conventional screech tones. Baars and Tinney (2013) and Donald et al. (2014) have pointed at the possibility that the narrow spectral peaks observed in their experimental investigation of TIC and TOP nozzles could be attributed to transonic resonance, rather than screech: even though it is typically encountered in nozzles with sudden area changes, transonic resonance has also been reported for nozzles with smooth divergence from the throat, up to the nozzle exit (Zaman et al., 2002). The underlying mechanisms of said noise source, however, are yet to be fully defined: even though authors generally agree on the principal role that the shock foot unsteadiness plays in the generation of these acoustic tones, two opposed currents prevail in literature as to which process leads to noise generation, with some speculating that a feedback loop between shock and shear layer sustains the resonance (Olson and Lele, 2013), while others point that the resonance is due to the shock behaving like a vibrating diaphragm, thereby driving the downstream flow accordingly (Zaman et al., 2002, Lárusson et al., 2017).

Zaman et al. (2002) have carried out an extensive investigation on transonic resonance and were able to isolate the phenomenon, distinguishing it from screech, and draw conclusions on its main features.
The vertical lines of Figure 3.7b mark different flow regimes, with the region between the dashed and the dotted line representing a condition in which a shock is expected in the nozzle divergent and the region between the dotted and the chain-dashed line representing an overexpanded flow. Transonic resonance is, hereby, proven to only occur in the presence of a shock or during overexpanded operations, and only in converging-diverging nozzles (Zaman et al., 2002), as opposed to screech which was first documented in a convergent nozzle (Powell, 1953).

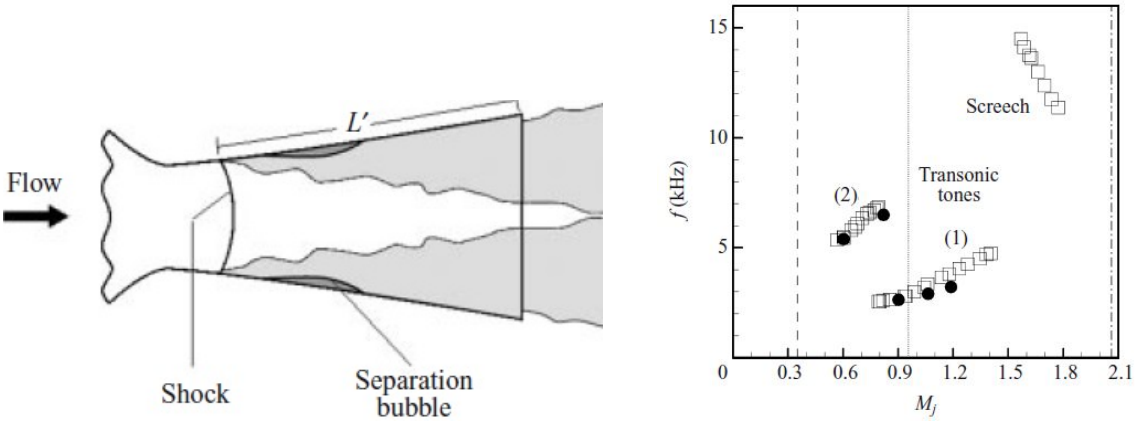

(a) Schematic of possible flow field causing transonic resonance

(b) Staging behaviour of resonance: frequency as a function of jet Mach number

Figure 3.7: Transonic resonance mechanism (Zaman et al., 2002)

A striking feature of transonic resonance, is that it has a staging behaviour as shown in Figure 3.7b: stage 1,

that is, the *fundamental*, which has been seen to involve the loudest tones, occurs at relatively higher jet velocities and larger pressure supplies and corresponds to a 1/4 standing wave. At lower velocities, the first odd harmonics, corresponding to a 3/4 standing wave, occurs. The length scale of the phenomenon, and the corresponding frequencies, are dictated by the distance between the shock foot - the wave node - and the nozzle exit - the wave antinode - as indicated in Figure 3.7a. By increasing the NPR, the shock foot moves downstream, thereby shortening the length $L^{'}$; this is followed by a decrease in wavelength and a corresponding frequency increase. With a further NPR increase, the decreasing $L^{'}$ cannot support 3/4 standing waves anymore, and the resonance drops to the fundamental 1/4 wave, with a corresponding frequency drop of a factor of approximately 3. Zaman et al. (2002), by using a comprehensive set of measurements of large area ratio nozzles with different throat-to-exit axial lengths x_L, angles of diverging wall section $\theta = tan^{-1}[(D_j - D^*)/2x_L]$, and exit and throat diameters D_j, D^*, proposed a polynomial fit to collapse the data and were able to provide an analytical approach for the computation of resonance frequencies:

$$f_r = \frac{a_\infty}{4\alpha}\sqrt{m^2 + \frac{8\alpha}{\pi^2 x_0}} \qquad \text{m} = 1, 3, 5... \qquad (3.8)$$

$$\alpha = x_L + \frac{4D_j}{3\pi} \qquad x_0 = \frac{D^*}{2tan\theta} \qquad (3.9)$$

For both stages, the frequency has been seen to increase with the jet Mach number, with the curve slope being dependent on the nozzle's divergent half angle θ. More specifically, the slope curve steepens with decreasing θ, and is directly linked to the different rate of the divergence experienced by the flow and to the shock movement given a certain pressure differential. Finally, the model predicts the resonant frequencies, but says nothing about their amplitude.

The findings of Olson and Lele (2013) agree well with the model proposed by Zaman et al. (2002), confirming that the resonance depends on the distance between the shock foot and the nozzle exit. The study further suggests that a feedback loop between the separated shear layer and the shock wave is the driver of the low-frequency unsteadiness: information moves upstream through pressure waves in the subsonic core flow, and downstream through the separated region. Downstream of the separation shock, in fact, the turbulent boundary layer is separated and obstructs the nozzle exit, effectively altering the geometry; the shock, therefore, moves upstream to readjust and accordingly its intensity decreases, thereby decreasing the degree of separation. With a weaker separated region, the nozzle exit geometry is less altered and the shock moves downstream, increasing its strength and the separation blockage, closing the loop.

3.5. Rocket noise

In many aspects rocket plumes and supersonic jets share various similarities, such that, overall, the treatise of chapter 3 are still valid in terms of sound generation mechanisms; in rockets the dominant noise source is turbulent mixing noise: Kuo et al. (2015) point that this could be mostly due to the combined effect of the high efficiency of Mach wave generation and BBSN saturation at high stagnation temperatures. Nevertheless, rocket plume's acoustic radiation phenomena are substantially different from those of other supersonic jets, such as military and afterburning turbojets, due to the extreme conditions at which rockets typically operate, thus often making prediction approaches difficult to be compiled in reliable methodologies. Just to name a few, typical values of rocket plume's static temperatures are on average 4 times higher than those of regular turbojets, and consequently, ambient Mach numbers for rockets are between 7 and 11, as opposed to values between 2 and 4 for military jets (McInerny, 1992). Furthermore, prediction methods have been mostly used to assess the acoustic environment of launch pads, where rockets typically operate at overexpanded conditions, thereby making geometric and plume physics parameters harder to gauge. Early on, Chobotov and Powell (1957) also showed that the power law for subsonic jets by Lighthill and Newman (1952), Lighthill (1954), that is, OASPL $\propto U_e^8$, is not valid for highly supersonic jets and proposed that sound power scales with U_e^3, instead. Said dependency was later proven also by Varnier (2001). For over 50 years, the work of Eldred (1971), published in NASA SP-8072 report, has represented the foundation for the prediction of launch vehicles' acoustics, and, despite known shortcomings, it is still being used today both in noise preliminary analyses and as a reference for improved models. In the following sections, a review of the state-of-the-art rocket noise research is presented, with a summary on the main parameters affecting acoustic loading, together with a comment on some limitations of the prediction methodologies currently used.

3.5.1. NASA SP-8072 and its heritage

NASA SP-8072 report (Eldred, 1971) was compiled by Eldred in 1971 as a mean to gather existing data from the Apollo programs of the 1960s. The result was an empirical model for the prediction of rocket plume acoustic signatures. Its main limitations, which are primarily due to some wrong assumptions, lack of comprehensive data and a generally poor understanding of supersonic jet noise during those years, were revealed relatively soon, when gross disagreements where found between the predictions and the measured data of the SSME during various launches (Lubert et al., 2022). It became soon clear that the SP-8072 could not represent an universally valid guide for acoustic prediction and many alternative studies started populating the literature: McInerny and Ölçmen (2005) studied the far field noise produced by the Titan and Scout programs, and found OASPLs as high as 160 dB during full flowing conditions; similarly, Plotkin et al. (2009) developed a predictive model for the acoustic environment around the Ares I launch pad, while Kenny et al. (2009) measured the far field noise and sound directivity of the solid boosters of the Space Shuttle.
Nevertheless, given its simplicity and relevance, the SP-8072 is hereby reported: simply put, the procedure employs sound power curves and directivity indices to predict acoustic levels as a function of distance and angle from the jet axis. For a single nozzle configuration, assuming $W_{ref} = 10^{-12}$ W, first, the overall sound power level L_w is computed from the acoustic power W_{OA}:

$$W_{OA} = \frac{\eta}{2} F U_e^2 \qquad \text{[W]} \qquad (3.10)$$

$$L_w = 10 \log_{10}\left(\frac{W_{OA}}{W_{ref}}\right) \qquad \text{[dB]} \qquad (3.11)$$

As seen in Equation 3.10, with the thrust F being proportional to U^2, the U^3 dependency, presumed by Chobotov and Powell (1957), is justified through the acoustic radiation efficiency η, which Eldred assumed to be 1%. Later assessments of η, however, showed that Eldred's assumption was rather overpredicting. Sutherland (1993) presented an alternative formulation for η dependent on plume parameters, which has been recently employed also by Donald et al. (2014) in the preliminary assessment of the acoustic power for sub-scale overexpanded rocket nozzles:

$$\eta = K \left(\frac{\gamma_j}{\gamma_\infty}\right)\left(\frac{a^*}{a_\infty}\right)^3 \left(\frac{1}{c_v}\frac{a^*}{U_j}\right)^2 \qquad (3.12)$$

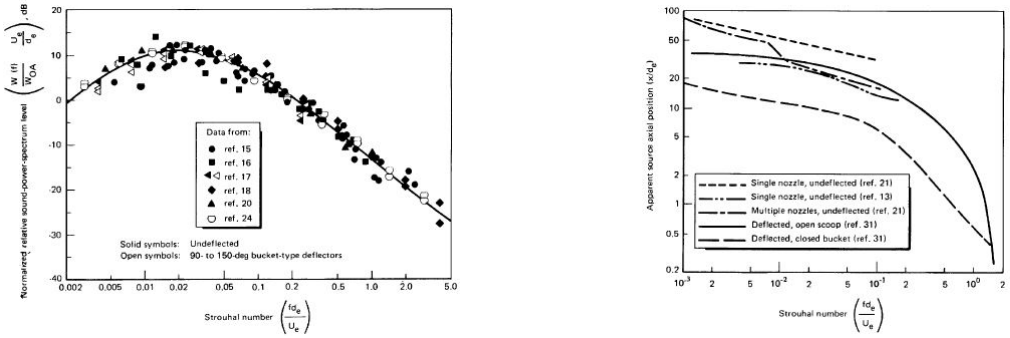

(a) Normalized relative power spectrum as a function of Strouhal number for rockets with a thrust range between 1.56 kN and 31.1 MN

(b) Axial location of apparent sources as a function of Strouhal number

Figure 3.8: NASA SP-8072 methodology (Eldred, 1971)

C_v is a nozzle velocity coefficient valued 0.98, whereas K = 0.0012. This expression, however, has been shown to be based on the wrong assumption that the subsonic region of the plume is the one producing the greatest portion of sound power (Lubert et al., 2022). Donald et al. (2014) also point that not only Sutherland wrongly assumes a constant mass flow between the nozzle exit and the supersonic region, instead of a linearly increasing function of distance, but that his formulation fails to give reliable results at very high temperatures, when ideal gas approximations are not valid. Alternatively, nowadays, the most commonly used approximation is $\eta \approx 0.5\%$, recently validated by the measurements of James et al. (2012a) and Mathews et al. (2021).

Once the value for the overall sound power level is obtained, Eldred's methodology is two-fold, that is, he provides two different source allocation methods, commonly referred to as DSM-1 and DSM-2. Both consist in diving up the plume in an array of sub-sources; however, the former assumes that each sub-source only radiates one frequency, with a corresponding sound power level defined as a function of the Strouhal number;

the latter, instead, consists in diving up the plume in multiple *slices*, such that each one has a corresponding sound power spectral shape $W(f)$.

As far as DSM-1 is concerned, the overall sound power level L_w is split into multiple power bandwidths, with the central frequency defining the Strouhal number for the calculation of $W(f)$ according to Figure 3.8a. The obtained values for each frequency bandwidth are, then, plugged into Equation 3.13.

$$L_{w,b} = 10\left[\log\left(\frac{W(f)}{W_{OA}}\frac{U_e}{D_e}\right) - \log\frac{U_e}{D_e} + \log\Delta f_b\right] + L_w \qquad \text{[dB]} \tag{3.13}$$

With a similar curve fitting approach, based on the calculated Strouhal numbers, each source is, then, allocated along the exhaust flow centerline using Figure 3.8b. Once $L_{w,b}$ and x/D_e are known, the sound pressure level at any point in space for each sub-source is computed based on their distance r and angle θ from the source:

$$SPL_{b,p} = L_{w,b} - 10\log r^2 - 11 + DI(b,\theta) \qquad \text{[dB]} \tag{3.14}$$

The overall sound pressure level is obtained by logarithmic summation of each $SPL_{b,p}$ contribution:

$$SPL_{OA,p} = 10\log\frac{\sum_{\text{All b}}\left[10^{SPL_{b,p}/10}\right]}{2\cdot 10^{-5}} \qquad \text{[dB]} \tag{3.15}$$

DSM-1, however, is not only too simplistic in its assumption that each sub-source only radiates at a single frequency, but Gee (2021) recently found that the method is based on a wrong plot (Figure 3.8a), whose error is propagated and amplified in the calculation of the final sound pressure level. Without recurring to lengthy calculations for the sources' array, McInerny (1992) provided a simple formula to obtain the maximum OASPL directly from the Overall Sound Power Level (OASWL) calculated in Equation 3.10:

$$OASPL_{max} = L_w - 10\log(4\pi r^2) + 8 \tag{3.16}$$

Alternatively, Greska et al. (2008) recently proposed a graphical approach for the computation of the OASPL, which agrees well with the experimental data of Mathews et al. (2021).

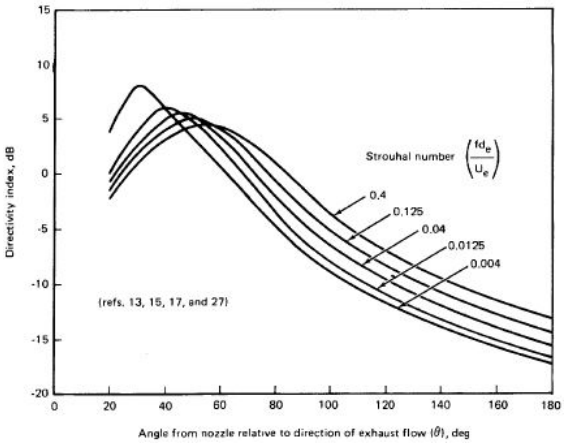

Figure 3.9: Directivity of far field noise as a function of Strouhal number Eldred (1971)

As far as the frequency scaling is concerned, the most common scaling parameter employed in the majority of prediction models, including Eldred's, is the Strouhal number, which, for rockets typically peaks at $St \approx 0.025$, as opposed to regular supersonic jets, that peak at $St = 0.2$ (Tam, 1995). Over the years, however, alternative formulations have been proposed, including a modified Strouhal number by Eldred:

$$Sr^* = \frac{fD_t}{a_a}\left[\left(\frac{2}{\gamma+1}\right)^{\gamma/\gamma-1}\left(\frac{p_0}{p_a}\right)\right]^{1/2} \tag{3.17}$$

Greska et al. (2008), on the other hand, have pointed that the Helmoltz number $Hm = fD_e/a_a$ - not dependent on plume parameters - is a more suitable alternative.

A better alternative to the DSM-1 is represented by the DSM-2: once L_w is obtained from Equation 3.11, this method assumes a distribution of W_{OA} based on the laminar core length x_t (here designated as L_C), computed as:

$$L_C/D_e = 3.45\left(1 + 0.38M_j^2\right)^2 \tag{3.18}$$

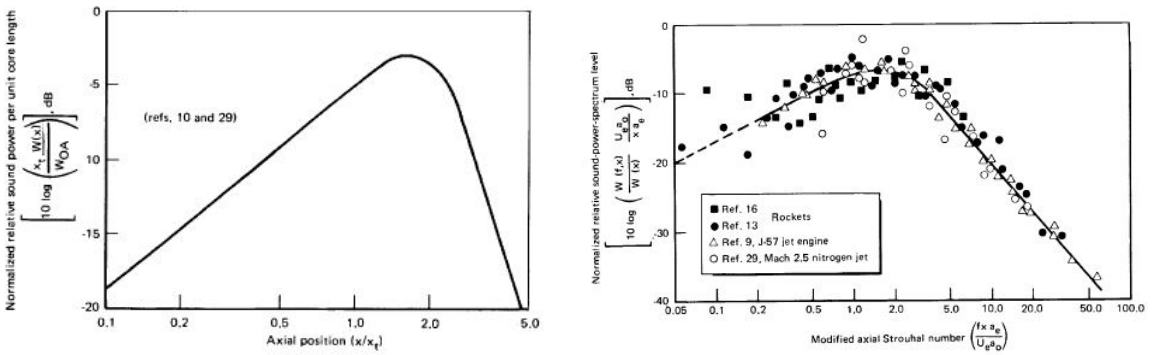

(a) Source power distribution along the jet axis

(b) Normalized relative power spectrum level as a function of axial position

Figure 3.10: DSM-2 method (Eldred, 1971)

The overall sound level is distributed along the jet axis: once the core length is known, the plume is divided into *slices* of arbitrary length Δx such that it is possible to compute the normalized aoustic power per unit core length, as per Figure 3.10a to later determine the overall acoustic power for each slice:

$$L_{w,s} = 10\log\left[\frac{L_C W(x)}{W_{OA}}\right] + L_w + 10\log\frac{\Delta x}{L_C} \qquad \text{[dB]} \tag{3.19}$$

From Figure 3.10a, it is also possible to see that the sound power peak is located at a distance from the nozzle of approximately $L_P \approx 1.5L_C$, whereas the acoustically effective length, that is the length over which 98% of the overall sound power is generated, has an approximate value of $L_A \approx 5L_C$.

Similarly to DSM-1, $L_{w,s}$ is, then, converted to a conventional acoustic bandwidth, as per Figure 3.10b. The obtained values for each frequency bandwidth are, then, plugged into Equation 3.20

$$L_{w,s,b} = 10\log\left[\frac{W(f,x)}{W(x)}\frac{U_e a_a}{x a_j}\right] + L_{w,s} - 10\log\left[\frac{U_e a_a}{x a_j}\right] + \log\Delta f_b \qquad \text{[dB]} \tag{3.20}$$

$$SPL_{s,b,p} = L_{w,s,b} - 10\log r^2 - 11 + DI(b,\theta) \qquad \text{[dB]} \tag{3.21}$$

$$SPL_{b,p} = 10\log\frac{\sum_{\text{All s}}\left[10^{SPL_{s,b,p}/10}\right]}{2\cdot 10^{-5}} \qquad \text{[dB]} \tag{3.22}$$

In a similar fashion to DSM-1, Equation 3.15 is finally applied to compute the overall sound pressure level at a point in space.

At this point, a few comments are deemed necessary to clarify the use of some parameters, namely, core length and its link to source distribution and sound directivity. As far as the source distribution is concerned, even though the DSM-2 method provides a more realistic alternative to source allocation compared to DSM-1, it was reported that, for instance, at $St = 0.025$ the source is estimated to be located at around $50D_e$, value for which no experimental justification was found. Even though it is true that, as opposed to regular supersonic jets, for rockets the region over which the plume is efficiently convective is longer, field measurements have shown that the region of maximum radiation is around $17-20D_e$ (Crocker and Potter, 1966). Varnier (2001) also pointed that to match the predictions based on DSM-2 to his measurements, an unrealistic $\eta \approx 3-4\%$ would be necessary. In light of this, he suggested an improved formulation for the core length, based on the theoretical Mach and diameter of the jet:

$$L_C/D_j = 1.75\left(1+0.38M_j\right)^2 \tag{3.23}$$

$$D_j = (2/M_j)(m^* V_j/\pi P_a \gamma_j)^{1/2}$$

Yet, Varnier (2001) further points that in a supersonic flow the core length L_C is difficult to define in the presence of shock cells and a relation between the supersonic core length and the sound peak location should be preferred: $L_S/L_P \approx M_j^{0.85}$. Nagamatsu and Horvay (1970) had earlier proposed:

$$L_S/D_j = 5M_e^{1.8} + 0.8 \tag{3.24}$$

None of these formulations, however, accounts for the jet temperature: two alternatives have been proposed by Koudriavtsev et al. (2004) and Greska et al. (2008), shown, respectively, below:

$$L_C/D_j = 6 + \frac{8/3U_j^2 + 3c_{p,a}T_a}{c_{p,j}T_j} \qquad L_C/D_j = 3.134e^{(1.043M_j - M_c)}$$

Nevertheless, as much as using core lengths represents a useful simplification, there are still too many uncertainties when it comes to empirical formulations and, to this day, experimental reconstruction of the acoustic field from sub-scale testing still is the most reliable approach.

As for the directivity indices in Equation 3.14 and 3.21, these were used by Eldred to correct the shapes of the spectra due to the wrong assumption of incoherently radiating sources. According to said indices, the maximum radiation angle is around 50° from the jet axis, however Eldred did not clarify what links there are between jet parameters and radiation directivity: indeed, it was seen that the angles predicted by SP-8072 are lower than the ones obtained through the convective Mach number, which are around 65°. Considering turbulent mixing as being the major noise component of rocket noise, and assuming efficient Mach wave radiation, the maximum radiation direction is dominated by the convective Mach number:

$$\mu_{peak} = cos^{-1}\left(\frac{1}{M_c}\right) \qquad M_c = \frac{kU_e}{a_a}$$

In literature $0.6 < k < 0.85$, although, recently Mathews et al. (2021) predicted $k \approx 0.31$ based on Falcon-9 launch data. Many alternative formulations of the convective Mach number have been suggested: for instance, Greska (2005) proposed the following formulation, which has been proven accurate on the measurements of Baars et al. (2014) and Mathews et al. (2021):

$$M_c = \frac{U_j + 0.5a_j}{a_a + a_j}$$

James et al. (2012b) argues that a possible discrepancy between the experimentally determined angles and those theoretically obtained is due to the use of a polar microphone array placed at the nozzle exit - rather than at $x \approx 17D_e$ - and at a small radius from the jet centerline; this effectively provokes a shift of the directivity at smaller angles to the axis. James et al. (2012b) proposed a modification of the directivity curves and provided a more physics-based approach, whose results more closely match with Greska's convective Mach number.

Furthermore, it should be pointed that NASA-SP8072 and the models that followed were mostly based on test data taken either from static firings of full-scale solid rocket boosters mounted parallel to the ground, or during actual launches, to mainly assess the acoustic environments around launch pads. In both scenarios, the effect of the reflections coming from the ground, which effectively induce larger OASPL readings, has not been accounted, thereby making the prediction models inaccurate.
Finally, regardless of the various shortcomings described above, little emphasis was placed on understanding transient ignition noise, responsible for high vibroacoustic loads. Apart from the conventional jet noise sources - turbulent mixing, BBSN and resonance effects - the complex shock system developing inside the nozzle during the initial ignition phases is, in fact, responsible for increased acoustic loading, especially during FSS to RSS transition (Donald et al., 2014), as it will be confirmed from the results of the current research.

4

Experimental methodology

In order to fulfill the research objective, a number of test cases have been conducted on two distinct nozzles. In this chapter, a detailed characterisation of the specimens used is provided, together with a summary of their manufacturing method. Furthermore, a description of facilities, operating conditions and measurement systems employed during testing is given. Finally, acquisition control strategies are detailed.

4.1. Test articles

Experimental investigations have been performed using two axysimmetric TOP contoured nozzles, with a PAR3 contour, based on the design by Ruf et al. (2009), in order to simulate the separated flow behaviour typically observed during the ignition transient of rocket engines. The coordinates of the contour can be found in Appendix C. In the following sections, the design and manufacturing strategies of the compliant nozzle are reviewed. In particular, subsection 4.1.1 presents an overview of the nozzles' gasdynamics properties and highlights the main differences between the stiff and flexible test article, while providing a preliminary acoustic assessment. Subsection 4.1.2, then, elaborates on the manufacturing method implemented to produce the compliant walled nozzle.

4.1.1. Nozzle design

Both nozzles feature identical geometrical and ideal gasdynamics properties, as presented in Table 4.1, and only differ in material and wall thickness.

Property	Symbol	Value	Unit
Throat radius	r^*	8.175	mm
Throat expansion angle	θ^*	40	°
Exit radius	r_e	44.99	mm
Axial length	l	102.2	mm
Expansion ratio	ϵ	30.29	-
Mass flow	$\dot{m}$	2	kg/s
Thrust	F	827	N
Exit pressure	p_e	20148.3	Pa
Exit Mach number	M_j	4.2	-
Exit velocity	v_e	671.56	m/s
NPR at optimal expansion	NPR_{opt}	699.8	-

Table 4.1: Nozzle properties - Operating conditions based on $p^o = 40$ bar

For both nozzles the wall coordinates are obtained using TDK, a two dimensional kinematics software commonly employed in the evaluation of 2D effects on the performance of full scale rocket nozzles, which uses the Method of Characteristics to account for non-equilibrium processes.
Contrary to typical TOP contoured nozzles, the expansion angle at the throat for the test articles used in the present study is chosen slightly higher, to ensure that FSS to RSS transition occurs within the available

NPR range of the testing facility. A comparison between previous studies by Ruf et al. (2009) and Tinney et al. (2017) shows, in fact, that for the same expansion ratio and nozzle length, transition and EER occur at a higher NPR for bigger throat radii. In particular, from the study by Tinney et al. (2017), which employs a nozzle with $r^* = 6.35$ mm and $\epsilon = 30.29$, transition and EER were registered at NPR = 22 and NPR = 39, respectively. It can be, therefore, expected that for the nozzles used in the current study, having $r^* = 8.175$ mm, transition occurs at NPR = $22 \div 24$, as also observed by De Kievit (2021) and Pearse (2022), whereas the EER will not be observed due to the limitations of the testing facility, as later explained in subsection 4.3.1.

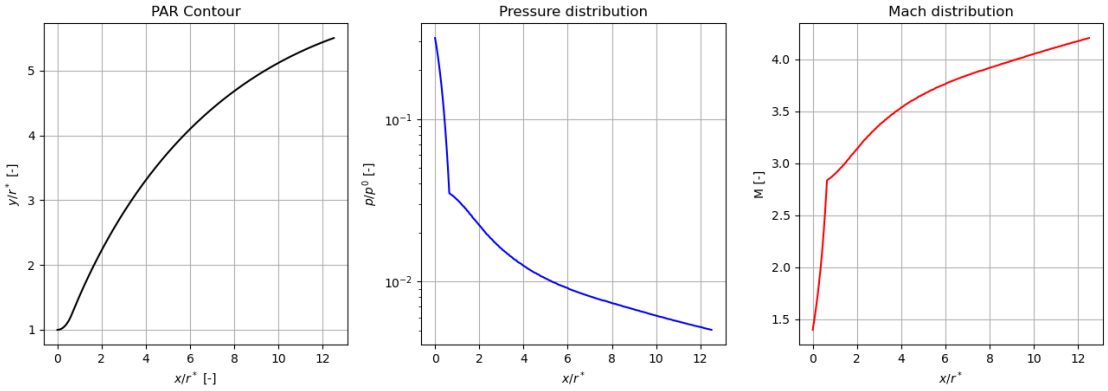

Figure 4.1: PAR3 contour ideal properties

As obtained from TDK, Figure 4.1 shows the main fluid dynamic properties of the nozzle, assuming ideal expansion throughout its whole length. In reality, however, during overexpanded operations, the flow separates, as explained in section 2.3. By using either Schmucker or Stark criteria (Equation 2.1 and 2.2, respectively), it is possible to estimate at which NPR separation will first occur. Analytically, the ratio p_{sep}/p^o can be rewritten as follows:

$$\frac{p_{sep}}{p^o} = \frac{p_{sep}}{p_a} \cdot \frac{p_a}{p^o} = \frac{p_{sep}/p_a}{NPR} \tag{4.1}$$

The ratio p_{sep}/p_a can be substituted with Equation 2.1 or Equation 2.2. Finally, the separation location can be obtained by finding the intersection point between the blue curve in Figure 4.1 and the curve defined by $p_{sep}/p_a/NPR$. The resulting trend is presented in Figure 4.2, and shows that separation can occur as early as $NPR \approx 2.5$, at locations very close to the nozzle's throat. As the NPR increases, the location gradually moves downstream. Even considering the limitations associated with using semi-empirical models, these approaches still provide a fair estimate of the separation location, as also demonstrated by the experiments of De Kievit (2021).

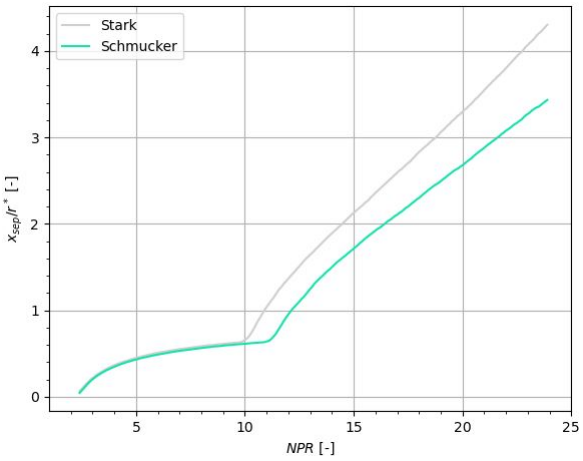

Figure 4.2: Separation location as a function of NPR

As far as the acoustic environment is concerned, the sound pressure levels produced by the nozzle can be predicted using the approach suggested by Varnier (2001): starting from the nozzle's mechanical power $W_M = \frac{1}{2}\dot{m}U_e^2$, and assuming uniform spherical spreading, the acoustic power follows as:

$$L_W = 10\log_{10}(W_A/W_{ref})$$

where $W_A = \eta W_M$ is the acoustic power, W_{ref} is valued at 1 pW and the acoustic efficiency is estimated using Equation 3.12 and assuming $\gamma_j \approx \gamma_\infty$. Finally, the sound pressure level at a designated distance from the nozzle axis can be calculated via Equation 3.16. Considering a range of NPRs comprised between 1 and 40, and based on the wall pressure distribution of Figure 4.1, it can be estimated that the sound pressure levels increase according to the curve in Figure 4.3.

Although the approach is inherently inaccurate as it assumes not only sound generation from a single point-wise source, but also a fully attached flow throughout the provided NPR range, it already shows which order of magnitude of sound levels to expect during operations.

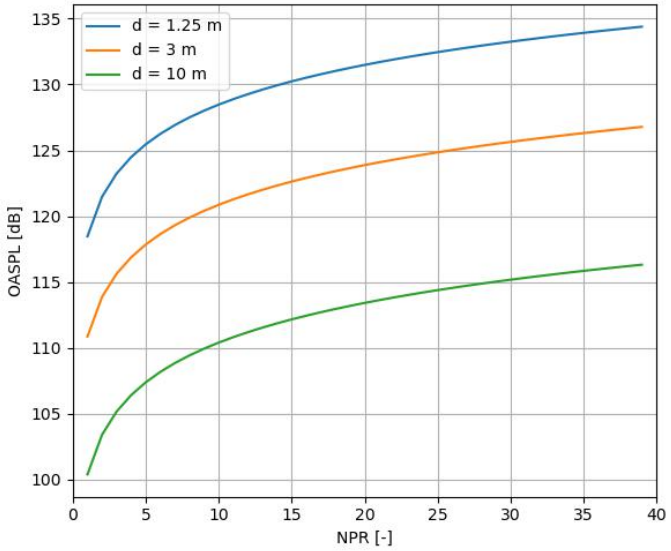

Figure 4.3: Prediction of maximum sound pressure levels as a function of NPR and distance from the nozzle axis

Finally, it should be noted that the above predictions do not account for the inherent differences between the pair of nozzles: as briefly hinted before, in fact, one nozzle, already available in the High Speed Laboratories of the Delft University of Technology, is, made out of aluminium and has a constant wall thickness of 5 mm, whereas the second one is made out of a urethane-based polymer and has a constant wall thickness of 2 mm. The former is used as a baseline test case in which structural vibrations are absent; the latter, on the other hand, ensures the occurrence of fluid-structure interactions.

Table 4.2: Nozzles material properties

Nozzle	**Wall thickness** [mm]	**Material**	ρ_m $[kg/m^3]$	f_y **[MPa]**
Stiff	5	ALU 6082-T6	2700	300
Compliant	2	Polyurethane 66D[1]	1102	10.76

[1] https://www.formx.nl/products/pu-harsen/semi-rigids/smooth-cast-66d---094--kg.php[Date accessed: 3-05-2022]

The choice of polyurethane 66D and the decision to opt for a wall thickness of 2 mm comes from the results of Pearse (2022) whom, having studied the structural behaviour of a number of compliant nozzle with different thicknesses under similar conditions to the ones of the current experimental effort, has observed good correlation with full scale behaviour.

4.1.2. Manufacturing

In order to carry out tests on a compliant nozzle, this had to be manufactured in-house. In order to do so, polyurethane pouring was used as production method and a purposely designed casting mould had to be fabricated to fulfill this objective.

Mould design

Because of its shape, a nozzle requires both an *inner* and an *outer* mould to be obtained. The former was already available at the High Speed Laboratories of the Delft University of Technology, and is based on the design by Pearse (2022). The latter, however, had to be designed in CAD using the faculty's software CATIA v6 R21.

The final design consists of two halves that have been obtained by creating, into a cylindrical block, a rotating groove having the cross-section shown in Figure 4.4. As it can be seen, the section was constructed starting

from the inner wall's coordinates. Then, because, during testing it was decided to use the same clamp that was originally designed to house the nozzles previously tested by (Pearse, 2022), a variable thickness curve had to be drawn and offset from the inner one. Up to an area ratio $A/A^* \approx 5$ downstream of the throat, in fact, the nozzle would be clamped, whereas the remaining part would be left free to vibrate. Therefore, to ensure that the nozzle would fit into the already available clamp to be used when mounting the specimen onto the test rig, two curves, offset of 5 and 2 mm respectively, were drawn.

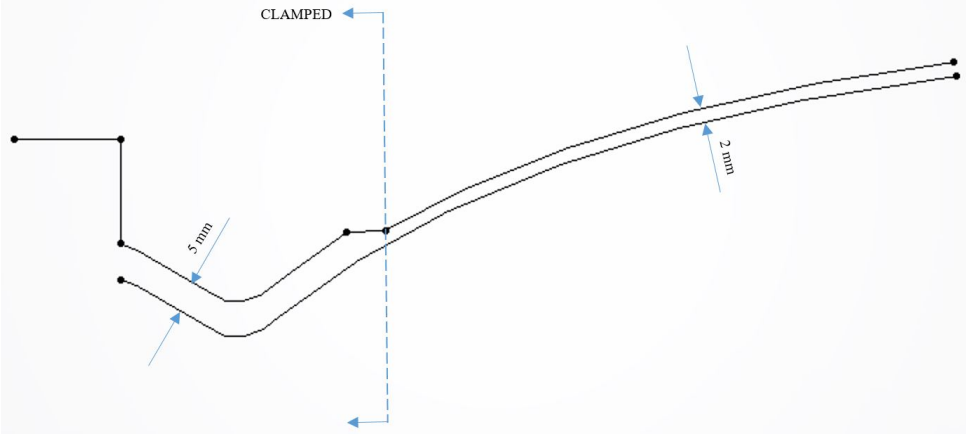

Figure 4.4: Sketch of the nozzle cross-section

To ensure vertical alignment of the two halves, holes were added to house 4 x ⌀4 mm dowel pins. Clamping of the halves was made possible by adding two threaded holes on one half and two simple holes on the other one, such that bolts could be used to tighten the parts together. Concentricity with the inner mould was guaranteed by adding a lip around the bottom circumference of the outer mould that would lock onto the base of the inner one. Furthermore, additional holes were drilled onto the base of the inner mould such that bolts could be used to fasten the two components together and avoid vertical sliding. Finally, to ease the disassembling procedure, a screw mechanism was added to the design, such that the two halves could be effortlessly pulled apart by taking advantage of the linear motion that would result from the rotation of a screw.

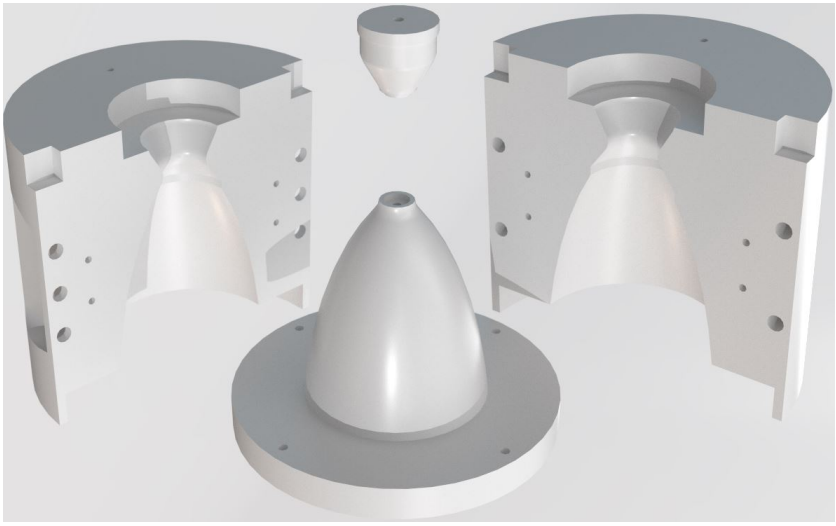

Figure 4.5: Exploded view of the mould assembly

Finally, arrangements with an external supplier[1] for its production have been subsequently made. Being lightweight and easy to machine, Aluminium was chosen as a suitable material for the mould. This combination of manufacturing process and material was preferred over 3D printing in order to achieve an assembly

[1] `https://www.tudelft.nl/en/electronic-and-mechanical-support-division`[Date accessed: 02-07-2022]

with higher tolerances that would ensure smoother nozzle surfaces and greater chances of obtaining a nozzle with constant thickness throughout its whole length.

Compliant nozzle manufacturing
Nozzle production was carried out at the Composite Lab of the Delft Aerospace Structures and Materials Laboratory[2] and pouring was used as production method. The outsourced material consists of two casting resins (Part A and Part B as shown in Figure 4.6) which are to be mixed with a mix ratio of 1A:1B by volume. In order to fill up the mould, a total of 120g of mixture is required, which roughly correspond to 62.18g of component A and 57.82g of component B.

The procedure requires a few main steps:

1. Polyurethane refrigeration
2. Components degassing
3. Application of a release agent on the internal surfaces of the mould
4. Mould assembly
5. Mixing of component A and B
6. Pouring into the mould
7. Overnight curing and demoulding
8. Nozzle refining

Figure 4.6: Smooth-on polyurethane 66D

Once the pots are removed from the refrigerator, the needed amounts are poured into two separate plastic containers with the help of a pipette and weighted on a precision scale. Because, in the process, air bubbles are introduced into the liquids, which could make the final result anisotropic, the containers are, then, placed into a degasser. In the meantime, the internal surfaces of the mould are first cleaned from any impurity with a dry cloth and, then, sprayed with a release agent to ensure an effortless removal of the nozzle. Next, the mould is assembled and placed on a working table. Once the degassing procedure is completed, the containers are removed from the vacuum chamber and component B is poured into the jar containing component A. From this moment, a timer should be started to make sure that all the following steps are completed within the curing time of the mixture, indicated to be roughly 7 minutes. A lid is used to close the container and, without stirring, the mixture is placed into the Speed Mixer DAC 400.2 VAC-P[3] available in the Materials Lab. The routine reported in Table 4.3 is used to ensure that thorough mixing of the resins is achieved while maintaining the mixture free of air bubbles.

Table 4.3: Speed mixer routine

Time [s]	90	10	10	10	10
Speed [rpm]	1200	1000	1000	800	0
Pressure [mBar]	200	400	600	800	1000

Optionally, the machine also acts as a vacuum chamber, so an additional degassing step can be implemented while mixing to obtain a finer result. However, it should be noted that once the components come into contact, an exothermic reaction is initiated and because vacuum lowers the boiling point of the mixture, thereby degrading it, a lower pressure values leads to a lower curing time. Once the Speed Mixer routine is completed, the jar is taken out, and the mixture is poured onto the mould. This step could, again, entrain some air bubbles into the liquid. Therefore, if available, and making sure that the mould is securely fastened, a vibrating table can be employed, to allow any remaining bubble to rise to the top as quickly as possible. Next, the mixture is left to cure overnight and once the nozzle is extracted from the mould, alcohol is used to remove excess release agent. Finally, sand paper is used to refine the external surfaces and peel off any excess material.

Not just one, but multiple nozzles have been produced using this technique. This was done for a number of reasons: the first few nozzles have been sectioned to inspect that they had a constant wall thickness through-

[2] `https://www.tudelft.nl/en/ae/organisation/departments/dasml` [Date accessed: 10-06-2022]
[3] `https://www.speedmixer.ie/dac400.2vac-p.php` [Date accessed: 25-08-2022]

out their length such as to verify that the mould was manufactured according to the specifications, and to also ensure that they did not contain any air bubble. After this quality control phase, more nozzles were manufactured to ensure not only that enough were available during testing in case one would fail, but especially to be able to run tests under similar operating conditions on different specimens, as to later verify the repeatability of the manufacturing process.

4.2. Ground vibration testing

In order to characterise the dynamic behaviour of both the stiff and compliant nozzle, that is, to infer on their natural frequencies and mode shapes, a GVT campaign was carried out.
GVT is an experimental methodology which relies on modal analysis to derive the modal model of a structure. Under the assumption of a linear time-invariant system, it does so by taking advantage of the fact that its vibration response can be expressed as a linear combination of natural frequencies.
In a nutshell, the technique consists in determining a set of Frequency Response Function (FRF)s, which mathematically define the relationship between the vibration response of the structure $X(\omega)$ and the excitation force $F(\omega)$ as a function of frequency ω (He and Fu, 2001). For an idealised measurement scenario where no noise is present, the FRF is commonly defined as:

$$H(\omega) = \frac{X(\omega)}{F(\omega)} \tag{4.2}$$

In the context of modal testing, the excitation force is commonly exerted by either a hammer or an electromagnetic shaker, which apply, on the structure, a force of sufficient frequency content. In the case of an impact hammer, the frequency content can be easily controlled by choosing a hammer tip having the appropriate hardness. Tips can be made of rubber, plastic or steel and, the harder the tip, the wider the spectrum upon which energy is distributed. As far as the amplitude content is concerned, an essential assumption of modal testing is that the structure behaves linearly. This hypothesis is a prerequisite to obtaining accurate and repeatable FRF data and satisfy Equation 4.2: only for a linear and time-invariant structure, in fact, the vibration response is an exact multiple of the force input.
Accelerometers or laser scanning vibrometers, on the other hand, are the sensors which are most commonly used to measure the vibration response of the structure. Accelerometers are mounted directly on the structure and this, in some cases, might constitute a drawback; if the test object is lightweight, the accelerometers' mass, which becomes non-negligible with respect to the structure, could have an impact on the response function, thereby overpredicting the natural frequencies. Scanning Laser Doppler Vibrometry, on the contrary, is a non-intrusive full-field vibration imaging measurement technique, which uses a laser beam to scan the structure.

For the current research, test preparation has involved the selection of a structure's support, a type of excitation force, a type of vibration response sensor, and the appropriate hardware to measure force and response. A description of this effort is presented in the following section, which gives an overview of the hosting facility, the employed equipment and the final test arrangement.

4.2.1. Facility, equipment and setup

Modal testing was carried out at the Mechanical Testing Lab of the Delft Aerospace Structures and Materials Laboratory[4]. Both stiff and compliant nozzle were tested to assess their resonant properties. As far as the compliant nozzle is concerned, 9 different specimens were tested, to infer on the robustness of the manufacturing process, as outlined in subsection 4.1.2.
The presence of a Thorlabs optical table fitted with active vertical and horizontal vibration isolation legs [5] was determining in choosing this specific facility. In order to secure the test structure, the nozzle was first clamped at the throat and the clamp fastened onto the table, as shown in Figure 4.7. The clamp is the same that is used on the ASCENT Test rig and provides a physical boundary condition to the structure up to an area ratio of 5. In this way, the same boundary conditions that the nozzle would experience during cold flow testing would be complied thereby offering clearer indication on its resonant behaviour.
The internal lip of the nozzle was equipped with equally spaced IPC[6] accelerometers. A small quantity of

[4] `https://www.tudelft.nl/en/ae/organisation/departments/dasml` [Date accessed: 10-06-2022]
[5] `https://www.thorlabs.com/newgrouppage9.cfm?objectgroup_id=5930` [Date accessed: 29-10-2022]
[6] `https://www.pcb.com/products?m=352A24` [Date accessed: 03-10-2022]

wax was used to make sure they would adhere to the surface. A total of 8 accelerometers were used in order to detect bending mode shapes up to the 4^{th}. The excitation force, applied at a single excitation point, was provided using a Maul-Theet vImpact-61 automatic modal hammer[7], equipped with a metal tip.

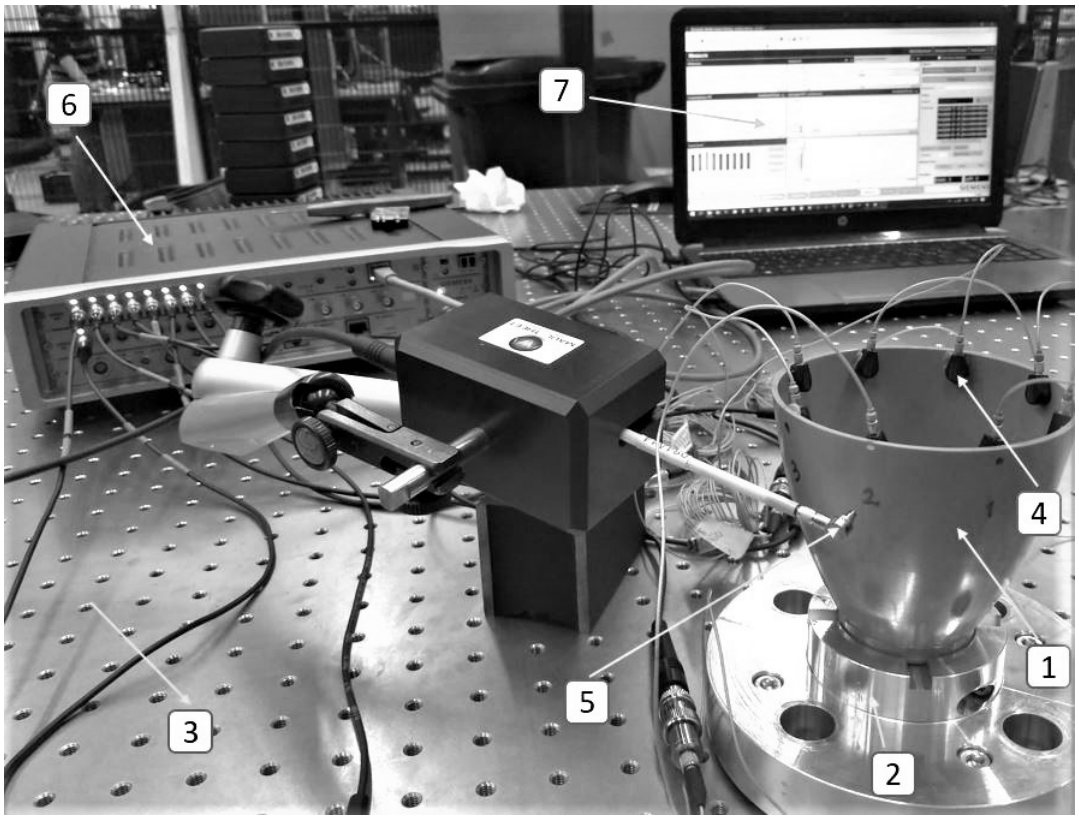

Figure 4.7: Ground vibration testing setup. 1. Nozzle, 2. Clamp, 3. Optical table with leg isolators, 4. Accelerometer, 5. Impact hammer, 6. Signal generator and data recorder, 7. Acquisition PC

The hammer tip had to be placed near the nozzle lip, in a position such that to avoid any undesired double hits or cell overloading. Both accelerometers and hammer were connected to different channels on a Siemens Simcenter SCADAS Mobile Recorder, in turn connected to an acquisition PC on which a SIEMENS TESTLAB MIMO FRF program file was setup and each channel configured using the parameters presented in Table 4.4. The next step was to define the coordinates system of the structure-accelerometers assembly, such as to recreate a digital 2D model of the test geometry. Apart from recording the system response, SCADAS also generates the FRFs from the acceleration measured by the sensors. In order to improve the signal-to-noise ratio, for each nozzle, 5 consecutive measurements were taken, and an averaged FRF was obtained.

Parameter	Value/Type	Unit
Source		
Signal	Periodic chirp	-
Level	0.1	V
Sweep direction	Up	-
Sweep	Linear	-
Sweep time	95	%
Sweep ramp time	0	s
Acquisition		
Mode	Burst	-
Bandwidth	2048	Hz
Spectral lines	8192	-
Resolution	0.25	Hz
Static bandwidth	256	Hz
Averaging Parameters		
Number of averages	5	-

Table 4.4: MIMO FRF Setup

In this regard, a few trial runs were performed in order to check the quality of the system's response. In particular, as shown in Figure 4.8, FRF and coherence were plotted.

[7] https://www.maul-theet.com/products/vibration-modal/hardware/automatic-modal-hammer/[Date accessed: 01-10-2022]

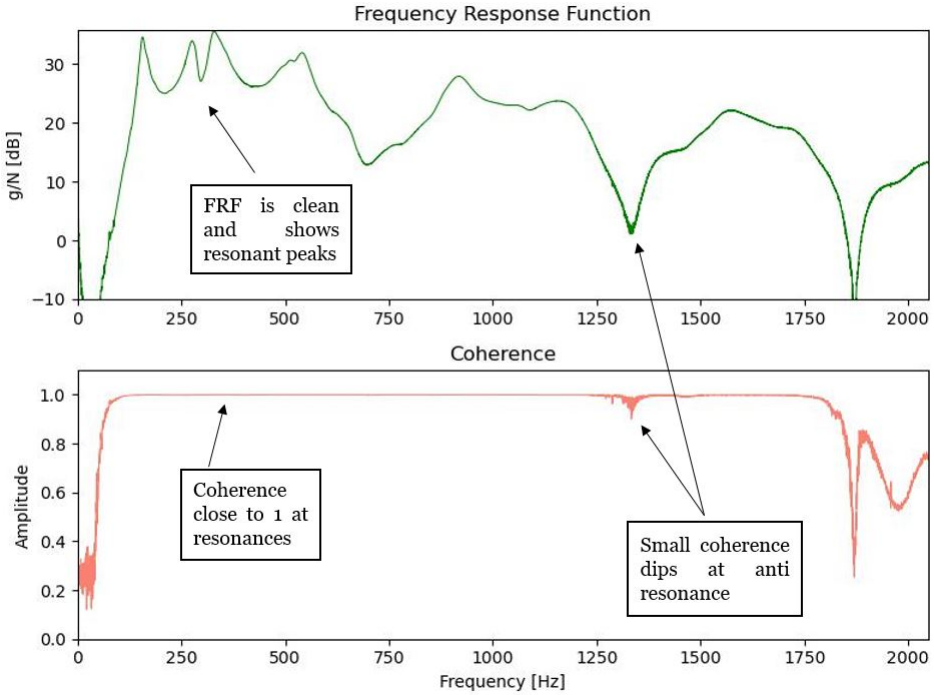

Figure 4.8: GVT measurement system's quality check during a trial run

4.3. Cold flow testing

In this section, the facility and equipment that have been employed to perform the main experimental activities will be presented. A description of the testing facility is first given in subsection 4.3.1. This is followed by a description of the instrumentation employed for acoustic sensing, nozzle lip tracking and schlieren imaging, in subsection 4.3.2, together with an overview of the data acquisition control.

4.3.1. ASCENT Test rig

The main experimental activities have been conducted employing the ASCENT test rig. The rig is located where the diffuser tube of the ST-15 supersonic wind tunnel[8] usually sits at the High Speed Laboratories of the Delft University of Technology and its schematic is provided in Figure 4.9.

The working fluid is dry unheated air (T^o = 288 K), which is drawn from an external pressure vessel with a storage capacity of 300 m^3. When fully charged, the reservoir can contain approximately 484 kg of air, corresponding to a maximum attainable stagnation pressure of 40 bar. Given the large volume of the pressure vessel, the rig can be operated for an estimated duration of 18 minutes, before recharging is required: De Kievit (2021) assessed that if a nozzle with r^* = 1 cm were to be used, the pressure drop in the tank would be of approximately 0.5 bar for a 60 seconds run. This means that for tests lasting in the order of tens of seconds, the pressure can be considered constant and no active flow control is required. It is, however, known that pressure losses through the feed system between tank and nozzle amount to approximately 8 bar, thereby reducing the maximum NPR to 32 and making the investigation of the EER unattainable.

The rig is operated using a flow control valve which needs to be hand-regulated: this implies that the NPR is manually adjusted, thereby limiting the possibility of achieving a uniform ramp. Moreover, at lower NPRs, the valve is more sensitive, in that it requires less turning to obtain a step increase of 1 bar compared to higher NPRs. Nevertheless, as shown in Figure 4.10, during the experimental campaign it was possible to operate repeatable transient tests. It should, however, be noted from Figure 4.10b that the maximum achieved ramp rate is around 7.5 s^{-1} for startup and -10s^{-1} for shutdown, which is 3 orders of magnitude slower than a typical ramp of a full-scale liquid propellant rocket engine (Rojo et al., 2016); therefore, even though it is

[8] https://www.tudelft.nl/lr/organisatie/afdelingen/aerodynamics-wind-energy-flight-//performance-and-propulsion/facilities/high-speed-wind-tunnels/st-15-supersonic-windtunnel [Date accessed: 07-03-2022]

possible to visualise changes in flow topology, test outcomes should be regarded as resulting from *quasi-steady* conditions.
Once open, pressurised air is fed to a diffuser, which is designed to slow the air flow down before it enters the settling chamber, in order to accurately measure total conditions. The flow velocity in the settling chamber is approximately 12 m/s. To achieve this condition while avoiding flow separation (Mehta and Bradshaw, 1979), the diffuser has an expansion ratio of 4.7 and a contraction angle of 12°, which result in a diffuser length of 97 mm.

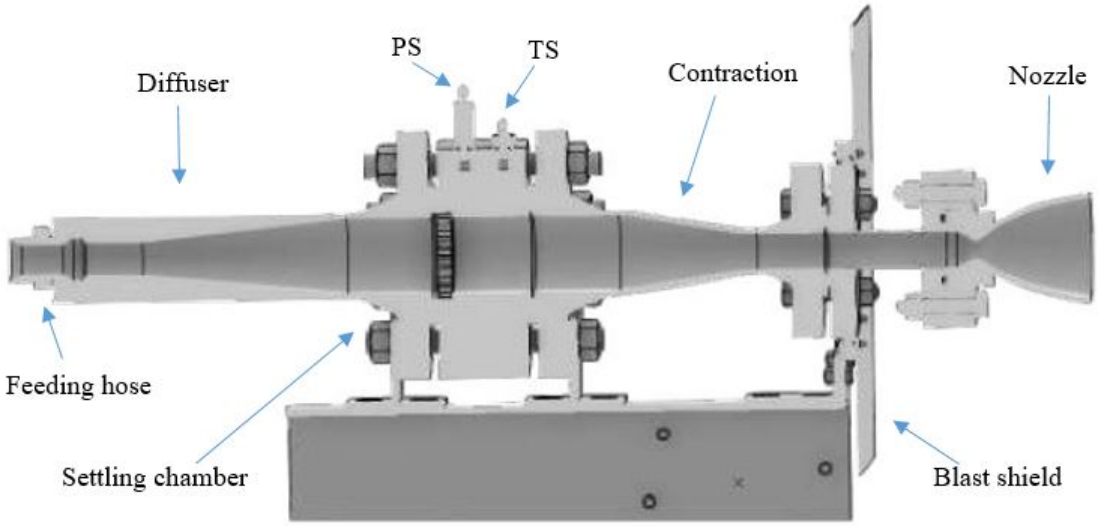

Figure 4.9: ASCENT test rig - Cut view of fluid components (De Kievit, 2021)

Total pressure in the settling chamber is measured employing a IFM PT5402[9] transmitter, which is directly screwed in the settling chamber via a 1/4" BSP thread. The transmitter outputs an analogue current signal up to 20 mA which can be later converted to a pressure value according to the following expression:

$$p[bar] = 6269.83 \cdot I[A] - 24.02 \tag{4.3}$$

Air is, then, fed through a contraction and, next, onto a nozzle, whose centerline is located 125 cm above the ground, at the same height as the ST-15 wind tunnel diffuser outlet, located at an axial distance of approximately $12D_e$ from the nozzle exit, in which the expanded supersonic gases are discharged.

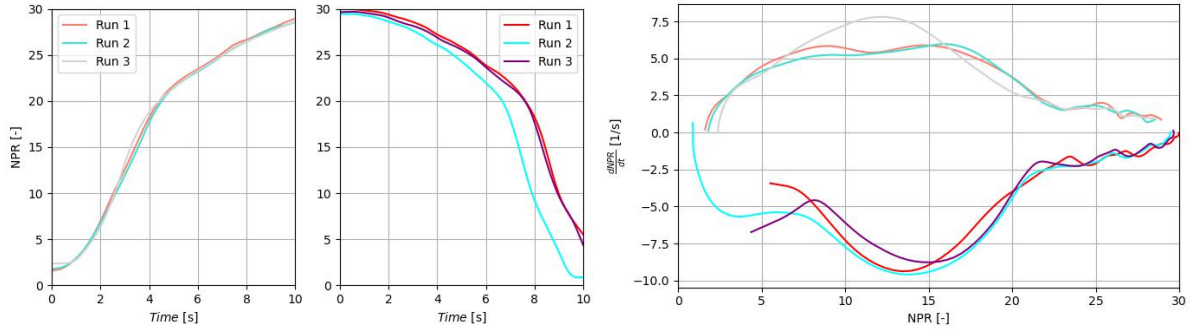

(a) NPR. Left: startup - Right: shutdown

(b) dNPR/dt. Up: startup - Down: shutdown

Figure 4.10: Comparison of NPR and NPR/dt for several transient runs

4.3.2. Test setup

In order to fulfill the research objective, a combination of experimental measurement techniques has been used. This has required preparing an elaborate test setup that could simultaneously record total pressure,

[9] https://www.ifm.com/nl/nl/product/PT5402[Date accessed: 14-10-2022]

acoustics, nozzle lip movement, and schlieren images of the flow, as shown in Figure 4.11. In the coming sections, an overview of the employed instrumentation is given, together with a short description of the working principle of each technique, and a final summary of the control strategies used during testing.

Parameter	Value/Type	Unit
Pressure		
Sensor	IFM PT5402	-
Acquisition frequency	2000	Hz
Lip tracking		
Camera type	Photron FASTCAM SA1.1	-
# of cameras	2	-
Lens focal length	60	mm
Aperture $f_\#$	4	-
Exposure time	50	μs
Image resolution	512 x 512	pixels
Acquisition frequency	2000	Hz
Acoustics		
Microphone type	GRAS 46BE 1/4" CCP	-
# of microphones	8	-
Distance from nozzle exit plane	$d = 32$	cm
Distance from nozzle axis	$r = 25$	cm
Acquisition frequency	51200	Hz
Schlieren imaging		
Parabolic mirror focal length	1500	mm
Camera type	Photron FASTCAM SA.1	-
# of cameras	1	-
Exposure time	12	μs
Image resolution	896 x 896 (Transient)	pixels
	1024 x 1024 (NPR = const)	pixels
Acquisition frequency	500 (Transient)	Hz
	2000 (NPR = const)	Hz
Transient run duration	10	s
Constant NPR run duration	3.5	s

Table 4.5: Summary of acquisition settings for all measurement techniques

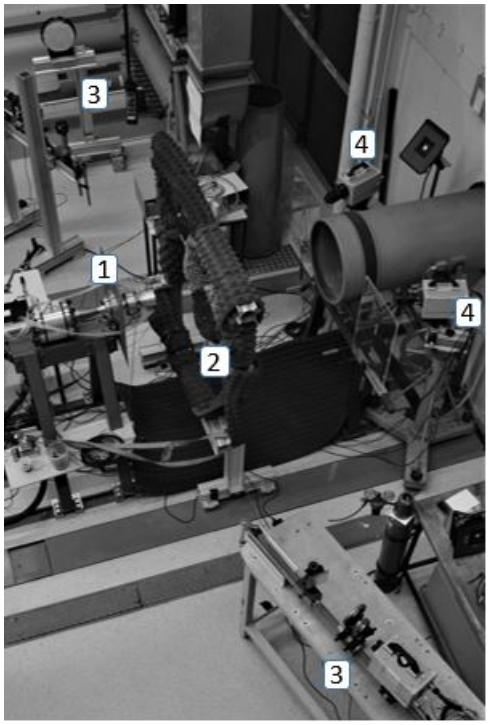

Figure 4.11: Test setup seen from above. 1.ASCENT test rig, 2. Acoustic array, 3. Schlieren setup, 4. Lip tracking

Acoustic sensing system

Since the main objective of this research consists in investigating the acoustic signature of TOP nozzles, a number of IEPE-powered GRAS 46BE 1/4" CCP Free-field microphones[10] have been employed. Specific details of this model include a 3.6 mV/Pa nominal sensitivity, a frequency response range between 4 Hz and 100 kHz (±3 dB error) and a dynamic range up to 160 dB (ref: 20μPa).

A nominal acquisition frequency of 51.2 kHz has been selected for all test runs and two different microphone configurations have been opted for, as depicted in Figure 4.12a and 4.12b, respectively. A preliminary test campaign, in fact, was carried out and consisted in only employing 4 microphones, located at the nozzle's sideline, at a distance from the jet axis r = 1.23 m, with the microphones' diaphragm placed at grazing incidence to the jet axis. Having chosen to place the origin of the coordinate system at the nozzle's exit plane, the streamwise (x) position of the microphones relative to this origin is: x = [0, 0.47, 0.94, 1.41] m. This corresponds to polar angles relative to the jet axis and nozzle exit plane of ϕ = [90, 69, 52.6, 41.1] deg. This placement should be, in principle, able to cover both shallow and steep angle observer locations, thereby offering useful insights onto noise directionality. An additional reason that motivated this test configuration consisted in obtaining an initial estimate of the jet's sound pressure levels at that distance, to later consider the possibility of moving the microphones closer to the jet without damaging them. Given the OASPL value obtained at r = 1.23 m, a combination of spherical and cylindrical decay was assumed, which resulted in a limit *safe* distance of 5 cm from the jet axis.

A second investigation was, then, carried out employing a circular array of 8 equally spaced microphones ($\phi = 45°$) placed concentrically to the nozzle jet axis. Appropriate positioning of the array was determined by processing the line-array measurements: as demonstrated in Figure 4.13, albeit with minimal differences, the highest sound pressure levels during the most critical flow activity are registered between microphones 2

[10] `https://www.grasacoustics.com/products/measurement-microphone-sets/constant-current-power-ccp/product/143-46be`[Date accessed: 08-07-2022]

and 4, independently of the nozzle employed. Based on this premise and on the requirement of the Schlieren system to prevent any blockage of the optical test section, it was, therefore, opted to place the array at a radial distance $r = 23.5$ cm, and at an axial distance to the nozzle's exit plane of $d = 32$ cm, corresponding to a polar angle of $\phi \approx 36°$. For all microphones, this corresponds to a fixed observer angle of $\theta \approx 36°$. Finally, contrary to the previous configuration, the microphones' diaphragm was placed in such a way to directly face the jet plume.

Based on the pressure decaying laws by Arndt et al. (1997), presented in section 3.1, it appears that for both configurations - the azimuthal one in particular - microphones are placed in the acoustic *near field*, especially when considering low frequency waves. This implies that the detected signals might not be purely acoustic and could have an hydrodynamic component to it.

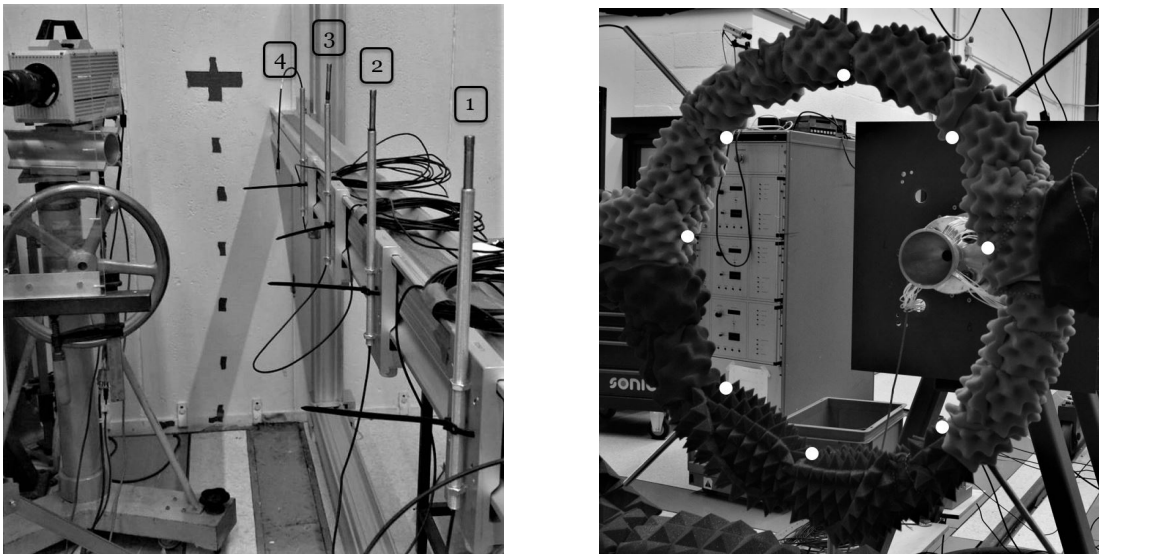

(a) Setup of the microphone's line array during preparation

(b) Circular array of microphones - White dots indicate microphone positions

Figure 4.12: Microphone configurations used during testing

When using both microphone configurations, these were secured on purposefully built beam structures, that were later wrapped with sound absorbing foam sheets, to reduce sound reflections as much as possible. However, given the fact that acoustic insulation of the whole facility was not feasible, sound reflections should still be expected. Generally speaking, sound reflections are determined by the acoustic impedance mismatch between the 2 medium (to simplify, one can consider air and the concrete of the walls). Due to the fact that denser media impede the higher frequency waves more, and because concrete is denser than air, the greater mismatch is often registered at the higher frequencies, which are the ones more likely to be reflected. For this purpose, the foam sheets that were employed feature a short height and width of their wedges, such that are best suited to absorb high frequency (low wavelength) reflected sound waves.

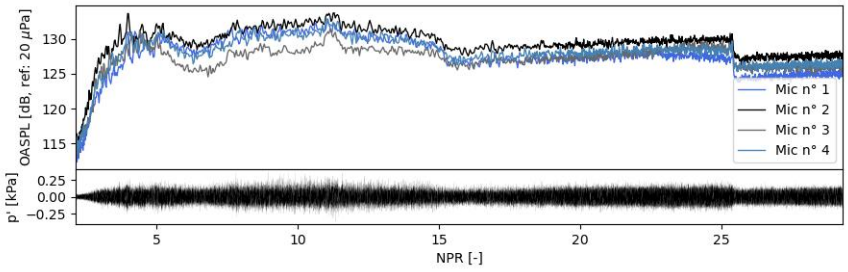

Figure 4.13: Preliminary survey of maximum overall sound pressure level directionality during transient startup

Stereo lip tracking system

Investigating nozzle's aeroelasticity also constitutes a fundamental part of this experimental effort. In the framework of the current research, this practically consisted in determining the deformation of the nozzle, when subjected to the high loads occurring during FSS and RSS flow states, by measuring the instantaneous displacement of its lip. To do so, a non-intrusive, full-field optical technique, similar to Particle Tracking Velocimetry (PTV), was employed, which consisted in performing structural measurements by imaging and tracking reflective fiducial markers distributed on the compliant nozzle lip. As shown in Figure 4.14, the compliant nozzle was first spray-painted with a matte black color to minimise reflections. Next, 24 equally spaced, highly reflective white circular dots, with an approximate diameter of $\varnothing 1.5 \pm 0.5$ mm, were manually painted on the surface. Even distribution was possible with the help of a purposely designed and 3D printed mask having a predefined circular pattern.

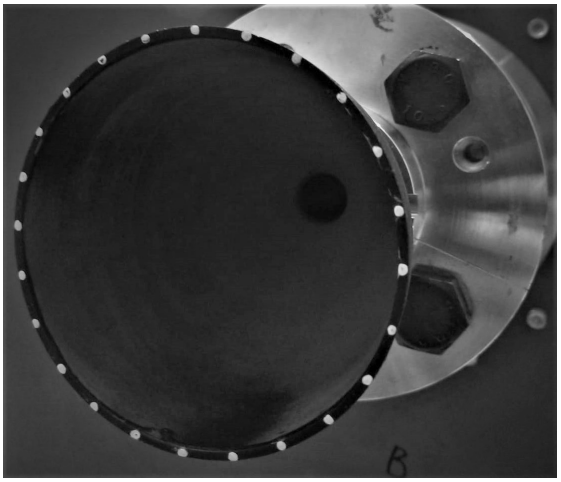

Figure 4.14: Detail of fiducial markers on compliant nozzle lip surface

Depending on the number of cameras and their arrangement, either 2D or 3D reconstruction of the displacement field is possible: the light scattered by markers is digitally recorded by a camera system, and, based on the processing algorithm used, their position over time can be tracked, as later illustrated in subsection 5.2.2. First, however, calibration of the optical system is necessary in order to be able to compute the marker's displacement in the *world plane*. As a matter of fact, geometric calibration of any camera system is essential when quantitative measurements need to be executed. It, refers, in fact, to the process of determining and correcting perspective distortions, while defining the mm-scaling of the images. In general, this is essential when results shall be analysed in units representing the *world* dimensions; but it is even more so in the case of stereo or tomo measurements, when the position of each camera relative to the test plane/volume, and relative to each other is needed.

For the current experimental effort, 2 Photron FASTCAM SA1.1[11] were employed to allow for stereoscopic reconstruction of the nozzle lip displacement. The decision of using more than 1 camera came about after the observations made by Pearse (2022), who noticed a coupling between bending and ovalisation mode of the nozzle lip. Nevertheless, having employed just a single camera, the author was not able to point whether said coupling was, indeed, a reliable observation or just the result of camera distortions. By using 2 cameras, the goal is that of better assessing the occurence of said frequency coupling. As shown in Figure 4.15a, these were placed at opposite sides of the ST-15 wind tunnel's diffuser outlet, with their height with respect to the test object adjusted via 2 tripods on which they were mounted and secured. Additional protection of both cameras and lenses, from dangerous and unwanted debris that could have been scattered in case of nozzle failure during testing, was accomplished by mounting transparent plexiglas screens in front of them. To ensure that recorded images were bright enough, additional illumination was provided with an LED light placed behind the cameras and directed towards the nozzle. The cameras, having a 1024x1024 pixel camera sensor, with a pixel size of 20x20 μm, have been operated in single-pulse mode, and their resolution has been cropped to 512x512 pixels to increase the acquisition time to a maximum of 10s, for an acquisition frequency of 2000

[11] `https://www.highspeedimaging.com/wp-content/uploads/2020/02/FASTCAM_SA1_manual_legacy.pdf` [Date accessed: 22-09-2022]

Hz. The Photrons communicate with a LaVision Programmable Timing Unit (PTU-X)[12] by means of an I/O connector and BNC cables. The I/O connector is attached to the camera by means of the I/O port, located at the center of the rear of the camera; on the other extremity of the I/O cable, BNC cables are attached and connected to the PTU-X by means of a second connector. Each camera transfers images to the PC by means of an ethernet cable. In order to use the cameras for high-speed acquisition it was necessary to use a PC with a high-speed card installed; for this reason, the acquisition was controlled by an acquisition computer equipped with dual processor (Intel(R) Xeon(R) CPU E5-2630 v3 2.40 GHz with each one 10 physical cores and 20 threads) and 64 GB of Random Access Memory (RAM), and running DaVis 10.2.1[13].

(a) Lip tracking cameras setup, with frontal LED light illumination

(b) Calibration plate placed in front of the nozzle

Figure 4.15: Lip tracking setup

System calibration was achieved by recording preliminary images of a reference object of known size; in this case, a LaVision dual level Type 10 calibration plate, featuring 171 markers per side, equally spaced by 10 mm, with a thickness of 5 mm, was placed in front of the nozzle, as shown in Figure 4.15b.

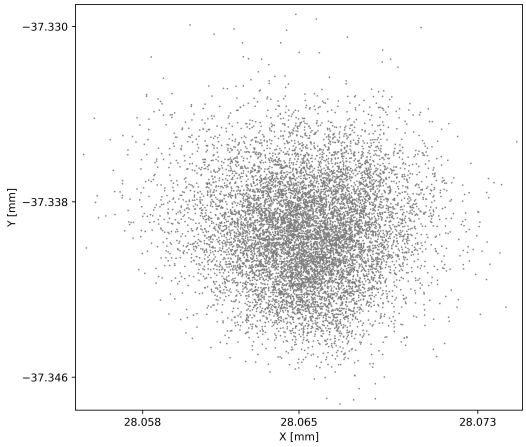

Figure 4.16: Time series of reference marker position in 2D space during a static recording

Finally, to ensure that both cameras were firmly secured onto the tripods and that no background oscillations would compromise the system's calibration, a dry run was carried out. This consisted in taking pictures of a static nozzle lip at f_s = 2000 Hz for 3 seconds while no other system was being operated. The outcome of said preliminary check, referred to a single fiducial marker, that is, yet, representative of the full view field, is presented in Figure 4.17. The plots show minimal displacements both in radial and azimuthal direction,

[12] 4https://www.lavision.de/en/products/cameras/programmable-timing-unit-ptu-x/[Date accessed: 28-06-2022]
[13] https://www.lavision.de/en/products/davis-software/[Date accessed: 11-04-2022]

and that should be simply regarded as an unavoidable consequence of camera disparity, as later explained in subsection 5.2.2, which will in no way affect test results.

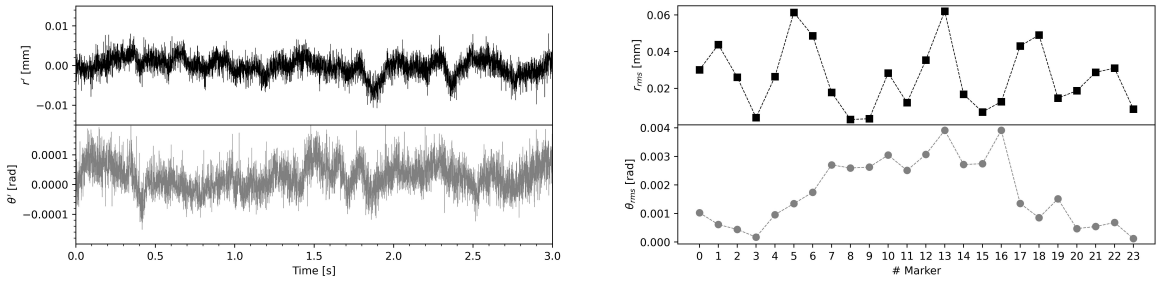

(a) Time series of radial (upper) and azimuthal (lower) reference marker fluctuation

(b) Standard deviation of fluctuation residuum for all markers

Figure 4.17: Lip tracking system check against background oscillations

Information on the behaviour of the cameras during testing is, however, not known. Nevertheless, even though high flow pressures induce some vibrations onto the whole building, the cameras have been mounted on tripods equipped with vibration suppression pads that are able to dampen environmental oscillations; it is, therefore, possible to confidently assume that even during testing the same background camera noise levels reported during dry testing occur. As an ultimate test, it was thought to paint a separate marker onto the test rig structure and track it separately to check for camera vibrations. Nevertheless, even assuming that the cameras move, it is expected that the rig itself shakes more strongly than the cameras, resulting in a biased camera background noise analysis.

Schlieren imaging system

Non-intrusive optical-based methods like Schlieren take advantage of the physical properties that light has when it propagates through an inhomogeneous and compressible medium; when interacting with matter, light is refracted based on the medium density, following the Gladstone-Dale relation, and bent by an angle θ at the boundary of two substances having different refractive index according to Snell's law:

$$n = 1 + K\rho \qquad\qquad n_1 \sin\theta_1 = n_2 \sin\theta_2$$

with n and K being the gas refractive index and the Gladstone-Dale constant ($2 \cdot 10^{-4} m^3/kg$ for air).
More specifically, when interacting with gases, light rays are always bent toward the region of higher density. By illuminating a test region, using a point-wise light source shaped through a series of lenses and mirrors, as shown in Figure 4.11, it is possible to obtain a schlieren image of the phenomenon of interest, that is, an optical image in which spatial density gradients $\nabla\rho$ of an otherwise transparent medium become noticeable (Settles, 2001) and are proportional to the image's pixel intensity, according to:

$$\frac{\Delta I}{I} = \frac{f}{a} KW \frac{\partial \rho}{\partial x}$$

with f and a being, respectively, the focal length of the camera and the fraction of light hitting the camera sensor, and K and W being the Gladstone-Dale constant and the width of the light source.
What differentiates Schlieren from, for instance, shadowgraphy, is the use of a *knife-edge*, pictured in Figure 4.18b. Once light has passed through the test section, this instrument is used to block the light after it has been focused using a parabolic mirror: when a flow experiences density gradients, those light rays that are bent can now pass and hit the camera sensor. On the other hand, those light rays that have not been bent, and that would have been able to pass had there not been a knife-edge, are now blocked. As seen in the formula, the higher the amount of light that is blocked (smaller a), the higher the sensitivity of the pixel intensity to density changes.

For this experimental campaign, given the limited space available, a Z-configuration schilieren setup was built. It consists of two branches, as shown in Figure 4.18, placed on opposite sides of the test section. On one side, a continuous light source shines a collimated light beam onto a lens, which focuses it on a pinhole. Next, the point-source light produced by the pinhole, located at a distance from a parabolic mirror equal to

its focal length, hits the mirror and is reflected as a cylindrical light column illuminating the test section. Said light ray hits, in turn, a second parabolic mirror located on the other side. Once converged on the parabolic mirror, light is, again, reflected by a plane mirror and directed onto a knife-edge located at a distance from the second parabolic mirror equal to its focal length. Finally, the diverted light rays can fall onto a camera sensor. For this, a Photron FASTCAM SA1.1, with a CMOS sensor of 1024x1024 pixels was used. Images were acquired using Photron FastCam Viewer 4.0. To allow for acquisition control and later transfer of data, the camera was connected via an Ethernet cable to the same acquisition PC that was being used for stereo lip tracking acquisition. However, given the camera's limited internal storage of 8 GB, and to allow for sufficient filming time, the image size has been reduced to 896x896 pixels during transient tests, and an acquisition frequency of 500 Hz was chosen. Finally, even though these type of cameras can provide a quasi-instantaneous characterisation of the flow, the representation of the latter might be limited by the choice of the exposure time. Ideally, the smaller the exposure time, the higher the chances of obtaining a frame depicting a flow that is *frozen* in time; this, however, is limited by the fact that the shorter the exposure, the lower the image brightness. During the current experimental effort, an exposure time of $12\mu s$ was selected, which means that, assuming a flow particle having velocity $v \approx 340$ m/s, in the span of a frame, it has travelled approximately $\Delta x = v \cdot t = 340 \text{ m/s} \cdot 12\mu s = 4,1$ mm.

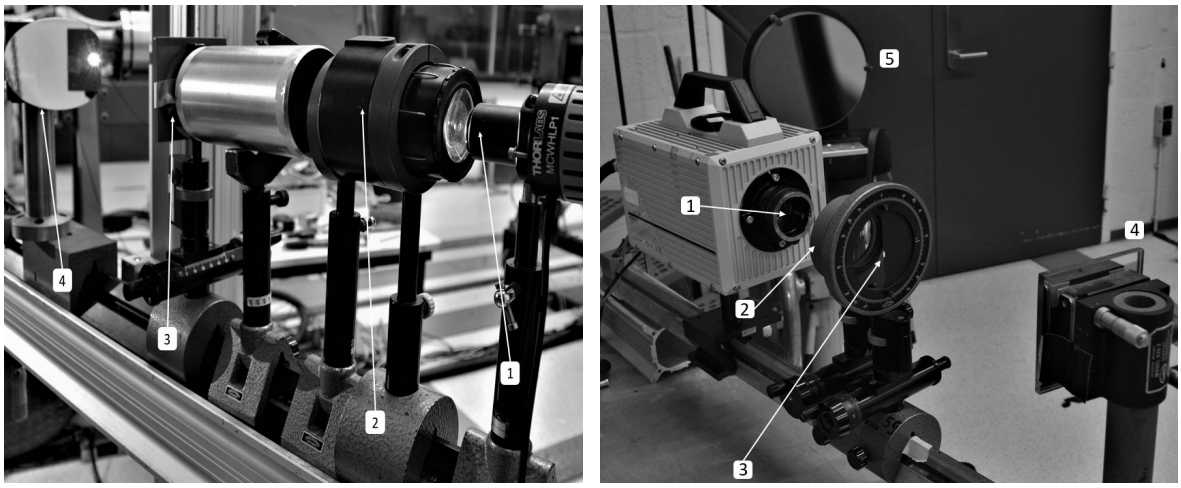

(a) Configuration of 1^{st} branch of the Z-schlieren setup: 1. Light source, 2. Lens, 3. Pinhole, 4. Plane reflective mirror

(b) Configuration of 2^{nd} branch of the Z-schlieren setup: 1. Camera sensor, 2. 80 mm lens, 3. Vertical knife, 4. Plane reflective mirror, 5. 1500mm parabolic mirror

Figure 4.18: Z-type schlieren setup

Acquisition control

Connecting all systems to allow for simultaneous acquisition required a complex setup, which is illustrated in Figure 4.19. Once everything was properly connected, a few trial runs were carried out to check that all hardware was functioning properly. Next, a number of test runs were operated. These consisted in both transient and constant NPR test runs, with transient tests comprising either start-up and shutdown ramps, according to the test matrix presented in Table 4.6.

Table 4.6: Cold flow test matrix

Nozzle type	Run	NPR	Microphones - Line array	Microphones - Azimuthal array	Stereo lip tracking	Schlieren imaging
Stiff nozzle	**Startup**	✓	✓	×	×	×
	Shutdown	✓	✓	×	×	×
	Startup	✓	×	✓	×	✓
	NPR = 24.5	✓	×	✓	×	✓
Compliant nozzle	**Startup**	✓	✓	×	✓	×
	Shutdown	✓	✓	×	✓	×
	Startup	✓	×	✓	✓	✓
	NPR = 11.3	✓	×	✓	✓	✓
	NPR = 18.9	✓	×	✓	✓	✓
	NPR = 22.3	✓	×	✓	✓	✓

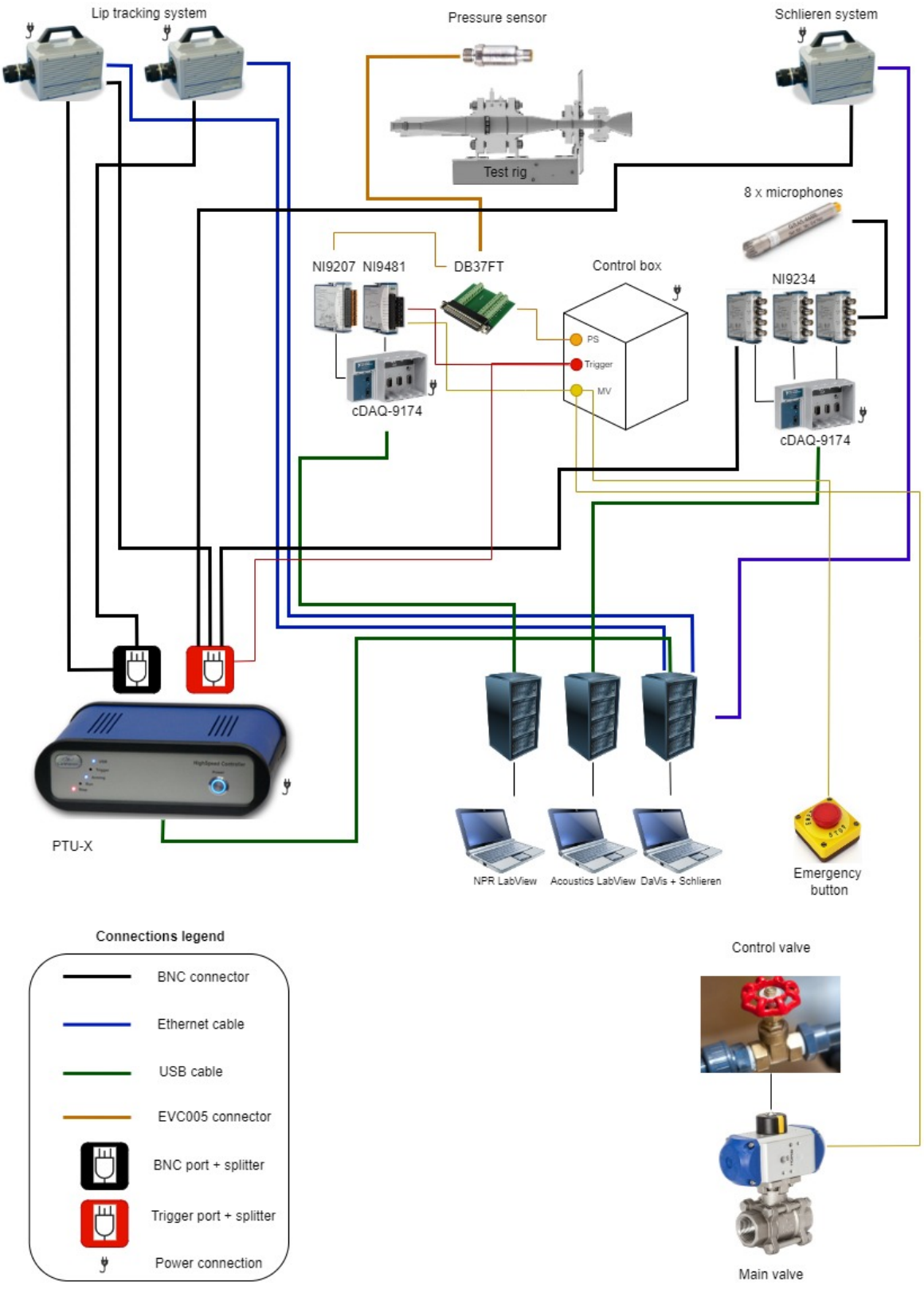

Figure 4.19: Cold flow testing acquisition system flow chart

5

Data processing strategies

During the experimental campaigns, multiple measurement systems have been employed, as described in chapter 4. As a result, a large quantity of data was acquired in the form of FRFs from the GVT, images from Schlieren and lip markers tracking, and text files from NPR and acoustic pressure readings. In order to properly analyse the forenamed data to answer the research questions presented in section 1.1, a few processing strategies have been implemented and are hereby described. First, a summary of the pre-processing steps required to obtain nozzle structure's natural frequencies and lip displacements during operation is given in section 5.1 and 5.2, respectively; next, the foremost theoretical frameworks employed to extract meaningful results from each typology of data are presented in section 5.3 and 5.4.

5.1. Modal analysis

In a process often referred to as *modal curvefitting*, FRF data acquired during GVT is used to extract a meaningful set of modes and their associated modal parameters, which include natural frequencies, damping values and mode shapes. As the name suggests, a mathematical model that fits the acquired FRF is computed using the SIEMENS TESTLAB Modal Analysis application. Using polynomials with increasing order number and coefficients, a fit is found when the error between the mathematical equation and the data points is minimum. In a few steps, outlined in Figure 5.1, the software performs said mathematical calculations and suggests which is the best combination of natural frequencies and damping ratios that would explain the FRF data.

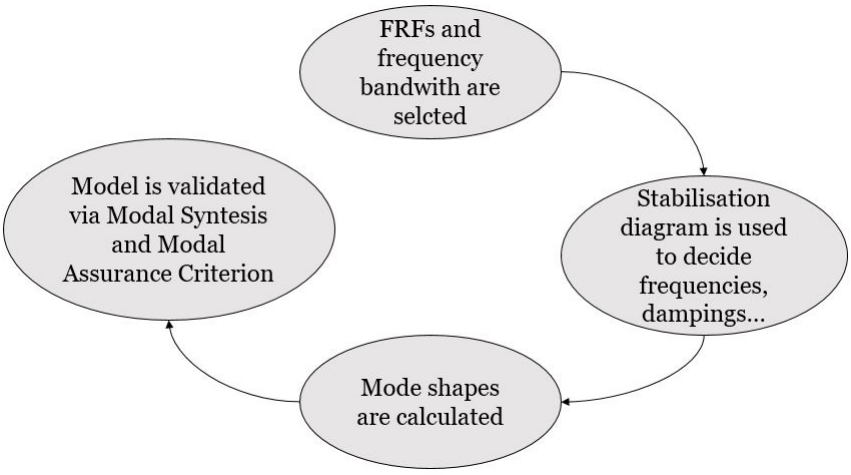

Figure 5.1: Workflow of the modal curvefitting process

Within the "Band" worksheet of the Polymax interface, the measured FRFs are selected and a suitable frequency bandwidth is set. Additionally, the Mode Indicator Function (MIF) was displayed to check for repeated roots, that is, the possibility of having two modes at the same frequency. Such likelihood was rejected

since no "double dips" were seen. Next, as shown in Figure 5.2, in the "Stabilisation" worksheet, a diagram streamlines the selection of potential modes: in the bottom toolbar, a model size, which represents the order of the polynomial used to fit the FRF data, is selected. This prompts the software to output, at certain frequencies, columns of letters, each indicating the quality of a potential mode. One should aim to select only *stable* solutions, defined by the letter "S", as it indicates that frequency, damping and modal vectors are all stable.

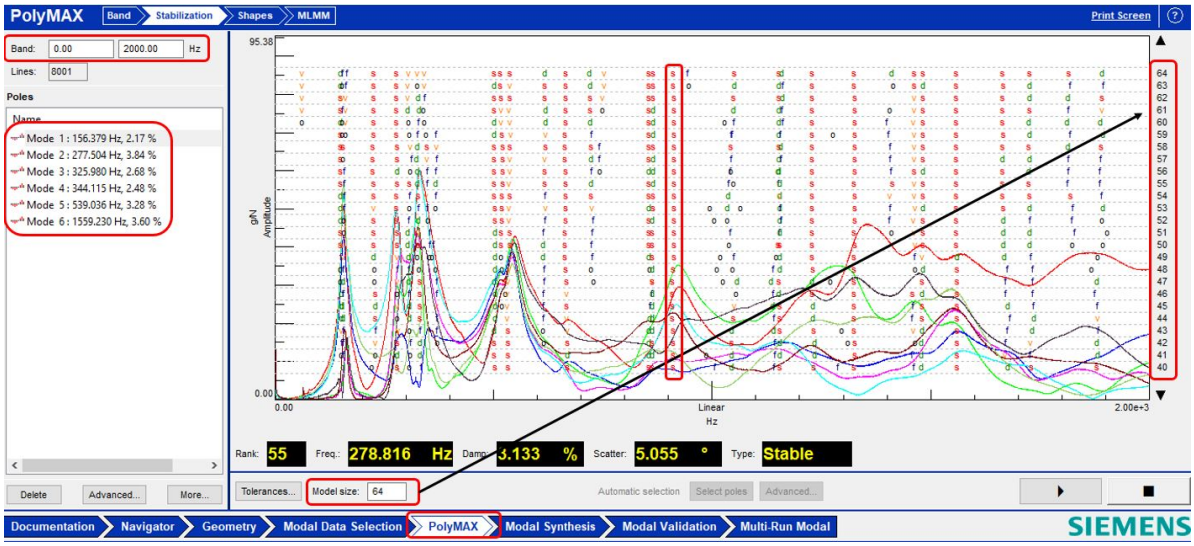

Figure 5.2: Modal stabilisation diagram using the Polymax algorithm

Once a suitable number of stable solutions, i.e. frequencies, are selected, their corresponding mode shape is calculated in the "Shapes" worksheet. As an optional step, also the Maximum Likelihood estimation of a Modal Model (MLMM) interface is used: by automatically iterating over the parameters of the initial model, it performs an optimization of both frequencies and dampings in order to obtain better matches with the FRF data.

Figure 5.3: Modal synthesis between measured (red) and synthesized (green) FRF

Finally, the verify the robustness of the model, the "Modal synthesis" interface is used. The process of modal synthesis consists in comparing the measured FRF data with the synthesized FRFs obtained through modal curvefitting. For the current processing, results show very good levels of correlation for all the cases run and a low error percentage, as presented in Figure 5.3.

5.2. Markers processing

When acquiring high-speed frames of the vibrating compliant nozzle, the results that are obtained consist in a series of images of which the pixel count, i.e. their intensity, is known throughout the whole view field

and at each time instant. Having taken preventive measures such as painting the lip with highly reflecting markers, against a matte black background, the quality of the raw images is already quite high. However, images still feature some level of background noise and reflections that could compromise the quality of the final results. For this reason, some preliminary image filtering and masking operations are carried out to improve their quality, and are explained in subsection 5.2.1. Next, the procedure that was used to obtain markers coordinates at each time step is outlined in subsection 5.2.2.

5.2.1. Images pre-processing

As briefly mentioned, a number of pre-processing operations have been carried out to improve image quality before implementing any marker tracking algorithm. An overview of the operations that have been applied to the raw images, together with details of the parameters employed in each pre-processing step is given in Table 5.1.

Intensity normalisation to 1^{st} image	
Geometric mask	
Set above/below intensity to constant	
Set above [counts]	$100 \rightarrow 250$
Set below [counts]	$90 \rightarrow 10$
Smoothing	
Type	Gaussian
Kernel area [pix x pix]	9x9

Table 5.1: Pre-processing operations for fiducial markers tracking

First of all, it was observed that, a slight positioning asymmetry, combined with the flickering effect of the LED light placed behind the cameras during recording, as previously shown in Figure 4.15a, caused the pixel intensities of raw images to change considerably between consecutive frames and between different cameras. For this reason an intensity normalisation to the 1^{st} image was carried out to eliminate said effect. Next, a geometric mask was applied to remove any area of the frame which did not contain lip markers such as to avoid that unwanted reflections or saturated pixels could be later mistaken for markers. This also speeded up subsequent processing steps, as a smaller section of each image had to be analysed. Afterwards, a further step was taken to standardize pixel counts and facilitate particle recognition: specifically background intensity was decreased to 10 counts, whereas markers intensity increased to 250 counts. Finally, a Gaussian smoothing over an area of 9x9 pixels was applied to uniform markers shape. A comparison between a raw and a processed frame can be seen in Figure 5.4a and 5.4b.

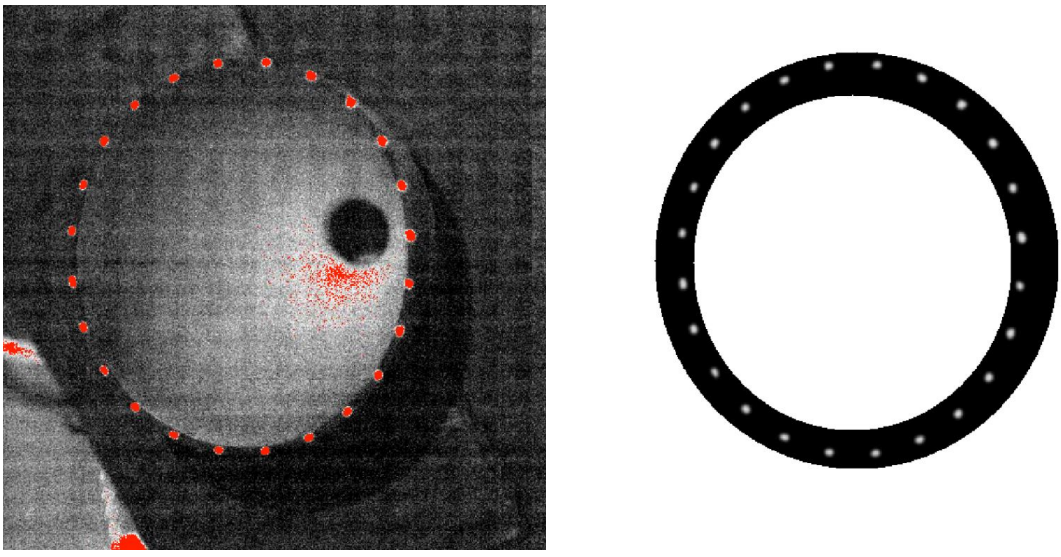

(a) Raw image

(b) Processed image

Figure 5.4: Comparison between a raw and processed nozzle image as seen from Camera 1 of the stereo-lip tracking imaging system

5.2.2. Iterative Particle Reconstruction

Having performed a perspective calibration on the basis of the calibration target images acquired before testing, it is now possible to reconstruct the markers field and analyse the nozzle's dynamics using the IPR algorithm (Wieneke, 2012), implemented in DaVis 10.2.1. Before this processing routine can be launched, a Volume Self-Calibration (VSC) has to be performed and an Optical Transfer Function (OTF) defined. The former consists in removing any residual disparity coming from the geometrical calibration, whereas the latter removes the negative effects of optical distortions due to blurring and astigmatism, thereby improving the reconstruction quality and the accuracy of the particle peak positions (Schanz et al., 2012).

VSC is a 2-step procedure consisting in the computation of the disparity vectors, which are later used to correct the perspective calibration. When performing perspective calibration, in fact, the *lines-of-sight* for each pixel are obtained, under the assumption that each pixel of each camera sensor collects light only from particles located along its line-of-sight. In this context, disparity vectors designate the errors in the intersection of the lines-of-sight for each camera when, due to incorrect calibration, they do not intersect at a single point, as shown in Figure 5.5. In other words, VSC consists in estimating a position which is closest to the lines-of-sight of each camera for each pixel, and to later use the perspective calibration's mapping functions to project this new position onto each camera sensor.

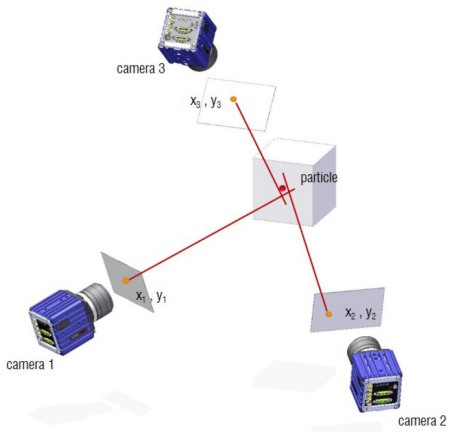

Figure 5.5: Visual representation of camera disparity (LaVision, 2022)

When replicating this step for each pixel, a disparity map, which combines the disparity information of all particles in discrete sub-volumes, is obtained, as shown in Figure 5.6a. Finally, from the disparity map, average disparity vectors, whose lengths signify the deviation of the lines-of-sight, can be calculated. By selecting an allowed *triangulation error* ϵ_{max}, that is a maximum tolerated disparity length, only particles with $\epsilon < \epsilon_{max}$ are used to build up the disparity maps. Those with higher values are discarded. This step is iteratively repeated until a small enough disparity is achieved and the perspective calibration is, then, updated to account for the obtained disparities.

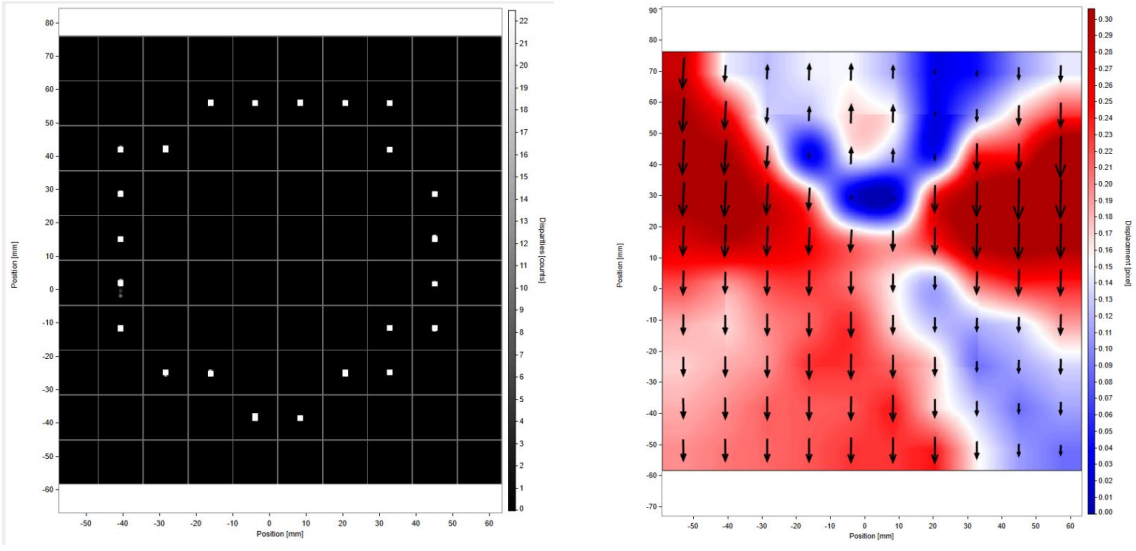

(a) Disparity map

(b) Disparity field

Figure 5.6: Example of Volume Self-Calibration iteration result

Next, an OTF is automatically generated to optimize particle positions and intensities. An overview of the

workflow leading up to the definition of the OTF is presented in Figure 5.7.

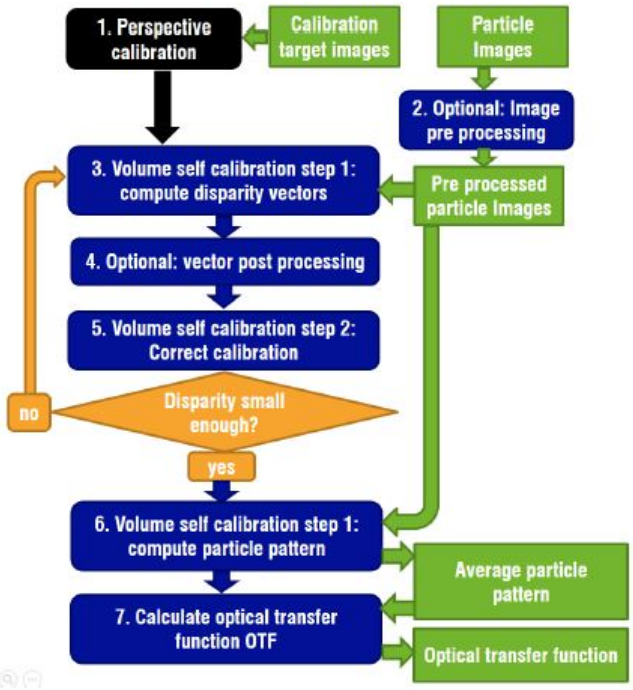

Figure 5.7: DaVis 10.2.1 workflow to compute the Volume Self-Calibration and the Optical Transfer Function (LaVision, 2022)

Having obtained a suitable OTF, the IPR routine can be launched. Contrary to traditional Particle Image Velocimetry (PIV) algorithms which divide the test volume in multiple interrogation windows and compute the movement of particles by cross-correlating the same window at two subsequent time instants, IPR consists in tracking each marker individually, in a similar fashion to PTV. At its core, a triangulation process that employs the calibrated camera mapping functions is used. Next, an iterative optimization procedure that searches for the best particle position by minimizing the intensity residuals in the image plane by shaking the particles in world coordinate location is implemented. The IPR routine parameters that have been used in the current experimental effort are summarised in Table 5.2. First, a 2D particle detection threshold of 200 counts is selected to avoid the detection of potential outliers. Next, to improve detection of particle matches between cameras, a maximum triangulation error of 1 voxel is chosen. As for the shaking procedure, 4 outer loops are defined, whereas 8 inner refining iterations are implemented. Furthermore, in order to minimise the residuum as much as possible, as suggested by Schanz et al. (2012), particles are *shaked* by 0.05 voxels, thereby increasing the final overall accuracy. Finally, concerning the OTF, default values have been used.

Particle detection	
Threshold for 2D particle detection [counts]	200
Allowed triangulation error [vox]	1.0
Shaking	
Outer loop iterations	4
Inner loop iterations	8
Shaking particle position [vox]	0.05
Remove particles closer than [vox]	20
Remove particles weaker than [vox]	0.1
Particle image shape & intensity	
OTF size factor [-]	1.0
OTF intensity factor	1.0
OTF radius [pix]	Auto

Table 5.2: IPR parameters used to track fiducial markers

Ultimately, to further manipulate the obtained data and to implement tailored analysis methods such as those described below in section 5.3 and 5.4, access to the coordinates field was streamlined using the Python library lvreader v1.2.0[1]. From a preliminary analysis of said data, two main concerns emerged. First, the IPR routine was not always able to track *all* 24 markers at each time step.

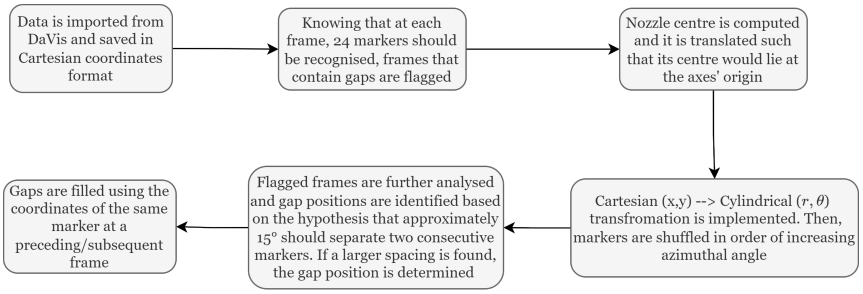

Figure 5.8: Python routine workflow to obtain ordered markers data

This resulted in a few frames presenting some gaps; to overcome this issue it was decided that, due to the high acquisition frequency employed during testing, said gaps could be *filled* with the marker's position associated with the subsequent time instant. Furthermore, it was noticed that the IPR routine did not always output markers positions in the same order, so they had to be reshuffled in order of increasing azimuthal angle. A concise workflow of the implemented steps is presented in Figure 5.8, while the outcome of said pre-processing steps is reported in Figure 5.9b.

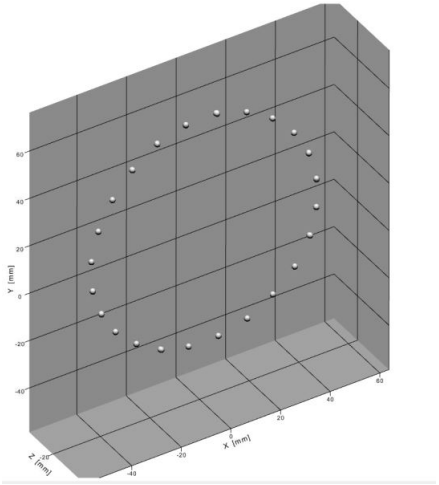

(a) 3D reconstruction as outputted by the IPR routine

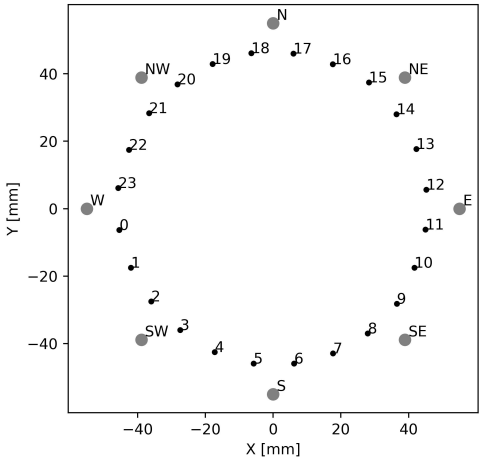

(b) 2D markers reconstruction as outputted by the Python routine, re-arranged in order of increasing azimuthal angle. Grey dots represent microphone azimuthal positions with compass naming convention

Figure 5.9: Fiducial markers reconstruction

5.3. Fourier azimuthal mode decomposition

Having obtained markers displacements from processing the acquired images in DaVis, as detailed in section 5.2, the nozzle's vibrational behaviour can be deduced. Given the versatility of the approach, the same strategy is employed to study also the modal behaviour of the acoustic pressure waveforms.
As a matter of fact, any time-periodic signal can be regarded as an infinite series of sine and cosine waves:

$$f(t) = a_0 + \sum_{n=1}^{\infty} a_n \cos\left(\frac{2\pi n}{N} t\right) + \sum_{n=1}^{\infty} b_n \sin\left(\frac{2\pi n}{N} t\right) \tag{5.1}$$

[1] `https://www.lavision.de/en/downloads/software/python_add_ons.php`[Date accessed: 28-10-2022]

Both the deflection of the nozzle lip, and the acoustic pressure waveforms acquired with the circular microphone array, however, have not only a time dependence, but are also function of the angle θ. When analysing said data, it is convenient to use a framework which transforms the spacial information to a spacial-frequency space, that depends on mode numbers m and time. Any signal that has an angular dependency can be Fourier transformed in azimuth to obtain time-dependent complex Fourier coefficients, that are closely related to the coefficients a_n and b_n of Equation 5.1:

$$x(m,t) = \mathbb{F}_\theta[x(\theta,t)],$$

with m being the mode number. Depending on the discretisation of the grid, mode coefficients run from the negative to the positive azimuthal Nyquist wave number, in the following order: $m = [0,1,2,3,...,k_n,-k_n,...,-3,-2,-1]$, with $k_n = N/2$, with N being the number of discretised azimuthal points. This means that, in the current work, decomposition up to the 4^{th} and 12^{th} mode is possible for microphone and marker's data, respectively.

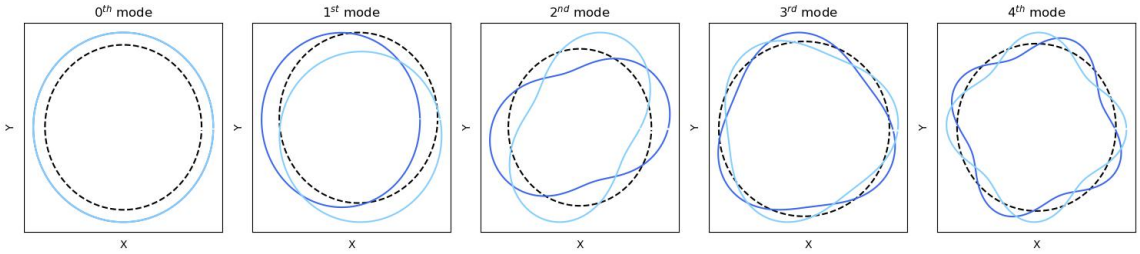

Figure 5.10: Fundamental and higher harmonics of the bending mode: 0^{th} = breathing mode, 1^{th} = pure bending, 2^{th} = ovalization, 3^{th} = traingular mode, 4^{th} = square mode. Dashed line correspond to the undeformed state; dark blue lines represent the positive modes; light blue lines represent the negative modes

Except for $m = 0$, positive and negative mode coefficients of the same order form conjugate pairs, that is:

$$x(m,t) = x^*(-m,t)$$

This means that, even though they represent the same mode shape, their physical orientation in Cartesian space is shifted, since, as seen in Equation 5.1, a_n is associated with a cosine wave, whereas b_n, with a sine wave. A graphical representation of this feature is given in Figure 5.10, in which it is also possible to notice that individual vibrational/acoustic mode shapes can be obtained when performing an *inverse* Fourier transform of the mode coefficients matrix, with all but the desired mode coefficients set to zero. From this it can be concluded that, each mode coefficient can be regarded as the the m^{th} contribution to the original unsteady signal, and their magnitude gives an indication of how *active* one mode is within the signal. In particular a key parameter for the analysis of azimuth-dependent data, defined in Equation 5.2, is the modal activity ρ:

$$\rho = \sqrt{a_n^2 + b_n^2} \tag{5.2}$$

5.4. Spectral analysis

Spectral analysis was used to investigate the frequency content of a multitude of acquired datasets. Given its versatility, it was used, among others, to inspect the spectral content of the acoustic pressure waveforms or that of Fourier-azimuthal mode coefficients. Depending on a series of factors, a number of different approaches were used, as described below.

5.4.1. Fourier Analysis

Spectral content of data obtained from steady NPR tests was analysed by means of the Fast Fourier Transform (FFT), with the Power Spectral Density (PSD) obtained using Welch's method with 50% bin overlapping, in order to account for non-linearity and non-periodicity of the signal (Welch, 1967). Even with limited data storage capacity, it was still possible to opt for acquisition lengths that would allow to obtain converged spectra in the frequency range of interest. Throughout the remainder of this thesis, results are presented by taking the one-sided PSD:

$$G_{uu}(f) = 2\sum \langle X_i(f)\bar{X}_i(f)\rangle \tag{5.3}$$

where $X_i(f) = \mathbb{F}(x_i(t))$ is the temporal FFT of each windowed bin and $\bar{X}_i(f)$ its complex conjugate. Finally, brackets $\langle\rangle$ signify ensemble averaging. Window size was chosen based on signal length, to ensure appropriate frequency resolution.

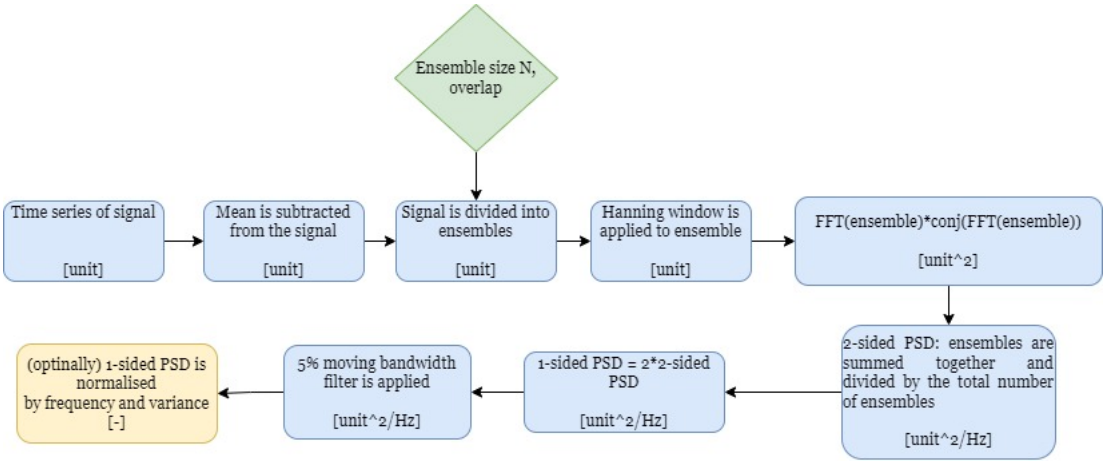

Figure 5.11: Welch's method to obtain the PSD from the time series of a signal

Finally, in order to verify that signal energy is conserved between time and frequency domain, Parseval's theorem is applied:

$$\frac{1}{T}\int_{-\infty}^{\infty}|e(t)|^2 dt = \int_{-\infty}^{\infty}|E(f)|^2 df \tag{5.4}$$

This practically translates to checking that the ratio between the variance of the signal in the time domain and the integral under the PSD curve is close to unity.

In the specific case of microphone signals in the form of acoustic pressure, the spectra are presented in terms of Sound Pressure Spectrum Level (SPSL) in dB, with $p_{ref} = 20\mu Pa/\sqrt{Hz}$:

$$SPL(f) = 10\log_{10}\left(\frac{G_{uu}(f)}{p_{ref}^2}\right) \tag{5.5}$$

5.4.2. The Morlet Wavelet Transform

When dealing with non-stationary signals, these cannot be processed in a 1D space in which they are only function of frequency (Fourier analysis), but, rather, need to be decomposed in time-frequency space. In order to extract spectral content from the acoustic pressure waveforms and the Fourier-azimuthal mode coefficients which result from transient test runs, a joint time-frequency analysis needs to be carried out and is hereby described.

Wavelet analysis involves a transform from a 1D time series to a diffuse 2D joint time-frequency image. If its definition stopped here, it could be easily confused with windowed Fourier analysis. However, one of the main differences between the two approaches is that the latter features an inefficiency that comes from the fact that a *single* sliding window of fixed size N is chosen apriori. This limits the accuracy in both time and frequency domain: if the window size is taken to be rather long, one can get a better low frequency accuracy df = $f_s/2/N$, with $f_s/2$ being the Nyquist frequency, but poor time precision; on the other hand, a short window size can yield good time precision dt = N/f_s but poor frequency resolution. In other words, windowed Fourier transforms fix the temporal width of their basis vector to the length of the transform, thus independently to any bin frequency. On the contrary, in wavelet analysis window size changes according to frequency, and is an approach that should be favoured when studying signals featuring a wide range of dominant frequencies,

and for which a predetermined scaling is not appropriate.

Having proved itself as a powerful approach when analysing similar data to the one of the current research (Rojo et al., 2016, Donald et al., 2012), an analogous methodology, based on the theoretical framework outlined by Torrence and Compo (1998), was applied to the acoustic pressure waveforms and the real-valued acoustic pressure and marker's displacement mode coefficients. In the current work, a complex-valued Morlet wavelet ($|\omega_\psi = 6|$) was chosen as the mother wavelet; as opposed to other conventional wavelet, the Morlet wavelet features a high-frequency resolution and consists in a plane wave modulated by a Gaussian.

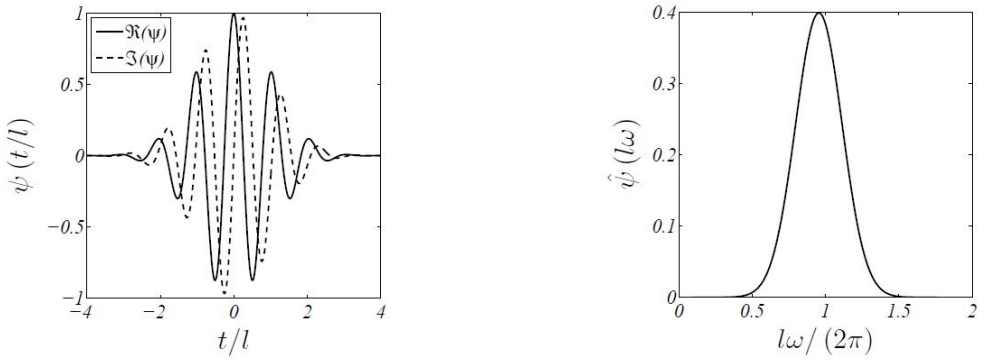

(a) Morlet wavelet in the time domain

(b) Morlet wavelet in the frequency domain

Figure 5.12: Morelet wavelet $\psi \in \mathbb{C}$

The wavelet and its transform are defined as follows, and are shown in Figure 5.12:

$$\psi(t/l) = e^{j\omega_\psi t/l} e^{-|t/l|^2/2} \tag{5.6}$$

$$\hat{\psi}(l\omega) = 2\pi^{-1/2} e^{-(l\omega-\omega_\psi)/2} \tag{5.7}$$

Based on this definition, the continuous wavelet transform of a discrete signal x_n consists in convolving the signal with a scaled and translated version of ψ. Convolving in the time domain equals to pointwise multiplication in the frequency domain, so the wavelet coefficients are obtained as:

$$\tilde{x}(l,t) = \int x(t') \bar{\psi}\left(\frac{t'-t}{l}\right) dt, \tag{5.8}$$

where $\bar{\psi}$ indicates its complex conjugate. By varying the wavelet scale l it is possible to obtain a *picture* illustrating both the amplitude of any feature vs the scale (that is, frequency), and how such amplitude varies in time. In the current work, a range of frequencies comprised between 10 Hz and $f_s/2$ was resolved, employing a base-2 logarithmic set of 89 scales l_j:

$$l_j = l_0 2^{j\delta j}, \qquad j = 0, 1, ..., J, \qquad \text{with } J = \delta j^{-1} \log_2(N\delta t / l_0)$$

Specifically, $\delta j = 0.2$ and $l_0 = 2dt$ were chosen. Similarly to the time-invariant case, the results are checked against energy conservation using. In this case, however, the ratio between the variance of the signal in the time domain and that of the signal in the frequency domain is verified, with the variance in the frequency domain defined as follows:

$$\sigma^2 = \frac{\delta j \delta t}{C_\delta N} \sum_{n=0}^{N-1} \sum_{j=0}^{J} \frac{\left|\tilde{x}(l_j)\left(l_j\right)\right|^2}{l_j} \tag{5.9}$$

with $C_\delta = 0.776$, when using the Morlet wavelet (Torrence and Compo, 1998). Next, the energy density is obtained as:

$$E(l,t) = \frac{|\tilde{x}(l,t)|^2}{l} \tag{5.10}$$

Finally, the wavelet scale is converted to the equivalent Fourier frequency: $E(l,t) \rightarrow E(f,t)$, and, in the specific case of microphone signals, the spectra are presented in dB levels according to Equation 5.5.

6

Results

Based on the processing strategies outlined in chapter 5, this chapter presents the results obtained during the GVT and cold flow campaigns, and aims at answering the research questions introduced in section 1.1. The discussion begins in section 6.1 with a short summary of the GVT findings, consisting in a brief overview of the mechanical properties of both stiff and compliant nozzles. This forms the basis for further discussions that are, then, presented in section 6.2. More specifically, subsection 6.2.1 provides some introductory observations that result from the initial cold flow campaign. Since the methodology used mirrors that of previous investigations by Donald et al. (2012) and Rojo et al. (2016), where the stiff nozzle is concerned, and Tinney et al. (2017), for the compliant nozzle, the main goal of this section is that of assessing possible similarities and discrepancies in the findings. Furthermore, a preliminary attempt is made to compare the acoustic behaviour of stiff and compliant nozzles, by giving a general outline of their dominant vibroacoustic properties. Next, subsection 6.2.2 delves more into the modal behaviour of both structure and acoustics and aims at gaining insights on the effects that aeroelasticity has on noise generation and propagation. Finally, to streamline the treatise, only the most representative findings are presented here; however, as a complement to this chapter, additional results can be found in Appendix A.

6.1. Modal analysis results

Ground vibration tests were conducted on 9 urethane-based nozzles and 1 aluminium nozzle in order to gain insights on their mechanical properties and, in the case of the compliant nozzles, also to infer on the quality and repeatability of the manufacturing process. As detailed in section 4.2, 8 accelerometers were mounted on each structure, therefore, reconstruction of the modal behaviour is possible up to the 4^{th} harmonics. Before presenting the results, it should be noted that due to the accelerometers having each a mass of approximately 5 mg, when mounted on the structure, they make it *stiffer*. Therefore, the results obtained come with a slight overprediction. Even though it was not possible to quantitatively infer on results discrepancy, it is expected that sensitivity of results to the presence of accelerometers is greater for the compliant nozzle cases, given their lighter mass.

Table 6.1: Aluminium and urethane-based nozzle's fundamental and higher harmonics of the bending mode as found from GVT

	Aluminium nozzle		**Compliant nozzle**	
Bending mode	**Resonant frequency [Hz]**	**Damping [%]**	**Resonant frequency [Hz]**	**Damping [%]**
0^{th}	16113.36	1.91	1559.14	3.60
1^{st}	1009.67	3.42	277.15	3.85
2^{nd}	1688.66	0.16	156.38	2.17
3^{rd}	4712.02	0.53	325.87	2.63
4^{th}	7783.33	2.25	538.60	3.13

The findings referred to the aluminium nozzle and the single compliant nozzle that was later used for cold flow testing are summarised in Table 6.1, and have been obtained employing the procedure outlined in section 5.1.

For both cases, Modal Assurance Criterion (MAC) analysis was carried out to determine the degree of similarity of the selected mode shapes, with the MAC value between two modes calculated as the normalized dot product of the complex modal vector at each common node. As illustrated in Figure 6.1, results show that while each mode is identical to itself - hence the single red bar of value 1 along the diagonal - off diagonal values for this mode set are close to zero, thereby proving that each mode is uniquely observed and has a different mode shape.

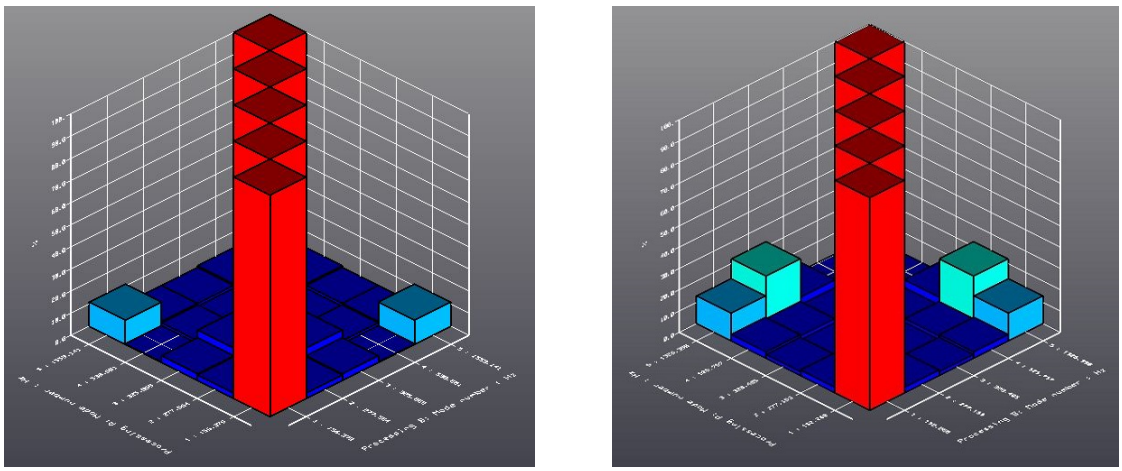

(a) Compliant nozzle's MAC matrix

(b) Compliant nozzle's MAC matrix

Figure 6.1: MAC matrix comparing a set of 5 modes. Red values are 100% MAC values; dark blue is less than 10% MAC value

Predictably, the results of Table 6.1 highlight that, due to a larger wall thickness and a stiffer material, resonant frequencies of the aluminium nozzle are one order of magnitude higher than those of the compliant nozzle. Other than that, a remarkable observation concerns the values of the 1^{st} and 2^{nd} mode frequencies: for the aluminium nozzle, the trend is monotonically increasing from 1^{st} to 4^{th} mode; for the compliant nozzles, on the other hand, the oscillation frequency of the ovalization mode results in a smaller value than that of the pure bending mode. This is not an isolated result: the same tendency was also observed on the remaining compliant nozzles, as shown in Figure 6.2.
In the plot it can be clearly seen that all nozzles have comparable mechanical properties, thereby confirming the quality of the manufacturing method. Standard deviations appear to be greater for breathing and pure bending mode, while they are almost negligible for higher order modes. Manufacturing defects or discrepancies during GVT setup and acquisition are expected to be the main causes of said deviations.

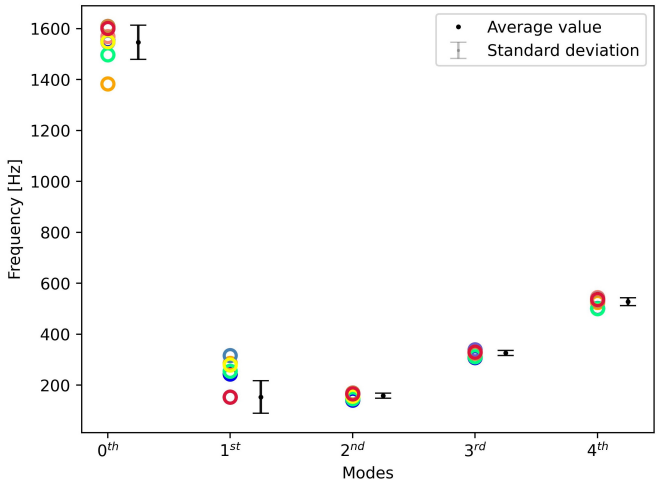

Figure 6.2: Fundamental and higher harmonics of the bending mode as found from the GVT campaign of 9 urethane-based nozzle specimens

6.2. Cold flow test campaign results

Having assessed the mechanical properties of both stiff and compliant nozzle, the results of the cold flow tests are hereby presented and critically discussed. As a first instance, a general outline of the acoustics behaviour of both nozzles is given in subsection 6.2.1, where the main focus is on the evidences gathered when using the microphone line array. In this section, much of the emphasis is placed in comparing the aluminium nozzle acoustic signature with that of previous experimental efforts found in literature, whilst assessing major analogies and differences between the in-print of the stiff and the compliant nozzle of the current setup. Specifically, jet noise mechanisms are investigated, while some hypotheses are discussed as to which phenomena might be responsible for said acoustic behaviour. Next, in subsection 6.2.2, data gathered when using the circular microphone array is studied. In particular, an effort is made to investigate the relationship between the compliant nozzle's structural and acoustics modal behaviour to infer on the influence that aeroelasticity has on jet noise.

6.2.1. Noise generation mechanisms and sound directivity

An overview of the results obtained by analysing the far-field acoustic signature of both stiff and compliant nozzle during transient operations is hereby given. Both startup and shutdown transients are considered and refer to the operating conditions presented in terms of NPR and dNPR/dt, in Figure 6.3, which shows that runs have been carried out to be as repeatable as possible.

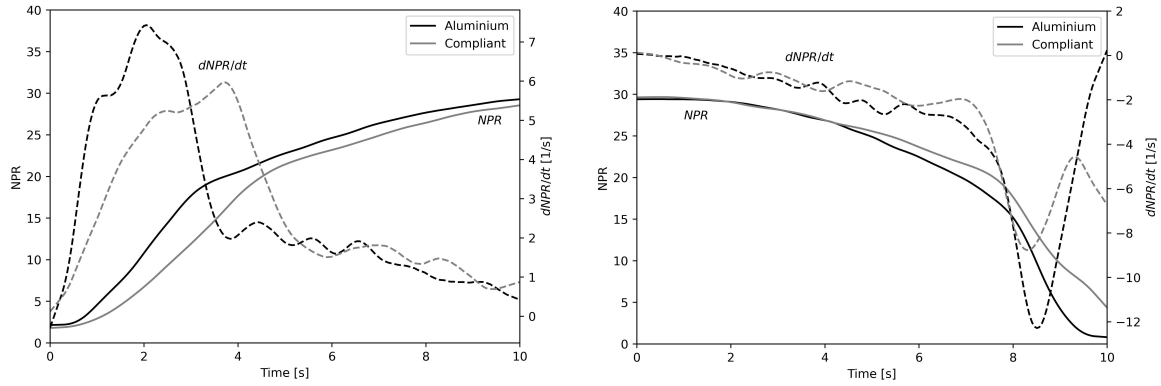

(a) Startup (b) Shutdown

Figure 6.3: NPR and NPR/dt during the transient operations when the microphone line array is employed

Much of the emphasis is placed primarily on the jet noise behaviour during startup, whereas shutdown ramps are marginally discussed to mainly infer on possible hysteresis effects. Furthermore, wavelet analysis has shown that, probably owing to the short distance between each microphone, the spectral content of the acoustic pressure waveforms captured at each station is almost identical. Therefore, it was decided that, to avoid redundancy, from hereon the results are mainly going to refer to data gathered from Microphone 2, unless otherwise indicated. This particular microphone has been chosen because, assuming spherical decay, it was seen that the sound pressure levels of all microphone scale quite accurately to those of Microphone 2. Based on a $1/r$ inverse law, in fact, Microphone 3 and 4 should account for a + 1.4 dB and a + 3 dB gain, respectively, which would bring their signals to approximately the same levels as that captured by Microphone 2.

Stiff nozzle

To begin with, the acoustic signature of the stiff nozzle is discussed and, where possible, parallels are drawn with similar findings present in literature.

As a general outline, it can be seen that, when compared to the sound pressure levels assessed in subsection 4.1.1, and depicted in Figure 6.4 with the dashed black line, the estimates are not too far-off from the actual maximum noise levels recorded during testing. However, the preliminary estimate does not account for flow separation and, therefore, fails to predict not only the exact instants in which OASPL_{max} is recorded, but, especially, the occurrence of sudden acoustic energy drops, between NPR $\approx 11 \div 15$ and NPR ≈ 25. In particular, $\text{OASPL}_{max,2} \approx 133$ dB is registered at NPR = 11.3; then, acoustic energy drops by 5 dB until NPR = 15,

and rises again by 2 dB until NPR = 25. Finally, at transition, it drops again by 3 dB. A detailed explanation as to why this occurs is given later. However, as a preliminary assessment, it can already be said that comparable noise levels are also reported in previous research. In a former study by Donald et al. (2012), a similar microphone arrangement was used; however, the overall setup was different from the one of the current study in that the nozzle is larger in size ($r^* = 19.04$, $\epsilon = 38$), and the microphones are placed further away from the jet axis, at approximately 2.20 m, as opposed to 1.23 m of the current setup. Nevertheless, sound pressure levels are comparable and are attested between 125 and 133 dB, in a similar fashion to what is presented in Figure 6.4.

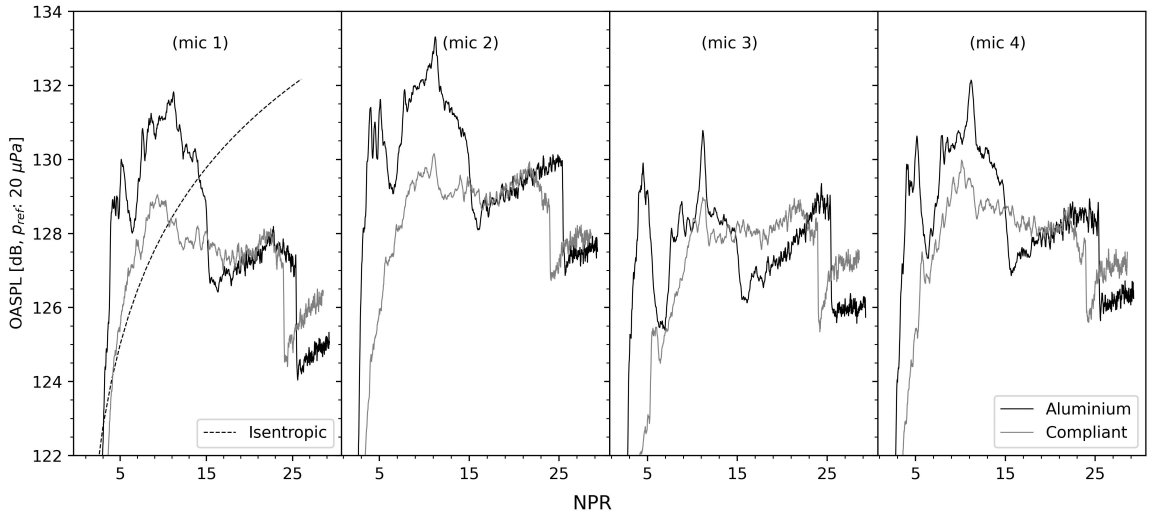

Figure 6.4: OASPL [dB, ref: 20μPa] of aluminium and compliant nozzle during transient operations. Dashed line indicates the preliminary results presented in Figure 4.3

Similarly, Canchero et al. (2016a) have used an almost exact replica of the nozzle employed in the current study, in twin configuration, while a single microphone mounted flush with the surface of the base plate located behind the nozzle cluster was used. In this case, even though the recorded noise levels are slightly higher owing to, not only the closer distance between microphone and jet plume, but also the fact that two nozzles are tested, periods of acoustic energy drop are also reported at almost matching NPRs.

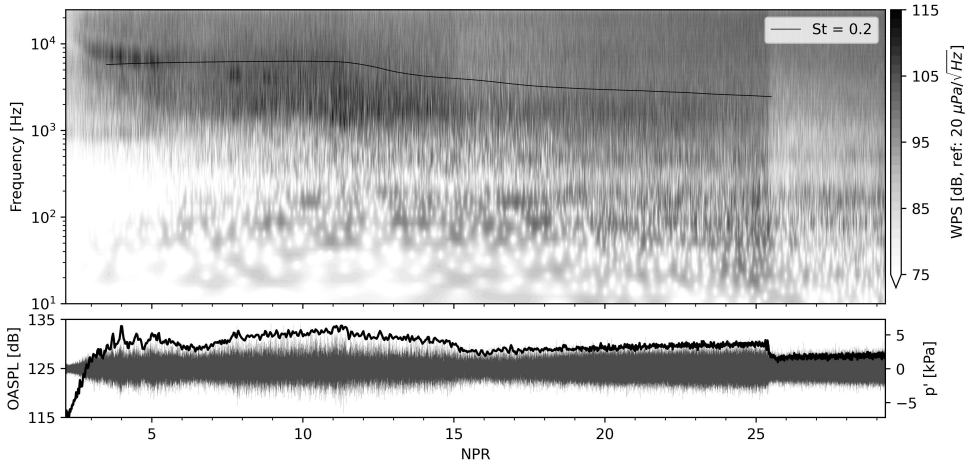

Figure 6.5: **Stiff nozzle startup** - Morlet wavelet power spectra of the acoustic pressure measured from **mic n° 2** and expressed as $10\log_{10}(E(f,t)/ref^2)$ [dB, ref: 20$\mu Pa/\sqrt{Hz}$]. Raw pressure signal (grey) is displayed at the bottom [kPa] with a moving window-averaged OASPL (black) [dB, ref: 20μPa]

A similar outlook can be observed from Figure 6.5, which presents the results of the joint time-frequency space decomposition of the non-stationary acoustic pressure waveforms detected by microphone 2. The

Wavelet Power Spectrum (WPS) topography of the stiff nozzle, in fact, displays a few discernible features that can be clearly linked to the unsteady flow behaviour.
At a first glance, in fact, flow transition is clearly visible at NPR = 25.7, and features a sudden drop of acoustic energy at all frequencies. A companion study by De Kievit (2021) on the same test article has reported flow transition at NPR = 24.7 from wall pressure measurements. This discrepancy could be due to a number of reasons, but only two main opposing views are to be discussed here. On one hand, as also noted by De Kievit (2021), the flow experiences a partial transition in the top part of the nozzle around NPR = 24.5. However the flow stays attached for a very short amount of time, before separating again. It could, therefore, be determined that said flapping motion, which is also at the core of side load generation, has induced an erroneous reading by the pressure sensors, which have, somehow, brought transition forward, whereas the correct reading would be that of the microphones. On the other hand, however, it could be argued that, indeed, flow transition occurs at NPR = 24.7. Nevertheless, due to the finite amount of time required by the plume to adjust to the new flow, a slight delay occurs as far as acoustic detection is concerned.

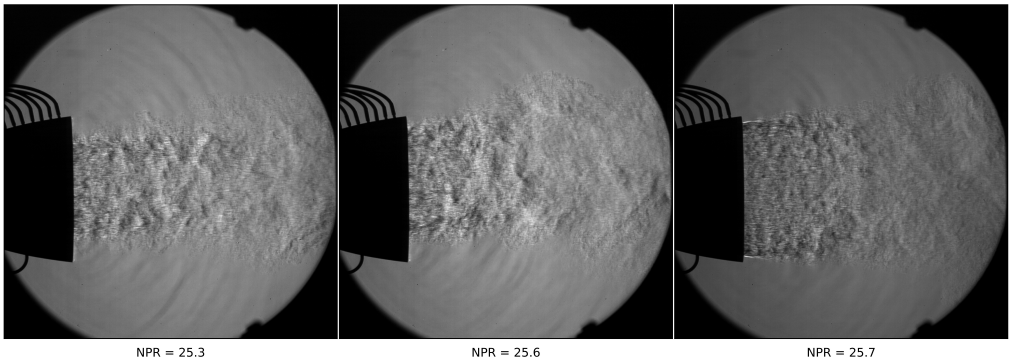

Figure 6.6: Aluminium nozzle: Schlieren images depicting FSS → RSS transition occurring

As far as noise mechanisms are concerned, the spectral trends feature a high frequency band centred around 6.6 kHz, and extending between f = 5.5 kHz and f = 9 kHz. This fringe is comprised between NPR = 3 and NPR = 5.5 and has a slight decreasing trend as the NPR increases. This behaviour, owing, most likely, to a broadening of the shock spacing, supports the hypothesis that these tones are associated with BBSN, as also documented by Donald et al. (2012) and Canchero et al. (2016a).

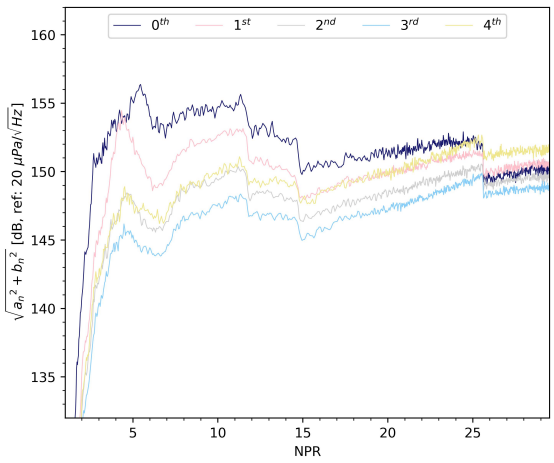

Figure 6.7: **Aluminium nozzle** - Azimuthal mode activity of the acoustic sound pressure during transient operations, expressed as a moving window-averaged OASPL [dB, ref: $20\mu Pa$]

Given the highly non-ideal flow behaviour at these pressures, typical predictive models for BBSN (Tam and Tanna, 1982, Kandula, 2011) are unsuccessful in providing further evidences, since their prediction range is for values of the shock parameter $\beta < 2$. In this case, the combined effect of measuring higher values of β

before the Mach disk, together with the fact that a large portion of subsonic flow forms downstream of it, does not allow for a linear scaling of the predictive models. Nevertheless, although it was not possible to ascertain the peculiar Doppler effect that is often associated with BBSN as no distinct peak frequency shift was measurable at different stations, further proof of the presence of BBSN tones is revealed through acoustic signal Fourier decomposition in azimuth. For this, data gathered when employing the circular microphone array is analysed based on the theoretical framework outlined in section 5.3. The results, presented in Figure 6.7, show a SPSL evolution similar to the one reported in Figure 6.4 in terms of acoustic activity peaks and drops. However, what is especially revealed is that the dominant acoustic mode is represented by the 0^{th} mode, with the higher order modes being progressively a few dB weaker. Interestingly, however, for the stiff nozzle, at low NPRs the asymmetric mode seems to have a more dominant contribution. Similar findings on a shock-containing jet (Wong et al., 2020) suggest the presence of BBSN, thereby confirming the aforementioned hypothesis.

As far as the low frequency bands around 100 Hz are concerned, this acoustic signature is the result of turbulent mixing noise in the form of Mach waves that radiate from the turbulent structures that develop in the jet shear layer and gradually grow into larger eddies. This observation is compatible with the fact that turbulent mixing energy dominates at shallower angle observers due to its downstream propagation (Microphone 4, as shown in Appendix A), whereas tones are less dominant at steeper angles (Microphone 1).

A higher acoustic impedance is clearly discernible in the highest frequency bands after NPR = 11, which progressively becomes more significant, as also detected by the 5 dB drop in Figure 6.4. Acoustic impedance is a property of the medium rather than the acoustic wave itself and is broadly defined by a real term, *resistance*, and an imaginary term, *reactance*:

$$Z(\omega) = r(\omega) + i\,x(\omega)$$

Reactance, in turn, has a positive and negative component:

$$x(\omega) = x_L(\omega) - x_C(\omega)$$

In particular, the *inertive* reactance $x_L(\omega)$ is associated with the density of the medium and scales with frequency: $x_L(\omega) \propto \omega$. This means that denser media are more likely to impede higher frequency waves. This observation matches with the fact a progressive opening of the subsonic core which forms downstream of the Mach disk occurs. At the lower NPRs, in fact, the subsonic region only extends for a short distance before being enclosed, again, around a region of supersonic flow, resulting in a supersonic *circular* jet, as shown in Figure 6.8a. However, as the NPR is increased, the portion of subsonic and denser flow that forms, extends further downstream since it resides for less time inside the nozzle, where it can mix. In this way, the flow advances to an *annular* supersonic jet which is surrounded by an open-ended subsonic core, which explains the gradual acoustic energy reduction at the higher frequencies.

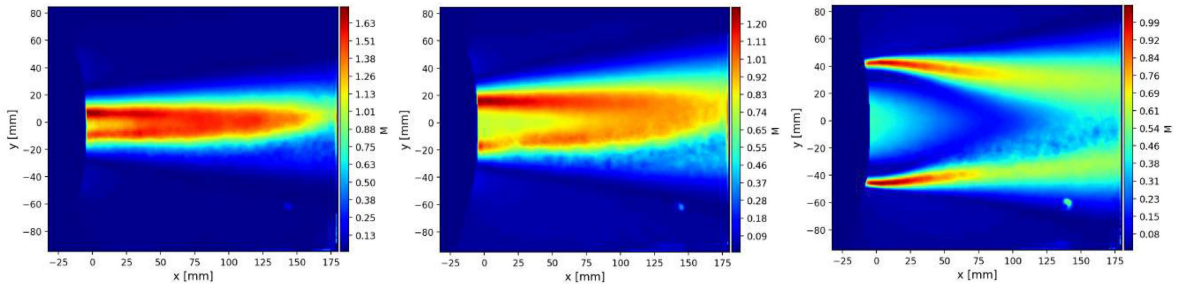

(a) NPR = 10.52 (b) NPR = 16.42 (c) NPR = 24.48

Figure 6.8: Aluminium nozzle: Mach number contours at different NPRs from PIV data (De Kievit, 2021)

Between NPR = 15 and transition, on the other hand, even though the flow still progresses into an annular jet, a 3 dB increase is registered. This is likely caused by the vertical flapping motion of the flow due to the shock foot instability closer to the transition instant, which enhances turbulent mixing. From Figure 6.5, in fact, acoustic energy in the highest frequencies is unvaried, whereas acoustic energy can be seen increasing

at the bottom of the spectrum.

Finally, as far the OASPL peak at NPR = 11.3 is concerned, a time-averaged Fourier spectrum is computed between NPR = 11 and NPR = 12, to verify whether, similarly to the results of Canchero et al. (2016b), the narrowband tone could be associated with transonic resonance, and is presented in Figure 6.9.

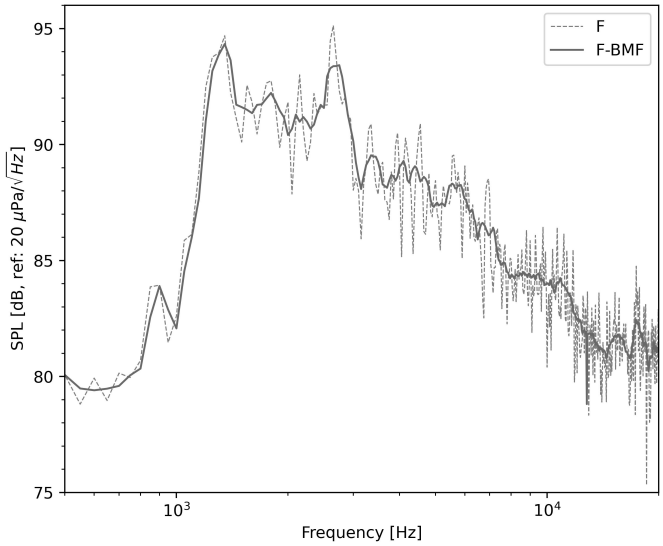

Figure 6.9: Raw and filtered 1-sided PSD of the averaged acoustic pressure between NPR 11 and 12, expressed in [dB]

Assuming flow separation according to the criterion of Schmucker (1984b), at NPR = 11, the distance between the shock foot and the nozzle lip is $\lambda_{tr}/r^* \approx 12.6$. Assuming $a_\infty = 340$ m/s, this corresponds to a resonant tone (m = 3) of:

$$f_{tr} = \frac{m a_\infty}{4\lambda_{tr}} \approx 2.5 \text{ kHz}$$

which agrees well with the peak in Figure 6.9. As a confirmation that this tone could be linked to TR, the same peak is also clearly noticeable from the acoustic signature of the other microphones, in the same frequency band, since the jet's convective speeds have no influence on TR. The second peak at $f = 1.3$ kHz, instead, is probably due to reflections owing to the non-anechoic environment of the testing facility. Computing the difference between the two peaks, in fact, yields a wavelength of approximately 25 cm, which corresponds to the distance between the microphones and some equipment that was left behind them and was not covered with sound suppressing panels.

It can be, therefore, concluded that due to the complexity of the flow development, the many phenomena that are involved in sound production and propagation are not easily predictable. This is also proven by the great mismatch between the acoustic spectrum and the constant Strouhal number curve plotted on Figure 6.5. There is, in fact, no indication that the signature scales to a constant Strouhal number, as is the case with most subsonic and perfectly expanded supersonic flows.

As for the shutdown ramp, the recorded noise levels are comparable to those of a startup ramp, in a OASPL range comprised between 125 dB and 132 dB. However, the interval of time characterised by a quieter activity, that is associated with RSS flow, is longer, due to a significant hysteresis effect. Observing Figure 6.10, in fact, the flow can be seen to retransition at around NPR = 15.5. This phenomenon, as introduced in subsection 2.4.1, occurs due to the fact that when the flow is in RSS state, the separation shock is shorter due to the separation point being moved further downstream. In this way, the conical shock is able to impart more momentum towards the wall, keeping the flow attached for a longer interval (Frey and Hagemann, 1999). As far as the current results are concerned, since no detailed accounts of re-transition from previous studies (De Kievit, 2021, Pearse, 2022) on the same test article are available, it is not possible, as opposed to the startup case, to

infer on the likelihood that retransition occurs at the exact NPR registered by the microphones. Nevertheless, during RSS, turbulent mixing noise is the dominant noise mechanism at the lower frequencies, similarly to the startup case, with a band centred around 100 Hz. On the contrary, as the flow retransitions to FSS state, a higher acoustic activity is registered at higher frequencies bands comprised between 1 and 10 kHz.

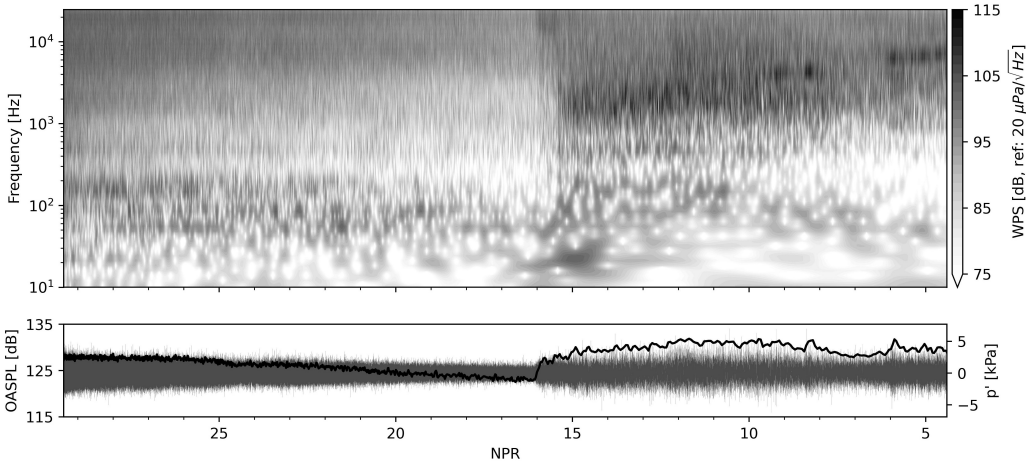

Figure 6.10: **Stiff nozzle shutdown** - Morlet wavelet power spectra of the acoustic pressure measured from **mic n° 2** and expressed as $10\log_{10}(E(f,t)/ref^2)$ [dB, ref: $20\mu Pa/\sqrt{Hz}$]. Raw pressure signal (grey) is displayed at the bottom [kPa] with a moving window-averaged OASPL (black) [dB, ref: $20\mu Pa$]

Noise mechanisms almost identically mirror those of the startup phases, with BBSN occurring at the lower NPRs between NPR = 7 and NPR = 4.5. This time, the most energetic fringe is monotonically increasing in frequency as the NPR is decreased. Nevertheless, at all microphone stations, it seems that the onset of a higher acoustic impedance is less apparent.

Compliant nozzle

As far as the compliant nozzle is concerned, some significant differences can be outlined when comparing the acoustic signature with that of its stiff counterpart.

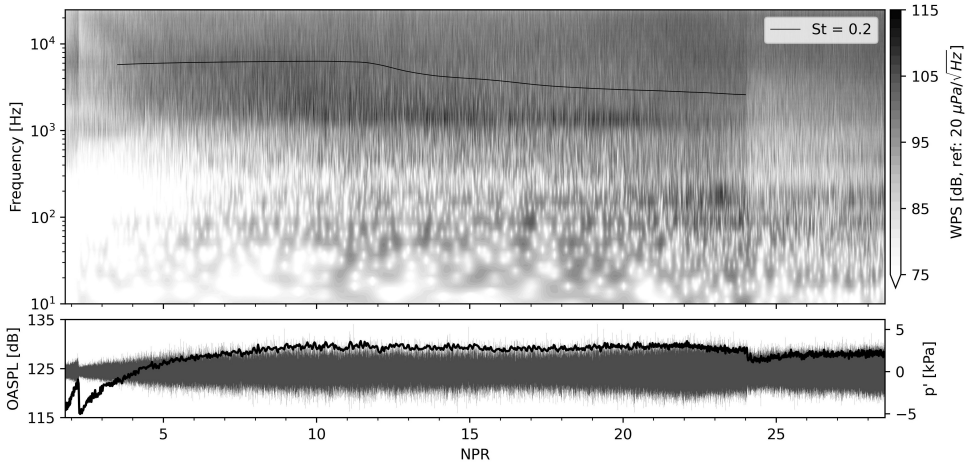

Figure 6.11: **Compliant nozzle startup** - Morlet wavelet power spectra of the acoustic pressure measured from **mic n° 2** and expressed as $10\log_{10}(E(f,t)/ref^2)$ [dB, ref: $20\mu Pa/\sqrt{Hz}$]. Raw pressure signal (grey) is displayed at the bottom [kPa] with a moving window-averaged OASPL (black) [dB, ref: $20\mu Pa$]

As previously hinted in Figure 6.4, sound pressure levels differ quite substantially, with the stiff nozzle over-predicting the OASPL_{max} by 3.5 dB in its period of maximum noise propagation around NPR = 11. Apart from a sudden drop at transition, sound pressure levels remain quite steady throughout the whole FSS interval, at approximately the same levels that the stiff nozzle has between NPR = 15 and NPR = 23, in which the main

noise component has been attested to be turbulent mixing. This should already give an indication that, for the compliant nozzle, acoustic energy is attenuated at the higher frequencies. The claim is, in fact, confirmed by the WPS presented in Figure 6.11. In the spectrum, in fact, there seems to be no evidence of BBSN at high frequencies. This feature has also been reported by Rojo et al. (2016) when analysing the WPS of full-scale engines. Further proof is provided by acoustic signal's Fourier decomposition in azimuth. Contrary to the stiff nozzle case, at all NPRs, in fact, Figure 6.12 does not present a dominant contribution of the asymmetric mode, that is typical of shock containing jets. Stark et al. (2019), having observed similar results, attributes the suppression of distinct tones to the free flow separation.

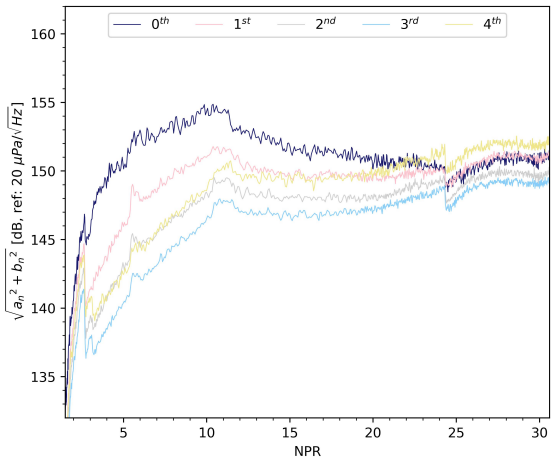

Figure 6.12: **Compliant nozzle** - Azimuthal mode activity of the acoustic sound pressure during transient operations, expressed as a moving window-averaged OASPL [dB, ref: 20μPa]

Furthermore, lack of a sudden increase in acoustic impedance, as already reported by looking at Figure 6.4, can also be seen in a rather constant energy content at all frequencies and throughout the whole ramp, apart from a more energetic narrowband at $f \approx 1.4$ kHz that extends between NPR = 9 and NPR = 22. This frequency band is, most likely, the result of the non-anechoic environment, which causes sound reflections. As already predicted in subsection 4.3.2, the higher frequencies are, in fact, more prone to be reflected when there is a bigger mismatch between the impedance of two mediums. Finally, another band centred around $f \approx 190$ Hz at NPR = 23.2 is going to be investigated further in subsection 6.2.2, to better assess whether it is the result of aeroelastic effects. Similarly to the stiff nozzle case, then, transition is recognisable by a sudden drop of acoustic energy at all frequencies at approximately NPR = 24.4. Again, because no pressure sensor was mounted on the structure, it is not possible to assess from pressure readings whether transition would be registered at the same NPR as the one logged by the microphones. Nevertheless, this already shows how transition occurs earlier in a compliant nozzle, as opposed to the rigid case, in a similar way to what was also experimentally observed by Tinney et al. (2017) on a TOP nozzle of the same contour.

To understand the underlying source of such behaviour, the foundational work of Génin et al. (2015) should be looked into. As already introduced in subsection 2.5.3, in fact, an inward bent nozzle wall subjected to a separated flow state, experiences a higher wall pressure, which tends to shift the separation point further downstream, thereby amplifying the bending force due to an increased lever arm, and reinforcing the effect of outward bending. Consequently, an outward bended nozzle wall subjected to a separated flow state, experiences a lower wall pressure, which tends to shift the separation point upstream, thereby amplifying the upward bending force which produces, again, an inward bent wall. In a 2D flexible geometry, the two effects coexist and produce an ovalised nozzle contour, that periodically switches its major and minor axes. In terms of the flow structure, Génin et al. (2015) have also noted how this mechanism produces a so-called *Mach saddle*, namely a Mach disk that is inward bent with respect to its major axis, and outward bent with respect to its minor axis. As for the wall pressure profile, Wang et al. (2014) have shown how the instability magnitude of the shock foot in the stiff and compliant case cannot be linearly compared. Its mean position, in fact, differs for the two cases: even though, when considering an outward bent wall the shock foot moves upstream, its position is still shifted forward with respect to the rigid nozzle case, thereby explaining the earlier transition to RSS state.

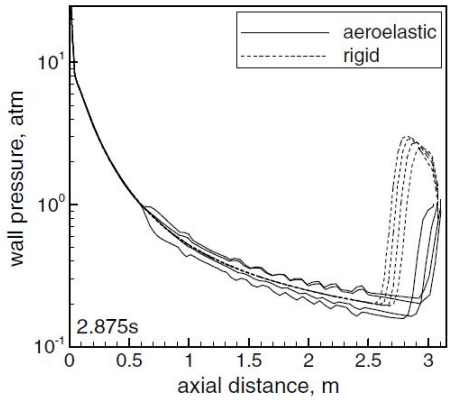

Figure 6.13: Comparison between wall pressure profiles at 4 monitor azimuthal sections as taken from the coupled FSI model of Wang et al. (2014)

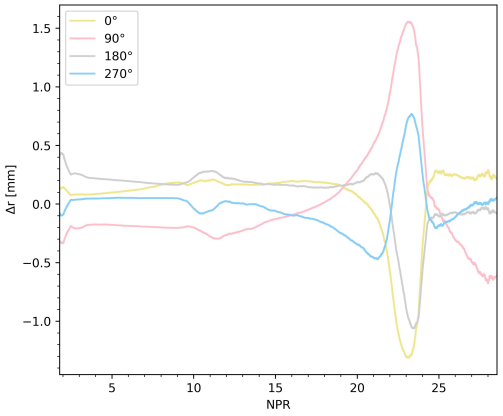

Figure 6.14: Physical displacement history during startup of 4 fiducial markers

Such erratic instability of the separation shock foot is also confirmed by a preliminary analysis of the markers movement, as shown in Figure 6.14, which already suggests that a peak in lip displacement occurs between NPR = 21.9 and NPR = 23.7. This behaviour, as previously studied by Baars et al. (2012), who has reported increased loading activity before transition, could signify an incipient shift from a FSS to an RSS flow. By studying the displacement history of 4 fiducial markers located at 0, 90, 180 and 270 degrees circumferentially the mean shape of the nozzle can be easily deduced. In a *mean* sense, the markers located on the right and left experience an inward bending, whereas the other two an outward bending. In other words the nozzle can be thought of as an ellipse with a vertical major axis. An in-depth analysis of this behaviour shall be further discussed in subsection 6.2.2.
Additional evidences of said vertical ovalisation are also provided by the Schlieren images in Figure 6.15 that show how the flow is heavily asymmetric and attached to the bottom of the nozzle before flowing full. This, apart from producing evident side loads, also causes an outward vertical stretching that is balanced out, on the other two sides, by an inward shrinking of the walls.
Finally, an extensive study on this aspect is further investigated in subsection 6.2.2.

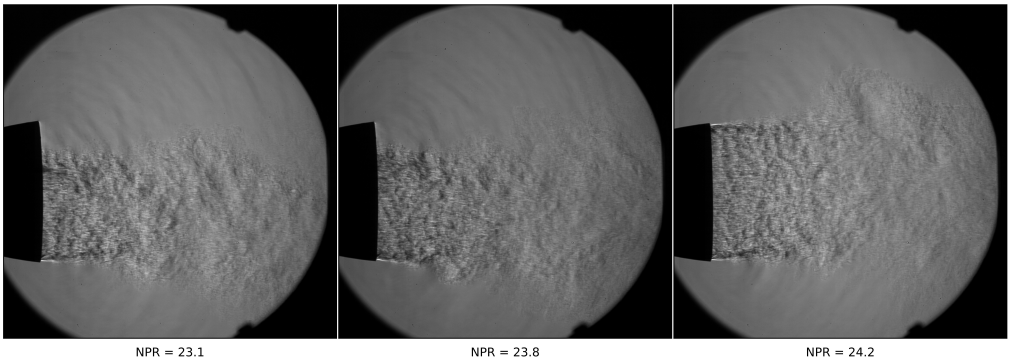

Figure 6.15: Compliant nozzle: Schlieren images depicting FSS → RSS transition occurring

On a final note, a short discussion on the compliant nozzle's shutdown behaviour is hereby given. A strong hysteresis effect can be noticed. Retransition to FSS occurs at approximately NPR = 14.4, so *later* compared to the rigid nozzle case. This is, again, in agreement with the assumption of a forward separation point for the same NPR: being the separation shock shorter, and the conical shock more energetic, the flow can stay attached for longer. Other than that, a similar acoustic in-print can be observed from the WPS, which features turbulent mixing noise at the lower frequency, and higher frequency bands while in FSS state.

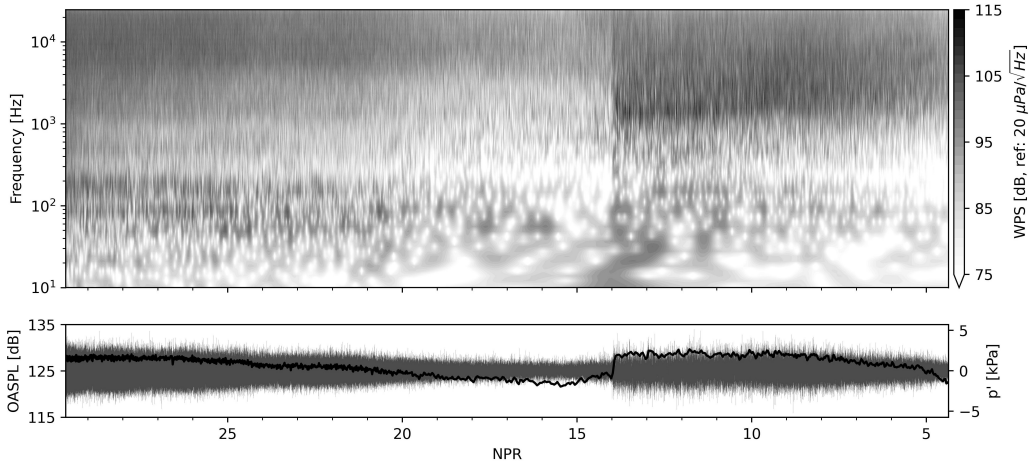

Figure 6.16: **Compliant nozzle shutdown** - Morlet wavelet power spectra of the acoustic pressure measured from **mic n° 2** and expressed as $10\log_{10}(E(f,t)/ref^2)$ [dB, ref: $20\mu Pa/\sqrt{Hz}$]. Raw pressure signal (grey) is displayed at the bottom [kPa] with a moving window-averaged OASPL (black) [dB, ref: $20\mu Pa$]

6.2.2. Aeroelasticity effects on vibroacoustic loading

Having assessed the main acoustic features of rigid and compliant nozzles in terms of sound directivity and jet noise mechanisms, the attention is now turned to a more in-depth investigation of the relationship between noise generation and structure's aeroelasticity. In particular, an attempt is made to understand in what ways structural vibrations are responsible for a different acoustic signature. The following discussion is based on the analysis of the data gathered while using the circular microphone array, which allows, in a similar way to the fiducial markers study, for a spatial Fourier decomposition in azimuth up to the 4^{th} mode. In this occasion, both transient and steady state runs are going to be discussed, with the latter serving as a detailed study of specific NPRs at which features of interest have been observed.

Energy content in lip motion and acoustics

In a similar fashion to the previous section, two distinct transient runs based on the operating conditions depicted in Figure 6.17 are briefly discussed.

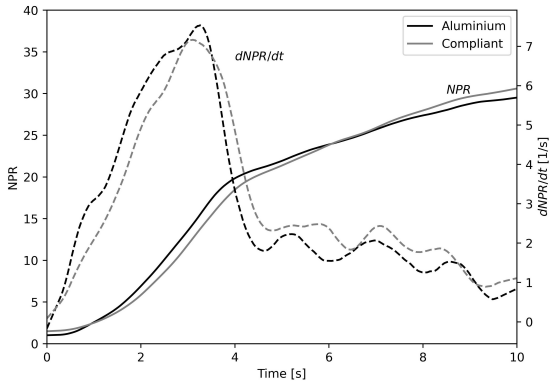

Figure 6.17: NPR and NPR/dt during startup operations when the azimuthal microphone array is employed

Having now 8 microphones mounted azimuthally around the nozzle at an axial distance from the lip of approximately 32 cm and a radial distance from the jet plume axis of 23.5 cm, which roughly corresponds to a fixed polar angle $\phi \approx 36°$, sound pressure levels have resulted to be slightly higher that what previously recorded with the line array, given the closer distance to the jet.

However, as observed in Figure 6.18, features that are similar to those of Figure 6.4 are found. Acoustic levels are, on average, more elevated during testing of the stiff nozzle compared to the compliant one, while in both cases acoustic energy peaks and drops are revealed at similar NPRs as those of the previously discussed cases, thereby confirming repeatability of the runs and robustness of the test setup.

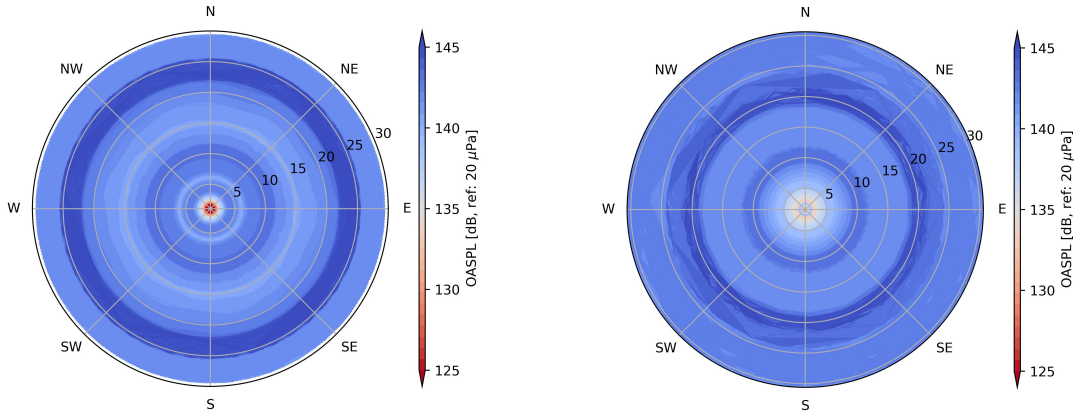

(a) Aluminium nozzle

(b) Compliant nozzle

Figure 6.18: Moving window-averaged OASPL [dB, ref: $20\mu Pa$] at each azimuthal microphone station during transient startup. Radial axis represents the NPR evolution

This is also confirmed by the WPS of the acoustic pressure waveforms detected at the NORTH microphone, and shown below in Figure 6.19. The spectrum reveals a similar pattern to the one previously shown in Figure 6.5 and 6.11, and, as for the stiff nozzle, the instants that precede transition are characterised by a broadband signature up to, approximately, 300 Hz, lending support to the hypothesis that this behaviour is purely the result of increased turbulent mixing noise. On the other hand, as far as the compliant nozzle is concerned, the spectrum appears to be more uniform, whereas the presence of a more energetic narrowband around 180 Hz at NPR ≈ 22.3 is confirmed.

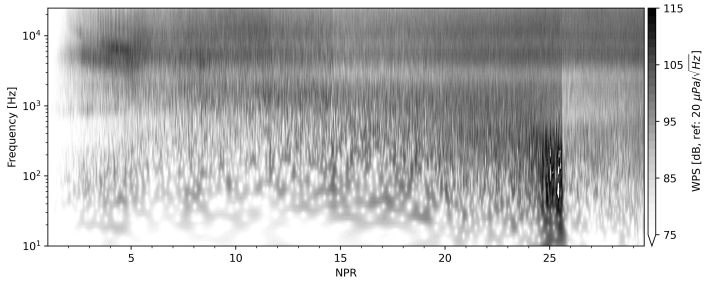

(a) Aluminium nozzle

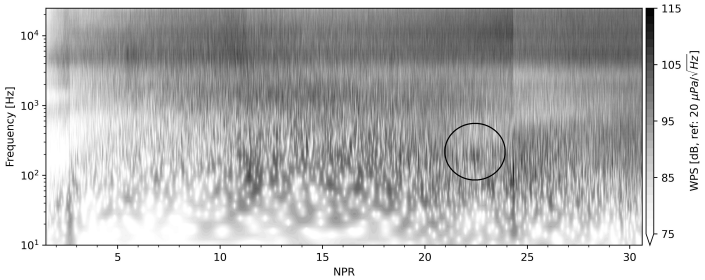

(b) Compliant nozzle

Figure 6.19: Morlet wavelet power spectra of the acoustic pressure expressed as $10\log_{10}(E(f,t)/ref^2)$ [dB, ref: $20\mu Pa/\sqrt{Hz}$] and recorded at Microphone NORTH

In order to assess whether this could be the direct result of aeroelasticity effects, a study of the nozzle lip activity is carried out in order to get a better insight into the structure's dynamics. Even though, as shown in Figure 6.20, markers also move azimuthally and not just radially, the analysis presented in Figure 6.21 only refers to radial displacements. From the modal decomposition carried out, based on the methodology presented in section 5.3, the activity of the fundamental and higher order harmonics can be analysed. Even though recovery up to the 12^{th} mode is possible, only modes up to the 4^{th} are discussed, given the progressive energy weakening of higher order modes. The predominance of ovalisation that was hypothesized earlier

is clearly confirmed by an increased activity of the m = 2 mode around NPR = 22.3. This result is in line with the findings of the GVT campaign, which revealed the ovalisation mode to be oscillating at the fundamental, namely the lowest, natural frequency. Also the harmonics intensify their activity around that NPR, but at an order of magnitude lower than ovalisation. Furthermore, it can be seen that the pure bending mode experiences its maximum activity slightly earlier, which suggests either the inception of an heightened shock foot instability that causes greater off-load axis, or an asymmetric separation.

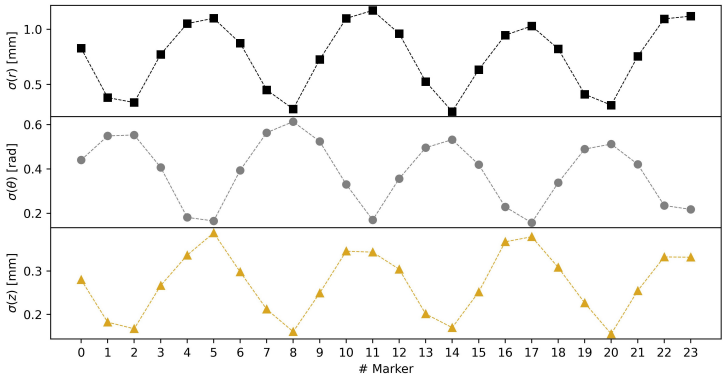

Figure 6.20: Standard deviation of markers displacement in r, θ, z for steady run at NPR = 22.3

In light of these observations, a steady case run was carried out at NPR = 22.3 to perform a detailed study of flow, acoustic and structural conditions, in order to develop a better understanding of the vibrational activity of the compliant nozzle when subjected to the unsteady loads of a transient startup run. A second run employing the stiff nozzle was also carried out at NPR= 24.5. Even though these pressure ratios differ, they still provide comparable operating conditions given the delayed flow transition to RSS for the rigid nozzle case.

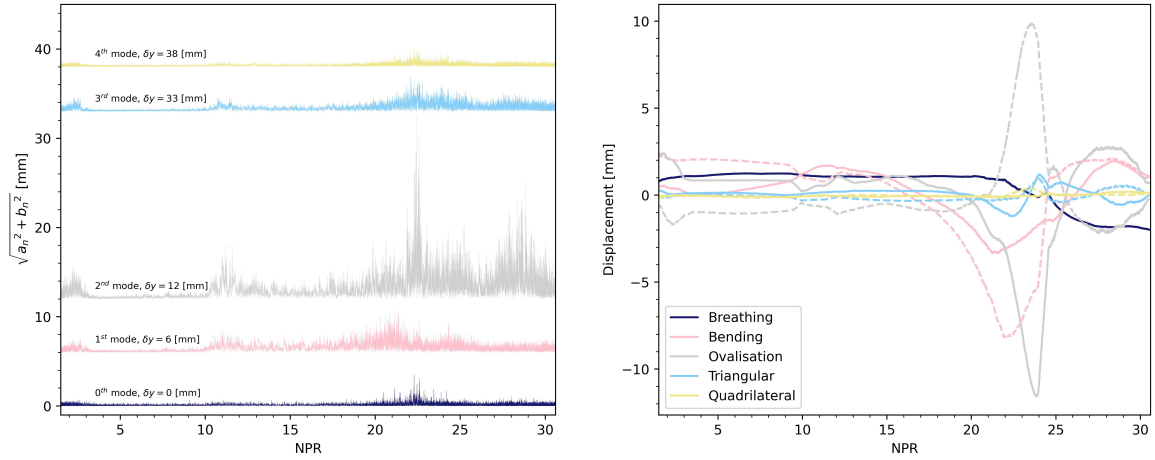

(a) Azimuthal mode activity of the fiducial markers fluctuation

(b) Generalized modal displacement. Solid lines indicate positive mode coefficients a_n. Dashed lines the negative ones b_n

Figure 6.21: Compliant nozzle dynamics loads during transient startup

Based on the aforementioned operating conditions, Figure 6.23 presents the acoustic power spectra computed at each microphone station for both nozzles. The flow asymmetry that was already hinted at from the instantaneous schlieren images in Figure 6.6 and 6.15, is also confirmed by the different energy levels detected at each microphone station. In particular, due to the flow being mostly tilted downwards, the microphones located at the bottom of the array detect greater acoustic levels as opposed to those placed in the upper part of the array, as depicted in Figure 6.22. This effect is particularly exacerbated during operation of the compliant nozzle, in which the flow asymmetry is larger compared to its stiff counterpart. This also explains why, on average, in these bottom microphone stations the overall acoustic energy emitted by the

compliant nozzle results to be greater than that of the rigid nozzle, as opposed to the observation of Figure 6.4, which had proven how stiff nozzle operations results to be *louder*. To a lesser extent, the greater noise levels registered in the bottom half of the array could be also due to the acoustic reflections from the ground or to a slight non-concentricity of the array with respect to the jet plume axis; however, these effects would be equally detected during operations of both nozzles.

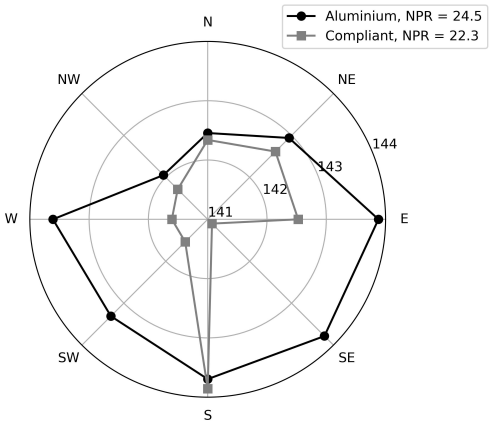

Figure 6.22: Comparison between OASPLs [dB, ref: $20\mu Pa$] detected at each microphone station

Even though most of the variance of the signal is contained at the higher frequencies, a noticeable peculiarity of the acoustic spectra presented in Figure 6.23a is an energetic peak centred around $f = 180$ Hz that is, on the contrary, not present in the spectra of the stiff nozzle, confirming the observation made when discussing the transient results in Figure 6.11 and 6.19b.

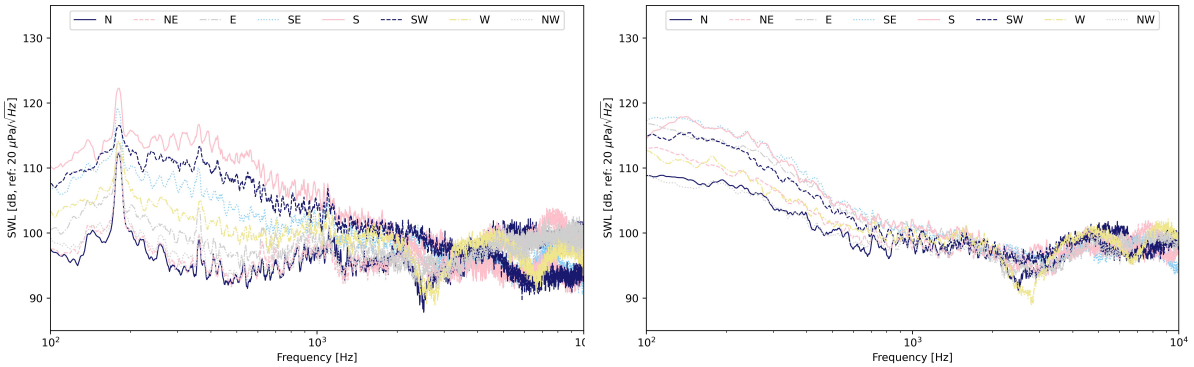

(a) Compliant nozzle - NPR = 22.3

(b) Aluminium nozzle, NPR = 24.5

Figure 6.23: 1-sided PSD of the acoustic pressure waveforms detected at each azimuthal microphone location during steady state operations. Expressed in dB, [dB, ref: $20\mu Pa$]

Such behaviour is also clearly highlighted in Figure 6.24, which, not only compares the acoustic performance of stiff and compliant nozzle, but also reports the energy spectra during operations of the compliant nozzle at lower fixed NPRs (11.3 and 18.9, repsectively). From the graph, it can be seen how the energetic peak around $f = 180$ Hz only becomes relevant before RSS transition in the compliant nozzle, and is not present in the spectra at the lower NPRs. The absence of the peak during operations of the stiff nozzle, or at lower NPR conditions of the compliant nozzle clearly suggest a link with structural vibrations.

An almost identical outlook is also given by the spectral analysis of the acoustic mode coefficients, which also presents a similar peak around $f = 180$ Hz. From Figure 6.25, it can be seen that, for both nozzles, the breathing mode is dominant. Nevertheless, apart from excluding the presence of possible shock tones, it is not possible to draw any other conclusion as to which is the source of such energetic peak. In conclusion,

presence of aeroelastic effects does not result in a greater predominance of higher order acoustic modes and, therefore, this analysis tool alone is insufficient in detecting the presence of tones linked to fluid-structure interactions.

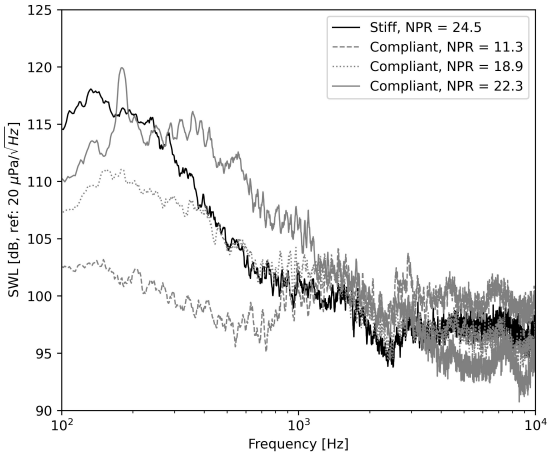

Figure 6.24: Comparison between stiff and compliant nozzle's 1-sided PSD of the acoustic pressure waveforms detected from the SOUTH microphone, during steady state operations. Expressed in dB, [dB, ref: $20\mu Pa$]

For this reason, a coupled investigation of acoustic and structural characteristics is warranted. Considering the observation previously made by looking at Figure 6.21a, the attention is now turned to a more thorough analysis of the nozzle lip fluctuation during fixed operations at NPR = 22.3. From the spectral analysis of each of the markers raw fluctuation, presented in Figure 6.26, it can be seen how each of them oscillates predominantly in a fixed frequency range comprised between 175 Hz and 185 Hz, thereby hinting again to the presence of an aeroelastic tone.

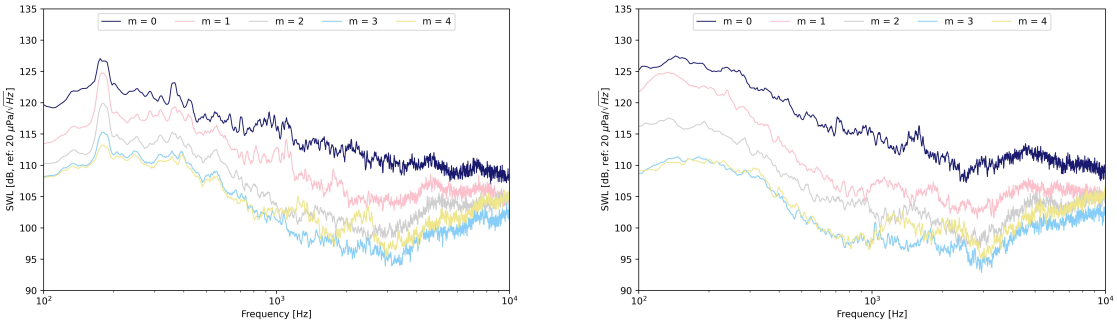

(a) Compliant nozzle - NPR = 22.3

(b) Aluminium nozzle, NPR = 24.5

Figure 6.25: 1-sided PSD of the acoustic pressure modal activity during steady state operations. Expressed in dB, [dB, ref: $20\mu Pa$]

For a more in-depth analysis, modal decomposition is, again, carried out and presented in Figure 6.27. Predictably, ovalisation is the dominant oscillation mode, with a modal activity of an order of magnitude greater than that of the higher order harmonics. Next, from the spectral analysis of each mode, a series of highly energetic narrowbands are visible. The fact that these develop quite close to the natural frequencies of the static nozzle, as found in Table 6.1, lends support to a possible link with the natural oscillation modes of the nozzle. As theory (Östlund et al., 2004, Pekkari, 1993) suggests, in fact, the presence of an aerodynamic torque can have an effect on the natural frequency of a coupled system. More specifically, it is possible to observe that for n = 1, 2, 3 and 4, $\Omega_n > \omega_n$ meaning that the coupled system results to be stiffer; more specifically, the pure bending mode oscillates at 360 Hz, whereas the triangular mode has a stronger activity around 475 Hz. As for the quadrilateral mode, it presents a weak energetic peak around 900 Hz. Finally, given the test setup acquisition frequency of 2 kHz, it was not possible to retrieve further information on the oscillation behaviour of the breathing mode above 1000 Hz. Even though each mode resonates at a stiffer eigenfrequency, they are also fully coupled with the fundamental frequency of ovalisation at 180 Hz.

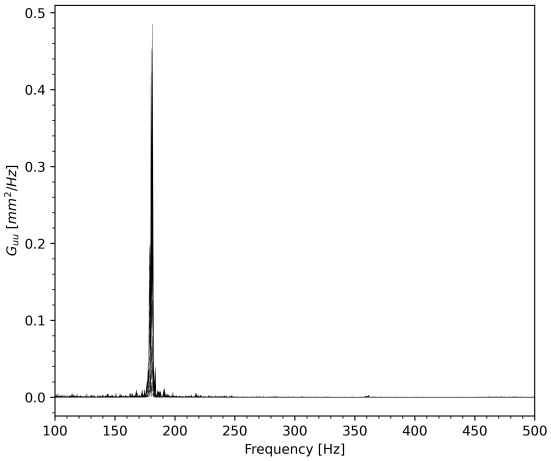

Figure 6.26: 1-sided PSD of the 24 markers' fluctuation at NPR = 22.3

These findings confirm the preliminary observations of Pearse (2022), and go further into revealing how also the higher order harmonics osciallate at their own stiffer eigenfrequency, but are also coupled with the fundamental tone of the ovalisation mode at 180 Hz.

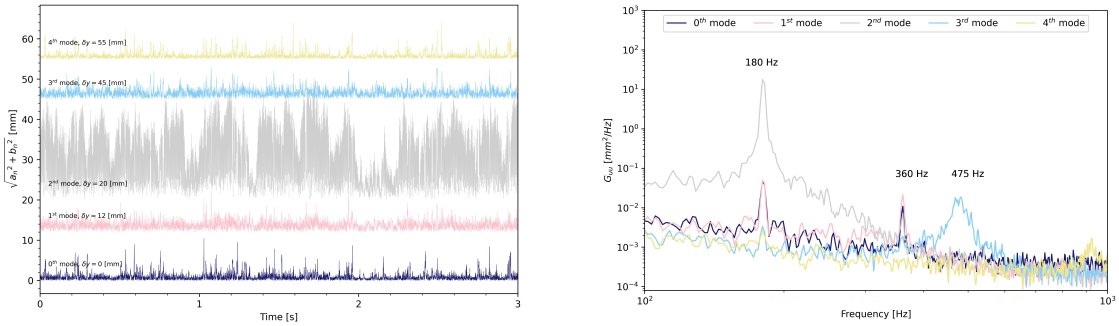

(a) Time series of the markers activity at NPR = 22.3

(b) 1-sided PSD of the markers' modal coefficients at NPR = 22.3

Figure 6.27: Markers modal analysis during steady state operation

A useful indicator that can be employed to better assess the coupling between an input x and an output signal y of a coupled system is *coherence*, denoted with γ^2_{xy}.

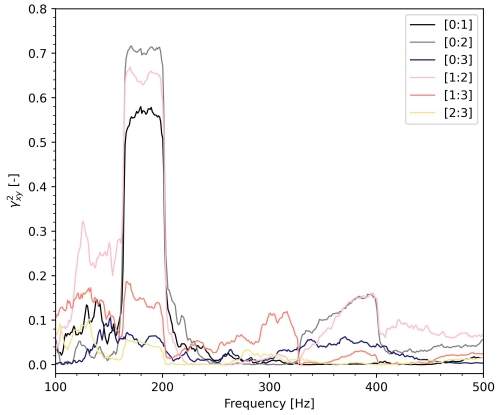

Figure 6.28: Linear coherence spectrum between structural mode coefficients during a steady run at NPR = 22.3. Labels refer to the modes that have been reciprocally considered

Broadly speaking, coherence quantifies a transfer of energy and is defined as:

$$\gamma^2_{xy}(f) = \frac{\left|G_{xy}(f)\right|^2}{G_{xx}(f)G_{yy}(f)}$$

where G_{xy} is the cross-spectral density between x and y, and G_{xx} and G_{yy} are the auto-spectral of x and y, respectively. Based on this definition, starting from the observations of Figure 6.27b, the results presented in Figure 6.28 represent the coherence computed using a linear transfer kernel between different structural mode coefficients. From this analysis it is clearly shown that breathing, bending and ovalisation modes are highly coupled around 180 Hz, whereas the degree of coupling of the triangular mode is less strong.

Production mechanism of the aeroelastic tone

In order to better visualise the global flow phenomena that are associated with the nozzle bending frequency, DMD is performed (Schmid, 2010). For this, the snapshots that have been considered to contruct the DMD matrix include the instantaneous schlieren images, the lip markers positions and the acoustic signals of the 8 microphones. Starting from 7000 snapshots, taken during test runs of 3.5 s at f_s = 2000 Hz, snapshots were downsampled to N_s = 1750, allowing for a modal reconstruction up to 200 Hz. To reduce computational intensity while also removing small scales effects, images resolution has been lowered using a 3x3 pixels linear interpolation. Given the matrix imbalance due to the larger portion of schlieren data, normalisation was also performed such that flow, acoustic and structural effects would be equally captured. The obtained modal amplitudes and frequencies can be seen in Figure 6.29. A strong mean mode (f = 0 Hz) is identified together with 825 conjugate pairs, each having a certain amplitude α and mode stability β. Here only the most stable modes are plotted, with $-0.08 < \beta < 0.08$, and, aside a number of spurious or heavily damped modes, the fundamental oscillation frequency f = 180 Hz is clearly captured in the DMD solution.

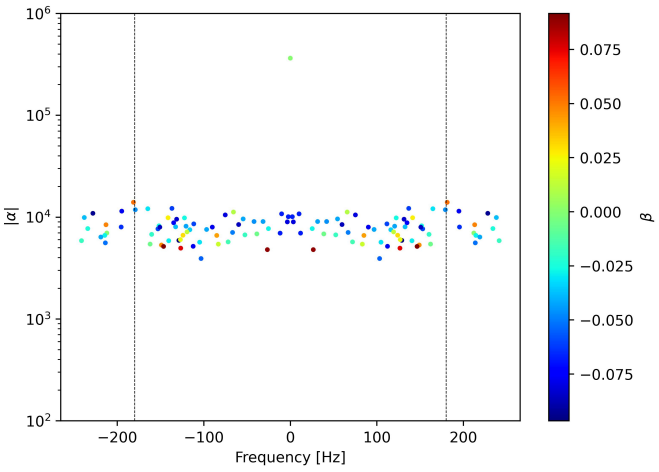

Figure 6.29: Modal amplitude distribution for the coupled acoustic-flow-structure interaction

The reconstruction of the nozzle dynamics and the flow field fluctuations associated with the ovalisation mode of the nozzle lip is shown in Figure 6.30. At a first glance, from the nozzle lip reconstruction, it can be seen how, compared to the lip shape in static conditions (black contour), the mean shape (blue contour) during oscillation is slightly ovalised, thereby revealing a pre-stressed structure, which requires a higher driving frequency to resonate.

As for the schlieren snapshots associated with the DMD mode, a number of observations can be made, which clearly highlight how the unsteadiness can be linked to the shock foot oscillation. Red areas in the figures represent positive gradient fluctuations in the shear layer, that indicate a greater turbulent intensity. On the other hand, blue areas describe negative gradient fluctuations, that indicate a region of weakened turbulence. In the context of shock foot unsteadiness, Figure 6.30a and 6.30c distinctly show how the red-blue patterns are inverted: this could be interpreted as the direct result of the periodic shifting of the shock foot from a

downstream position (Figure 6.30a) to a more upstream location (Figure 6.30c). A shock foot that is shifted further downstream, in fact, will also result in a mostly attached shear layer, which, in terms of the DMD solution, configures itself with the red contours positioned in the outer parts of the plume. In a similar way to the findings of Laguarda et al. (2023) on a flexible flat panel, the clear pattern alternation further supports the idea that the low-frequency shock foot unsteadiness coexists with that arising from the dynamic coupling with the moving wall.

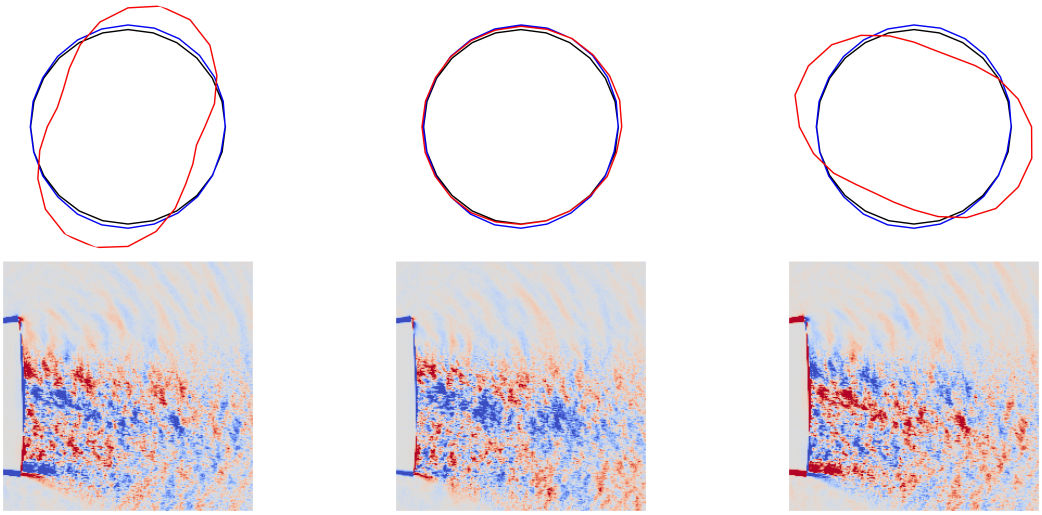

(a) $\omega t = 0$ - Downstream separation point (b) $\omega t = \pi/2$ - Receding separation point (c) $\omega t = \pi$ - Upstream separation point

Figure 6.30: Data field reconstruction associated with the ovalisation mode at 180 Hz. Top: nozzle lip deformation; Black = static nozzle, Blue = mean shape at 180 Hz, Red = instantaneous deformation. Bottom: schlieren images of the instantaneous DMD mode flow; Red = positive fluctuation, Blue = negative fluctuation

Next, when comparing the flow field and structure dynamics together, it can be seen that the vibrational response and the plume behaviour are in phase, confirming the model hypothesised by Génin et al. (2015). Taking as a reference a point in the bottom part of the nozzle lip, when the shock foot is shifted upstream, in fact, a larger portion of the nozzle walls experiences a greater load that comes from the sudden recompression aft of the mach saddle, inducing the walls to bend inwards. In turn, this causes a higher wall pressure which gradually moves the shock foot downstream, hence inducing the walls to bend outwards.

Finally, now that a strong FSI coupling at 180 Hz has been confirmed, coherence is, again, computed to draw further conclusions on the coupling strength of the vibrational tone with the acoustic signal. Referring to the naming convention of Figure 5.9b, coherence is computed between each of the detected microphone signals and their neighboring marker's fluctuation.

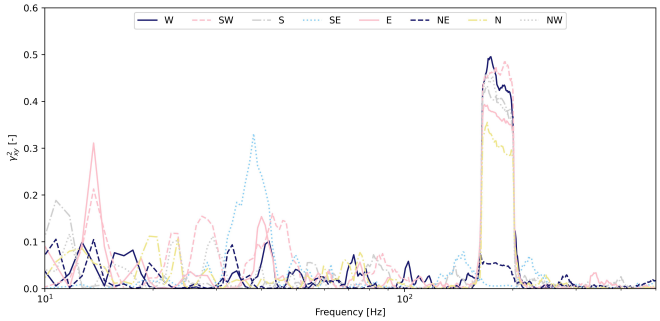

Figure 6.31: Linear coherence spectrum between acoustic pressure and marker displacement at 8 different locations at NPR = 22.3

Figure 6.31 confirms a strong transfer of energy from the vibrating walls to the acoustic field around 180 Hz. Further insights are gathered from the DMD solution; depicted in Figure 6.32a is the reconstruction of the

DMD solution for the acoustic signal of the 8 microphones and their adjacent lip markers. Since multiple nozzle wall points have an influence on each microphone's signal, the degree of phase shift varies for the different combinations of microphone/marker. Nevertheless, it can be broadly seen that in those instants when the wall is stretching in one direction, that is, when the displacement is positive, the corresponding acoustic signal is experiencing a negative pressure fluctuation, and viceversa. This is also confirmed in Figure 6.32b, which presents the low-pass filtered raw acoustic and lip displacement signals, and highlights their opposite evolution. As a result, it can also be deduced that, whenever the nozzle is experiencing the largest deformations, the acoustic signal has a phase shift of approximately π with respect to the flow and the wall dynamics, thereby lending support to the hypothesis that the acoustic peak at 180 Hz cannot be the result of a speaker-like mechanism in which the stretching of the wall would result in a positive acoustic pressure fluctuation.

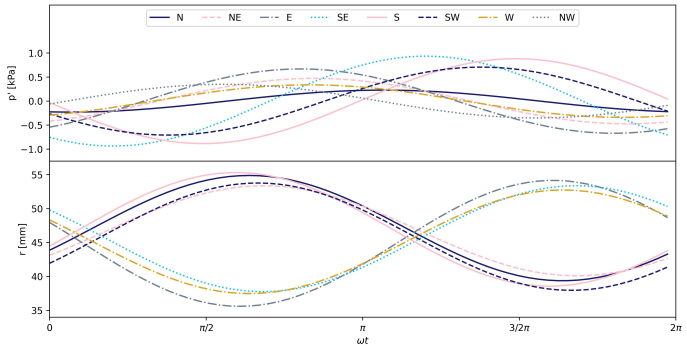

(a) Reconstruction of the acoustic field and markers displacement associated with the 180 Hz DMD mode

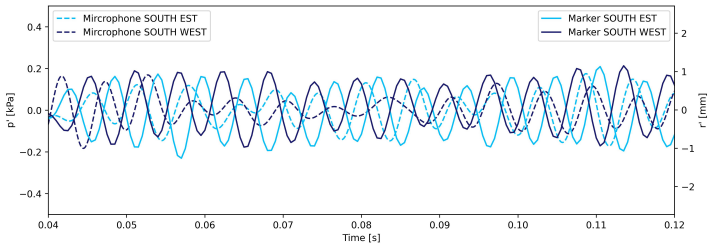

(b) Superimposed raw time series of markers displacement and acoustic pressure fluctuations at the SOUTH EST location

Figure 6.32: Analysis of the acoustic response based on markers displacement (naming based on Figure 5.9b)

On the contrary, a possible explanation for this behaviour can be given considering, again, the shock foot unsteadiness and its effects on the turbulent shear layer that is formed aft of the separation shock. Considering, again, Figure 6.30, it can be seen how the shear layer is thinner when the shock resides closer to the nozzle lip, whereas it is thicker when separation occurs more upstream. In conclusion, the source of the aeroelastic tone detected by the microphones originates in the shear layer and is the result of the periodically amplified or dampened turbulent fluctuations that occur in response of the shock foot unsteadiness.

7

Conclusions and recommendations

In this chapter, the most relevant conclusions that can be drawn based on the results obtained in chapter 6 are presented in section 7.1. The outcomes of the coupled structural-acoustic experimental investigation of a sub-scale, cold flow TOP contoured compliant nozzle are critically discussed under the framework of the research objective outlined in section 1.1 and the research questions are answered. Finally, a number of recommendations are given in section 7.2, in order to provide useful indications for future investigations.

7.1. Conclusions

Experimental studies are still needed nowadays to investigate the acoustic signature of TOP contoured nozzles to identify the most relevant phenomena involved in the propagation of noise that is generated under a broad spectrum of mechanisms. This is especially necessary during the ignition transient, which has been documented to be the phase producing the largest vibroacoustic loads. Nevertheless, the main limitation of the currently available literature on the topic revolves around the fact that only stiff walled nozzles in which structural vibrations are suppressed have been employed.

This thesis is part of a research effort to overcome the shortcomings associated with the currently available results, and to provide a preliminary understanding on the effects that aeroelasticity has in noise generation during transient startup of compliant walled nozzles. In this way, an improved dataset is gathered such that it can be used to validate numerical studies involving FSI or as a reference for empirical predicition methods.

The aim of this research project is to take a step further in investigating the acoustic signature of sub-scale TOP contoured compliant nozzles, as a way to provide a more robust framework that allows for the development of methodologies that are scalable to full-scale engine acoustic prediction studies. To do so, the following research objective was defined:

Identify the dominant vibroacoustic features of stiff and compliant walled sub-scale TOP contoured rocket nozzles during transient startup and shutdown operations, to assess which role different flow regimes play in sound production and radiation and what impact fluid-structure interactions have on the noise generated by a supersonic overexpanded jet.

To reach this goal, a GVT and two cold flow test campaigns have been carried out. The former, performed in the Mechanical Testing Lab of the Delft Aerospace Structures and Materials Laboratory, consisted in characterising the modal behaviour of both stiff and compliant nozzles to get a full insight on their natural oscillation frequencies. This was achieved by mounting on each nozzle a number of accelerometers and providing a impact force by means of a hammer tip, thereby allowing for a measure of the structure's frequency response function. On the other hand, the cold flow tests were carried out using the ASCENT test rig situated where the diffuser tube of the ST-15 supersonic wind tunnel usually sits in the Aerodynamics department High Speed Laboratory. These consisted in performing both transient and steady state runs that would allow for the simultaneous reconstruction of the flow, structure and acoustic field. The compliant nozzle was, first, spray-painted with a matte black color to minimise reflections and, then, provided with 24 equally spaced highly reflective circular markers to enable the reconstruction of the structural response during unsteady loading.

Due to the larger stiffness of the aluminium nozzle, lip tracking was not performed on this test article. In both cases, however, microphones were mounted either on a line array on the jet side, or azimuthally around the plume. Finally, a Z-schlieren system was setup to allow for the observation of the flow development.

Having conducted the experimental campaigns, quality of the lip tracking frames was enhanced via a number of pre-processing steps and later analysed by means of the IPR algorithm using DaVis 10.2.1. Eventually, spectral analysis of both markers displacement and acoustic data was performed to extract meaningful information about the nozzle dynamics and the acoustic field it generates when subjected to unsteady aerodynamic forces. Qualitative and quantitative observations of the Schlieren images have also aided in reconstructing the relationship between acoustic propagation and structural vibrations.

From the GVT campaign, natural oscillation frequencies and mode shapes have been obtained for both nozzles. The fundamental oscillation mode of the aluminium nozzle is the 1^{st} bending mode, which oscillates at 1009.67 Hz. On the other hand, the fundamental oscillation mode of the compliant nozzle is the 2^{nd} bending mode, namely the *ovalisation* mode, with an oscillation frequency attested around 156.38 Hz.

The first acoustic analysis was conducted on data gathered from the line array of microphones, which was mainly intended to study the different noise mechanisms involved in the transient startup. Results have shown that analysis of the acoustic spectra allows for the reconstruction of the different flow structures that develop with varying NPR. First of all, flow transition is clearly identified with a sharp drop of acoustic energy at all frequencies; the stiff nozzle experiences transition around NPR = 25.7, whereas the compliant nozzle brings flow reattachment forward and transitions at around NPR = 24.4. Similarly, during shutdown, retransition occurs at NPR = 15.5 for the stiff nozzle, whereas it is delayed at NPR = 14.4 in the compliant nozzle. Overall, during the FSS regime, in the flexible nozzle, turbulent mixing noise is the most dominant noise contributor due to the fact that wall compliancy suppresses the inception of higher frequency noise mechanisms like BBSN and TR. On the other hand, BBSN and TR tones are identified when testing the stiff nozzle. The former are detected between NPR = 3 and NPR = 5.5 and are revealed with a monotonically decreasing frequency band centred around f = 5.5 kHz. Further proof is also provided by an increased activity of the m = 1 acoustic mode. TR, instead, occurs around NPR = 11.3 and it resonates with f = 2.3 kHz.
These behaviours directly impact OASPLs, that are, overall, greater for the stiff nozzle. This nozzle, in fact, overpredicts the compliant nozzle performance by approximately 3.5 dB in its period of maximum noise generation around NPR = 11. For both nozzles, however, periods of increased acoustic impedance are revealed at almost comparable NPRs and are the result of a gradual opening of the subsonic core that develops downstream of the Mach stem, bringing the flow from a circular to an annular supersonic jet.
Ultimately, in both cases, owing, most likely, to the complexity of the flow development and the many phenomena that are involved in sound production and propagation, there is no indication that the signature scales to a constant Strouhal number, making preliminary noise mechanisms hard to predict.

The signature of the compliant nozzle reveals a highly energetic narrowband around f = 180 Hz at NPR = 22.3. This is also confirmed by azimuthal decomposition of the acoustic signals gathered using the circular array, which highlights a peak around f = 180 Hz, which is absent in the spectrum of the aluminium nozzle, when tested under similar operating conditions. Nevertheless, predominance of the acoustic breathing mode is attested in both cases, thereby demonstrating that acoustic mode decomposition alone cannot fully aid in the investigation of aeroelasticity sources. From the analysis of the nozzle lip structural dynamics behaviour, a strong coupling of the oscillation modes was identified, with the ovalisation mode being the most active and driving the oscillation at a slightly higher frequency than what found from GVT. DMD has further demonstrated that the mean shape of the nozzle is also slightly ovalised, thereby presenting a pre-stressed structure that requires a larger driving frequency to resonate. Wall ovalisation, that is brought about by the shock foot unsteadiness, has, then, a direct and in-phase effect on the flow structure: a downstream shift of the shock foot results in a shear layer that is mostly attached and thinner. The opposite, instead, occurs when the shock foot is shifted upstream. A study on signal coherence has, then, further evidenced the modes coupling behaviour. Combining raw acoustic signals and markers fluctuations has revealed a strong coherence around 180 Hz, proving, again, the strong transfer of energy from the vibrating walls to the acoustic field. Evidences on the source mechanism driving the genesis of this tone were gathered from the DMD analysis. An out-of-phase behaviour of approximately π between the wall vibration and the acoustic pressure reveals how the aeroelastic tone detected by the microphones is the result of the periodically amplified or dampened turbu-

lent intensity that is modulated by the shock foot fluctuation.

All in all, these results have shown the feasibility of investigating the relationship between flow, structural dynamics and acoustic signature of a compliant nozzle subjected to the unsteady loads of a transient startup, by means of non-intrusive optical techniques and acoustic sensing. The outcome of the tests carried out using the stiff nozzle has served as a baseline reference, against which flexible nozzle results have been compared to. Finally, it can be concluded that wall compliancy has two major effects on the overall acoustic signature of TOP nozzles. These are explicited in 1) a predominance of turbulent mixing noise, with the consequent suppression of higher frequency noise mechanisms such as BBSN and TR, and 2) in the inception of a narrowband tone closer to flow transition to RSS, which is directly related to the oscillation frequency of the structure and the shock foot unsteadiness.

7.2. Recommendations

The objective of this last section is that of providing useful indications for future research investigations. These have been formulated during execution of the experimental project, as well as during the later stages of data processing, and span from practical suggestions to account for during test setup and acquisition, to possible research paths to consider in future projects.

- At a first glance, as much as the proposed experimental setup was effective in retrieving the desired results, the quality of these could be further improved if tests were to be conducted in an anechoic environment. However, given the limited working characteristics of the A-Tunnel, which can only accommodate subsonic flows, the only two feasible changes that could be operated are the following:
  - Build a structure around the test rig that can support sound adsorbing wedges, such as to isolate the test section from unwanted reflections coming from the laboratory's walls and the large number of instrumentation present in the room. This, however, could restrict the access to the test section and limit the use of optical techniques
  - Conduct testing outside of the lab, in an open field that can be considered reflection-free. This however, adds the complexity of having to secure the equipment against adverse weather conditions
- Having ascertained the strong coupling of the structure's vibration modes, the lip tracking setup could be simplified and a single camera could be used. However, this compromises the use of the IPR algorithm, which requires a system of multiple cameras to run
- Schlieren imaging has two main drawbacks: first, being a line-of-sight technique it yields images of the flow field that represent an average flow through the test plane; secondly, it measures density gradients, which, in the context of the currently obtained results, limit the possibility to further delve into the nature of the aeroelastic tone. For these reasons, tomo-PIV measurements shall be favoured to better investigate the behaviour of the shear layer. Furthermore, due to the fact that ovalisation causes two *sides* of the nozzle to elongate, while the other two are bent inwards, a system that allows for the simultaneous observation of the flow dynamics that results from the opposing wall movements shall be considered
- Given the large flow asymmetry observed during tests that have employed compliant nozzles, an improved manufacturing method and/or materials shall be considered. In terms of manufacturing, a sensitivity study using compliant nozzles with different materials and/or wall thicknesses in order to verify whether a similar frequency coupling occurs and how it reflects on the acoustic spectrum is suggested. Also, the possibility to perform wall pressure measurements to track the evolution and the magnitude of the shock foot unsteadiness with varying NPR could be also considered
- Perform additional tests using the stiff nozzle while equipping it with wall pressure sensors to investigate the frequency associated with the shock foot unsteadiness such as to draw parallels with the compliant nozzle case as well as to investigate if a tone associated with it is also detected by the microphones

Appendices

A

Additional acoustic data

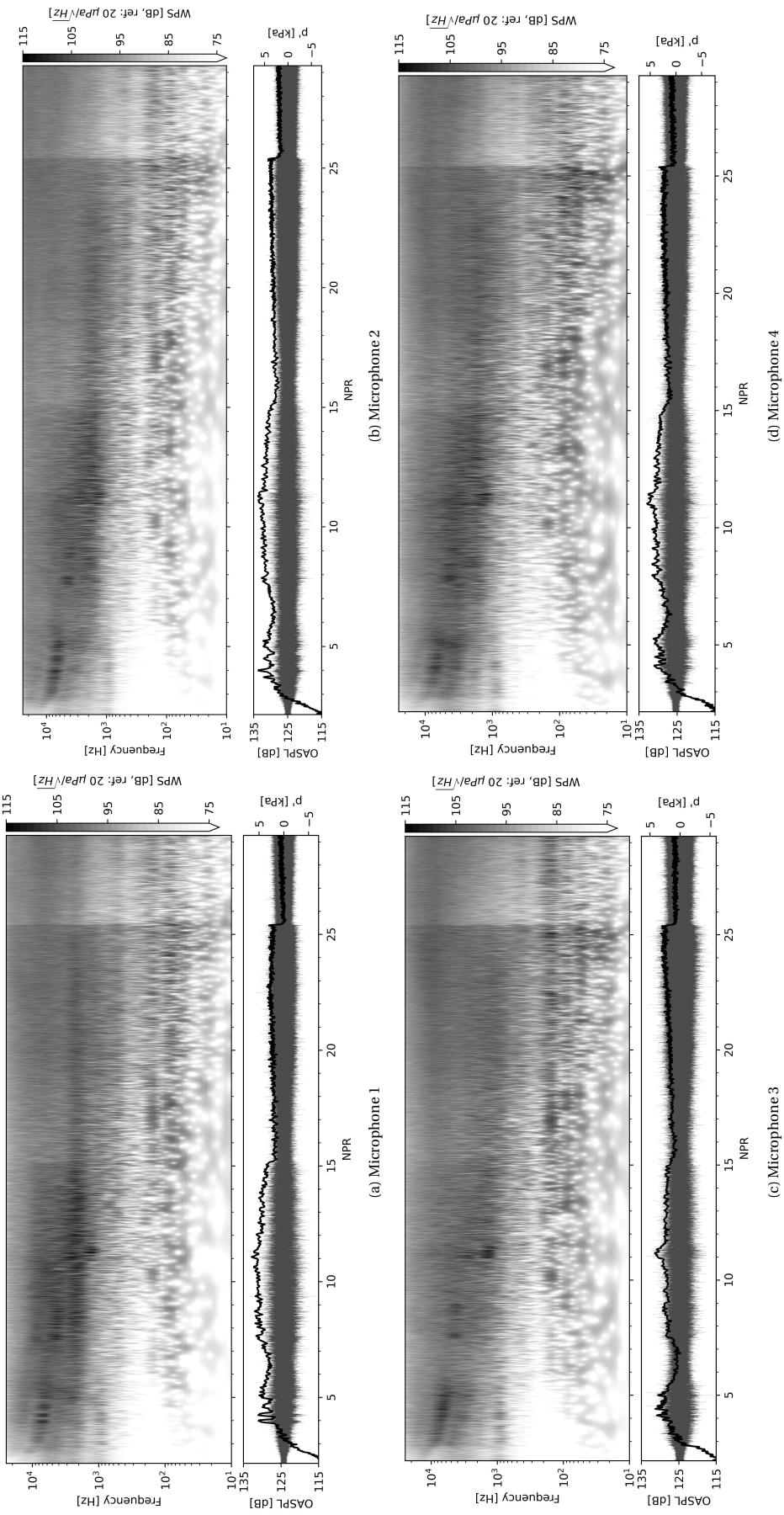

Figure A.1: **Stiff nozzle - Startup, line array** - Morlet wavelet power spectra of the acoustic pressure expressed as $10\log_{10}(E(f,t)/ref^2)$ [dB, ref: $20\mu Pa/\sqrt{Hz}$]. Raw pressure signal (grey) is displayed at the bottom [kPa] with a moving window-averaged OASPL (black) [dB, ref: $20\mu Pa$]

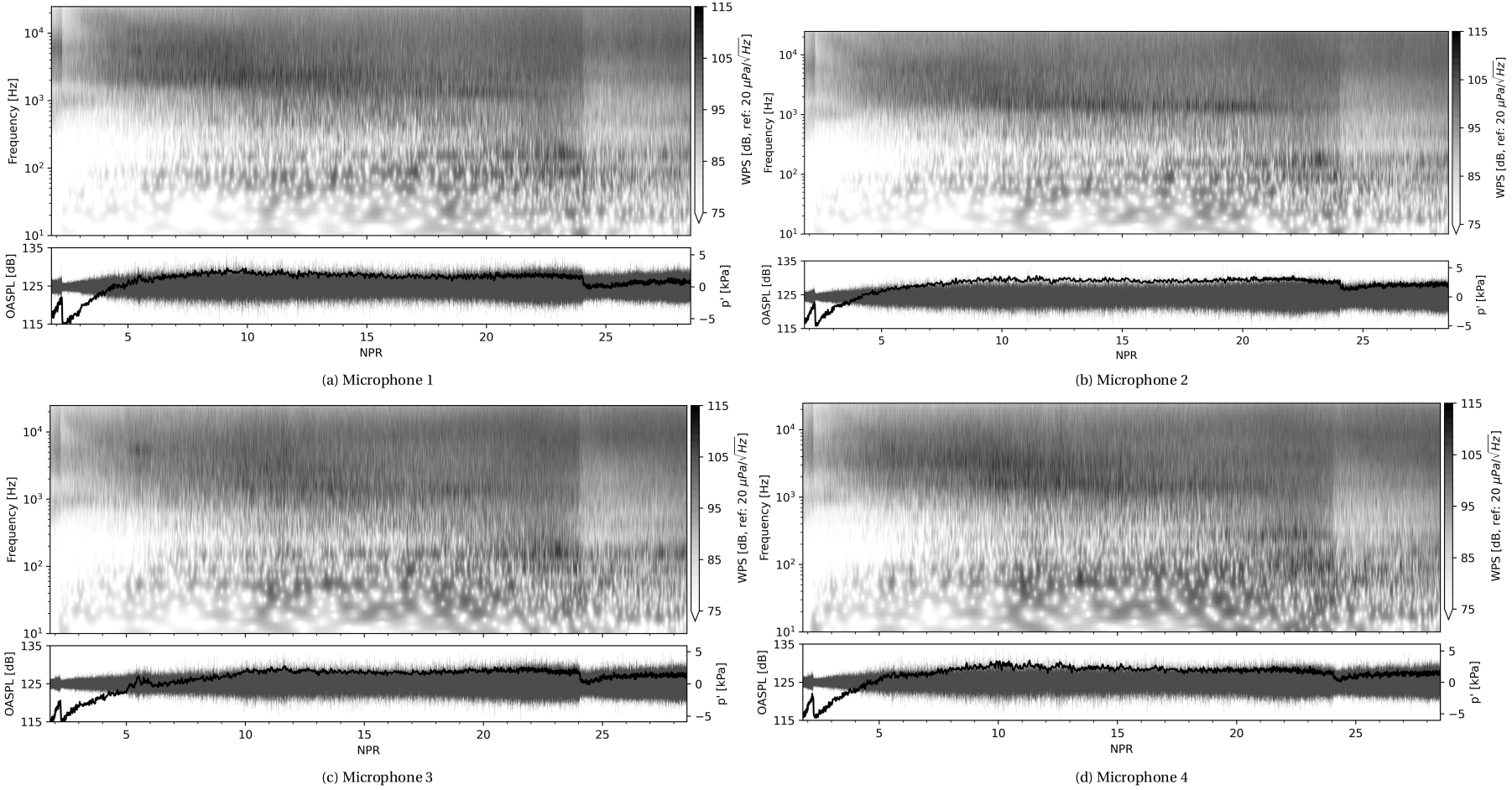

(a) Microphone 1

(b) Microphone 2

(c) Microphone 3

(d) Microphone 4

Figure A.2: **Compliant nozzle - Startup, line array** - Morlet wavelet power spectra of the acoustic pressure expressed as $10\log_{10}(E(f,t)/ref^2)$ [dB, ref: $20\mu Pa/\sqrt{Hz}$]. Raw pressure signal (grey) is displayed at the bottom [kPa] with a moving window-averaged OASPL (black) [dB, ref: $20\mu Pa$]

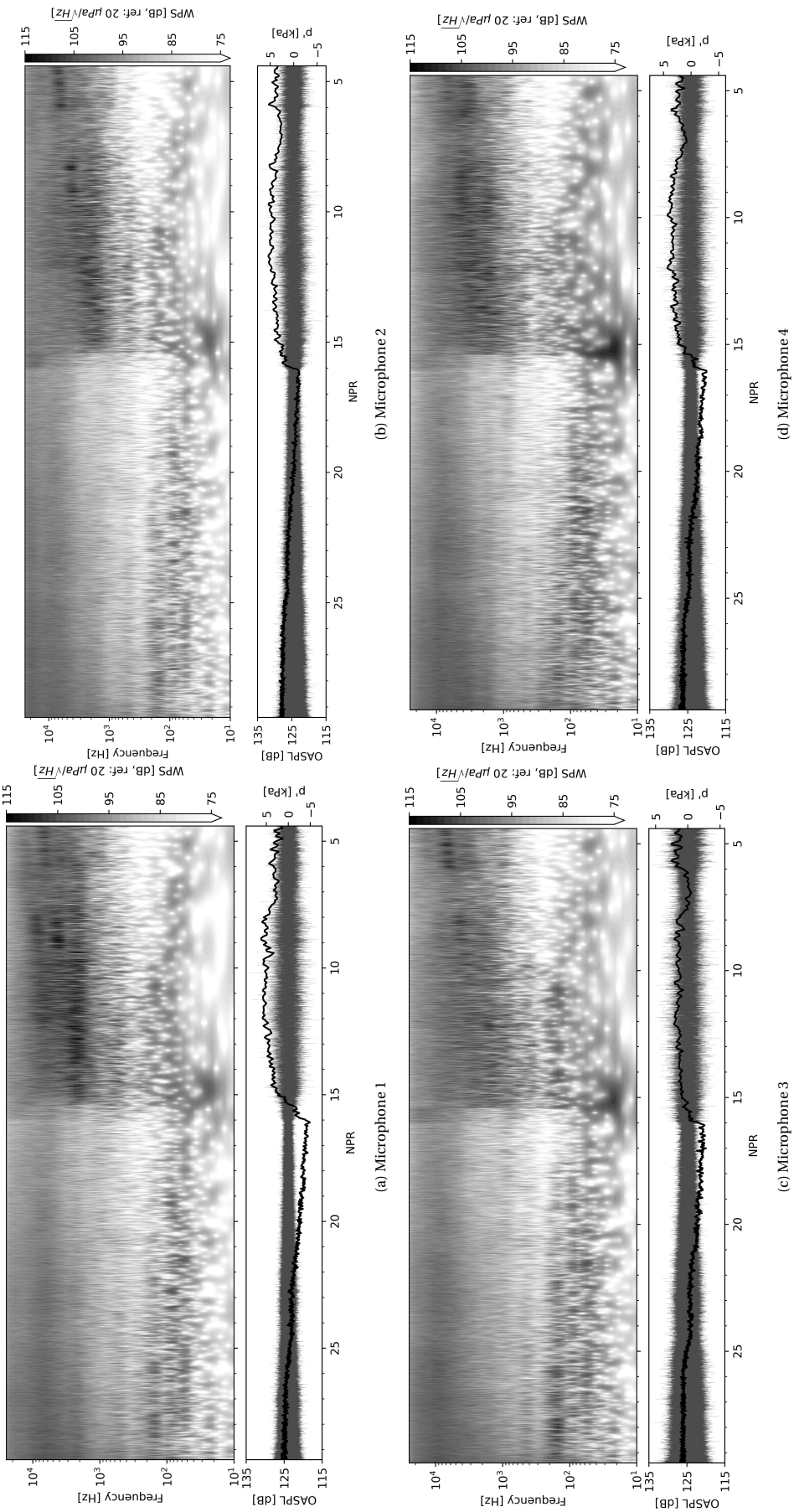

Figure A.3: **Stiff nozzle - Shutdown, line array** - Morlet wavelet power spectra of the acoustic pressure expressed as $10\log_{10}(E(f,t)/ref^2)$ [dB, ref: $20\mu Pa/\sqrt{Hz}$]. Raw pressure signal (grey) is displayed at the bottom [kPa] with a moving window-averaged OASPL (black) [dB, ref: $20\mu Pa$]

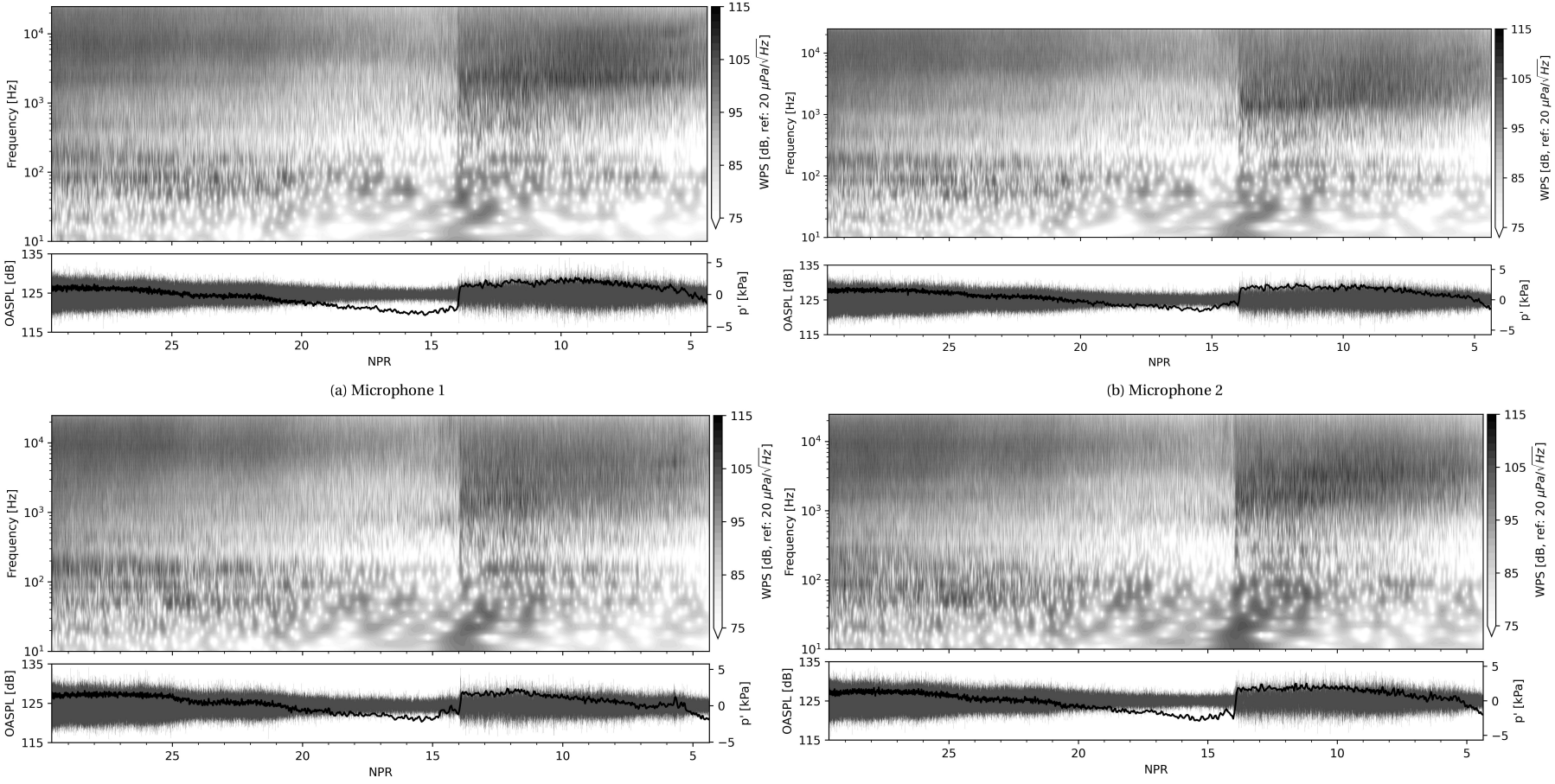

(a) Microphone 1

(b) Microphone 2

(c) Microphone 3

(d) Microphone 4

Figure A.4: **Compliant nozzle - Shutdown, line array** - Morlet wavelet power spectra of the acoustic pressure expressed as $10\log_{10}(E(f,t)/ref^2)$ [dB, ref: $20\mu Pa/\sqrt{Hz}$]. Raw pressure signal (grey) is displayed at the bottom [kPa] with a moving window-averaged OASPL (black) [dB, ref: $20\mu Pa$]

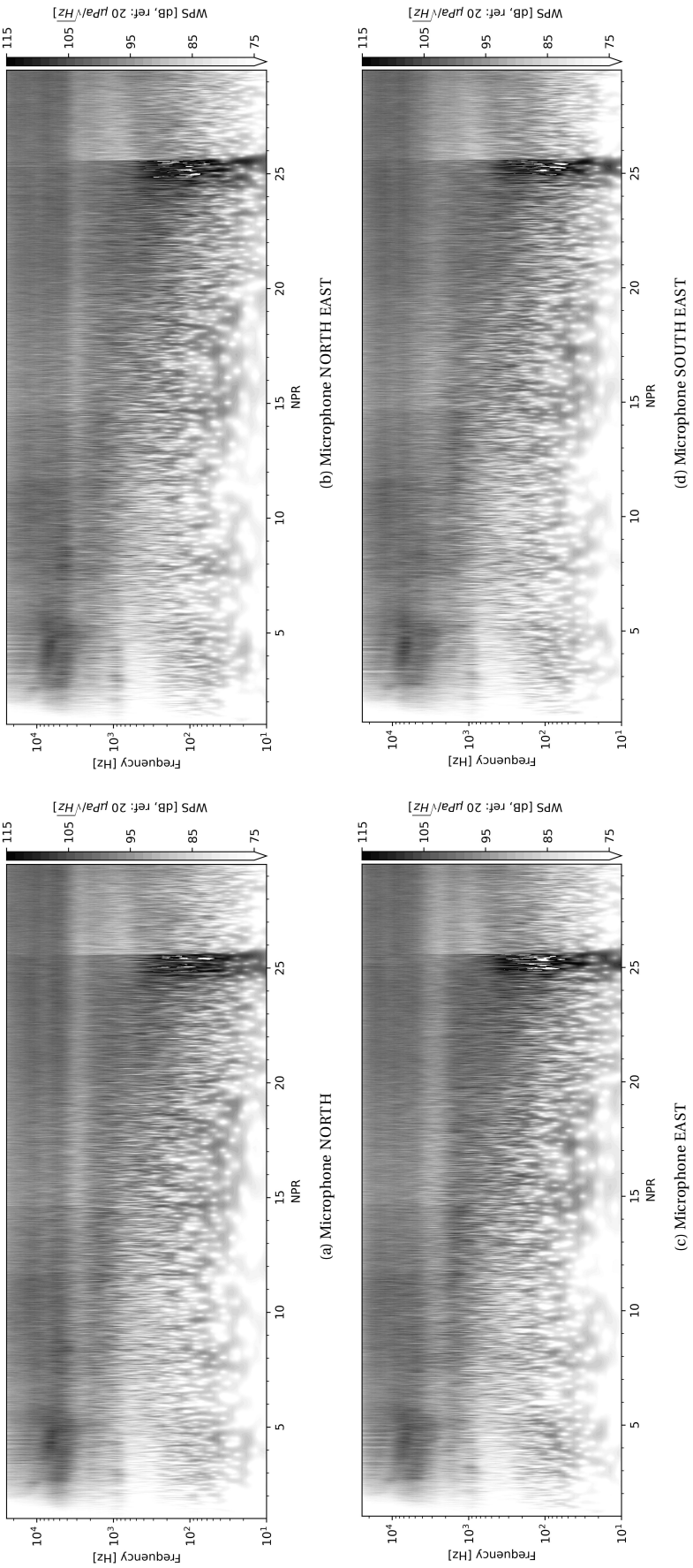

(a) Microphone NORTH (b) Microphone NORTH EAST

(c) Microphone EAST (d) Microphone SOUTH EAST

Figure A.5: **Stiff nozzle - Shutdown, azimuthal array** - Morlet wavelet power spectra of the acoustic pressure expressed as $10\log_{10}(E(f,t)/ref^2)$ [dB, ref: $20\mu Pa/\sqrt{Hz}$]. Raw pressure signal (grey) is displayed at the bottom [kPa] with a moving window-averaged OASPL (black) [dB, ref: $20\mu Pa$]

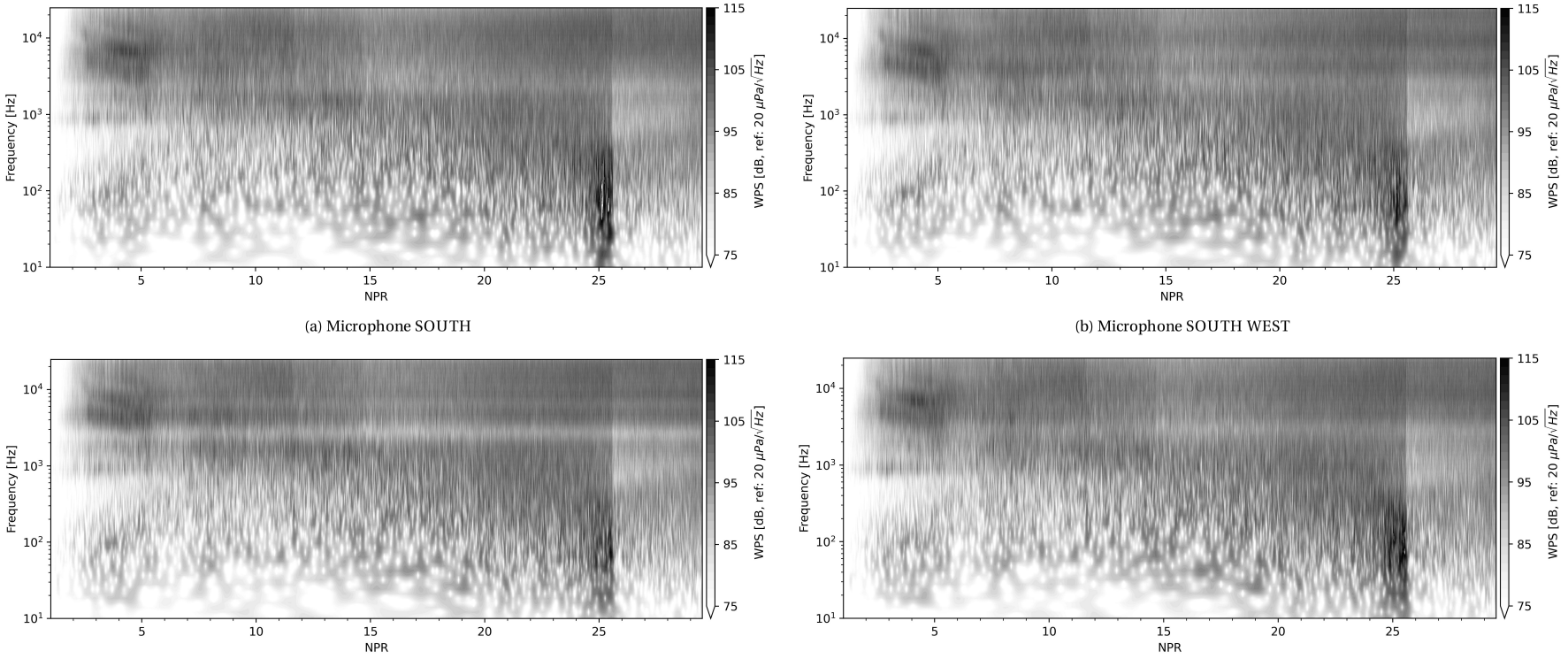

(a) Microphone SOUTH

(b) Microphone SOUTH WEST

(c) Microphone WEST

(d) Microphone NORTH WEST

Figure A.6: **Stiff nozzle - Shutdown, azimuthal array** - Morlet wavelet power spectra of the acoustic pressure expressed as $10\log_{10}(E(f,t)/ref^2)$ [dB, ref: $20\mu Pa/\sqrt{Hz}$]. Raw pressure signal (grey) is displayed at the bottom [kPa] with a moving window-averaged OASPL (black) [dB, ref: $20\mu Pa$]

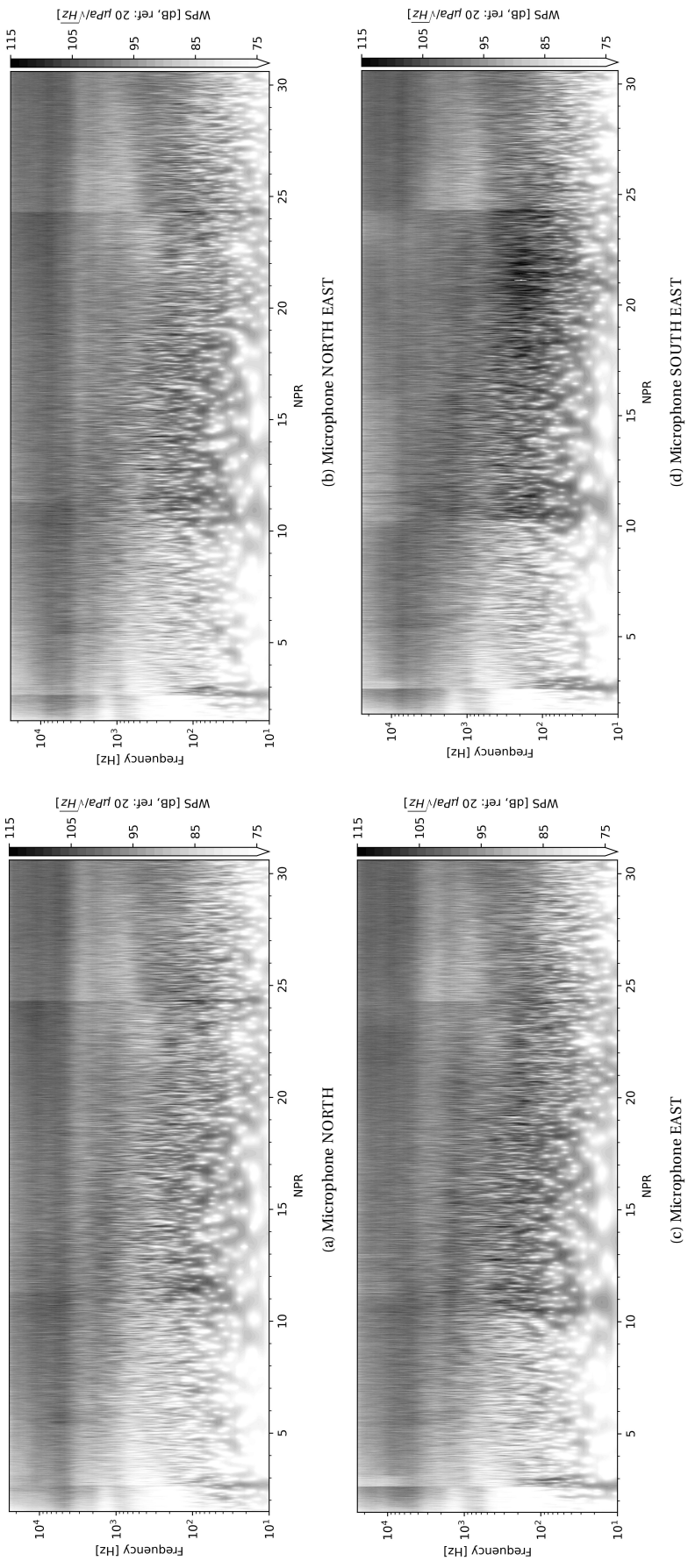

Figure A.7: **Compliant nozzle - Shutdown, azimuthal array** - Morlet wavelet power spectra of the acoustic pressure expressed as $10\log_{10}(E(f,t)/ref^2)$ [dB, ref: $20\mu Pa/\sqrt{Hz}$]. Raw pressure signal (grey) is displayed at the bottom [kPa] with a moving window-averaged OASPL (black) [dB, ref: $20\mu Pa$]

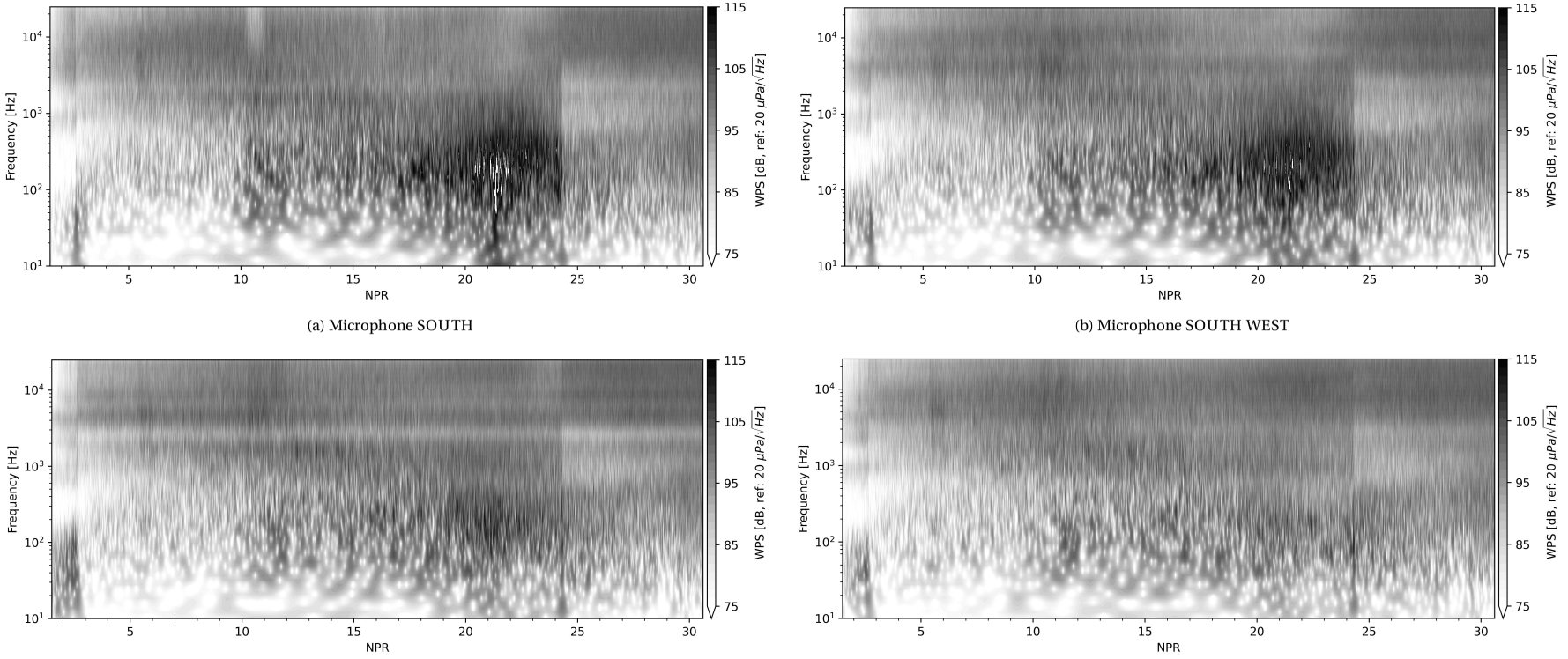

(a) Microphone SOUTH

(b) Microphone SOUTH WEST

(c) Microphone WEST

(d) Microphone NORTH WEST

Figure A.8: **Compliant nozzle - Shutdown, azimuthal array** - Morlet wavelet power spectra of the acoustic pressure expressed as $10\log_{10}(E(f,t)/ref^2)$ [dB, ref: $20\mu Pa/\sqrt{Hz}$]. Raw pressure signal (grey) is displayed at the bottom [kPa] with a moving window-averaged OASPL (black) [dB, ref: $20\mu Pa$]

B

Technical drawings

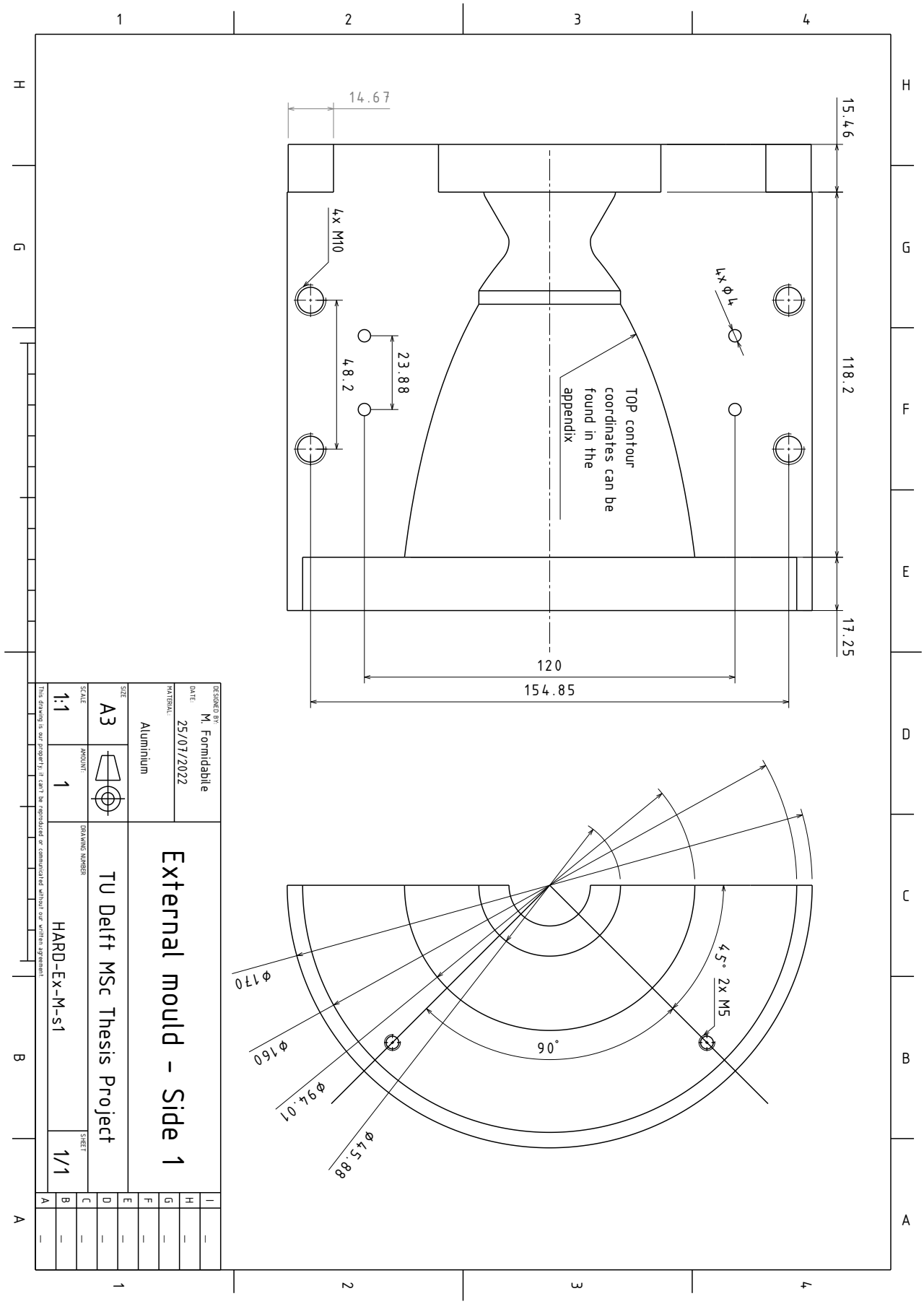

Figure B.1: General dimensioning of side 1 of the external mould

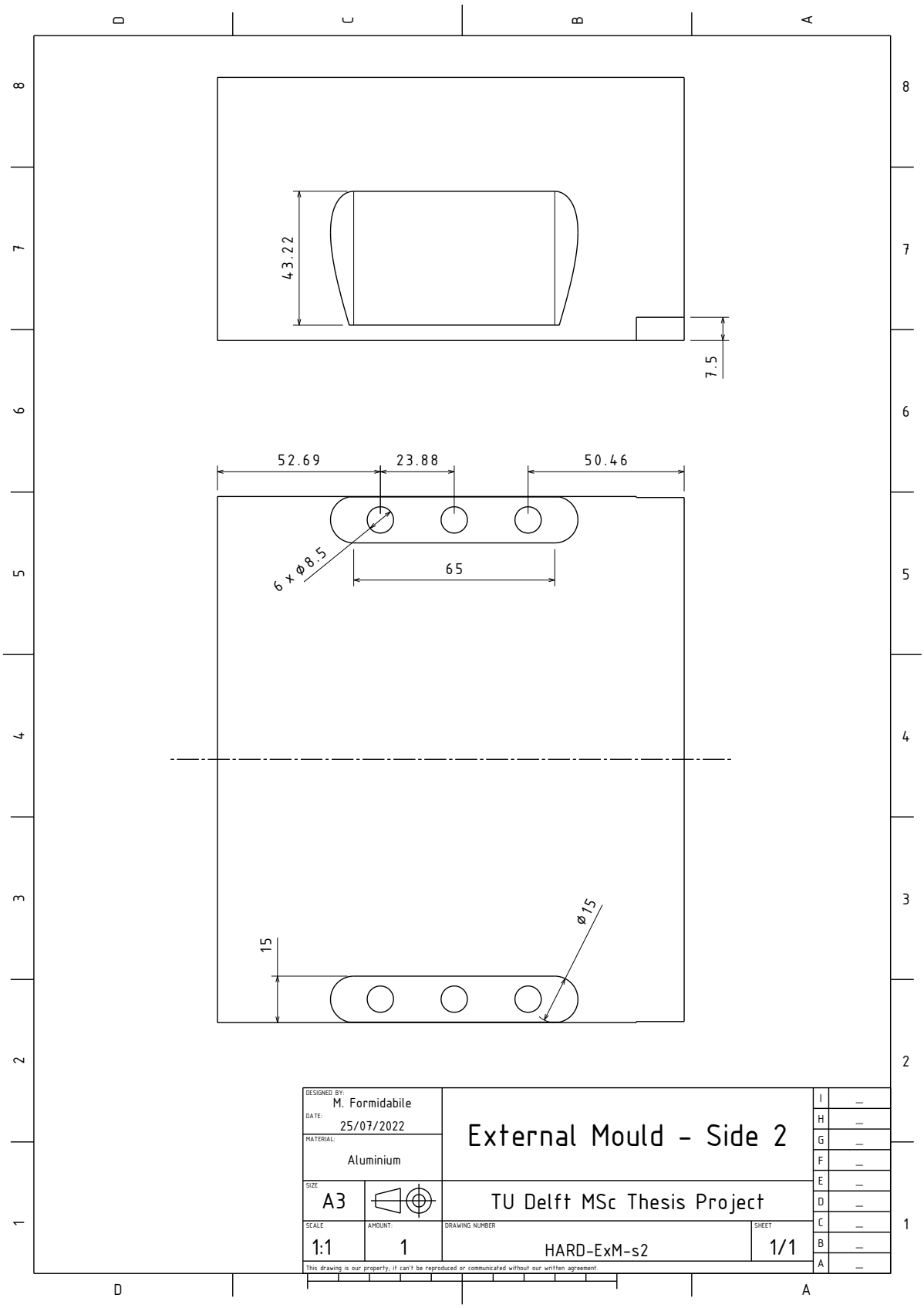

Figure B.2: General dimensioning of side 2 of the external mould

C

TOP contour coordinates

x/r^*	y/r^*	x/r^*	y/r^*	x/r^*	y/r^*
-1.9590727836	1.998324799	-0.4856749943	1.203048481	2.05660E-01	1.02138E+00
-1.9181407673	1.993248797	-0.4447465779	1.179424072	2.13162E-01	1.02298E+00
-1.8772207509	1.984692794	-0.4038193615	1.155794862	2.20651E-01	1.02465E+00
-1.8362887345	1.972440789	-0.3628909452	1.132165653	2.28127E-01	1.02637E+00
-1.7953567181	1.956204782	-0.1991808797	1.041386817	2.35589E-01	1.02815E+00
-1.7544367018	1.935540774	-0.1582524633	1.025705210	2.43038E-01	1.02998E+00
-1.7135046854	1.911948765	-0.1173248869	1.013960806	2.50473E-01	1.03188E+00
-1.6725726690	1.888308755	-0.0763970706	1.005871602	2.57893E-01	1.03383E+00
-1.6316526527	1.864680746	-0.0354693742	1.001260001	2.65297E-01	1.03583E+00
-1.5907206363	1.841052736	0	1	2.72686E-01	1.03790E+00
-1.5498006199	1.817424727	7.67170E-03	1.00003E+00	2.80059E-01	1.04002E+00
-1.5088686035	1.793796718	1.53430E-02	1.00012E+00	2.87416E-01	1.04219E+00
-1.4679365872	1.770168708	2.30133E-02	1.00026E+00	2.94755E-01	1.04443E+00
-1.4270165708	1.746540699	3.06823E-02	1.00047E+00	3.02077E-01	1.04672E+00
-1.3860845544	1.722900689	3.83495E-02	1.00074E+00	3.09382E-01	1.04906E+00
-1.3451525381	1.699272680	4.60144E-02	1.00106E+00	3.16668E-01	1.05146E+00
-1.3042325217	1.675644670	5.36766E-02	1.00144E+00	3.23936E-01	1.05392E+00
-1.2633005053	1.652016661	6.13357E-02	1.00188E+00	3.31184E-01	1.05643E+00
-1.2223684889	1.628388651	6.89911E-02	1.00238E+00	3.38413E-01	1.05900E+00
-1.1814460726	1.604760642	7.66425E-02	1.00294E+00	3.45622E-01	1.06163E+00
-1.1405188562	1.581132632	8.42894E-02	1.00356E+00	3.52811E-01	1.06431E+00
-1.0995904398	1.557504623	9.19313E-02	1.00423E+00	3.59979E-01	1.06704E+00
-1.0586620235	1.533864614	9.95678E-02	1.00497E+00	3.67126E-01	1.06983E+00
-1.0177360071	1.510236604	1.07198E-01	1.00576E+00	3.74251E-01	1.07267E+00
-0.9768075907	1.486608595	1.14823E-01	1.00661E+00	3.81354E-01	1.07557E+00
-0.9358791744	1.462980585	1.22440E-01	1.00752E+00	3.88435E-01	1.07852E+00
-0.8949519580	1.439352576	1.30051E-01	1.00849E+00	3.95493E-01	1.08153E+00
-0.8540235416	1.415724566	1.37654E-01	1.00952E+00	4.02527E-01	1.08459E+00
-0.8130963252	1.392096557	1.45248E-01	1.01060E+00	4.09538E-01	1.08771E+00
-0.7721691089	1.368456547	1.52834E-01	1.01175E+00	4.16525E-01	1.09088E+00
-0.7312406925	1.344828538	1.60411E-01	1.01295E+00	4.23487E-01	1.09410E+00
-0.6903134761	1.321200528	1.67979E-01	1.01421E+00	4.30425E-01	1.09737E+00
-0.6493850598	1.297572519	1.75537E-01	1.01553E+00	4.37337E-01	1.10070E+00
-0.6084578434	1.273944510	1.83084E-01	1.01690E+00	4.44223E-01	1.10408E+00
-0.5675294270	1.250316500	1.90621E-01	1.01834E+00	4.51083E-01	1.10752E+00
-0.5266022106	1.226688491	1.98146E-01	1.01983E+00	4.57917E-01	1.11100E+00

x/r^*	y/r^*	x/r^*	y/r^*	x/r^*	y/r^*
4.64723E-01	1.11454E+00	2.09156E+00	2.28595E+00	5.30335E+00	3.85091E+00
4.71502E-01	1.11814E+00	2.14103E+00	2.31696E+00	5.38938E+00	3.88295E+00
4.78254E-01	1.12178E+00	2.19127E+00	2.34820E+00	5.47638E+00	3.91493E+00
4.84977E-01	1.12547E+00	2.24234E+00	2.37964E+00	5.56427E+00	3.94681E+00
4.91672E-01	1.12922E+00	2.29418E+00	2.41127E+00	5.65294E+00	3.97855E+00
4.98338E-01	1.13302E+00	2.32039E+00	2.42716E+00	5.74241E+00	4.01017E+00
5.04975E-01	1.13687E+00	2.34679E+00	2.44308E+00	5.83266E+00	4.04165E+00
5.11582E-01	1.14077E+00	2.40018E+00	2.47505E+00	5.92364E+00	4.07294E+00
5.18158E-01	1.14472E+00	2.42713E+00	2.49107E+00	6.01530E+00	4.10406E+00
5.24704E-01	1.14872E+00	2.45425E+00	2.50712E+00	6.06131E+00	4.11952E+00
5.31220E-01	1.15277E+00	2.48154E+00	2.52320E+00	6.15373E+00	4.15026E+00
5.37704E-01	1.15687E+00	2.50901E+00	2.53931E+00	6.24667E+00	4.18075E+00
5.44156E-01	1.16102E+00	2.56448E+00	2.57160E+00	6.34008E+00	4.21098E+00
5.50577E-01	1.16522E+00	2.59243E+00	2.58774E+00	6.43388E+00	4.24092E+00
5.56965E-01	1.16946E+00	2.62054E+00	2.60390E+00	6.52802E+00	4.27057E+00
5.63320E-01	1.17376E+00	2.64878E+00	2.62007E+00	6.62246E+00	4.29989E+00
5.69642E-01	1.17811E+00	2.67719E+00	2.63624E+00	6.71712E+00	4.32888E+00
5.75931E-01	1.18250E+00	2.73442E+00	2.66860E+00	6.81196E+00	4.35752E+00
5.82185E-01	1.18694E+00	2.76320E+00	2.68475E+00	6.90694E+00	4.38582E+00
5.88406E-01	1.19143E+00	2.79210E+00	2.70089E+00	7.00204E+00	4.41376E+00
5.94591E-01	1.19597E+00	2.85025E+00	2.73312E+00	7.09724E+00	4.44133E+00
6.00742E-01	1.20056E+00	2.87945E+00	2.74919E+00	7.19258E+00	4.46857E+00
6.06858E-01	1.20519E+00	2.90874E+00	2.76522E+00	7.28809E+00	4.49548E+00
6.12937E-01	1.20987E+00	2.93810E+00	2.78123E+00	7.38383E+00	4.52207E+00
6.18981E-01	1.21459E+00	2.99705E+00	2.81309E+00	7.47990E+00	4.54840E+00
6.24988E-01	1.21937E+00	3.02657E+00	2.82894E+00	7.57644E+00	4.57446E+00
6.30959E-01	1.22418E+00	3.05612E+00	2.84473E+00	7.67365E+00	4.60036E+00
6.36892E-01	1.22905E+00	3.11531E+00	2.87611E+00	7.77170E+00	4.62608E+00
6.42479E-01	1.23370E+00	3.14488E+00	2.89168E+00	7.87076E+00	4.65172E+00
6.83410E-01	1.26788E+00	3.20396E+00	2.92254E+00	7.97102E+00	4.67728E+00
7.52730E-01	1.32510E+00	3.26279E+00	2.95298E+00	8.07272E+00	4.70282E+00
8.23735E-01	1.38283E+00	3.32125E+00	2.98295E+00	8.17619E+00	4.72842E+00
8.96621E-01	1.44120E+00	3.37915E+00	3.01234E+00	8.28155E+00	4.75409E+00
9.26364E-01	1.46476E+00	3.46451E+00	3.05516E+00	8.38906E+00	4.77988E+00
9.71628E-01	1.50034E+00	3.51997E+00	3.08267E+00	8.49886E+00	4.80580E+00
1.01775E+00	1.53623E+00	3.57389E+00	3.10919E+00	8.61115E+00	4.83186E+00
1.06478E+00	1.57249E+00	3.65066E+00	3.14653E+00	8.72606E+00	4.85809E+00
1.11279E+00	1.60915E+00	3.69769E+00	3.16919E+00	8.84372E+00	4.88448E+00
1.16185E+00	1.64624E+00	3.71924E+00	3.17952E+00	8.96419E+00	4.91102E+00
1.22899E+00	1.69640E+00	3.78428E+00	3.21046E+00	9.08750E+00	4.93770E+00
1.28076E+00	1.73462E+00	3.84631E+00	3.23968E+00	9.15024E+00	4.95109E+00
1.33382E+00	1.77340E+00	3.90966E+00	3.26922E+00	9.21372E+00	4.96451E+00
1.35178E+00	1.78642E+00	3.97429E+00	3.29905E+00	9.27791E+00	4.97794E+00
1.40664E+00	1.82593E+00	4.04021E+00	3.32917E+00	9.34284E+00	4.99140E+00
1.44397E+00	1.85258E+00	4.10741E+00	3.35956E+00	9.40849E+00	5.00486E+00
1.48199E+00	1.87952E+00	4.14149E+00	3.37484E+00	9.47488E+00	5.01835E+00
1.52069E+00	1.90675E+00	4.21062E+00	3.40561E+00	9.54202E+00	5.03185E+00
1.54026E+00	1.92043E+00	4.28102E+00	3.43661E+00	9.60985E+00	5.04536E+00
1.57999E+00	1.94806E+00	4.35265E+00	3.46778E+00	9.67842E+00	5.05886E+00
1.62046E+00	1.97598E+00	4.42554E+00	3.49916E+00	9.74771E+00	5.07236E+00
1.66164E+00	2.00419E+00	4.49964E+00	3.53071E+00	9.81773E+00	5.08586E+00
1.68247E+00	2.01838E+00	4.57495E+00	3.56240E+00	9.88847E+00	5.09936E+00
1.72478E+00	2.04700E+00	4.61303E+00	3.57829E+00	9.95994E+00	5.11284E+00
1.76786E+00	2.07592E+00	4.69014E+00	3.61018E+00	1.00321E+01	5.12630E+00
1.81172E+00	2.10511E+00	4.72909E+00	3.62615E+00	1.01050E+01	5.13974E+00
1.85636E+00	2.13460E+00	4.80790E+00	3.65816E+00	1.01786E+01	5.15317E+00
1.90180E+00	2.16434E+00	4.88780E+00	3.69023E+00	1.02530E+01	5.16656E+00
1.94803E+00	2.19437E+00	4.96883E+00	3.72235E+00	1.03280E+01	5.17993E+00
1.99507E+00	2.22464E+00	5.05091E+00	3.75450E+00	1.04038E+01	5.19328E+00
2.04292E+00	2.25518E+00	5.13406E+00	3.78666E+00	1.04802E+01	5.20657E+00
2.09156E+00	2.28595E+00	5.21820E+00	3.81880E+00	1.05575E+01	5.21984E+00

x/r^*	y/r^*
1.06354E+01	5.23306E+00
1.07140E+01	5.24624E+00
1.07934E+01	5.25937E+00
1.08735E+01	5.27245E+00
1.09543E+01	5.28548E+00
1.10359E+01	5.29847E+00
1.11182E+01	5.31138E+00
1.12013E+01	5.32424E+00
1.12851E+01	5.33705E+00
1.13697E+01	5.34978E+00
1.14551E+01	5.36245E+00
1.15411E+01	5.37505E+00
1.16281E+01	5.38759E+00
1.17158E+01	5.40005E+00
1.18042E+01	5.41243E+00
1.18935E+01	5.42473E+00
1.19836E+01	5.43696E+00
1.20745E+01	5.44910E+00
1.21662E+01	5.46115E+00
1.22587E+01	5.47312E+00
1.23521E+01	5.48500E+00
1.24463E+01	5.49678E+00
1.25000E+01	5.50340E+00

Bibliography

M. Frey and G. Hagemann. Flow separation and side-loads in rocket nozzles. In *35th Joint Propulsion Conference and Exhibit*, Los Angeles,CA,U.S.A., June 1999. American Institute of Aeronautics and Astronautics. doi: 10.2514/6.1999-2815. URL https://arc.aiaa.org/doi/10.2514/6.1999-2815.

L. Nave and G. Coffey. Sea level side loads in high-area-ratio rocket engines. In *9th Propulsion Conference*, Joint Propulsion Conferences. American Institute of Aeronautics and Astronautics, Nov. 1973. doi: 10.2514/6.1973-1284. URL https://arc.aiaa.org/doi/10.2514/6.1973-1284.

Y. Watanabe, N. Sakazume, and M. Tsuboi. LE-7A Engine Nozzle Problems during Transient Operations. In *38th AIAA/ASME/SAE/ASEE Joint Propulsion Conference & Exhibit*. American Institute of Aeronautics and Astronautics, 2002. doi: 10.2514/6.2002-3841. URL https://arc.aiaa.org/doi/abs/10.2514/6.2002-3841. _eprint: https://arc.aiaa.org/doi/pdf/10.2514/6.2002-3841.

G. Hagemann, J. Alting, and D. Preclik. Scalability for Rocket Nozzle Flows Based on Subscale and Full-Scale Testing. *Journal of Propulsion and Power*, 19(3):321–331, May 2003. ISSN 0748-4658, 1533-3876. doi: 10.2514/2.6123. URL https://arc.aiaa.org/doi/10.2514/2.6123.

G. V. R. Rao. Exhaust Nozzle Contour for Optimum Thrust. *Journal of Jet Propulsion*, 28(6):377–382, June 1958. doi: 10.2514/8.7324. URL https://arc.aiaa.org/doi/10.2514/8.7324. Publisher: American Institute of Aeronautics and Astronautics.

H. Himelblau, D. Kern, L., and J. E. Manning. NASA Handbook 7005 - Dynamics Environmental Criteria. Technical report, NASA, 2001. URL https://ntrs.nasa.gov/citations/20190026820.

J. Onoda and K. Minesugi. Estimation of mechanical environment of m-v satellite launcher. In *JSASS/JSME Structures Conference*, pages 229–232, 1997.

C. P. Lubert, K. L. Gee, and S. Tsutsumi. Supersonic jet noise from launch vehicles: 50 years since NASA SP-8072. *The Journal of the Acoustical Society of America*, 151(2):752–791, Feb. 2022. ISSN 0001-4966. doi: 10.1121/10.0009160. URL https://asa.scitation.org/doi/full/10.1121/10.0009160. Publisher: Acoustical Society of America.

S. Griffin, S. Lane, and D. Leo. Innovative vibroacoustic control approaches in space launch vehicles. In *29th International Congress and Exhibition on Noise Control Engineering*, Nice, France, 2000.

B. Henderson, C. Gerhart, E. Jensen, S. Griffin, and A. Lazzaro. Vibro-acoustic launch protection experiment (valpe). In J. A. S. Am., editor, *29th International Congress and Exhibition on Noise Control Engineering*, volume 144(4), page 2384, 2003.

J. Seiner and J. Yu. Acoustic near field and local flow properties associated with broadband shock noise. In *7th Aeroacoustics Conference*, Aeroacoustics Conferences. American Institute of Aeronautics and Astronautics, Oct. 1981. doi: 10.2514/6.1981-1975. URL https://arc.aiaa.org/doi/10.2514/6.1981-1975.

K. B. M. Q. Zaman, M. D. Dahl, T. J. Bencic, and C. Y. Loh. Investigation of a 'transonic resonance' with convergent–divergent nozzles. *Journal of Fluid Mechanics*, 463:313–343, July 2002. ISSN 1469-7645, 0022-1120. doi: 10.1017/S0022112002008819. URL https://www.cambridge.org/core/journals/journal-of-fluid-mechanics/article/investigation-of-a-transonic-resonance-with-convergentdivergent-nozzles/21C10ECCA016D14FCFCA3FD443539505. Publisher: Cambridge University Press.

G. Raman. Supersonic Jet Screech: Half-Century from Powell to the Present. *Journal of Sound and Vibration*, 225(3):543–571, Aug. 1999. ISSN 0022460X. doi: 10.1006/jsvi.1999.2181. URL https://linkinghub.elsevier.com/retrieve/pii/S0022460X99921818.

K. M. Eldred. Acoustic loads generated by the propulsion system. Technical Report SP-8072, NASA Langley Research Center, 1971.

D. Casalino, S. Santini, M. Genito, and V. Ferrara. Rocket Noise Sources Localization Through a Tailored Beam-Forming Technique. *AIAA Journal*, 50(10):2146–2158, Oct. 2012. ISSN 0001-1452, 1533-385X. doi: 10.2514/1.J051479. URL https://arc.aiaa.org/doi/10.2514/1.J051479.

K. Plotkin, L. Sutherland, and B. Vu. Lift-Off Acoustics Predictions for the Ares I Launch Pad. In *15th AIAA/CEAS Aeroacoustics Conference*, Miami, FL, 2009. AIAA. doi: 10.2514/6.2009-3163.

S. A. McInerny and S. M. Ölçmen. High-intensity rocket noise: Nonlinear propagation, atmospheric absorption, and characterization. *The Journal of the Acoustical Society of America*, 117(2):578–591, Feb. 2005. ISSN 0001-4966. doi: 10.1121/1.1841711. URL http://asa.scitation.org/doi/10.1121/1.1841711.

W. J. Baars, C. E. Tinney, J. H. Ruf, A. M. Brown, and D. M. McDaniels. Wall Pressure Unsteadiness and Side Loads in Overexpanded Rocket Nozzles. *AIAA Journal*, 50(1):61–73, Jan. 2012. ISSN 0001-1452, 1533-385X. doi: 10.2514/1.J051075. URL https://arc.aiaa.org/doi/10.2514/1.J051075.

W. J. Baars and C. E. Tinney. Transient wall pressures in an overexpanded and large area ratio nozzle. *Experiments in Fluids*, 54(2):1468, Feb. 2013. ISSN 0723-4864, 1432-1114. doi: 10.1007/s00348-013-1468-8. URL http://link.springer.com/10.1007/s00348-013-1468-8.

T.-S. Wang, X. Zhao, S. Zhang, and Y.-S. Chen. Development of an Aeroelastic Modeling Capability for Transient Nozzle Flow Analysis. *Journal of Propulsion and Power*, 30(6):1692–1700, Nov. 2014. ISSN 0748-4658, 1533-3876. doi: 10.2514/1.B35277. URL https://arc.aiaa.org/doi/10.2514/1.B35277.

J. Östlund, T. Damgaard, and M. Frey. Side-Load Phenomena in Highly Overexpanded Rocket Nozzles. *Journal of Propulsion and Power*, 20(4):695–704, July 2004. ISSN 0748-4658, 1533-3876. doi: 10.2514/1.3059. URL https://arc.aiaa.org/doi/10.2514/1.3059.

X. Zhao, S. Bayyuk, and S. Zhang. Aeroelastic response of rocket nozzles to asymmetric thrust loading. *Computers & Fluids*, 76:128–148, May 2013. ISSN 00457930. doi: 10.1016/j.compfluid.2013.01.022. URL https://linkinghub.elsevier.com/retrieve/pii/S0045793013000467.

C. E. Tinney, K. Scott, M. Routon, J. Sirohi, and J. Ruf. Effect of Aeroelasticity on Vibroacoustic Loads during Startup of Large Area Ratio Nozzles. In *23rd AIAA/CEAS Aeroacoustics Conference*, Denver, Colorado, June 2017. American Institute of Aeronautics and Astronautics. ISBN 978-1-62410-504-3. doi: 10.2514/6.2017-3361. URL https://arc.aiaa.org/doi/10.2514/6.2017-3361.

B. W. Donald, W. J. Baars, C. E. Tinney, and J. H. Ruf. Sound Produced by Large Area-Ratio Nozzles During Fixed and Transient Operations. *AIAA Journal*, 52(7):1474–1485, 2014. ISSN 0001-1452. doi: 10.2514/1.J052588. URL https://doi.org/10.2514/1.J052588. Publisher: American Institute of Aeronautics and Astronautics _eprint: https://doi.org/10.2514/1.J052588.

A. Canchero, C. E. Tinney, N. Murray, and J. H. Ruf. Flow and Acoustics of Clustered Rockets During Startup. *AIAA Journal*, 54(5):1660–1669, May 2016a. ISSN 0001-1452, 1533-385X. doi: 10.2514/1.J054622. URL https://arc.aiaa.org/doi/10.2514/1.J054622.

A. Canchero, C. E. Tinney, N. Murray, and J. H. Ruf. Acoustic Imaging of Clustered Rocket Nozzles Undergoing End Effects. *AIAA Journal*, 54(12):3778–3786, Dec. 2016b. ISSN 0001-1452. doi: 10.2514/1.J055053. URL https://arc.aiaa.org/doi/10.2514/1.J055053. Publisher: American Institute of Aeronautics and Astronautics.

R. Rojo, C. E. Tinney, and J. H. Ruf. Effect of Stagger on the Vibroacoustic Loads from Clustered Rockets. *AIAA Journal*, 54(11):3588–3597, Nov. 2016. ISSN 0001-1452, 1533-385X. doi: 10.2514/1.J055017. URL https://arc.aiaa.org/doi/10.2514/1.J055017.

R. Stark, D. Schneider, J. Martin, and S. General. Experimental Study on Jet Acoustics of Subscale Rocket Nozzles with a Different Divergent Contour Design. In *8th EUCASS Conference*, page 9 pages, Madrid, Spain, 2019. Proceedings of the 8th European Conference for Aeronautics and Space Sciences. Madrid, Spain, 1-4 july 2019. doi: 10.13009/EUCASS2019-514. URL https://www.eucass.eu/doi/EUCASS2019-0514.pdf. Artwork Size: 9 pages Medium: PDF.

B. Donald, W. Baars, C. Tinney, and J. Ruf. Acoustic characterization of sub-scale rocket nozzles. In *50th AIAA Sciences Meeting*, Nashville, TN, Jan. 2012. AIAA. ISBN 978-1-60086-936-5. doi: 10.2514/6.2012-544. Journal Abbreviation: 50th AIAA Aerospace Sciences Meeting Including the New Horizons Forum and Aerospace Exposition Publication Title: 50th AIAA Aerospace Sciences Meeting Including the New Horizons Forum and Aerospace Exposition.

B. Wieneke. Iterative reconstruction of volumetric particle distribution. *Meas. Sci. Technol.*, 24(2):024008, Dec. 2012. ISSN 0957-0233. doi: 10.1088/0957-0233/24/2/024008. URL https://dx.doi.org/10.1088/0957-0233/24/2/024008. Publisher: IOP Publishing.

C. Torrence and G. Compo. A practical guide to wavelet analysis. *Bulletin of the American Meteorological Society*, 79(1):64–78, 1998.

G. S. Settles. *Schlieren and Shadowgraph Techniques - Visualizing Phenomena in Transparent Media*. Springer, 2001.

G. V. R. Rao. Recent Developments in Rocket Nozzle Configurations. *ARS Journal*, 31(11):1488–1494, Nov. 1961. ISSN 1936-9972. doi: 10.2514/8.5837. URL https://arc.aiaa.org/doi/10.2514/8.5837.

E. Martelli, F. Nasuti, and M. Onofri. Numerical calculation of FSS/RSS transition in highly overexpanded rocket nozzle flows. *Shock Waves*, 20(2):139–146, Apr. 2010. ISSN 1432-2153. doi: 10.1007/s00193-009-0244-4. URL https://doi.org/10.1007/s00193-009-0244-4.

J. H. Ahlberg, S. Hamilton, D. Migdal, and E. N. Nilson. Truncated Perfect Nozzles in Optimum Nozzle Design. *ARS Journal*, 31(5):614–620, 1961. doi: 10.2514/8.5577. URL https://doi.org/10.2514/8.5577. Publisher: American Institute of Aeronautics and Astronautics _eprint: https://doi.org/10.2514/8.5577.

D. Huzel, K. and D. Huang, H. *Design of Liquid Propellant Rocket Engines*. Rocketdyne Division, North American Aviation, Inc., ii edition, 1967.

E. Martelli, L. Saccoccio, P. P. Ciottoli, C. E. Tinney, W. J. Baars, and M. Bernardini. Flow dynamics and wall-pressure signatures in a high-Reynolds-number overexpanded nozzle with free shock separation. *Journal of Fluid Mechanics*, 895:A29, July 2020. ISSN 0022-1120, 1469-7645. doi: 10.1017/jfm.2020.280. URL https://www.cambridge.org/core/product/identifier/S0022112020002803/type/journal_article.

H. Babinsky and J. Harvey, editors. *Shock wave-boundary-layer interactions*. Cambridge aerospace series. Cambridge University Press, Cambridge, 1st edition, 2011. ISBN 978-0-521-84852-7.

B. Edney. Anomalous heat transfer and pressure distributions on blunt bodies at hypersonic speeds in the presence of an impinging shock. Technical Report FFA–115, 4480948, Aeronautical Research Institute of Sweden, Jan. 1968. URL http://www.osti.gov/servlets/purl/4480948/.

W. J. Baars, J. H. Ruf, and C. E. Tinney. Non-stationary shock motion unsteadiness in an axisymmetric geometry with pressure gradient. *Experiments in Fluids*, 56(5):92, Apr. 2015. ISSN 1432-1114. doi: 10.1007/s00348-015-1958-y. URL https://doi.org/10.1007/s00348-015-1958-y.

S. B. Verma, R. Stark, and O. Haidn. Relation between shock unsteadiness and the origin of side-loads inside a thrust optimized parabolic rocket nozzle. *Aerospace Science and Technology*, 10(6):474–483, Sept. 2006. ISSN 1270-9638. doi: 10.1016/j.ast.2006.06.004. URL https://www.sciencedirect.com/science/article/pii/S1270963806000782.

R. H. Schmucker. Flow processes in overexpanded chemical rocket nozzles. Part II: Side loads due to asymmetric separation. Technical Report NASA-TM-77395, NASA, Feb. 1984a. URL https://ntrs.nasa.gov/citations/19840011403. NTRS Author Affiliations: NASA Headquarters NTRS Document ID: 19840011403 NTRS Research Center: Legacy CDMS (CDMS).

G. Dumnov. Unsteady side-loads acting on the nozzle with developed separation zone. In *32nd Joint Propulsion Conference and Exhibit*, Lake Buena Vista,FL,U.S.A., July 1996. American Institute of Aeronautics and Astronautics. doi: 10.2514/6.1996-3220. URL https://arc.aiaa.org/doi/10.2514/6.1996-3220.

B. J. Olson and S. K. Lele. A mechanism for unsteady separation in over-expanded nozzle flow. *Physics of Fluids*, 25(11):110809, Nov. 2013. ISSN 1070-6631. doi: 10.1063/1.4819349. URL https://aip.scitation.org/doi/10.1063/1.4819349. Publisher: American Institute of Physics.

F. Bakulu, G. Lehnasch, V. Jaunet, E. G. d. Silva, and S. Girard. Jet resonance in truncated ideally contoured nozzles. *Journal of Fluid Mechanics*, 919, July 2021. ISSN 0022-1120, 1469-7645. doi: 10.1017/jfm.2021.351. URL https://www.cambridge.org/core/journals/journal-of-fluid-mechanics/article/jet-resonance-in-truncated-ideally-contoured-nozzles/5B0EFB49AD0741EF23DC1EDB23107C4F. Publisher: Cambridge University Press.

M. A. Eitner, Y.-J. Ahn, L. Vanstone, M. N. Musta, J. Sirohi, and N. Clemens. Effect of Shock-Wave Boundary Layer Interaction on Vibratory Response of Compliant Panel. In *AIAA Aviation Forum*. American Institute of Aeronautics and Astronautics, 2021. doi: 10.2514/6.2021-2493. URL https://arc.aiaa.org/doi/abs/10.2514/6.2021-2493. _eprint: https://arc.aiaa.org/doi/pdf/10.2514/6.2021-2493.

Z. Du, C. Shen, Y. Shen, W. Huang, and L. Yan. Design exploration on the shock wave/turbulence boundary layer control induced by the secondary recirculation jet. *Acta Astronautica*, 181:468–481, Apr. 2021. ISSN 0094-5765. doi: 10.1016/j.actaastro.2021.01.063. URL https://www.sciencedirect.com/science/article/pii/S0094576521000746.

D. S. Dolling. Fifty Years of Shock-Wave/Boundary-Layer Interaction Research: What Next? *AIAA Journal*, 39(8):1517–1531, 2001. ISSN 0001-1452. doi: 10.2514/2.1476. URL https://doi.org/10.2514/2.1476. Publisher: American Institute of Aeronautics and Astronautics _eprint: https://doi.org/10.2514/2.1476.

N. T. Clemens and V. Narayanaswamy. Low-Frequency Unsteadiness of Shock Wave/Turbulent Boundary Layer Interactions. *Annual Review of Fluid Mechanics*, 46(1):469–492, 2014. doi: 10.1146/annurev-fluid-010313-141346. URL https://doi.org/10.1146/annurev-fluid-010313-141346.

M. E. Erengil and D. S. Dolling. Physical causes of separation shock unsteadiness in shock wave/turbulent boundary layer interactions. In *AIAA 24th Fluid Dynamics Conference*, 1993-3134, Orlando, FL, 1994. AIAA.

B. Ganapathisubramani, N. T. Clemens, and D. S. Dolling. Effects of upstream boundary layer on the unsteadiness of shock-induced separation. *Journal of Fluid Mechanics*, 585:369–394, Aug. 2007. ISSN 1469-7645, 0022-1120. doi: 10.1017/S0022112007006799. URL https://www.cambridge.org/core/journals/journal-of-fluid-mechanics/article/effects-of-upstream-boundary-layer-on-the-unsteadiness-of-shockinduced-separation/2EE3AE26FA67FED65BAC892DF01356AC. Publisher: Cambridge University Press.

S. Piponniau, J. P. Dussauge, J. F. Debiève, and P. Dupont. A simple model for low-frequency unsteadiness in shock-induced separation. *Journal of Fluid Mechanics*, 629:87–108, June 2009. ISSN 1469-7645, 0022-1120. doi: 10.1017/S0022112009006417. URL https://www.cambridge.org/core/journals/journal-of-fluid-mechanics/article/simple-model-for-lowfrequency-unsteadiness-in-shockinduced-separation/A823BCD0E74CA39AC0DA1362B73FC474. Publisher: Cambridge University Press.

A. L. Kistler. Fluctuating Wall Pressure under a Separated Supersonic Flow. *The Journal of the Acoustical Society of America*, 36(3):543–550, Mar. 1964. ISSN 0001-4966. doi: 10.1121/1.1918998. URL https://asa.scitation.org/doi/abs/10.1121/1.1918998. Publisher: Acoustical Society of America.

M. Arens and E. Spiegler. Shock-induced boundary layer separation in over-expanded conical exhaust nozzles. *AIAA Journal*, 1(3):578–581, Mar. 1963. ISSN 0001-1452. doi: 10.2514/3.1598. URL https://arc.aiaa.org/doi/10.2514/3.1598. Publisher: American Institute of Aeronautics and Astronautics.

A. A. Aghababaie and R. Theunissen. Modeling Free Shock Separation Induced Side Loads in Overexpanded Rocket Nozzles. *AIAA Journal*, 53(1):93–103, Jan. 2015. ISSN 0001-1452, 1533-385X. doi: 10.2514/1.J053014. URL https://arc.aiaa.org/doi/10.2514/1.J053014.

R. H. Stark. Flow Separation in Rocket Nozzles - An Overview. In *49th AIAA/ASME/SAE/ASEE Joint Propulsion Conference*, San Jose, CA, July 2013. American Institute of Aeronautics and Astronautics. ISBN 978-1-62410-222-6. doi: 10.2514/6.2013-3840. URL https://arc.aiaa.org/doi/10.2514/6.2013-3840.

F. Nasuti and M. Onofri. Shock structure in separated nozzle flows. *Shock Waves*, 19(3):229–237, July 2009. ISSN 0938-1287, 1432-2153. doi: 10.1007/s00193-008-0173-7. URL https://link.springer.com/10.1007/s00193-008-0173-7.

W. J. Baars, C. E. Tinney, and J. H. Ruf. Time-Frequency Analysis of Rocket Nozzle Wall Pressures during Start-up Transients. *Journal of Physics: Conference Series*, 318(9):092001, Dec. 2011. ISSN 1742-6596. doi: 10.1088/1742-6596/318/9/092001. URL https://doi.org/10.1088/1742-6596/318/9/092001. Publisher: IOP Publishing.

M. Summerfield, C. Foster, and W. Swan. Flow Separation in Overexpanded Supersonic Exhaust Nozzles. *Jet Propulsion*, 24(9):319–321, 1954.

R. Schmucker, H. Flow processes in Overexpanded Chemical Rocket Nozzles. Part I: Flow separation. Technical Report NASA-77396, NASA, Redwood City, Jan. 1984b.

R. Stark and B. Wagner. Experimental study of boundary layer separation in truncated ideal contour nozzles. *Shock Waves*, 19(3):185–191, July 2009. ISSN 1432-2153. doi: 10.1007/s00193-008-0174-6. URL https://doi.org/10.1007/s00193-008-0174-6.

J. Östlund. *Flow processes in rocket engine nozzles with focus on flow separation and side-loads*. Licentiate Thesis, Royal Institute of Technology, Stockholm, Sweden, 2002.

E. E. Zukoski. Turbulent boundary-layer separation in front of a forward-facing step. *AIAA Journal*, 5(10):1746–1753, Oct. 1967. ISSN 0001-1452. doi: 10.2514/3.4299. URL https://arc.aiaa.org/doi/10.2514/3.4299. Publisher: American Institute of Aeronautics and Astronautics.

P. Carriere, M. Seriexix, and J. L. Solignac. Properties de Similitude des Phenomenes de Decollement Laminaires ou Turbulents en Ecoulement Supersonic Nonuniforme. In *Proceedings of the 12th International Congress of Applied Mechanics*, pages 145–157. Stanford University Press, Stanford, CA, 1968.

A. P. Vasilev, V. M. Kudryavtsev, V. A. Kuznetsov, V. D. Kurpatenkov, and A. M. Obelnitskii. Fundamentals of Theory and Calculation of Liquid-Propellant Rocket Engines. Technical Report AD688729, Foreign Technology Div Wright-Patterson AFB Ohio, 1969. URL https://ntrl.ntis.gov/NTRL/dashboard/searchResults/titleDetail/AD688729.xhtml. Num Pages: 310.

P. Reijasse and J. Birkemeyer. Semi-Empirical Flow Separation Model for Subscale Nozzles. In *Fourth Symposium on Aerothermodynamics for Space Vehicles*, Capua, Italy, Oct. 2001. European Space Agency. URL https://articles.adsabs.harvard.edu//full/2002ESASP.487..407R/0000414.000.html.

M. Frey and G. Hagemann. Restricted Shock Separation in Rocket Nozzles. *Journal of Propulsion and Power*, 16(3):478–484, May 2000. ISSN 0748-4658, 1533-3876. doi: 10.2514/2.5593. URL https://arc.aiaa.org/doi/10.2514/2.5593.

C. L. Chen, S. R. Chakravarthy, and C. M. Hung. Numerical investigation of separated nozzle flows. *AIAA Journal*, 32(9):1836–1843, 1994. URL https://doi.org/10.2514/3.12181.

G. Hagemann, M. Frey, and W. Koschel. Appearance of Restricted Shock Separation in Rocket Nozzles. *Journal of Propulsion and Power*, 18(3):577–584, May 2002. doi: 10.2514/2.5971. URL https://arc.aiaa.org/doi/10.2514/2.5971. Publisher: American Institute of Aeronautics and Astronautics.

J. Mattsson, U. Högmann, and L. Torngren. A Sub Scale Test Programme on Investigation of Flow Separation & Side Loads in Rocket Nozzles. In *Aerothermodynamics for space vehicles*, volume 426, page 373, 1999.

A. T. Nguyen, H. Deniau, S. Girard, and T. Alziary de Roquefort. Unsteadiness of Flow Separation and End-Effects Regime in a Thrust-Optimized Contour Rocket Nozzle. *Flow, Turbulence and Combustion*, 71(1):161–181, Mar. 2003. ISSN 1573-1987. doi: 10.1023/B:APPL.0000014927.61427.ad. URL https://doi.org/10.1023/B:APPL.0000014927.61427.ad.

C. Génin, R. Stark, and S. Jack. Flow separation in out-of-round nozzles, a numerical and experimental study. In *Progress in Flight Physics – Volume 7*, volume 7, pages 269–282. EDP Sciences, 2015. ISBN 978-5-94588-165-5. doi: 10.1051/eucass/201507269. URL https://www.eucass-proceedings.eu/articles/eucass/abs/2015/01/eucass7p269/eucass7p269.html.

L.-O. Pekkari. Aeroelastic stability of supersonic nozzles with separated flow. In *29th Joint Propulsion Conference and Exhibit*, Monterey,CA,U.S.A., June 1993. American Institute of Aeronautics and Astronautics. doi: 10.2514/6.1993-2588. URL https://arc.aiaa.org/doi/10.2514/6.1993-2588.

S. Zhang and T. Fuchiwaki. Aeroelastic Coupling and Side Loads in Rocket Nozzles. In *38th Fluid Dynamics Conference and Exhibit*, Seattle, Washington, June 2008. American Institute of Aeronautics and Astronautics. ISBN 978-1-60086-989-1. doi: 10.2514/6.2008-4064. URL https://arc.aiaa.org/doi/10.2514/6.2008-4064.

E. Blades, E. Luke, and J. Ruf. Fully Coupled Fluid-Structure Interaction Simulations of Rocket Engine Side Loads. In *48th AIAA/ASME/SAE/ASEE Joint Propulsion Conference & Exhibit*, Atlanta, Georgia, July 2012. American Institute of Aeronautics and Astronautics. ISBN 978-1-60086-935-8. doi: 10.2514/6.2012-3969. URL http://arc.aiaa.org/doi/abs/10.2514/6.2012-3969.

J. A. Zhang, B. Shotorban, and S. Zhang. Numerical Experiment of Aeroelastic Stability for a Rocket Nozzle. *Journal of Aerospace Engineering*, 30(5):04017041, Sept. 2017. ISSN 1943-5525. doi: 10.1061/(ASCE)AS.1943-5525.0000746. URL https://ascelibrary.org/doi/abs/10.1061/%28ASCE%29AS.1943-5525.0000746. Publisher: American Society of Civil Engineers.

W. J. Tuovila and N. S. Land. Experimental study of aeroelastic instability of overexpanded rocket nozzle extensions. Technical Report TN D-4471, Langley Research Center, NASA, 1968.

A. Brown, R. Keanini, J. Ruf, D. Reed, and M. D'Agostino. Characterization of Side Load Phenomena Using Measurement of Fluid/Structure Interaction. In *38th AIAA/ASME/SAE/ASEE Joint Propulsion Conference & Exhibit*. American Institute of Aeronautics and Astronautics, 2002. doi: 10.2514/6.2002-3999. URL https://arc.aiaa.org/doi/abs/10.2514/6.2002-3999. _eprint: https://arc.aiaa.org/doi/pdf/10.2514/6.2002-3999.

M. J. Lighthill and M. H. A. Newman. On sound generated aerodynamically I. General theory. *Proceedings of the Royal Society of London. Series A. Mathematical and Physical Sciences*, 211(1107):564–587, Mar. 1952. doi: 10.1098/rspa.1952.0060. URL https://royalsocietypublishing.org/doi/10.1098/rspa.1952.0060. Publisher: Royal Society.

M. J. Lighthill. On sound generated aerodynamically II. Turbulence as a source of sound. *Proceedings of the Royal Society of London. Series A. Mathematical and Physical Sciences*, 222(1148):1–32, Feb. 1954. doi: 10.1098/rspa.1954.0049. URL https://royalsocietypublishing.org/doi/10.1098/rspa.1954.0049. Publisher: Royal Society.

C. K. W. Tam, K. Viswanathan, K. K. Ahuja, and J. Panda. The sources of jet noise: experimental evidence. *Journal of Fluid Mechanics*, 615:253–292, Nov. 2008. ISSN 1469-7645, 0022-1120. doi: 10.1017/S0022112008003704. URL https://www.cambridge.org/core/journals/journal-of-fluid-mechanics/article/sources-of-jet-noise-experimental-evidence/338F77F82719469AA9F6CDE3BA89D5F9. Publisher: Cambridge University Press.

S. B. Pope. *Turbulent flows*. Cambridge University Press, Cambridge ; New York, 2000. ISBN 978-0-521-59125-6 978-0-521-59886-6.

R. E. A. Arndt, D. F. Long, and M. N. Glauser. The proper orthogonal decomposition of pressure fluctuations surrounding a turbulent jet. *Journal of Fluid Mechanics*, 340:1–33, June 1997. ISSN 0022-1120, 1469-7645. doi: 10.1017/S0022112097005089. URL https://www.cambridge.org/core/product/identifier/S0022112097005089/type/journal_article.

H. Oertel Sen. Mach wave radiation of hot supersonic jets investigated by means of a shock tube and new optical techniques. In *12th International Symposium on Shock-Tubes and Waves*, Israel, 1980.

C. K. W. Tam and D. E. Burton. Sound generated by instability waves of supersonic flows. Part 1. Two-dimensional mixing layers. *Journal of Fluid Mechanics*, 138:249–271, Jan. 1984a. ISSN 1469-7645, 0022-1120. doi: 10.1017/S0022112084000112. URL https://www.cambridge.org/core/journals/journal-of-fluid-mechanics/article/sound-generated-by-instability-waves-of-supersonic-flows-part-1-twodimensional-//mixing-layers/3763B2A1D884D37A574B46D3FFC06A07. Publisher: Cambridge University Press.

C. K. W. Tam and D. E. Burton. Sound generated by instability waves of supersonic flows. Part 2. Axisymmetric jets. *Journal of Fluid Mechanics*, 138:273–295, Jan. 1984b. ISSN 1469-7645, 0022-1120. doi: 10.1017/S0022112084000124. URL https://www.cambridge.org/core/journals/journal-of-fluid-mechanics/article/sound-generated-by-instability-waves-of-supersonic-flows-part-2-axisymmetric-jets/88C0FA4ED39BFE3895EBA8A37C1C2865. Publisher: Cambridge University Press.

C. K. W. Tam and F. Q. Hu. On the three families of instability waves of high-speed jets. *Journal of Fluid Mechanics*, 201:447–483, Apr. 1989. ISSN 1469-7645, 0022-1120. doi: 10.1017/S002211208900100X. URL https://www.cambridge.org/core/journals/journal-of-fluid-mechanics/article/on-the-three-families-of-instability-waves-of-highspeed-jets/63E947E2B6D747B8E3CAC870644375B9. Publisher: Cambridge University Press.

C. K. W. Tam and P. Chen. Turbulent mixing noise from supersonic jets. *AIAA Journal*, 32(9):1774–1780, Sept. 1994. ISSN 0001-1452, 1533-385X. doi: 10.2514/3.12173. URL https://arc.aiaa.org/doi/10.2514/3.12173.

H. Ortel Sen, F. Seiler, and J. Srulijes. New Explanation of Noise Production by Supersonic Jets with Gas Dredging. In A. Dillmann, G. Heller, M. Klaas, H.-P. Kreplin, W. Nitsche, and W. Schröder, editors, *New Results in Numerical and Experimental Fluid Mechanics VII*, Notes on Numerical Fluid Mechanics and Multidisciplinary Design, pages 389–397, Berlin, Heidelberg, 2010. Springer. ISBN 978-3-642-14243-7. doi: 10.1007/978-3-642-14243-7_48.

H. Ortel Sen, F. Seiler, and J. Srulijes. Mach Wave Noise of a Supersonic Jet. In *15th International Symposium on Flow Visualization*, page 10, Minsk, Belarus, 2012.

H. Oertel Sen, F. Seiler, and J. Srulijes. Visualization of Mach waves produced by a supersonic jet and theoretical explanations. *Journal of Visualization*, 16(4):303–312, Nov. 2013. ISSN 1875-8975. doi: 10.1007/s12650-013-0185-y. URL https://doi.org/10.1007/s12650-013-0185-y.

C. K. W. Tam and K. C. Chen. A statistical model of turbulence in two-dimensional mixing layers. *Journal of Fluid Mechanics*, 92(2):303–326, May 1979. ISSN 1469-7645, 0022-1120. doi: 10.1017/S002211207900063X. URL https://www.cambridge.org/core/journals/journal-of-fluid-mechanics/article/statistical-model-of-turbulence-in-twodimensional-mixing-layers/6B09F0693E564F44F00896060B5B7C71. Publisher: Cambridge University Press.

M. Harper-Bourne and M. Fisher. The Noise from Shock Waves in Supersonic Jets. In *AGARD CP-131*, Sept. 1973.

S. P. Pao and J. M. Seiner. Shock-associated noise in supersonic jets. *AIAA Journal*, 21(5):687–693, May 1983. ISSN 0001-1452, 1533-385X. doi: 10.2514/3.8134. URL https://arc.aiaa.org/doi/10.2514/3.8134.

T. D. Norum and J. M. Seiner. Broadband Shock Noise from Supersonic Jets. *AIAA Journal*, 20(1):68–73, Jan. 1982. ISSN 0001-1452, 1533-385X. doi: 10.2514/3.51048. URL https://arc.aiaa.org/doi/10.2514/3.51048.

C. K. W. Tam. Supersonic Jet Noise. *Annual Review of Fluid Mechanics*, 27(1):17–43, 1995. doi: 10.1146/annurev.fl.27.010195.000313. URL https://doi.org/10.1146/annurev.fl.27.010195.000313. _eprint: https://doi.org/10.1146/annurev.fl.27.010195.000313.

C. K. W. Tam and H. K. Tanna. Shock associated noise of supersonic jets from convergent-divergent nozzles. *Journal of Sound and Vibration*, 81(3):337–358, Apr. 1982. ISSN 0022-460X. doi: 10.1016/0022-460X(82)90244-9. URL https://www.sciencedirect.com/science/article/pii/0022460X82902449.

H. S. Ribner. Cylindrical sound wave generated by shock-vortex interaction. *AIAA Journal*, 23(11):1708–1715, Nov. 1985. ISSN 0001-1452, 1533-385X. doi: 10.2514/3.9155. URL https://arc.aiaa.org/doi/10.2514/3.9155.

M. A. Hollingsworth and E. J. Richards. A Schlieren Study of the Interaction between a Vortex and a Shock Wave in a Shock Tube. *British Aeronaut. Research Council Rept. 17,985*, 1955. URL https://cir.nii.ac.jp/crid/1570291224167945856.

J. L. Ellzey, M. R. Henneke, J. M. Picone, and E. S. Oran. The interaction of a shock with a vortex: Shock distortion and the production of acoustic waves. *Physics of Fluids*, 7(1):172–184, Jan. 1995. ISSN 1070-6631, 1089-7666. doi: 10.1063/1.868738. URL http://aip.scitation.org/doi/10.1063/1.868738.

M. Kandula. A Theoretical Basis for the Scaling Law of Broadband Shock Noise Intensity in Supersonic Jets. *Advances in Acoustics and Vibration*, 2011:e573209, Mar. 2011. ISSN 1687-6261. doi: 10.1155/2011/573209. URL https://www.hindawi.com/journals/aav/2011/573209/. Publisher: Hindawi.

A. Powell. On the Mechanism of Choked Jet Noise. *Proceedings of the Physical Society. Section B*, 66(12):1039–1056, Dec. 1953. ISSN 0370-1301. doi: 10.1088/0370-1301/66/12/306. URL https://doi.org/10.1088/0370-1301/66/12/306. Publisher: IOP Publishing.

G. Raman. Advances in Understanding Supersonic Jet Screech: Review and Perspective. *Progress in Aerospace Sciences*, 34(1):45–106, Jan. 1998. ISSN 0376-0421. doi: 10.1016/S0376-0421(98)00002-5. URL https://www.sciencedirect.com/science/article/pii/S0376042198000025.

D. Edgington-Mitchell. Aeroacoustic resonance and self-excitation in screeching and impinging supersonic jets – A review. *International Journal of Aeroacoustics*, 18(2-3):118–188, Apr. 2019. ISSN 1475-472X, 2048-4003. doi: 10.1177/1475472X19834521. URL http://journals.sagepub.com/doi/10.1177/1475472X19834521.

T. A. Manning and S. K. Lele. A Numerical Investigation of Sound Generation in Supersonic Jet Screech. Technical report, Stanford University, Dept. of Aeronautics and Astronautics, Nov. 2000. URL https://apps.dtic.mil/sti/citations/ADA385651. Section: Technical Reports.

D. Edgington-Mitchell, K. Oberleithner, D. R. Honnery, and J. Soria. Coherent structure and sound production in the helical mode of a screeching axisymmetric jet. *Journal of Fluid Mechanics*, 748:822–847, June 2014. ISSN 0022-1120, 1469-7645. doi: 10.1017/jfm.2014.173. Publisher: Cambridge University Press.

C. K. W. Tam. Excitation of instability waves by sound —A physical interpretation. *Journal of Sound Vibration*, 105:169–172, Feb. 1986. ISSN 0022-460X. doi: 10.1016/0022-460X(86)90228-2. URL https://ui.adsabs.harvard.edu/abs/1986JSV...105..169T. ADS Bibcode: 1986JSV...105..169T.

T. D. Norum. Screech suppression in supersonic jets. *AIAA Journal*, 21(2):235–240, Feb. 1983. ISSN 0001-1452. doi: 10.2514/3.8059. URL https://arc.aiaa.org/doi/10.2514/3.8059. Publisher: American Institute of Aeronautics and Astronautics.

C. K. W. Tam, J. M. Seiner, and J. C. Yu. Proposed relationship between broadband shock associated noise and screech tones. *Journal of Sound and Vibration*, 110(2):309–321, Oct. 1986. ISSN 0022-460X. doi: 10.1016/S0022-460X(86)80212-7. URL https://www.sciencedirect.com/science/article/pii/S0022460X86802127.

L. Prandtl. Stationary waves in a gaseous jet. *Phys. Z.*, 5:599–601, 1904.

R. Lárusson, N. Andersson, and J. Östlund. Dynamic Mode Decomposition of a Separated Nozzle Flow with Transonic Resonance. *AIAA Journal*, 55(4):1295–1306, 2017. ISSN 0001-1452. doi: 10.2514/1.J054876. URL https://doi.org/10.2514/1.J054876. Publisher: American Institute of Aeronautics and Astronautics _eprint: https://doi.org/10.2514/1.J054876.

C.-W. Kuo, D. K. McLaughlin, P. J. Morris, and K. Viswanathan. Effects of jet temperature on broadband shock-associated noise. *AIAA journal*, 53(6):1515–1530, 2015. Publisher: American Institute of Aeronautics and Astronautics.

S. A. McInerny. Characteristics and Predictions of Far-Field Rocket Noise. *Noise Control Engineering Journal*, 38(1):5, 1992. ISSN 07362501. doi: 10.3397/1.2827802. URL http://www.ingentaconnect.com/content/ince/ncej/1992/00000038/00000001/art00001.

V. Chobotov and A. Powell. On the prediction of acoustic environments from rockets. E.M.-7-7 GM-TR-190, Rama-Wooldridge Corp., 1957.

J. Varnier. Experimental Study and Simulation of Rocket Engine Freejet Noise. *AIAA Journal*, 39(10):1851–1859, Oct. 2001. ISSN 0001-1452. doi: 10.2514/2.1199. URL https://arc.aiaa.org/doi/10.2514/2.1199. Publisher: American Institute of Aeronautics and Astronautics.

J. Kenny, C. Hobbs, K. Plotkin, and D. Pilkey. Measurement and Characterization of Space Shuttle Solid Rocket Motor Plume Acoustics. In *15th AIAA/CEAS Aeroacoustics Conference*, Miami, FL, May 2009. AIAA. URL https://ntrs.nasa.gov/citations/20090023641. NTRS Author Affiliations: NASA Marshall Space Flight Center, Wyle Labs., Inc., ATK Space Systems, Inc. NTRS Report/Patent Number: AIAA Paper 2009-3161 NTRS Document ID: 20090023641 NTRS Research Center: Marshall Space Flight Center (MSFC).

L. C. Sutherland. Progress and problems in rocket noise prediction for ground facilities. In *15th Aeroacoustics Conference*, 93-4383. AIAA, 1993. doi: 10.2514/6.1993-4383. URL https://doi.org/10.2514/6.1993-4383. _eprint: https://arc.aiaa.org/doi/pdf/10.2514/6.1993-4383.

M. M. James, A. R. Salton, K. L. Gee, T. B. Neilsen, and S. A. McInerny. Full-scale rocket motor acoustic tests and comparisons with empirical source models. *Proceedings of Meetings on Acoustics*, 18(1):040007, Oct. 2012a. doi: 10.1121/1.4870984. URL https://asa.scitation.org/doi/abs/10.1121/1.4870984. Publisher: Acoustical Society of America.

L. T. Mathews, K. L. Gee, and G. W. Hart. Characterization of Falcon 9 launch vehicle noise from far-field measurements. *The Journal of the Acoustical Society of America*, 150(1):620–633, July 2021. ISSN 0001-4966. doi: 10.1121/10.0005658. URL https://asa.scitation.org/doi/10.1121/10.0005658. Publisher: Acoustical Society of America.

K. L. Gee. A tale of two curves and their influence on rocket and supersonic jet noise research. *The Journal of the Acoustical Society of America*, 149(4):2159–2162, Apr. 2021. ISSN 0001-4966. doi: 10.1121/10.0003938. URL https://asa.scitation.org/doi/full/10.1121/10.0003938. Publisher: Acoustical Society of America.

B. Greska, A. Krothapalli, W. Horne, and N. Burnside. A near-field study of high temperature supersonic jets. In *14th AIAA/CEAS Aeroacoustics Conference (29th AIAA Aeroacoustics Conference)*, page 3026, 2008.

M. J. Crocker and R. C. Potter. Acoustic prediction methods for rocket engines, including the effects of clustered engines and deflected exhaust flow. Technical Report NASA-CR-566, NASA, Oct. 1966. URL https://ntrs.nasa.gov/citations/19660030602. NTRS Author Affiliations: Wyle Labs., Inc. NTRS Document ID: 19660030602 NTRS Research Center: Legacy CDMS (CDMS).

H. Nagamatsu and G. Horvay. Supersonic jet noise. In *8th Aerospace Sciences Meeting*, Aerospace Sciences Meetings. American Institute of Aeronautics and Astronautics, Jan. 1970. doi: 10.2514/6.1970-237. URL https://arc.aiaa.org/doi/10.2514/6.1970-237.

V. Koudriavtsev, J. Varnier, and A. Safronov. A Simplified Model of Jet Aerodynamics and Acoustics. In *10th AIAA/CEAS Aeroacoustics Conference*. AIAA, 2004. doi: 10.2514/6.2004-2877. URL https://arc.aiaa.org/doi/abs/10.2514/6.2004-2877. _eprint: https://arc.aiaa.org/doi/pdf/10.2514/6.2004-2877.

B. J. Greska. *Supersonic jet noise and its reduction using microjet injection*. Doctoral Thesis, The Florida State University, Florida, 2005.

W. J. Baars, C. E. Tinney, M. S. Wochner, and M. F. Hamilton. On cumulative nonlinear acoustic waveform distortions from high-speed jets. *Journal of Fluid Mechanics*, 749:331–366, 2014.

M. M. James, A. R. Salton, K. L. Gee, T. B. Neilsen, S. A. McInerny, and R. J. Kenny. Modification of directivity curves for a rocket noise model. *Proceedings of Meetings on Acoustics*, 18(1):040008, Oct. 2012b. doi: 10.1121/1.4870986. URL https://asa.scitation.org/doi/abs/10.1121/1.4870986. Publisher: Acoustical Society of America.

J. Ruf, D. McDaniels, and A. Brown. Nozzle Side Load Testing and Analysis at MSFC. In *45th AIAA/ASME/SAE/ASEE Joint Propulsion Conference & Exhibit*, Denver, Colorado, Aug. 2009. American Institute of Aeronautics and Astronautics. ISBN 978-1-60086-972-3. doi: 10.2514/6.2009-4856. URL http://arc.aiaa.org/doi/abs/10.2514/6.2009-4856.

K. De Kievit. Development of a rocket nozzle test facility for measurements of fluid-structure interaction phenomena. Master's thesis, Delft University of Technology, 2021.

O. Pearse. Fluid-structure interactions in overexpanded rocket nozzles. Master's thesis, Delft University of Technology, 2022.

J. He and Z.-F. Fu. *Modal analysis*. Butterworth-Heinemann, Oxford ; Boston, 2001. ISBN 978-0-7506-5079-3.

R. D. Mehta and P. Bradshaw. Design rules for small low speed wind tunnels. *The Aeronautical Journal*, 83: 443–453, 1979.

D. Schanz, S. Gesemann, A. Schröder, B. Wieneke, and M. Novara. Non-uniform optical transfer functions in particle imaging: calibration and application to tomographic reconstruction. *Meas. Sci. Technol.*, 24(2): 024009, Dec. 2012. ISSN 0957-0233. doi: 10.1088/0957-0233/24/2/024009. URL https://dx.doi.org/10.1088/0957-0233/24/2/024009. Publisher: IOP Publishing.

LaVision. *1010175 FlowMaster Shake-the-Box D10.2 manual*, 2022.

P. Welch. The use of fast Fourier transform for the estimation of power spectra: A method based on time averaging over short, modified periodograms. *IEEE Transactions on Audio and Electroacoustics*, 15(2):70–73, June 1967. ISSN 1558-2582. doi: 10.1109/TAU.1967.1161901. Conference Name: IEEE Transactions on Audio and Electroacoustics.

M. H. Wong, R. Kirby, P. Jordan, and D. Edgington-Mitchell. Azimuthal decomposition of the radiated noise from supersonic shock-containing jets. *The Journal of the Acoustical Society of America*, 148(4):2015–2027, Oct. 2020. ISSN 0001-4966. doi: 10.1121/10.0002166. URL https://asa.scitation.org/doi/10.1121/10.0002166. Publisher: Acoustical Society of America.

P. J. Schmid. Dynamic mode decomposition of numerical and experimental data. *Journal of Fluid Mechanics*, 656:5–28, Aug. 2010. ISSN 1469-7645, 0022-1120. doi: 10.1017/S0022112010001217. URL https://www.cambridge.org/core/journals/journal-of-fluid-mechanics/article/dynamic-mode-decomposition-of-numerical-and-experimental-data/AA4C763B525515AD4521A6CC5E10DBD4. Publisher: Cambridge University Press.

L. Laguarda, S. Hickel, F. Schrijer, and B. van Oudheusden. Numerical study of shocl-wave/turbulent boundary-layer interaction over a flexible panel. In *57th 3AF International Conference on Applied Aerodynamics*, 2023.